Max-Planck-Institut
für Meteorologie

MAX-PLANCK-GESELLSCHAFT

International Max Planck Research School
on Earth System Modelling

Impact of Surface Heterogeneities on Land Surface Water and Energy Fluxes

Philipp de Vrese

Hamburg 2015

Berichte zur Erdsystemforschung
Reports on Earth System Science

172
2015

Hinweis

Die Berichte zur Erdsystemforschung werden vom Max-Planck-Institut für Meteorologie in Hamburg in unregelmäßiger Abfolge herausgegeben.

Sie enthalten wissenschaftliche und technische Beiträge, inklusive Dissertationen.

Die Beiträge geben nicht notwendigerweise die Auffassung des Instituts wieder.

Die "Berichte zur Erdsystemforschung" führen die vorherigen Reihen "Reports" und "Examensarbeiten" weiter.

Notice

The Reports on Earth System Science are published by the Max Planck Institute for Meteorology in Hamburg. They appear in irregular intervals.

They contain scientific and technical contributions, including Ph. D. theses.

The Reports do not necessarily reflect the opinion of the Institute.

The "Reports on Earth System Science" continue the former "Reports" and "Examensarbeiten" of the Max Planck Institute.

Anschrift / Address

Max-Planck-Institut für Meteorologie
Bundesstrasse 53
20146 Hamburg
Deutschland

Tel./Phone: +49 (0)40 4 11 73 - 0
Fax: +49 (0)40 4 11 73 - 298

name.surname@mpimet.mpg.de
www.mpimet.mpg.de

Layout

Bettina Diallo and Norbert P. Noreiks
Communication

Copyright

Impact of Surface Heterogeneities on Land Surface Water and Energy Fluxes

Philipp de Vrese

Hamburg 2015

Philipp de Vrese
aus Hamburg, Deutschland

Max-Planck-Institut für Meteorologie
Bundesstrasse 53
20146 Hamburg

Als Dissertation angenommen
vom Fachbereich Geowissenschaften der Universität Hamburg

auf Grund der Gutachten von
Prof. Dr. Martin Claußen
und
Dr. Stefan Hagemann (habilitiert an der Universität Hamburg)

Hamburg, den 2.7.2015
Professor Dr. Christian Betzler
Leiter des Departments Geowissenschaften

Berichte zur Erdsystemforschung / Max-Planck-Institut für Meteorologie 172
Reports on Earth System Science / Max Planck Institute for Meteorology 2015

ISSN 1614-1199

Evolution is
"a change from an indefinite, incoherent homogeneity, to a definite, **coherent heterogeneity**; through continuous differentiations and integrations"

Herbert Spencer
(1820 - 1903)

English philosopher and father of an all-embracing conception of evolution (taken from Carneiro (1973) page 78).

Contents

List of Figures

List of Tables

AMIP Atmospheric Model Intercomparison Project (Gates et al., 1999)

ALBEDO effects related to the albedo of a tile

AWAD area weighted absolute difference between two simulations

CRU Climate Research Unit data (Harris et al., 2013)

EBSF simulation with an explicit representation of the permanent bare soil fraction

ECHAM6 current atmospheric component of the Max Planck Institute for Meteorology's Earth System Model (Stevens et al., 2013)

ECHAM/JSBACH MPI-ESM's atmospheric model ECHAM6 coupled to the land surface component JSBACH

ERA ERA-Interim reanalysis (Dee et al., 2011)

ESM Earth System Model

FLUX referring to both flux aggregation schemes; simple flux and VERTEX

GCM general circulation model

GLOBCOVER Global Land Cover Map 2009 (Arino et al., 2012)

GPCC Global Precipitation Climatology Centre data (Schneider et al., 2013)

IMP impact due to irrigation

IMV internal model variability

IWV vertically integrated water vapour

JSBACH land component of the Max Planck Institute for Meteorology's Earth System Model (Raddatz et al., 2007; Brovkin et al., 2009; Ekici et al., 2014)

LAI leaf area index

LCCS UN Land Cover Classification System (Di Gregorio, 2005)

LT local time

MPI-ESM Max Planck Institute for Meteorology's Earth System Model (Raddatz et al., 2007; Jungclaus et al., 2013; Stevens et al., 2013)

NPP net primary production

PARAM parameter aggregation scheme

PDF	probability density function
PFT	plant functional type
PLASA	percentage of the land surface significantly affected
SA-REGION	region between 0° - 45°N; 40°E - 130°E that comprises $\approx 70\,\%$ of the world's irrigated areas
SIMPLE	simple flux aggregation scheme
SSGS	spatial sub-grid scale
REMS	ratio of ensemble mean impact and respective ensemble spread
TRANS	effects related to the transpirational abilities of a tile
VERTEX	VERtical Tile EXtension
WFD	WATCH Forcing Data (Weedon et al., 2011)

1. Introduction

The surface energy and moisture fluxes constitute a key component of the earth system. On one hand they connect the planet's surface to the atmosphere, on the other hand they link the earth's energy and hydrological cycles via the fraction of energy expended in evapotranspiration (Fig. 1). From the roughly $136\,W\,m^{-2}$ of solar radiation, which are absorbed by the land surface, about $66\,W\,m^{-2}$ leave the surface in form of thermal radiation (residual of longwave upward and downward radiation), while $32\,W\,m^{-2}$ are directed towards the surface sensible heat flux and $38\,W\,m^{-2}$ towards the surface latent heat flux (Wild et al., 2014). This latent heat flux corresponds to an evapotranspiration rate of close to $490\,mm\,a^{-1}$ which amounts to a total terrestrial evapotranspiration of roughly $73 \cdot 10^3\,km^3\,a^{-1}$.

The total terrestrial evapotranspiration can be disaggregated with respect to different landscapes. For example grasslands contribute about $21 \cdot 10^3\,km^3\,a^{-1}$ while covering about $49 \cdot 10^6\,km^2$, forests contribute about $29 \cdot 10^3\,km^3\,a^{-1}$ and cover about $40 \cdot 10^6\,km^2$ (Oki and Kanae, 2006). Hence, evapotranspiration rates vary quite strongly between different land cover types. For grasslands the average evapotranspiration rate is about $429\,mm\,a^{-1}$ while for forests it is about $723\,mm\,a^{-1}$. Accordingly, the way the available energy at the surface is distributed between sensible and latent heat flux varies significantly between different land cover types.

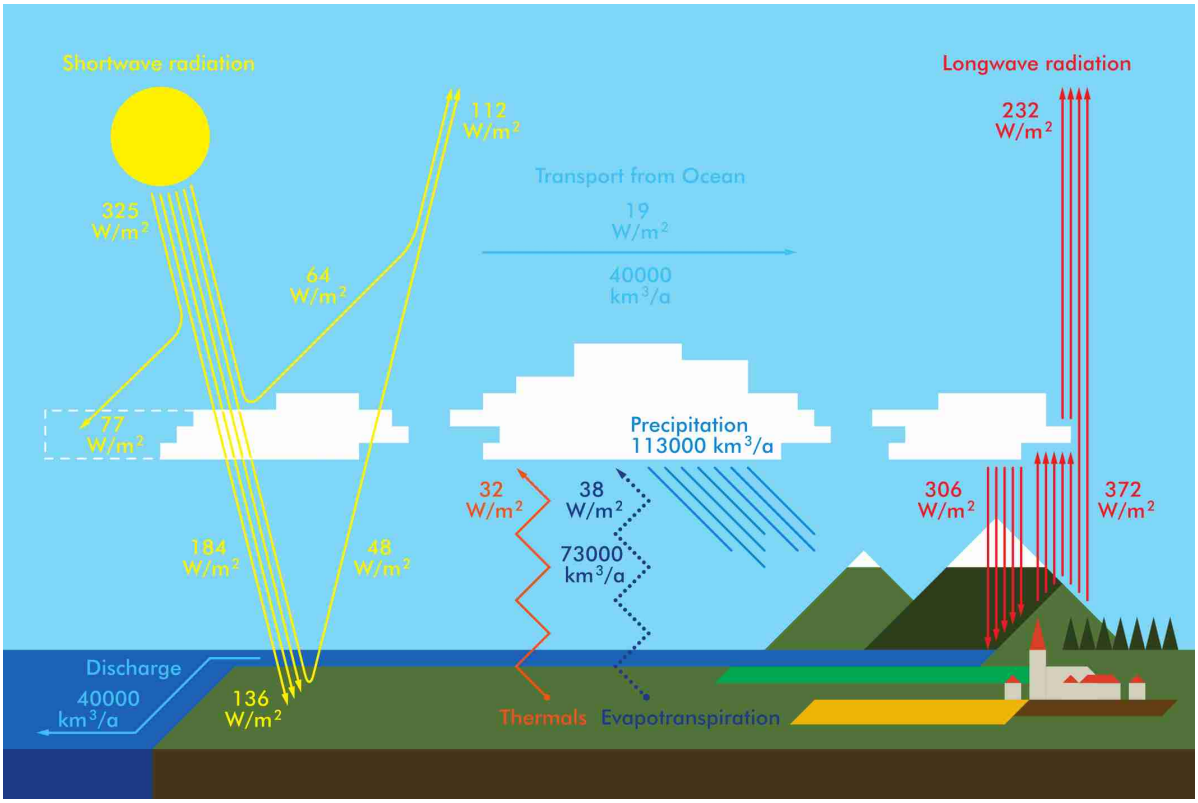

Figure 1: Terrestrial energy and water cycles

The surface fluxes have a non-linear dependency on the state of the surface and the atmosphere and are highly sensitive to variations in land surface characteristics such as land use, vegetation, topography, soil properties and hydrological characteristics, etc. The spatial and temporal scales on which these characteristics vary range from a few centimetres to kilometres and from minutes to millennia. Furthermore, many important processes, such as vegetation dynamics, the development of spatial patterns in the Subtropics and permafrost regions, the formation of wetlands and human-induced modifications of the surface take place on strongly diverging scales. Accordingly, the state of the land surface and the surface fluxes vary on the same broad range of scales (Sellers, 1991). This influence of heterogeneity on the vertical surface fluxes of energy and moisture constitutes the overarching leitmotif of this thesis and gives rise to countless scientific challenges, some of which can only be addressed via the use of numerical models.

The wide range of spatial scales, in combination with the non-linear nature of the relation between surface fluxes, processes and the state of surface and atmosphere, pose one of the fundamental difficulties in the representation of the surface fluxes in numerical models. In case of sub-grid scale heterogeneity, i.e. when the heterogeneity is not resolved by the horizontal structure of the grid, models require simplifying assumptions. Here, the aggregation schemes used in most Earth System Models (ESMs) presume that the surface fluxes within a model grid box have blended completely below the lowest model level of the atmosphere. Therefore, even though the surface is treated as heterogeneous, the atmosphere interacts with a mixed flux and remains spatially homogeneous (Fig. 2 b).

The following land surface schemes all represent surface heterogeneity explicitly, but provide grid box averaged surface fluxes or state variables as lower boundary condition for the respective atmospheric model: ORCHIDEE the land surface model of the Institut Pierre-Simon Laplace (Krinner et al., 2005; Dufresne et al., 2013), the National Center for Atmospheric Research's Community Land Model (Oleson et al., 2010), the Met Office's JULES (Best et al., 2011) and its predecessor MOSES2 (Essery and Clark, 2003), the Canadian land surface scheme CLASS, developed by the Canadian Climate Centre (Verseghy, 2009; Salzen et al., 2013) and LM3 from the Geophysical Fluid Dynamics Laboratory (Milly and Shmakin, 2002; Shevliakova et al., 2009).

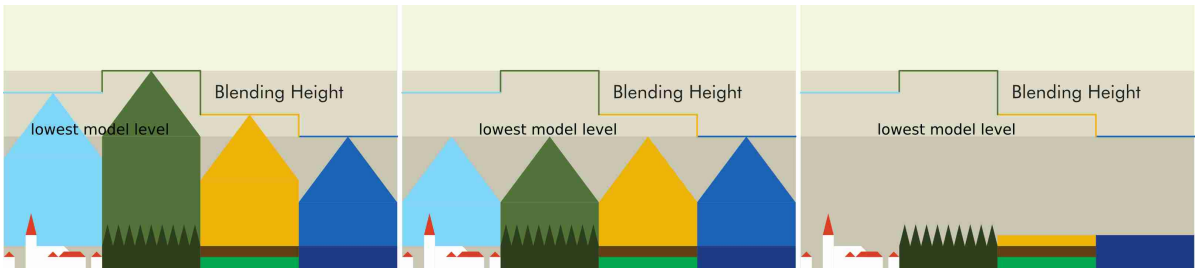

Figure 2: Different aggregation techniques: a) reality - ideal representation b) simple flux aggregation c) parameter aggregation

In other models the suppositions are even more simplistic and it is assumed that the heterogeneous surface within a grid box corresponds to an effective, homogeneous surface and can be represented by a set of parameters, which are valid for the entire grid box (Fig. 2 c). Here, the land component of the Max Planck Institute for Meteorology's Earth System Model (JSBACH) can be mentioned, but also earlier versions of SECHIBA as an element of ORCHIDEE (Schulz et al., 1998), MOSES as the predecessor of MOSES2 and JULES (Cox et al., 1999) and earlier versions of the Community Land Model (Bonan et al., 2002).

The validity of this assumption depends on the horizontal length scales of the represented surface heterogeneity. If these are small, i.e. heterogeneity consists of numerous, small and well mixed clusters (homogeneous subareas), the atmosphere may already be horizontally homogeneous close to the surface. However, with increasing length scales, the height increases up to which the vertical fluxes and the state of the atmosphere remain spatially heterogeneous. Many studies have investigated the relationship between the height above which the surface fluxes have blended, i.e. broadly speaking the blending height (Mahrt, 2000), and the horizontal length scale of surface heterogeneity. These studies place the blending height at roughly 1/200 - 1/10 of the heterogeneity's horizontal length scale (Mason, 1988; Claussen, 1995; Raupach and Finnigan, 1995; Best et al., 2004; Bou-Zeid et al., 2004). In many models the lowest atmospheric model level is located below a height of $50\,m$ (Arola, 1999). Thus, for these models the atmosphere can only be assumed to be spatially homogeneous for surface heterogeneities with a length scale of less than roughly $5000\,m$ ($500\,m$ - $10000\,m$).

In the context of this thesis a number of simulations were performed with the Max Planck Institute for Meteorology's Earth System Model (MPI-ESM), at a standard vertical resolution of 47 levels, of which the lowest is located on a height of approximately $30\,m$ and a horizontal resolution of $T63$, i.e. a grid-spacing of roughly $200\,km$ (Stevens et al., 2013). Before being able to address the research questions of this work, it needed to be established whether the assumption of spatial atmospheric homogeneity above a height of $\approx 30\,m$ possibly results in an inadequate description of spatial sub-grid scale heterogeneity. Consequently, a preliminary study was conducted that investigated blending heights on the global scale. In this qualitative study the blending height within a given model grid box is approximated by the characteristic length scales of the present sub-grid scale heterogeneity, derived from the Global Land Cover Map 2009 (GLOBCOVER), and a ratio of blending height and characteristic length scale of 1/100 (Section 6.1).

Based on these simple scale arguments, the study indicates that the blending height with respect to one third of global land surface heterogeneity is possibly located above a height of $30\,m$ and thus above the lowest model level of the MPI-ESM. Due to the distribution of heterogeneous areas, about half of the heterogeneous grid boxes on the land surface contain at least one surface type for which the assumption of spatial homogeneity on the lowest atmospheric level is invalid. From these results it may be inferred that a substantial share of the land surface is not correctly represented by the simpli-

fying assumptions on which the land surface-atmosphere coupling in most ESMs is based.

Motivated by these results and the overarching question regarding the relation between the state of the heterogeneous land surface and the surface fluxes, this thesis aims to answer the following research questions:

- How can spatial sub-grid scale (SSGS) heterogeneity of the atmosphere be accounted for in the coupling of land surface and atmosphere within ESMs?
- What is the effect of an explicit representation of surface and atmospheric SSGS heterogeneity on the simulated near surface processes with respect to different land cover types?
- What is the impact of an explicit representation of surface and atmospheric SSGS heterogeneity on climate on the global scale?

The issue of SSGS variability becomes especially relevant for heterogeneities exhibiting characteristics that strongly contrast the surrounding surfaces. In these constellations, a realistic coupling of land surface and atmosphere is crucial for accurately describing the relevant processes. One prominent example for this is irrigation-based agriculture. Here, on scales ranging between tens of metres and several kilometres, areas featuring highly saturated soils and a dense vegetation cover are often located in arid or semiarid regions and distinctly impact the energy and hydrological cycle (Fig. 3).

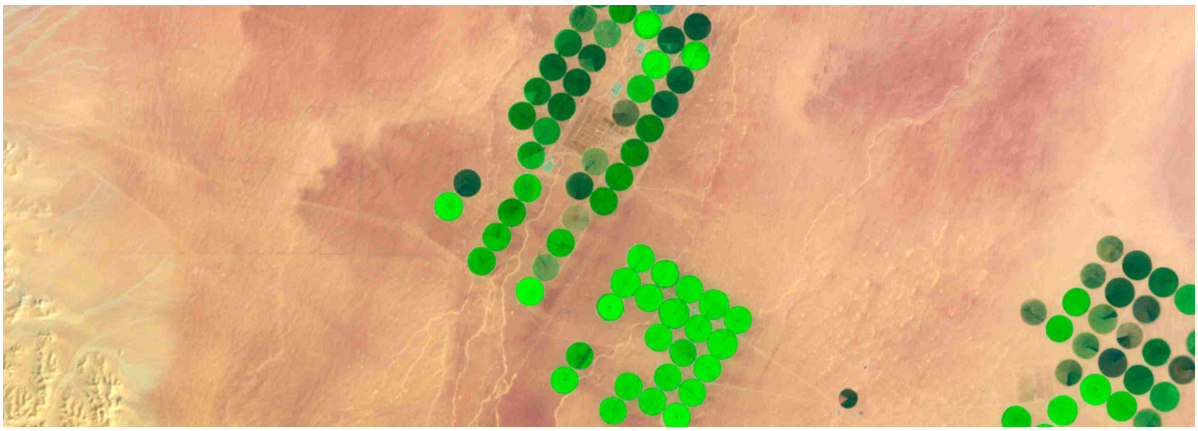

Figure 3: Irrigation in Saudi Arabia (scale of individual field $\approx 1\,km$; ©NASA Earth Observatory)

While covering only around 2 % of the global land surface, irrigation contributes about $2600\,km^3\,a^{-1}$ ($\approx$ 4 %) to the total terrestrial evapotranspiration (Gordon et al., 2005; Siebert et al., 2005; Oki and Kanae, 2006). Irrigation constitutes one of the major, land-use change related, anthropogenic influences on climate (Gordon et al., 2005; Lobell et al., 2006b), and numerous regional studies demonstrated a pronounced impact of irrigation on regional climate and regional circulations such as the Indian monsoon (Douglas et al., 2006; Kueppers et al., 2007; Douglas et al., 2009; Lobell et al., 2009; Saeed et al., 2009). Additionally, the importance of irrigation for the welfare of a large

share of the world's population makes it a very relevant scientific topic. Irrigation-based agriculture provides about 40 % of the global crop yield and contributes about 70 % to humanity's fresh water demand (Wada et al., 2013). Hence, as a final research question, this thesis addresses the following issue:

– How does irrigation-based agriculture in arid regions influence the regional and possibly global climate? Furthermore, which effect does the surface-atmosphere coupling have on the representation of irrigation and how large is the associated uncertainty in simulations?

The dissertation answers the above questions in the order they are listed, which results in the following document structure:

– In chapter 2, an improved approach for the land surface-atmosphere coupling is proposed. This approach accounts for SSGS heterogeneity on the lowest atmospheric model levels and resolves the vertical turbulent mixing process with respect to the heterogeneity [the corresponding paper has been submitted to "Boundary-Layer Meteorology" and is currently being updated according to the reviewers' specification].

– The 3rd chapter deals with the influence of SSGS heterogeneity on the simulated near surface processes in different land cover types. Furthermore, the impact of the surface-atmosphere coupling on the simulated global climate is investigated [the corresponding paper has been submitted to "Journal of Hydrometeorology" and is currently being reviewed].

– Chapter 4 focuses on the impact of irrigation on climate, especially its remote, even intercontinental effects [the corresponding paper is in preparation].

– Chapter 5 investigates uncertainties associated with the simulated impact of irrigation on climate. The respective sources of uncertainties are related to the general model structure, namely the surface-atmosphere coupling, and to the representation of certain irrigation characteristics such as the irrigation efficiency [the corresponding paper is in preparation].

Each of the chapters 2 - 5 is set up as an independent article, designed for publication in a peer reviewed journal. Hence, there is a certain extent of repetition of the basic concepts between the individual chapters. Furthermore, some important findings could not be included in the respective papers as they deviate from the article's immediate scope. The frame of this thesis provides the opportunity to cover the research questions more holistically and some findings can be presented that could not be included in the respective articles:

– Chapter 6 includes results which are important for the research questions of this thesis but could not be included in the above chapters:

* The preliminary study is presented in which blending heights were investigated on the global scale.

* With respect to chapter 3, the effect of differences in the albedo of different land cover types is investigated. Additionally, the impact on the state of individual tiles and related processes such as primary productivity is investigated. Contrary to chapter 3, the focus is on simulations in which atmospheric feedbacks are accounted for.

* The impact of explicitly representing areas uninhabitable for plants is presented, e.g. deserts or degraded areas featuring infertile soils.

– Chapter 7 summarizes the main findings of this work with respect to the above mentioned research questions and provides an outlook for future research.

2. On the Representation of Heterogeneity in Land Surface-Atmosphere Coupling

2.1. Introduction

Representing spatially heterogeneous processes taking place on scales below those resolved by present day numerical models is one of the key challenges in Earth System Modelling. Here, one aspect is to accurately describe the interaction between the land surface and the atmosphere.

Various land surface characteristics such as topography, land use, soil and vegetation characteristics etc. vary on diverging spatial scales and time scales, ranging from a few centimetres and minutes to hundreds of kilometres and years. Consequently, the state of the surface varies on the same scales. Surface energy, mass and momentum fluxes physically link the surface and the atmosphere and often have a highly non-linear dependency upon this horizontally strongly heterogeneous state of the land surface (Sellers, 1991). Thus, considering the range of scales which need to be accounted for reveals the difficulties that occur when attempting to represent the affected processes on the grid scale of an Earth System Model (ESM).

In present ESMs different strategies are pursued to describe the contribution of sub-grid variability and aggregate the sub-grid scale information of the land surface to match the grid of the atmosphere. Due to the non-linear nature of processes involved, every strategy results in a distinct representation of the land surface-atmosphere interaction. The nomenclature in respect to these strategies and their various implementations is confusing at best. Hence, a few definitions of terms that will be used in this work shall be given.

One general distinction between strategies can be made between those based on statistical and those based on discrete representations of sub-grid scale heterogeneity (Giorgi and Avissar, 1997). In methods belonging to the first group, sub-grid scale variability is represented by a variable specific probability density function (PDF), and the aggregation of the sub-grid scale parameter values is performed by integrating over the parameter phase space defined by the respective PDF. In this work, the focus will be placed on discrete representations of sub-grid scale heterogeneity and no further discussion of the statistical approach will follow. A good overview about this approach can, for example, be found in Avissar (1992).

The basic assumption of the discrete approaches is that a grid box can be sectioned into discrete subdivisions, the so-called “tiles” or “patches”, which themselves exhibit homogeneous characteristics. These are usually represented simply by their cover fraction, i.e. the fraction of the grid box area which they cover, ignoring the actual geographical location. However, methods exist in which the tiles represent clearly defined areas with a specific size and position within the grid box (Seth et al., 1994). The discrete schemes

further divide into two major branches. In one branch sub-grid scale heterogeneity is not explicitly accounted for but soil and vegetation parameters of the sub-grid scale patches are aggregated to one effective value representing the entire grid box. Based upon these effective values the surface fluxes are calculated. In this work this will be referred to as the "parameter aggregation". The most common approach to determine the effective grid parameters is by averaging all sub-grid scale parameter values usually weighted by their respective cover fractions. Another possibility, the so called "dominant approach", is to represent a grid box by the characteristics of the dominant tile i.e. the one that covers the largest fraction of the grid box (Dickinson, 1986). However, in this work the term parameter aggregation always refers to the aggregation based upon the area-weighted average.

The second branch explicitly accounts for sub-grid scale heterogeneity and calculates fluxes based upon the tile specific characteristics for all tiles in a grid box individually. Here, two approaches can be distinguished which Koster and Suarez (1992) define as the "mosaic" and the "mixture approach". The two approaches differ in the assumptions made about the extent to which the individual tiles interact. Note that here the use of terms substantially varies between studies. For instance, Ament and Simmer (2006) use a distinction, which is based upon the representation of the subdivisions either as a localized patch in the grid box or by their cover fraction to distinguish between the mosaic and a tile approach. In contrast to the use of terms of Koster and Suarez (1992), Molod and Salmun (2002) use the term mixture approach for a form of parameter aggregation.

The mosaic approach assumes that the different tiles or patches in one grid box are horizontally well separated and below the lowest computational level of the atmospheric model, the horizontal exchange between tiles is negligible in comparison to the vertical fluxes. Consequently, the interaction of each surface tile and the overlying atmosphere is completely independent of the other tiles present in the grid box. In the classical mosaic approach the assumption of the independence of each tile is valid only for the surface layer, and above all processes including the turbulent vertical fluxes are modelled based upon the grid mean state (Avissar and Pielke, 1989; Giorgi, 1997). However, the mosaic approach has been augmented to preserve the independence of tiles throughout the entire turbulent atmospheric boundary layer at least for the vertical turbulent transport (Molod et al., 2003).

In contrast to this, the mixture or tile approach assumes that surface heterogeneity occurs in the form of numerous small clusters. The tiles within one grid box are very well mixed and the horizontal turbulent fluxes are large compared to the vertical turbulent fluxes. Therefore, the properties of air parcels that originate from different tiles are perfectly mixed horizontally even below the lowest atmospheric model level and the atmosphere interacts only with these mixed fluxes (Koster and Suarez, 1992). Consequently, the state of the atmosphere is spatially homogeneous within a grid box. Both mosaic and mixture approach are often referred to as flux aggregation techniques but in the present study the term "simple flux aggregation" is reserved for the mixture or tile

approach.

Many observational and modelling studies suggest that both of these underlying assumptions are erroneous under certain conditions. The signal related to a specific surface heterogeneity may be detectable up to a given height within the planetary boundary layer that lies far above the surface layer. This indicates that the assumption of a complete mixing of fluxes below the lowest atmospheric model level (in many models this is below $50\,m$ (Arola, 1999)) is not valid in the respective conditions. In different conditions fluxes may not be in equilibrium with the local surface even low within the surface layer, indicating that the horizontal turbulent transport processes have a noticeable impact and are not negligible. This rebuts the assumption of the independence of tiles made in the mosaic approach (Wieringa, 1976; Mason, 1988; Claussen, 1995; Raupach and Finnigan, 1995; Avissar and Schmidt, 1998; Mahrt, 2000; Bou-Zeid et al., 2004; Patton et al., 2005; Ma et al., 2008).

In the following, a technique is proposed which supersedes the need for potentially invalid simplifications when coupling land surface and atmosphere. Therefore, when implemented in a land surface model such as JSBACH (Raddatz et al., 2007; Brovkin et al., 2009), this technique could improve the aggregation of sub-grid scale information for the coupling to an atmospheric general circulation model (GCM) such as ECHAM6 (Stevens et al., 2013). This coupling scheme, which provides a **VER**tical **T**ile **EX**tension (VERTEX), is capable of representing the turbulent mixing process more realistically as it resolves the process with respect to the surface tiles and at the same time explicitly accounts for the horizontal component of the process. Thus, within a model grid box the turbulent transport is treated as a two-dimensional process (vertical and horizontal) rather than a one-dimensional process (vertical only).

In Sect. 2.2 the VERTEX scheme will be introduced. Firstly (Sect. 2.2.1), we will discuss how the horizontal component of the turbulent mixing process i.e. the mixing between different tiles can be related to the blending height concept (see e.g. Mahrt (2000)). In Sect. 2.2.2 and Sect. 2.2.3 a concept will be presented to integrate an explicit horizontal component into an atmospheric model's (vertical) turbulent exchange scheme. This includes closing the surface energy balance based on the assumption of a horizontally varying state of the lowest atmospheric model levels within a model grid box.

In the subsequent section the VERTEX scheme will be employed in two example cases in order to demonstrate its impact on the simulated structure of the atmosphere (Sects. 2.3.1 and 2.3.2). Additionally, we will compare results of simulations with the different flux aggregation schemes, to gain further insights into the mechanisms and the magnitude of potential impacts on the simulated mean state of a grid box (Sect. 2.3.3). Many studies exist, usually focused on the local scale, which have compared parameter aggregating to flux aggregating techniques (e.g., Avissar and Pielke (1989); Polcher et al. (1996); Van den Hurk and Beljaars (1996); Cooper et al. (1997); Molod and Salmun (2002); Essery et al. (2003); Heinemann and Kerschgens (2005); Ament and Simmer (2006)). These

studies agree that by employing an aggregation of fluxes the representation of processes clearly improves compared to an aggregation of parameters. In addition to this many of the studies find an improvement of the simulated climate. Thus, we also compare the simulations performed with the different flux aggregation methods to simulations which are carried out using a parameter aggregation scheme and use these comparisons as a reference for the magnitude of potential impacts. Finally, the main findings are summarized in Sect. 2.4.

2.2. The VERTEX scheme

2.2.1. Blending height and horizontal mixing

Studies investigating the vertical extent to which the impact of surface heterogeneity is detectable often employ the concept of a blending height. The blending height can be understood as a scaling depth which "describes the decrease of the influence of surface heterogeneity with height" below a certain threshold (Mahrt, 2000). In reverse this means that below the blending height the influence of individual surface features is perceptible. Hence, the blending height can also be interpreted as the maximum distance that a surface feature perceptibly exerts its influence in the vertical direction. The blending height $h_{blend,i}$ can be expressed as a function of the friction velocity $u_{*,i}$, the horizontal wind speed U at the blending height, the characteristic length scale $L_{hetero,i}$ of a given surface feature and the two non-dimensional coefficients C and p (Raupach and Finnigan, 1995; Mahrt, 2000).

$$h_{blend,i} = C \cdot (\frac{u_{*,i}}{U})^p \cdot L_{hetero,i} \tag{1}$$

Equation 1 gives the general form of expressing the blending height, applicable in near-neutral or stable conditions, when shear driven turbulence predominate. In case of a convective boundary layer, turbulence is predominantly buoyancy driven. Under unstable conditions, the dependency of the blending height on instability (given by $\frac{u_{*,i}}{U}$) may be too weak and a formulation which accounts for a more explicit dependence on instability may be required. For a "thermal blending height" Wood and Mason (1991) suggest an approximation which is based on U, $L_{hetero,i}$, the spatially averaged surface sensible heat flux H_0, the spatially averaged potential temperature θ_0 and the coefficient C_{therm}.

$$h_{blend,i} = C_{therm} \cdot \frac{H_0}{U \cdot \theta_0} \cdot L_{hetero,i} \tag{2}$$

By assuming a fixed relation between height and the magnitude of the influence that a heterogeneity exerts on the flow at a height h_z, one can relate the ratio of a given height and the blending height to the strength of the influence which surface heterogeneity has at this height. By further assuming that the decrease of the influence of a surface feature with height can be attributed to horizontal mixing, one can describe the degree of mixing $deg\_mix_{z,i}$ at a given height h_z above a surface feature i of a given horizontal

length scale $L_{hetero,i}$ by the blending height $h_{blend,i}$ and the height h_z according to:

$$deg\_mix_{z,i} = f(h_z, h_{blend,i}) \qquad \text{, for } 0 \leq h_z \leq h_{blend,i} \tag{3}$$

Furthermore, in a grid box containing n tiles, $Fmix_{z,i,j}$, the proportion of the flux originating from a given surface feature j with cover fraction $sfrac_j$ which has mixed into the flux above a surface feature i at height z, is given by:

$$Fmix_{z,i,j} = deg\_mix_{z,i} \cdot \frac{deg\_mix_{z,j} \cdot sfrac_j}{\sum_{k=1}^{n} deg\_mix_{z,k} \cdot sfrac_k} \qquad \text{, for j} \neq \text{i} \tag{4a}$$

$$Fmix_{z,i,j} = (1 - deg\_mix_{z,i} \cdot (1 - \frac{deg\_mix_{z,j} \cdot sfrac_j}{\sum_{k=1}^{n} deg\_mix_{z,k} \cdot sfrac_k})) \qquad \text{, for j} = \text{i} \tag{4b}$$

The relation between the terms used in Eq.4 is summarized in Figure 4.

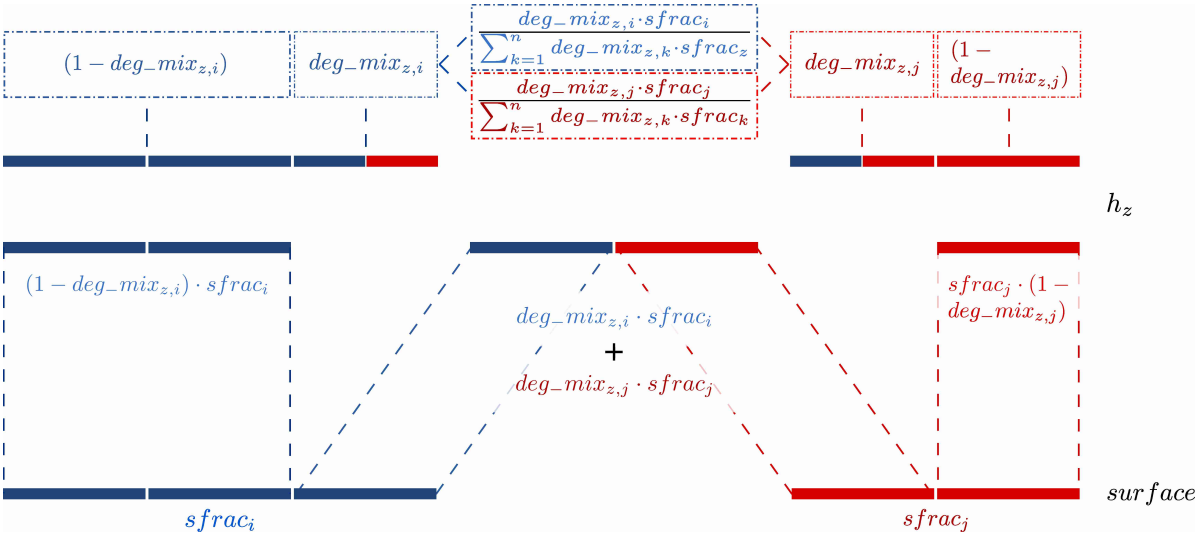

Figure 4: Terms constituting $Fmix$ in Eq.4 in case of two differing surfaces (blue and red)

So far the approach accounts only for the direct "aggregation" effects related to surface heterogeneity and neglects "dynamical" effects which are associated with sub-grid scale circulations (Molod et al., 2003). Due to spatial temperature and the consequent density and pressure variability, barocline circulations develop, which reduce strong spatial gradients. For low horizontal model resolutions, i.e. a typical GCM grid-spacing $> 100\,km$, these mesoscale circulations become increasingly important. There are indications that organized mesoscale circulations predominantly occur for length scales of $L_{hetero} > 10\,km$ (Baidya Roy, 2003). However, there is observational evidence for atmospheric spatial heterogeneity also on these scales (Segal et al., 1989; Angevine, 2003; Banta, 2003; Strunin et al., 2004). This suggests that, while mesoscale circulations have a balancing effect, spatially heterogeneous atmospheric structures prevail even on scales of $L_{hetero} > 10\,km$.

In general the concept of the tiling method does not allow to explicitly represent subgrid scale circulations, as it does not provide any information on the relative position of the tiles within the grid box. Nonetheless, it is conceivable to parametrize unresolved circulations by factoring them in in the formulation of horizontal mixing of vertical fluxes, i.e. in the calculation of $deg\_mix_{z,i}$ and $Fmix_{z,i,j}$ (Lynn et al., 1995a,b). For example, by assuming that mesoscale circulations act to reduce strong spatial gradients, $deg\_mix_{z,i}$ or $Fmix_{z,i,j}$ could be increased for strong differences in surface temperature between tile i and the the grid box mean temperature $\Delta t_{surf,i,1-n}$ or for temperature differences between tile i and j $\Delta t_{surf,i,j}$.

$$deg\_mix_{z,i} = f(\Delta t_{surf,i,1-n}, h_z, h_{blend,i}) \qquad \text{, for } 0 \leq h_z \leq h_{blend,i} \tag{5a}$$

$$Fmix_{z,i,j} = f(\Delta t_{surf,i,j}, deg\_mix_{z,1-n}, sfrac_{1-n}) \tag{5b}$$

Modelling the horizontal component of the turbulent mixing process requires quantifying the strength of the horizontal component of the process between two given vertical model levels $l-1$ and l. To calculate $Fmix_{l,i,j}$, the proportion of the flux from a given tile j on level $l-1$ that has mixed into the flux in tile i on level l the following equation can be used:

$$Fmix_{l,i,j} = (1 - \frac{1 - deg\_mix_{l,i}}{1 - deg\_mix_{l-1,i}}) \cdot \frac{deg\_mix_{l,j} \cdot sfrac_j}{\sum_{k=1}^{n} deg\_mix_{l,k} \cdot sfrac_k} \qquad \text{, for j} \neq \text{i} \tag{6a}$$

$$Fmix_{l,i,j} = \frac{1 - deg\_mix_{l,i}}{1 - deg\_mix_{l-1,i}} + (1 - \frac{1 - deg\_mix_{l,i}}{1 - deg\_mix_{l-1,i}}) \cdot \frac{deg\_mix_{l,j} \cdot sfrac_j}{\sum_{k=1}^{n} deg\_mix_{l,k} \cdot sfrac_k} \qquad \text{, for j} = \text{i} \tag{6b}$$

In the formulation the levels $l-1$ and l correspond to two given heights $z - \delta z$ and z above the surface. Here the fluxes have already mixed between the surface and level $l-1$, and $Fmix_{l,i,j}$ accounts only for the additional horizontal mixing that occurs between the levels $l-1$ and l. With the help of these mixing coefficients the turbulent mixing process can be represented as a two-dimensional process, which will be described in detail below.

2.2.2. Vertical diffusion and horizontal mixing

The (vertical) turbulent mixing process of humidity, sensible heat and momentum is often described by a diffusion equation:

$$\frac{\partial x}{\partial t} = \frac{\partial}{\partial z}(K \frac{\partial x}{\partial z}) \tag{7}$$

Where K $[m^2\, s^{-1}]$ denotes the vertical eddy diffusion coefficient ("Austauschkoeffizient" or eddy "diffusivity") and x the transported quantity. The transport of momentum can be modelled the same way as that of heat and moisture. However, we will limit the following explanation to the latter two and x represents either dry static energy or specific humidity.

For a horizontally homogeneous grid box, this can be written in a vertically discretized way, using an implicit time-stepping. The rate of change of humidity or sensible heat can be expressed at a given level l by the following finite difference formula:

$$\frac{x_l^{t+1} - x_l^t}{\Delta t} = \frac{1}{\Delta z_l} \cdot (K_{l+\frac{1}{2}} \cdot \frac{x_{l+1}^{t+1} - x_l^{t+1}}{\delta z_l} - K_{l-\frac{1}{2}} \cdot \frac{x_l^{t+1} - x_{l-1}^{t+1}}{\delta z_{l-1}}) \tag{8}$$

Where Δz_l pertains to the thickness of a layer encompassed by two full vertical model levels on which the variables are calculated, whereas δz_l pertains to a layer that is bounded by two intermediate levels on which the fluxes are calculated (see e.g., Polcher et al. (1998)). Following Richtmyer and Morton (1967), this set of equations can be solved for the entire atmosphere at time step $t + 1$. At the top of the atmospheric column ($l = N$) the fluxes are assumed to be zero which allows the top level dry static energy (specific humidity) to be describe by a function of the dry static energy (specific humidity) on the level below and the two coefficients $E_{x,l-1}^t$ and $F_{x,l-1}^t$:

$$x_l^{t+1} = E_{x,l-1}^t \cdot x_{l-1}^{t+1} + F_{x,l-1}^t \tag{9}$$

Here, the $E_{x,l-1}^t$ and $F_{x,l-1}^t$ at the top of the atmosphere are determined by Eq. 8 (for $l = N$) applying the zero flux condition.

When the $E_{x,l}^t$ and $F_{x,l}^t$ are known for the superjacent level, this process can be repeated for each level in a descending order from $l = N - 1$ to the surface ($l = 0$). Here the surface energy balance is solved which yields the dry static energy and humidity at the surface at time step $t + 1$. Having determined the surface dry static energy and humidity, these can be used in a back-substitution to calculate the new values for the entire atmospheric column using Eq. 9 (Schulz et al., 2001).

In the case of a horizontally heterogeneous grid box, Eq. 7 needs to be augmented to allow for different tiles and a turbulent mixing process which consists of not only a vertical component but also a quasi horizontal component i.e. the mixing of fluxes between tiles. When considering a horizontally heterogeneous atmosphere, the rate of change of a given variable within tile i is given by the following formula:

$$\frac{\partial X_i}{\partial t} = \frac{\partial}{\partial z}(\sum_{j=1}^{n} Fmix_{z,ij} \cdot K_{ij}^* \cdot \frac{\partial X_{ij}^*}{\partial z^*}) \tag{10}$$

In Eq. 10 $\frac{\partial X_{ij}^*}{\partial z^*}$ denotes the gradient of X_{ij}^* between two heights z_1 and z_2 and between two tiles i and j, K_{ij}^* is the vertical eddy-diffusivity between z_1 and z_2 and between the tiles i and j and $Fmix_{z,i,j}$ the degree of mixing between tile i and j (Fig. 5).

The discretization of Eq. 10 in the vertical and in time yields a representation of the turbulent mixing process, which takes into account a quasi horizontal, inter-tile compo-

nent.

$$\frac{x_{l,i}^{t+1} - x_{l,i}^{t}}{\Delta t} = \frac{1}{\Delta z_l} \cdot \Big(\sum_{j=1}^{n} Fmix_{l,j,i} \cdot K^*_{l+\frac{1}{2},j,i} \cdot \frac{x_{l+1,j}^{t+1} - x_{l,i}^{t+1}}{\delta z_l} - \sum_{j=1}^{n} Fmix_{l-1,i,j} \cdot K^*_{l-\frac{1}{2},i,j} \cdot \frac{x_{l,i}^{t+1} - x_{l-1,j}^{t+1}}{\delta z_{l-1}} \Big) \tag{11}$$

In order to be able to solve the set of equations analogous to the case of a horizontally homogeneous grid box, further simplifying assumptions are required (Fig. 5):

- For a given level l and tile i, the tile specific flux connecting level l to the level above $(l+1)$ is determined exclusively by the vertical gradient of x within the respective tile i,
- whereas the flux connecting level l to the subjacent level $l-1$ is a weighted average of the tile individual fluxes as the fluxes from different tiles $(1, .., j, .., n)$ have mixed to a certain degree (given by $Fmix_{l-1,i,j}$).

These simplifications allow Eq. 11 to be written using simple vertical gradients of x and the vertical eddy-diffusivity K instead of K^*. Equation 12 gives a simplified discretization of the vertical diffusion equation which takes into account horizontal mixing of the tile specific fluxes within a grid box.

$$\frac{x_{l,i}^{t+1} - x_{l,i}^{t}}{\Delta t} = \frac{1}{\Delta z_l} \cdot \Big(K_{l+\frac{1}{2},i} \cdot \frac{x_{l+1,i}^{t+1} - x_{l,i}^{t+1}}{\delta z_l} - \sum_{j=1}^{n} Fmix_{l-1,i,j} \cdot K_{l-\frac{1}{2},j} \cdot \frac{x_{l,j}^{t+1} - x_{l-1,j}^{t+1}}{\delta z_{l-1}} \Big) \tag{12}$$

The concept of solving the vertical diffusion scheme remains to describe the dry static energy (specific humidity) on a given level as a function of the dry static energy (specific humidity) on the subjacent level. However, when considering a given tile within a horizontally heterogeneous grid box, the formulation has not only to include the same tile on the level below but all the tiles within the grid box.

$$x_{l+1,i}^{t+1} = F_{x,l,i}^{t} + \sum_{j=1}^{n} x_{l,j}^{t+1} \cdot E_{x,l,i,j}^{t} \tag{13}$$

This formulation can be inserted into Eq. 12 and the resulting set of equations can be subsequently solved from the first level above the blending height until the second lowest atmospheric model level (see Sect. A). The system of representing the state on a given atmospheric level by the state on the subjacent level also provides the basis for the simplifying assumptions used in the scheme. For level l and tile i, it is possible to describe the fluxes between level l and the superajacent level $l+1$ simply by the local gradient of x, i, because the upper boundary used to calculate the fluxes, i.e. $x_{l+1,i}$ already includes the dependencies on the states of all the tiles on level l (Fig. 5). As the formulation of the coefficients $F_{x,l,i}^{t}$ and $E_{x,l,i,j}^{t}$ for each level (level l) is based upon the right hand side of Eq. 12 in respect of the level above (level $l+1$), the scheme

is conservative in terms of the transported variables i.e. specific humidity and dry static energy (see Appendix A). Here, Eq.11 and Eq.12 (when substituting $x^{t+1}_{l+1,i}$ with Eq.13), yield only minor differences, except during the transition between a stable and an unstable stratification. In these circumstances it is conceivable that $x^{t}_{l+1,i} \approx x^{t}_{l,i}$ and $x^{t}_{l+1,j} \approx x^{t}_{l,j}$, hence $K \approx 0$, but $x^{t}_{l+1,i} <> x^{t}_{l,j}$ and $x^{t}_{l+1,j} <> x^{t}_{l,i}$, hence $K^* > 0$. However, a preliminary investigation indicated that this results in differences in the exact time step in which the transition occurs, but did not cause large or lasting differences between the simulated states of the tiles.

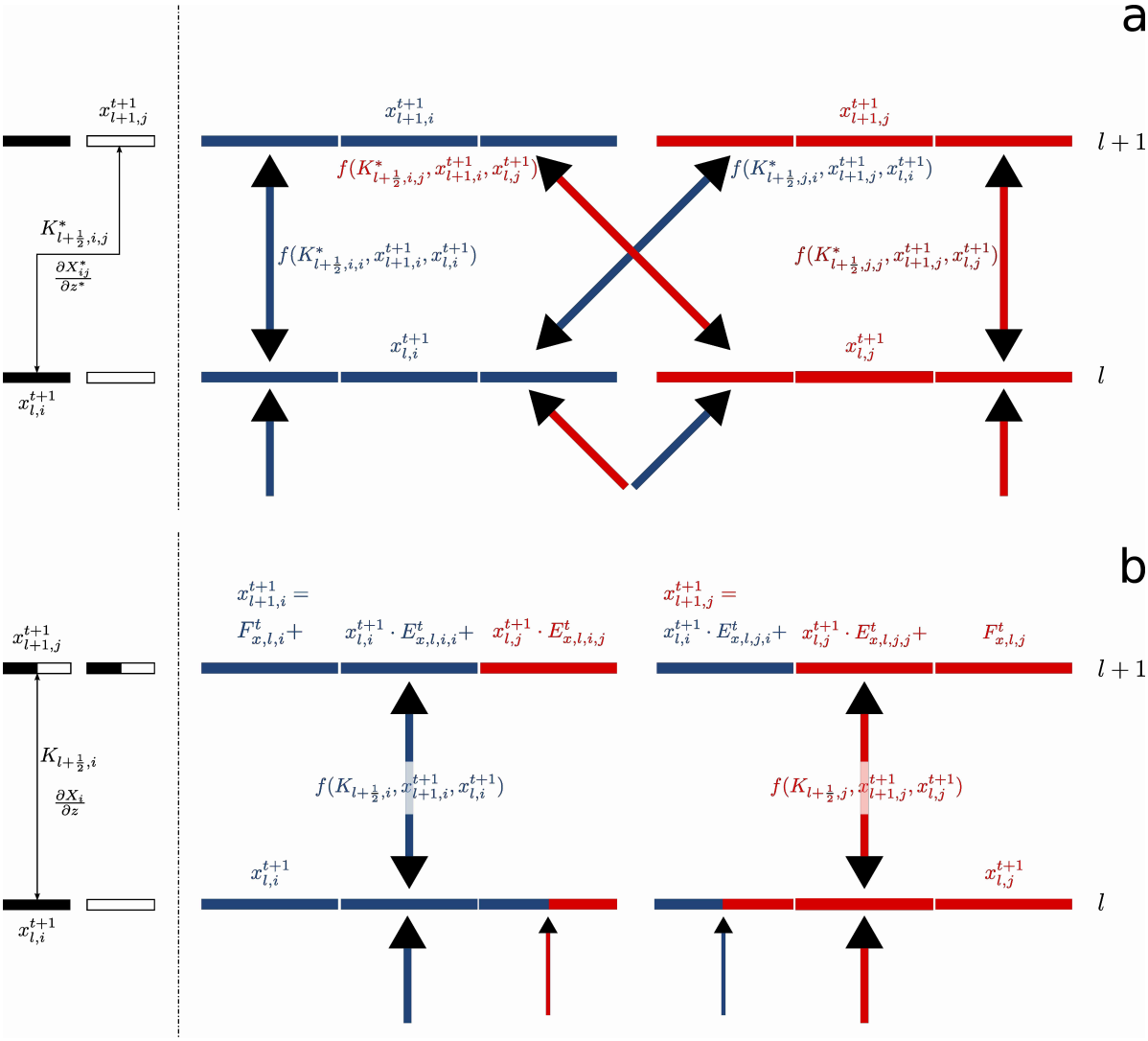

Figure 5: Simplifying assumptions for the vertical turbulent transport: a) Terms used in Eq.11, b) Terms used in Eq.12, substituting $x^{t+1}_{l+1,i}$ and $x^{t+1}_{l+1,j}$ with Eq.13

To describe the dry static energy and specific humidity on the lowest atmospheric level, the surface fluxes have to be utilized. This constitutes the link between surface and atmosphere.

2.2.3. Surface fluxes and surface energy balance

In order to couple the atmosphere to the land surface, a relation between the energy and moisture fluxes at the surface and the values of dry static energy and specific humidity at the lowest atmospheric model level is required (Best et al., 2004). The same simplifications which are applied higher up in the atmosphere are also applied to the surface fluxes. Conceptually this means that a distinction is being made between considering the fluxes just above the surface $Q_{x,j}^{t+1,*}$ and considering them just below the lowest atmospheric model level $Q_{x,i}^{t+1}$. At the surface tile specific fluxes are assumed to depend exclusively on local surface-atmosphere gradients and can be calculated according to:

$$H_i^{t+1*} = c_{couple,i} \cdot (s_{1,i}^{t+1} - s_{surf,i}^{t+1}) \tag{14a}$$

$$LE_i^{t+1*} = c_{couple,i} \cdot L \cdot \beta_i \cdot (q_{1,i}^{t+1} - \alpha_i \cdot q_{sat}(cp \cdot s_{surf,i}^{t+1})) \tag{14b}$$

Here $c_{couple,i}$ is the product of the surface drag coefficient and the horizontal wind speed, L the latent heat of evapotranspiration, α_i and β_i parameters to control evapotranspiration with respect to the availability of water.

At the lowest atmospheric level, fluxes have horizontally mixed to a certain degree and the energy and moisture fluxes on the lowest atmospheric level $Q_{x,i}^{t+1}$ can be described by the tile specific fluxes just above the surface $Q_{x,j}^{t+1,*}$ and the mixing coefficients $Fmix_{1,i,j}$ described in Sect. 2.2.1.

$$Q_{x,i}^{t+1} = \sum_{j=1}^{n} Fmix_{1,i,j} \cdot Q_{x,j}^{t+1,*} \tag{15}$$

The rate of change of dry static energy (specific humidity) on the lowest atmospheric level can, analogously to Eq. 36, be described by the following equation:

$$\frac{x_{1,i}^{t+1} - x_{1,i}^{t}}{\Delta t} = \frac{1}{\Delta z_l} \cdot (K_{1+\frac{1}{2},i} \cdot \frac{F_{1,i}^{t} + \sum_{j=1}^{n} x_{1,j}^{t+1} \cdot E_{1,i,j}^{t} - x_{1,i}^{t+1}}{\delta z_l} - Q_{x,i}^{t+1}) \tag{16}$$

Furthermore, the surface energy balance for each tile can be written as:

$$C_{s,i} \cdot c_p^{-1} \cdot \frac{\partial S_{surf,i}}{\partial t} = R_{n,i} + G_i + LE_i^* + H_i^* \tag{17}$$

In Eq. 17 the rate of surface temperature change (given by the product of surface heat capacity $C_{s,i}$, the conversion rate from temperature to dry static energy c_p^{-1} and the dry static energy at the surface $S_{surf,i}$) is balanced by the surface net radiation $R_{n,i}$, the ground heat flux G_i and the tile specific latent (LE_i^*) and sensible (H_i^*) heat fluxes. Together with the equations for the surface heat and moisture fluxes below the lowest level of the atmosphere (Eq. 16; Eq. 50), 3 times the number of tiles equations are obtained which can be solved for the 3 times the number of tiles unknowns $s_{1,i}^{t+1}$, $q_{1,i}^{t+1}$ and $s_{surf,i}^{t+1}$.

2.3. Single column model studies

Single column experiments are especially well suited to investigate processes and mechanisms related to the land surface-atmosphere coupling. On one hand they incorporate substantially less degrees of freedom than global scale GCMs and the absence of large scale atmospheric effects makes results much easier to interpret. On the other hand the entire vertical column including all relevant processes is simulated which allows the investigation of feed-back effects between surface and atmosphere.

A single column model can be considered as a very primitive model of atmosphere and surface. It reproduces the processes within a representative model grid box rather than those given at a specific location in the real world. Therefore, the following investigations do not attempt to prove that a given coupling scheme gives better results with respect to reality, but that the choice of coupling scheme may have a substantial impact on the simulated state of a grid box. In single column simulations, the prescription of an advective forcing is required in order to account for the atmospheric meridional heat and moisture transport from equatorial to polar regions. Disregarding the advective forcing leads to an excess in energy in equatorial regions and an energy deficit in high latitudes which leads to extreme and unrealistic states simulated in the respective regions. However, in extreme scenarios certain interdependencies e.g. surface temperature and soil moisture may become more clear. Thus, it may even be more instructive to investigate processes in the extreme scenarios given when an advective forcing is omitted.

Results are presented below using the one-dimensional version of ECHAM6 coupled to a version of JSBACH, in which the VERTEX scheme described in Sect. 2.2 has been included. In the operational setup, the atmospheric turbulent fluxes are modelled by a modified version of the turbulent kinetic energy scheme described in Brinkop and Roeckner (1995). The scheme uses the turbulent kinetic energy, the turbulent mixing length (Blackadar, 1962) and a stability function that depends on the moist Richardson number (Mellor and Yamada, 1982) to describe the turbulent viscosity and diffusivity. In the scheme the dissipation rate is dependant on the dissipation length-scale, which is assumed to be equal to the mixing length. For convectivly unstable situations the bottom boundary condition is determined by the stability of the surface-layer and depends on the the friction velocity, the convective velocity scale and the Monin-Obukhov length-scale (Mailhot and Benoit, 1982). In the VERTEX scheme, the formulations are kept essentially the same but calculations are performed for the individual tiles separately within the lowest three layers of the atmosphere.

The standard model version uses a parameter aggregation scheme in which the aggregation is performed according to Kabat et al. (1997); Feddes et al. (1998), more specifically the aggregation of the roughness length follows Mason (1988); Claussen (1991); Claussen et al. (1994) and the aggregation of the albedo Otto et al. (2011). Based on the effective parameters, the surface fluxes are calculated using a bulk-exchange formulation that applies approximate analytical expressions similar to those proposed by Louis (1979) to

determine the transfer coefficients. Evapotranspiration is given by (Schulz et al., 2001):

$$E = c_{couple} \cdot \beta \cdot (q_1 - \alpha \cdot q_{sat}(cp \cdot s_{surf})) \tag{18}$$

For evaporation without limitations to the availability of water and snow sublimation the coefficients are $\beta = \alpha = 1$ and whenever the soil is not fully saturated, bare soil evaporation is reduced according to Roeckner et al. (1996). For transpiration $\alpha = 1$ and β is calculated based on Sellers et al. (1986). In the VERTEX scheme the surface fluxes are calculated accordingly but for individual tiles and not for the entire grid box. In the soil a horizontal flow of water and heat is not represented in the model and the soil moisture and temperature in a given tile is independent of the other tiles.

The VERTEX scheme has been implemented in such a way that the atmospheric processes included in the model can be divided into grid resolved and tile resolved processes. The airmass properties i.e. temperature and specific humidity of the lowest model levels are resolved with respect to the surface tiles, but these tile specific characteristics are being considered only in the process of turbulent mixing. To maintain the level of complexity at a minimum, sub-grid scale heterogeneity of the wind field was not taken into account in the computation of turbulent kinetic energy. All other processes such as convection, radiative heating and precipitation are grid resolved processes, thus they exclusively depend on grid mean values.

To account for mesoscale circulations a simple approach was followed and they were factored in in the calculation of the blending height, rather than by a designated factor in the calculation of $deg\_mix_{z,i}$ and $Fmix_{z,i,j}$. It was assumed that mesoscale circulations occur exclusively due to differential surface heating during unstable conditions. In order to increase $Fmix_{z,i,j}$ accordingly, the blending heights were calculated based on more general formulation of the blending height (Eq. 1 with $C = 1$, $p = 2$) even though buoyancy driven turbulence (Eq. 2) result in much larger blending heights under these circumstances. It has to be acknowledged that, if the balancing effects of mesoscale circulations are small, this simplification leads to an underestimation of the blending height. $deg\_mix_{z,i}$ was calculated as the ratio of height above ground h_z and blending height $h_{blend,i}$ and $Fmix_{z,i,j}$ was calculated based on Eq.4.

$$h_{blend,i} = (\frac{u_{*,i}}{U})^2 \cdot L_{hetero,i} \tag{19a}$$

$$deg\_mix_{z,i} = min(1, \frac{h_z}{h_{blend,i}}) \tag{19b}$$

In the present model setup the resolution of air properties has been limited to the lowest two atmospheric model levels in order to limit computational expenses, even though the calculated blending height may lay much above the third lowest level. Therefore, on the lowest (around $30\,m$) and second lowest model level (around $150\,m$) the extent to which fluxes have horizontally mixed linearly depends upon the blending height whereas on the third lowest level (around $350\,m$) fluxes are assumed to be completely mixed. In

this study sub-grid heterogeneity is constituted by clusters of different land-cover types which can be found within a given model grid box. To approximate the characteristic length scales $L_{hetero,i}$ of these clusters at a the model resolution ($T\,63$) the Global Land Cover Map 2009 (GLOBCOVER) was used (Arino et al., 2012). An exception to this are the characteristic length scales in the first study, which were not derived from the dataset but chosen arbitrarily. The horizontal wind speed U at the blending height and the friction velocity $u_{*,i}$ are calculated within the model.

2.3.1. Wet vs. dry tile

The first simulation is performed for an idealized grid box located at $23.3\,^\circ N$, $75.0\,^\circ E$, which comprises a wet and a dry tile. Half of the grid box is assumed to be covered by irrigated crops (wet tile) and the other half by rainfed crops (dry tile), both of which exist in clusters with a characteristic length scale of $50000\,m$. The vegetation characteristics of both crops are identical and the two tiles only differ with respect to the treatment of soil moisture. At the beginning of each time step the soil moisture content within the wet tile is set to the value at which potential transpiration is reached i.e. $75\,\%$ of the water holding capacity ($0.53\,m$). In contrast to this the dry tile is initialized with the soil moisture content at the wilting point ($0.21\,m$), i.e the minimum soil moisture required for plants not to wilt. The simulation was performed for the months of July and August 1992, using ERA-Interim reanalysis (ERA) data for initialisation (Dee et al., 2011). In the following a period from the 16th to the 18th of July will be used to demonstrate some characteristic aspects of the new coupling scheme. Before and during this period no rainfall occurs and there is no drainage or evapotranspiration within the dry tile (as the soil moisture is at the wilting point) so that the soil moisture values of both tiles are identical to the initialisation values.

During the 3-day period the grid mean surface temperature ranges from about $295\,K$ ($294\,K$ in the wet and $296\,K$ in the dry tile) just before dawn at around 0600 local time (LT) to about $310\,K$ ($306\,K$ in the wet and $314\,K$ in the dry tile) at around 1300 LT (see Fig. 6a). The tile specific deviations from the grid mean surface temperature are largest with almost $4\,K$ when the daily maximum temperature is reached. They decay rapidly during the afternoon and slower during the night until they reach their lowest value of about $1\,K$ two hours after sunrise. It can be seen that the deviations in surface temperature do not start to increase again when surface temperature increases. In the early morning roughly between 0500 LT and 0800 LT all available energy at the surface is directed to a quite uniform (between the tiles) increase in surface temperature, indicated by the fact that the surplus in net radiation and ground heat flux is not balanced by the sensible or latent heat flux (see Fig. 6c).

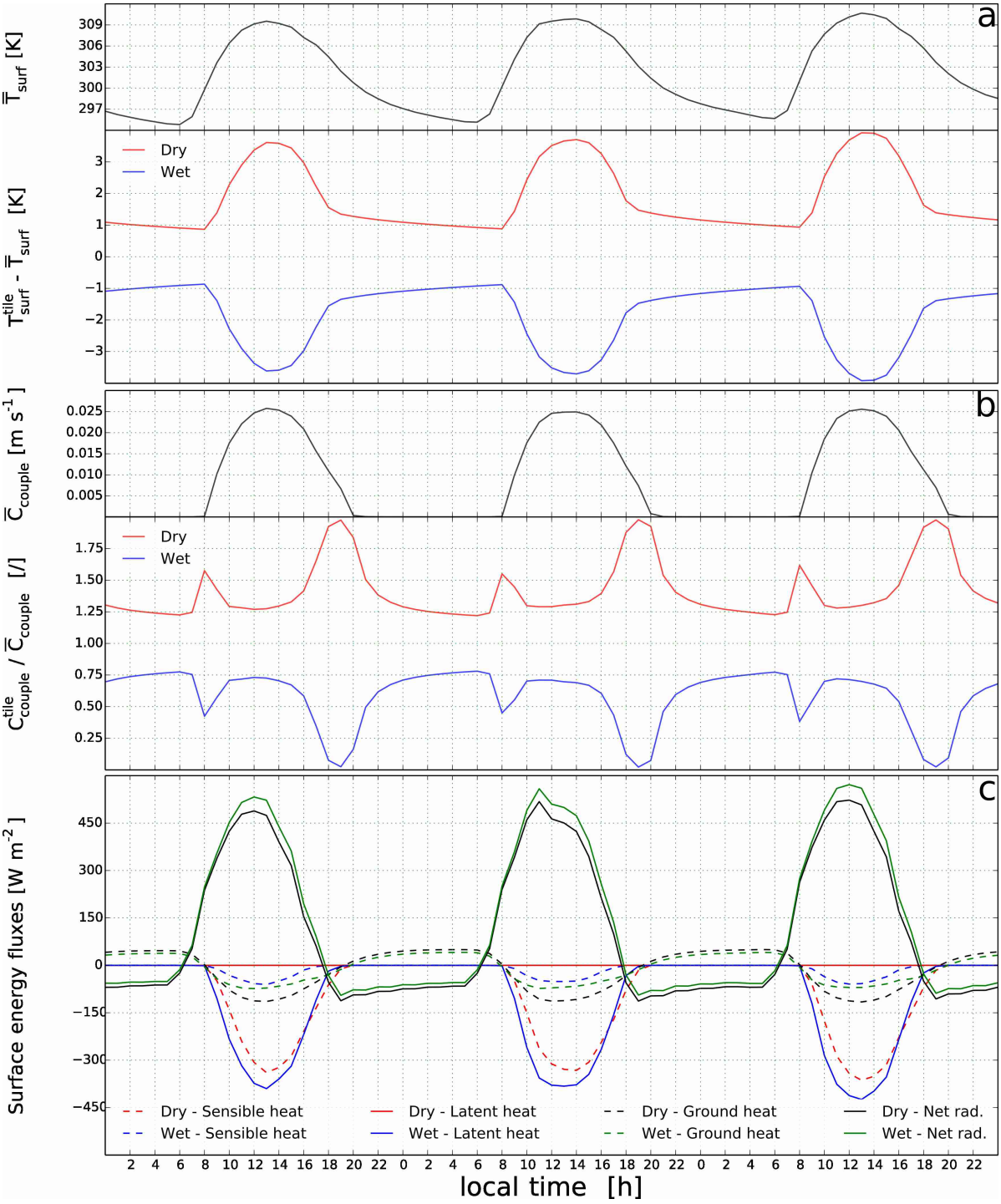

Figure 6: a) Grid box mean surface temperature (top) and tile specific deviations from the mean (bottom), b) Grid box mean surface coupling coefficient (top) and tile specific coupling coefficients relative to the mean (bottom), c) Surface energy fluxes; $23.3\,^\circ N$, $75.0\,^\circ E$

In ECHAM6 and JSBACH fluxes are defined in such a way that a flux towards the surface is positive and a flux away from the surface is negative. Thus, with the exception

of the ground heat flux, all downward fluxes are indicated by a positive algebraic sign. The sub-grid scale temperature variability starts to increase only after 0800 LT when the air between surface and lowest atmospheric level becomes unstable which causes a distinct increase in the surface upward latent and sensible heat fluxes. The strength of the surface-atmosphere coupling in JSBACH depends on the product of the horizontal wind speed and the surface drag coefficient which is dependent on the roughness length and the stability between surface and lowest atmospheric level. As the horizontal wind speed is calculated for the entire grid box and the roughness length is similar in both tiles, the product of horizontal wind speed and surface drag coefficient can be used as a proxy for differences in the stability of the surface layer between the tiles. In the following the coefficient indicating the coupling strength will be referred to as the coupling coefficient.

The coupling coefficient follows a diurnal cycle which is similar for all three days (see Fig. 6b). The coefficient varies between values very close to zero (10^{-5}) during the stable nocturnal periods and values close to 0.025 (0.032 in the dry tiles and 0.019 in the wet tile) around 1300 LT. The coefficient associated with the dry tile is much larger than the one in the wet tile. The reason is that the dry tile exhibits higher surface temperatures, which results in a less stable stratification of the lowest layers of the atmosphere. For the largest part of the 3-day period it is more than two thirds larger and in the periods of surface warming in the morning and cooling in the afternoon and evening, the coupling coefficient in the dry tile may even be orders of magnitude larger than in the wet tile. This means that the exchange of air properties between the surface and the atmosphere is distinctly more pronounced within the dry tile. As both tiles have the same roughness length this difference in surface-atmosphere coupling strength originates from the stability differences between the tiles.

In the 3-day period the total net radiation exhibits periodically similar diurnal cycles which show a minimum of $-100\,W\,m^{-2}$ at around 1900 LT and remain dominated by the outgoing long wave radiation until sunrise at around 0600 LT. During the day net radiation is dominated by incoming solar radiation and reaches a maximum of about $500\,W\,m^{-2}$ around noon. Compared to the latent and sensible heat fluxes the surface net radiation is very similar in both tiles and the differences, which are roughly around 10 %, are caused by the difference in outgoing long-wave radiation resulting from the sub-grid scale variability of surface temperature.

However, the way this energy is balanced by the other terms of the surface energy balance, in particular by the latent and sensible heat fluxes, differs largely between the tiles. Most prominent is the fact that, due to the water stress, evapotranspiration and thus the latent heat flux remains zero in the dry tile throughout the entire 3-day period. During the nocturnal periods between 1900 LT and 0800 LT of the following morning, the latent heat flux is zero also in the wet tile. But in contrast to the flux in the dry tile, the latent heat flux in the wet tile is the dominant upward surface energy flux during day time. With approximately $400\,W\,m^{-2}$ at noon and early afternoon it is several times larger

than the sensible heat flux. The upward sensible heat fluxes are very close to zero during the night (-$10^{-1}\,W\,m^{-2}$) and start to increase when the air between surface and lowest model level becomes unstable at 0800 LT. They reach their peak of about $350\,W\,m^{-2}$ in the dry tile and $50\,W\,m^{-2}$ in the wet tile when surface temperatures are highest at 1300 LT. For the greater part of the day (0900 LT to 1700 LT) the sum of upward sensible and latent heat fluxes and downward ground heat flux is larger in the wet tile than in the dry tile. This is partly balanced by a larger downward net radiation but also because less energy is expended in surface warming in this tile. This changes around 1700 LT when the ground heat flux and the net radiation in the tiles have converged and when the sum of upward latent and sensible heat flux become larger in the dry tile. The reason for this is the lower surface temperature in the wet tile which causes the air above it to be already close to neutral stratification. In contrast, the surface temperature in the dry tile is higher and the lowest part of the atmospheric column is still unstable which facilitates the upward energy fluxes. The difference in the strength of the vertical turbulent transport can be seen in the large differences in the coupling coefficient at that time.

Figure 7 shows the potential blending heights calculated for each tile using Eq. 1. Due to the large horizontal extents of the crop clusters on the surface, the blending height during the day reaches much higher than the lowest three atmospheric model levels. Between 0800 LT and 0900 LT the blending height quickly increases to roughly about $1000\,m$ and reaches its maximum height around noon, with values between $1500\,m$ and $2500\,m$ in the wet tile and between $3000\,m$ and $4500\,m$ in the dry tile.

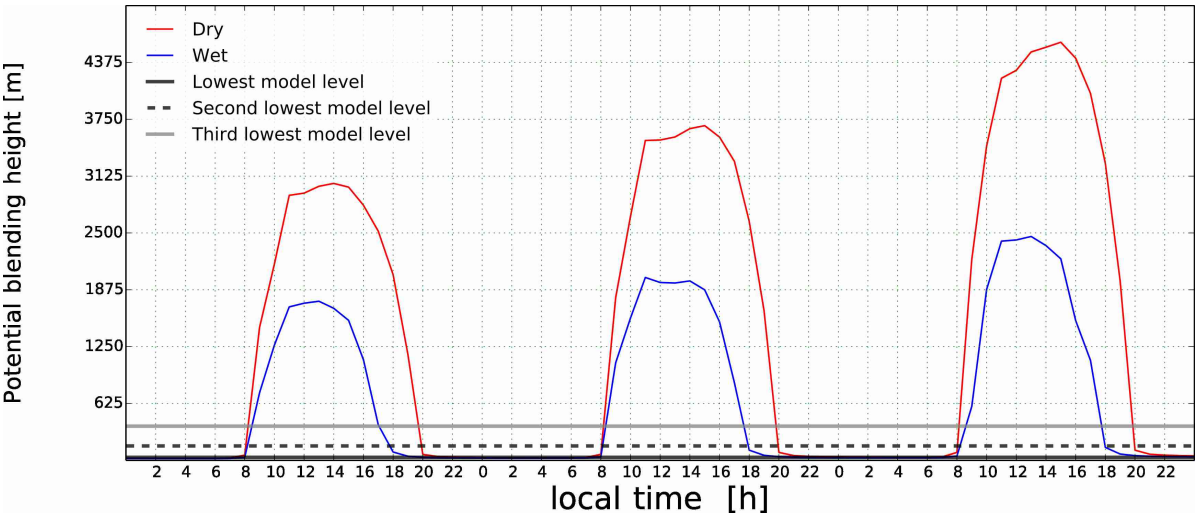

Figure 7: Potential blending height and heights of the lowest model levels; 23.3 ° N, 75.0 ° E

This means that in theory the vertical fluxes would not become horizontally homogeneous within the boundary layer for a large part of the day. Furthermore, between roughly 0900 LT and 1700 LT the extent to which fluxes have horizontally mixed at the lowest atmospheric level is below 3 % and at the second lowest level below 15 %. Hence, when looking at the development of certain variables at the respective levels (Figs. 8 a

and b), it should be kept in mind that the fluxes between surface and lowest and second lowest atmospheric level within the tiles are largely independent of each other. In Sect. 2.2 the numeration of model levels starts with the lowest level in the atmosphere as level 1 and numbers increase until the top of the atmosphere. Consequently in the following sections the lowest atmospheric level will be referred to as level lev_1, the second lowest and third lowest as levels lev_2 and lev_3.

For the horizontal length scales of the crop tiles the blending height can not be used to predict the height above which in reality the state of the atmosphere becomes horizontally homogeneous as the concepts on which it is based do not extend past the planetary boundary layer into the free atmosphere. Consequently, for these length scales the potential blending height merely represents the height at which the atmospheric state would become horizontally homogeneous if it was located below the boundary layer top. However, it is still conceivable to use the potential blending height as a scaling factor for the horizontal mixing of the vertical fluxes within the planetary boundary layer. There is evidence that even for length scales $L_{hetero,i} << 50000\,m$ the atmosphere is not necessarily horizontally homogeneous at heights of more than $1\,km$ and that heterogeneity extends to the top of the convective boundary layer when $L_{hetero,i}$ becomes significantly larger than the height of the convective boundary layer (Strunin et al., 2004). Here, the Raupach's length L_{RAU}, as a function of the Deardorff velocity scale, the height of the convective boundary layer and the wind speed, may be used as a horizontal length scale of surface features whose influence is confined to the convective boundary layer (Raupach and Finnigan, 1995). When assuming that the heterogeneity at the top of the boundary layer depends linearly on the ratio of L_{RAU} and $L_{hetero,i}$, $deg\_mix_{z,i}$ can also be expressed as a function of L_{RAU} and the height of the boundary layer h_{bl}:

$$deg\_mix_{z,i} = \frac{L_{RAU}}{L_{hetero,i}} \cdot \frac{h_z}{h_{bl}} \tag{20}$$

However, there is no conclusive evidence that this approach provides a more accurate description of the actual extent to which the vertical fluxes blend horizontally with height. As $deg\_mix_{z,i}$ is predominantly smaller for Eq. 20 than for Eq. 19, $deg\_mix_{z,i}$ was calculated based on the potential blending height with the aim of rather underestimating the effect of heterogeneity than to overestimating it.

The grid mean temperature at lev_1 (see top panel of Fig. 8 a) follows a diurnal cycle similar to that of the surface temperature, although its amplitude is dampened by about $10\,K$ and the temperature peak is reached much later during the day (between 1700 LT and 1800 LT).

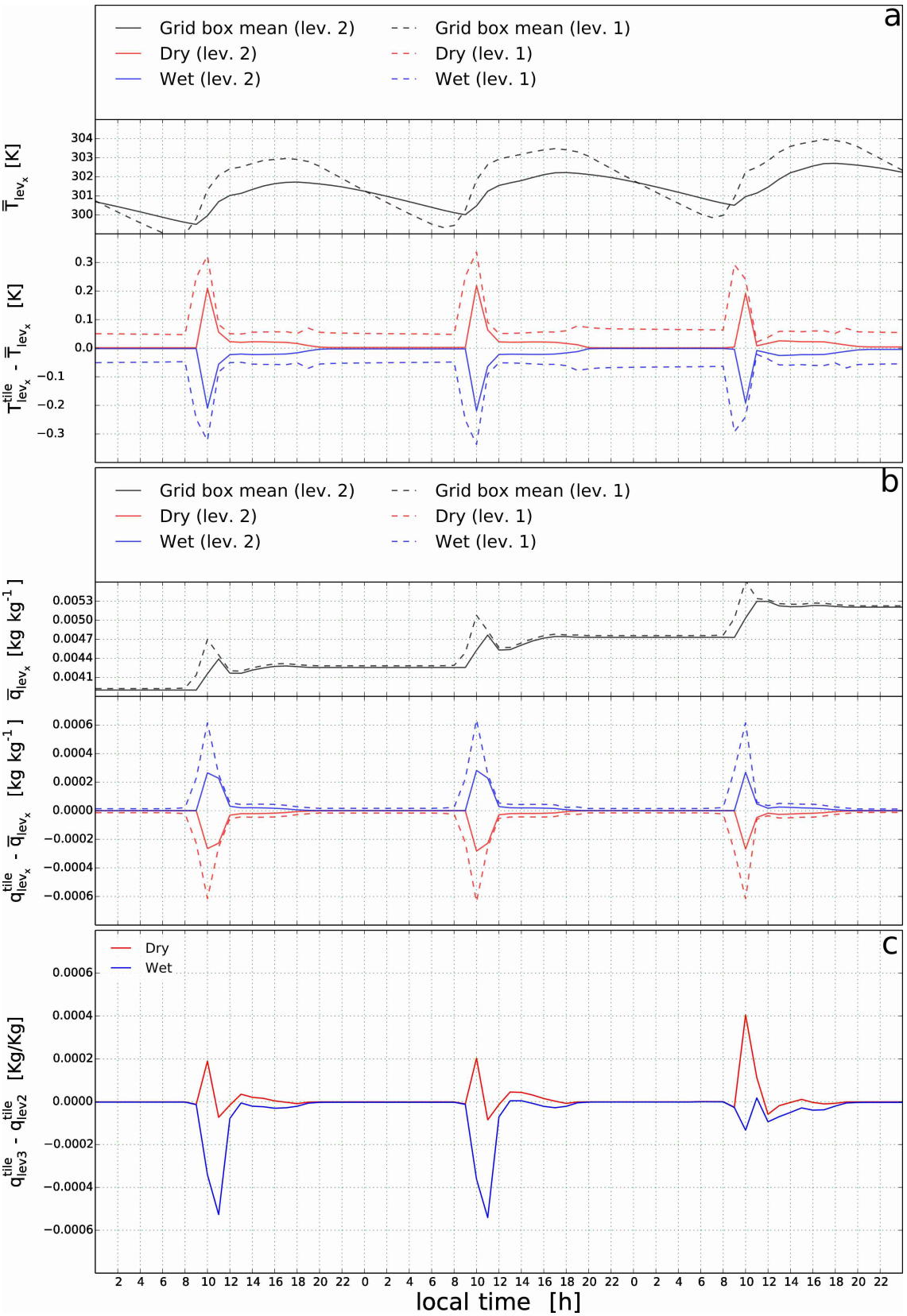

Figure 8: a) Grid box mean temperatures at lev_2 and lev_1 (top) and the respective tile specific temperature deviations (bottom), b) Grid box mean specific humidity at lev_2 and lev_1 (top) and the respective tile specific humidity deviations (bottom), c) Specific humidity difference between lev_3 and lev_2; 23.3 ° N, 75.0 ° E

However, the sub-grid scale temperature variability behaves very differently to that at the surface (see bottom panel of Fig. 8 a). At lev_1, with a maximum of around $0.3\,K$, tile specific temperature deviations from the grid mean have been reduced by more than an order of magnitude in comparison to the temperature deviations at the surface. Furthermore, the temperature deviations at lev_1 do not exhibit a pronounced diurnal cycle. They show a distinct increase between 0800 LT and 1000 LT followed by a sharp decrease which continues until noon. For the rest of the day and the night they remain quite constant at a value of about $0.05\,K$. The period with the strongest increase in the temperature deviations is between the hours of 0800 LT and 0900 LT. This is the time when, especially in the dry tile, the air between surface and lev_1 is already largely unstable whereas the air between lev_1 and lev_2 is still stable stratified and the eddy diffusivity between lev_1 and lev_2 is small.

The present model of the turbulent transport follows the K-theory, hence the fluxes between two levels are dependent upon the eddy diffusivity and the gradient of the respective variable (Eq. 7). In ECHAM6, the eddy diffusivity is parametrized in terms of the turbulent kinetic energy and a stability related length scale. Thus, it can be used as an indicator for the rate at which the properties of air are exchanged between the two levels, as well as a stability proxy (Fig. 9).

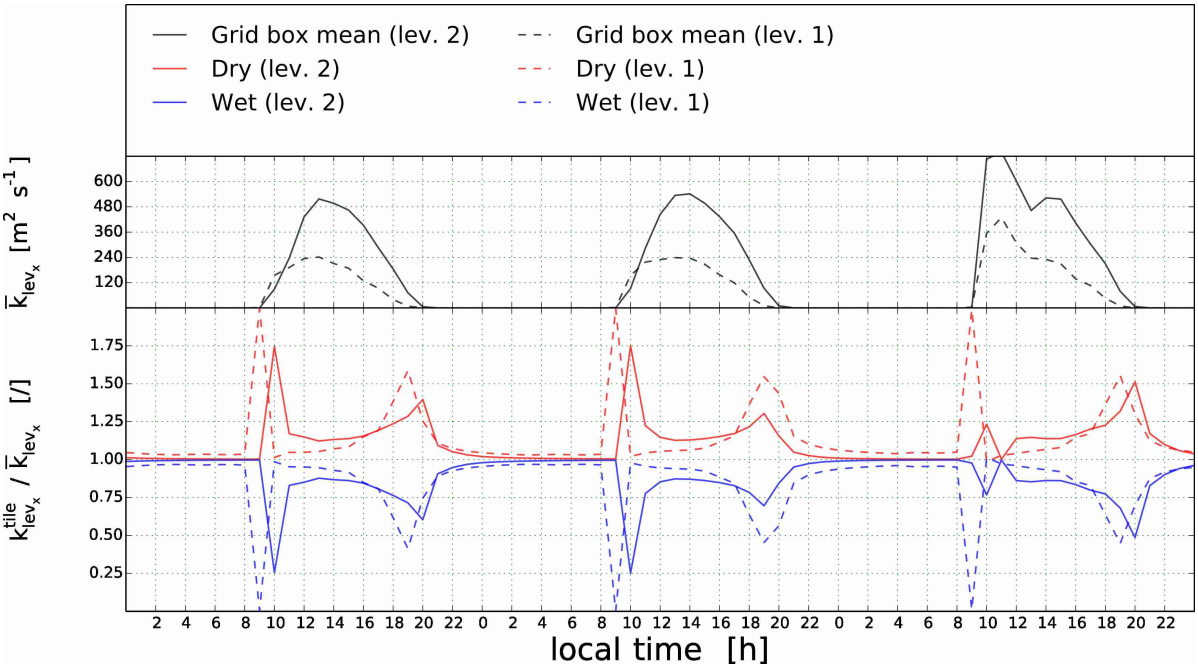

Figure 9: Grid box mean eddy diffusivity between lev_2 and lev_3 and between lev_1 and lev_2 (top) and the respective tile specific eddy diffusivity relative to the mean (bottom), (The eddy diffusivity between lev_1 and lev_2 is indexed by the lower level lev_1 and that between lev_2 and lev_3 is indexed by lev_2); $23.3\,^\circ N$, $75.0\,^\circ E$

Between 0800 LT and 0900 LT with the air between surface and lowest level being unstable, heat from the surface is mixed upwards towards lev_1. At the same time there

is no strong coupling between lev_1 and lev_2 so that this heat is not transported further upwards but warms the air in the lowest atmospheric layer. As the surface is warmer in the dry tile and also the respective coupling coefficient is much larger (resulting in a larger sensible heat flux) this process is much more pronounced in the dry tile which causes a non-uniform warming in the tiles at lev_1 and thus the distinct peak in temperature deviations.

Between 0900 LT and 1000 LT the mixed layer expands beyond the lowest atmospheric levels which can be seen in the pronounced increase in eddy diffusivity at that time. At this point the coupling between lev_1 and lev_2 becomes stronger and more heat is mixed upwards from lev_1 to lev_2. Therefore, the temperature increase at lev_2 starts about an hour after the warming at the level below. The diurnal cycle of grid mean temperature at lev_2 resembles that at lev_1 but with a smaller amplitude and the entire cycle being shifted by one hour. Consequently, an associated increase in tile specific temperature deviations does not occur before 0900 LT. However, the sub-grid scale temperature variability at lev_2 reaches its daily maximum at the time when the maximum deviations are also reached at the level below (1000 LT), making the time period when large deviations occur at lev_2 much shorter than at lev_1. The maximum deviations at lev_2 (about $0.2\,K$) are only about one third smaller than the deviations at lev_1, even though the extent to which the fluxes have horizontally mixed is about 4.5 times larger at lev_2 than at lev_1.

After 1000 LT the eddy diffusivity between lev_2 and lev_3 becomes much larger than that between lev_1 and lev_2. At this point the exchange with the homogeneous air from above the blending height predominates the exchange with the more heterogeneous air closer to the surface. Consequently, a pronounced decrease in the sub-grid scale temperature variability occurs between 1000 LT and 1200 LT. Around 1200 LT a balance between the upward mixing of heterogeneous air properties from the surface and the downward mixing of homogeneous air properties from above the blending height is established, in which temperature deviations of around $0.05\,K$ ($0.02\,K$) at lev_1 (lev_2) are sustained. The deviations at lev_2 further decrease in the late afternoon and evening and entirely vanish after 2000 LT when the blending height decreases below lev_2 and fluxes at this level become horizontally homogeneous again.

As stated above, for the largest part of the simulation the degree to which fluxes have become horizontally homogeneous was below 5 % at lev_1 and below 15 % at lev_2. Thus, it is remarkable that temperature deviations at lev_1 and lev_2 have been reduced by an order of magnitude in comparison to the deviations at the surface. The reason for this strong decline is a stability related mechanism which, in predominantly unstable situation, equilibrates the temperatures in the tiles. Assuming that the properties of air become horizontally more homogeneous with height, the stability in a tile decreases relative to the other tiles when the air in this tile becomes warmer than in the others. This causes an increase in vertical turbulent mixing relative to the colder tiles. Because the air at the level above is colder this relative increase in turbulent transport results in a relative increase in the mixing with colder air within the warmer tile, thus equilibrating

temperatures. Thus, the reduction of tile specific deviations with height does not scale linearly with the extent to which fluxes have become horizontally homogeneous. In the simulation this effect can be seen in the differences in eddy diffusivity between tiles. Between roughly 0800 LT (0900 LT at lev_2) and 2100 LT the eddy diffusivity between two levels is on average more than 50 % larger in the dry tile than in the wet tile.

The top panel of Fig. 8b shows that the atmospheric specific humidity is not in an equilibrium state. Due to the increasing temperatures and the abundance of moisture at the surface within the wet tile, the grid mean specific humidity at the two lowest atmospheric levels increases throughout the 3-days period by more than $1\,g\,kg^{-1}$. Furthermore, the development throughout a given day is very different to that of temperature. During the nights (2000 LT to 0800 LT) the grid mean specific humidity is constant. With the onset of evapotranspiration there is a distinct increase of specific humidity at lev_1 between 0800 LT and 1000 LT. In this example case, the grid mean evapotranspiration depends exclusively on the turbulent transport in the wet tile and thus on the coupling coefficient in this tile. As shown in Fig. 6 the air within the wet tile remains stable for longer and therefore the coupling coefficient in the wet tile is distinctly smaller than in the dry tile during the period between 0800 LT and 0900 LT. For this reason, the strongest increase in mean specific humidity does not occur between 0800 LT and 0900 LT (when specific humidity increases by about $0.20 - 0.25\,g\,kg^{-1}$) as is the case for temperature but between 0900 LT and 1000 LT (here the specific humidity increases by about $0.55 - 0.60\,g\,kg^{-1}$). At lev_2 the increase in specific humidity is much smaller and delayed by one hour ($0.25\,g\,kg^{-1}$ - $0.30\,g\,kg^{-1}$ between 0900 LT and 1000 LT and $0.22\,g\,kg^{-1}$ - $0.25\,g\,kg^{-1}$ between 1000 LT and 1100 LT). The shift in time follows the same reasoning as the shift in the development of temperature at lev_2 described above.

Following the sharp increase, between 1000 LT and 1300 LT the grid mean specific humidity at lev_1 (lev_2) is reduced by between $0.50\,g\,kg^{-1}$ - $0.35\,g\,kg^{-1}$ ($0.07\,g\,kg^{-1}$ - $0.27\,g\,kg^{-1}$), which at lev_1 is more than half of the initial increase. This decrease is caused by the increase in mixed layer height as the moisture from the surface, which initially remained in the lowest two levels of the atmosphere, is now mixed further upwards. At around 1300 LT stability starts to increase again in the wet tile, which can be seen by the decrease in blending height (see Fig. 7). Consequently, the vertical turbulent transport is again more confined to the lowest levels of the atmosphere resulting in a second period of increase in specific humidity between 1300 LT and 1600 LT at the respective levels. This is followed by a slight decrease until around 1900 LT after which the specific humidity remains constant again until the next onset of evapotranspiration in the following morning.

Between 0800 LT and 1000 LT the tile specific deviations in specific humidity are large compared to the grid mean with a peak of about $0.6\,g\,kg^{-1}$ at lev_1 and about $0.25\,g\,kg^{-1}$ at lev_2 (see Fig. 8b). This means that the increase in atmospheric humidity occurs to a large extent within the wet tile whereas the specific humidity in the dry tile increases only slightly. Exemplary at 1000 LT of the first day the specific humidity in the wet tile at lev_1 is about $5.3\,g\,kg^{-1}$ whereas the specific humidity in the dry tile is about $4.1\,g\,kg^{-1}$

meaning that between 0800 LT and 1000 LT the specific humidity in the wet tile has increased by about $1.4\,g\,kg^{-1}$ whereas in the dry tile the increase is only $0.2\,g\,kg^{-1}$. This agrees with the small extent to which fluxes have horizontally mixed.

Consequently, when the mixed layer grows and the properties of the relatively humid air, which is largely located above the wet tile, are being mixed with the properties of the dryer more homogeneous air from above, the sub-grid scale humidity variability is strongly reduced. Because the state of the individual tiles converges with increasing height the vertical moisture gradient is smaller in the dry tile than in the wet tile. Therefore, the upward moisture flux within this tile is very small when compared to the wet tile and the moisture which is mixed into the air above the dry tile from the wet tile largely remains within the lowest layers of the atmosphere. For certain periods the moisture fluxes within the tiles even have opposing directions so that a process develops which to some extent resembles a mesoscale circulation. In the dry tile between roughly 0900 LT and 1100 LT and noon and 1600 LT the specific humidity at lev_3 (here fluxes have become horizontally homogeneous) is larger than at lev_2 (see Fig. 8c). This means that during these periods moisture is being mixed upwards above the blending height within the wet tile and transported downwards within the dry tile, thus equilibrating the differences in specific humidity between the tiles. Thus, for the longest part of any day the sub-grid humidity variability is very small despite the fact that no evapotranspiration occurs in the dry tile and fluxes have horizontally mixed by less than 3 % at lev_1 and less than 15 % at lev_2.This is in accordance to studies which indicate that fluxes blend higher in the atmosphere than scalars (Brunsell et al., 2011).

2.3.2. Temperature inversion

The second idealized study was performed for a grid box located at $64.4\,^\circ N$, $114.4\,^\circ W$, which comprises evergreen trees (about 57 %), deciduous trees (24 %) and c3 grass (19 %). The respective average horizontal extents at the surface are about $2000\,m$ (evergreen trees), $1700\,m$ (deciduous trees) and $3000\,m$ (c3 grass). The simulation was performed for the months of January and February of 1992 and in the following a period from the 1st to the 5th of January will be used to demonstrate characteristic aspects of the new coupling scheme for the case of temperature inversion in the lowest layers of the atmosphere. A spin-up phase is not taken into consideration as the study is strongly idealized and some of the most interesting aspects related to the new coupling scheme are most eminent before an equilibrium state is reached.

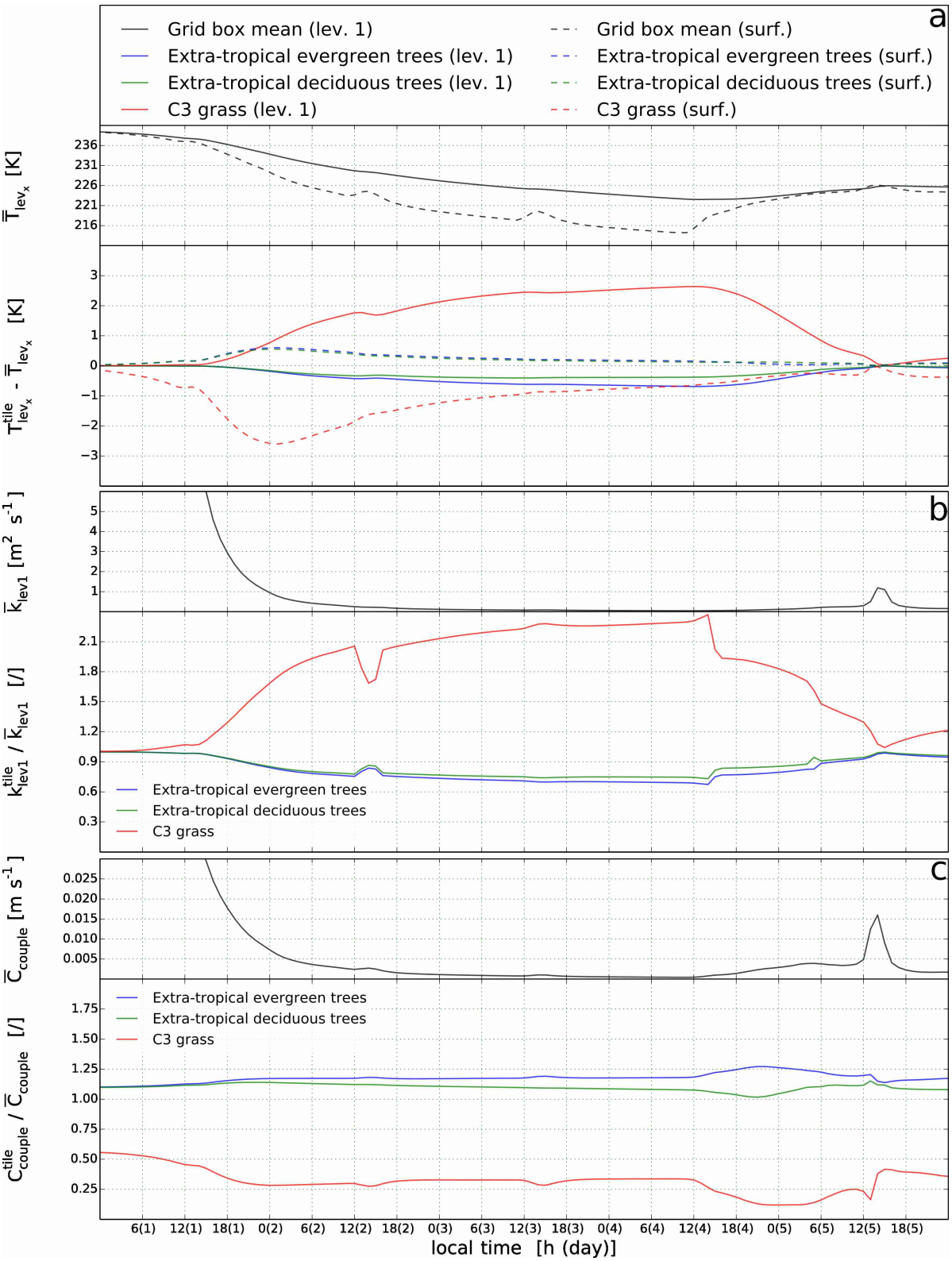

Figure 10: a) Grid box mean temperature at lev_1 and at the surface (top) and the respective tile specific temperature deviations (bottom), b) Grid box mean eddy diffusivity between lev_1 and lev_2 (top) and the respective tile specific eddy diffusivity relative to the mean (bottom), c) Grid box mean surface coupling coefficient (top) and the respective tile specific coupling coefficients relative to the mean (bottom); $64.4\,^\circ N$, $114.4\,^\circ W$

In this particular example the blending height is low and the fluxes originating from the individual tiles blend between the lowest and the second lowest atmospheric level (not shown here). Due to the absence of an advective forcing simulated temperatures deviate very quickly from their initial values which were taken from ERA data. The surface temperature drops by about $25\,K$ within the first 4 days of the simulation. As the cooling is less pronounced in the atmosphere (about $17.5\,K$ at lev_1) a temperature inversion forms in the lowest layers of the atmosphere and the resulting atmospheric column is very stable in the lowest levels throughout the first 4 days until it becomes only weakly stable around noon of the fourth day (see Fig. 10a).

In the simulation the roughness length of the tree tiles ($1.00\,m$) is 20 times larger than that of the grass tile ($0.05\,m$). Therefore, trees generate more shear driven turbulence in given wind conditions and consequently the coupling between surface and atmosphere is much stronger in the tree tiles than in the grass tile. The respective coupling coefficient is initially about twice as large as that of the grass tile (Fig. 10c). Under these circumstances a stronger coupling means that more heat is being mixed downward from the warmer atmosphere towards the colder surface. Therefore, the tree tiles exhibit higher surface temperatures than the grass tile. In order to isolate the effect of differences in roughness length from effects due to differences in albedo, the incoming radiation in the simulation was calculated based on the grid box mean albedo, i.e. all tiles receive the same incoming radiation. Because of the strong horizontal mixing of the fluxes, the temperature deviations at lev_1 are initially very small. However, they quickly become large enough to have a noticeable effect on stability as indicated by the increasingly different coupling and eddy diffusivity coefficients (Fig. 10b and c).

The temperatures at lev_2 are identical in all tiles, as the blending height is below this level (not shown here). At lev_1 the temperature of the grass tile increases relative to the temperature of the tree tile whereas the grass tile's surface temperature decreases relative to the surface temperature in the tree tiles. Thus, the stability between the surface and lev_1 increases in the grass tile (indicated by the relative decrease in coupling coefficient in this tile from about $60\,\%$ to about $30\,\%$ of the grid mean) whereas the stability between lev_1 and lev_2 decreases relative to the tree tiles (indicated by the relative increase in eddy diffusivity to about twice that of the grid mean). In the grass tile this causes a relative increase in the exchange between lev_1 and lev_2 and a relative decoupling of the atmosphere from the surface. Thus, more heat from above is mixed down towards lev_1 above the grass tile and less cold air is being mixed upwards from the surface. This results in very large deviations from the grid mean surface temperature in the tiles (e.g. $2.3\,K$ in the grass tile at the beginning of the second day) but also in increasingly large temperature deviations at the lowest atmospheric level (as much as $2.3\,K$ on noon of the 4th day).

At the beginning of the second day the surface-atmosphere temperature gradient in the grass tile becomes so large that, despite the weaker surface-atmosphere coupling, the sensible heat flux starts to approximate that of the tree tile (not shown here). Fur-

thermore, in the tree tiles there is more outgoing longwave radiation due to the higher surface temperatures in these tiles. The consequent difference in net radiation in combination with the harmonisation of sensible heat flux in the individual tiles causes a strong decrease in sub-grid scale temperature variability at the surface while the deviations at lev_1 continue to increase.

Around noon of the fourth day surface temperatures start to increase again and the air becomes less stable, which is indicated by the increases in the coupling coefficient and eddy diffusivity. The large temperature deviations between the tiles in the atmosphere can be sustained only when the coupling between surface and atmosphere is very weak in the warm grass tile. Consequently, they quickly decline when surface temperatures start to increase and the air between surface and lev_1 becomes less stable. The decrease in sub-grid scale temperature variability at the surface and increase at lev_1 continue until 1400 LT on the fifth day. At this point the air between surface and lev_1 is only weakly stable and the air between lev_1 and lev_2 is close to instability indicated by the sharp increase in the coupling coefficient and eddy diffusivity. At this moment the air at lev_1 becomes horizontally homogeneous again.

It is notable that during the simulation the tile specific temperature deviations at lev_1 become larger than those at the surface. They surpass them around noon of the second day and remain larger until noon of the fifth day. This is striking as the blending height during the experiment was very low (below lev_2) and the coupling scheme is setup in such a way that the vertical fluxes become horizontally more homogeneous with height. Furthermore, the local stratifications are such that relatively warmer air is located above the relatively colder surface and vice versa. Intuitively one would expect that a convergence of fluxes would necessarily result in a convergence of the states of the different tiles. However, the process described above is to a certain degree self enhancing, allowing the initially small deviations in the atmosphere to grow larger than those at the surface. Within the warmer tile the temperature deviations in the atmosphere facilitate a relative decrease in stability between the two lowest levels of the atmosphere and a relative decoupling from the surface. The consequent relative increase in exchange with the warmer air from above the blending height and the decrease in mixing with the cold near surface air in the warmer tile in turn promote the increase in temperature deviations at lev_1 and thus, an increase in stability differences. These again have a positive feedback on the downward mixing of heat towards lev_1 and a negative feedback on the downward mixing of heat towards the surface in the grass tile. This process is only interrupted when surface temperatures increase, due to an increase in incoming shortwave radiation (not shown here) and a consequent reduction of stability between surface and lev_1.

The air at lev_2 interacts only with the grid box average flux to which the different tiles contribute according to their share in grid box area. The grass tile has a comparatively low share in grid box area (19 %). Thus the relative temperature increase at lev_1 in the grass tile and the temperature decrease at lev_2, resulting from the vertical turbulent mixing between the two levels, are disproportional. This disproportionality prevents the

temperature at lev_2 to rapidly approximate to the temperature of the grass tile at lev_1, which would limit the downward transport of heat. In this constellation the horizontal convergence of fluxes with height does not result in a convergence of the states of the different tiles with increasing height but actually facilitates their divergence. Furthermore it makes possible a constellation in which relatively colder air is located above a relatively warmer surface and vice versa.

In this magnitude the process described above is not a generally observable feature of the VERTEX scheme as it was only found under the specific circumstances described at the beginning of this section. Furthermore, it is questionable whether atmospheric spatial variability that exceeds the causative variability at the surface can be observed in the real world. Therefore, the above example should merely be understood as an emphasis on the strong non-linearity in the processes involved. Nonetheless, small scale numerical studies indicate that local stratifications are plausible in which areas of warmer air located at a certain height above a smoother and colder surfaces adjoin rougher and warmer surfaces on top of which cooler air is located, resulting in distinct atmospheric spatial heterogeneity (Mott et al., 2014). Generally, the underlying mechanism of local decoupling is not well understood but could represent an important factor in e.g. snow patch survival (Derbyshire, 1999; Mott et al., 2013).

2.3.3. Comparison of different coupling schemes

The above simulations were analysed with respect to the behaviour of the turbulent vertical transport when the lowest atmospheric model levels are further partitioned into the same tiles as the surface. However, the resolved transport process has not yet been compared to the vertical turbulent transport under the assumption of the blending height below the lowest model level. Thus, one open question which needs to be addressed is whether the differences in the surface-atmosphere coupling also have a noticeable impact on the simulated mean state of a grid box. As stated above the magnitude of the vertical turbulent fluxes depends non-linearly on the state of the surface and the atmosphere. Therefore, it is plausible that e.g. the warming of the surface in one tile in the grid box is not balanced by the cooling in another but that the mean state of the grid box is affected. If the effect is pronounced enough to affect other key processes, which are only grid resolved, such as convection, precipitation or radiative heating, this could eventually lead to a distinct difference between simulations performed with different coupling schemes.

In order to investigate this, simulations of 35 grid boxes using a parameter aggregation scheme (PARAM), the simple flux aggregation scheme (SIMPLE) and the VERTEX scheme (VERTEX) were performed for the duration of one year. The grid boxes which cover different longitudes, latitudes and climate-zones were selected in such a way as to include tiles with diverse characteristics, large cover fractions and horizontal extents.

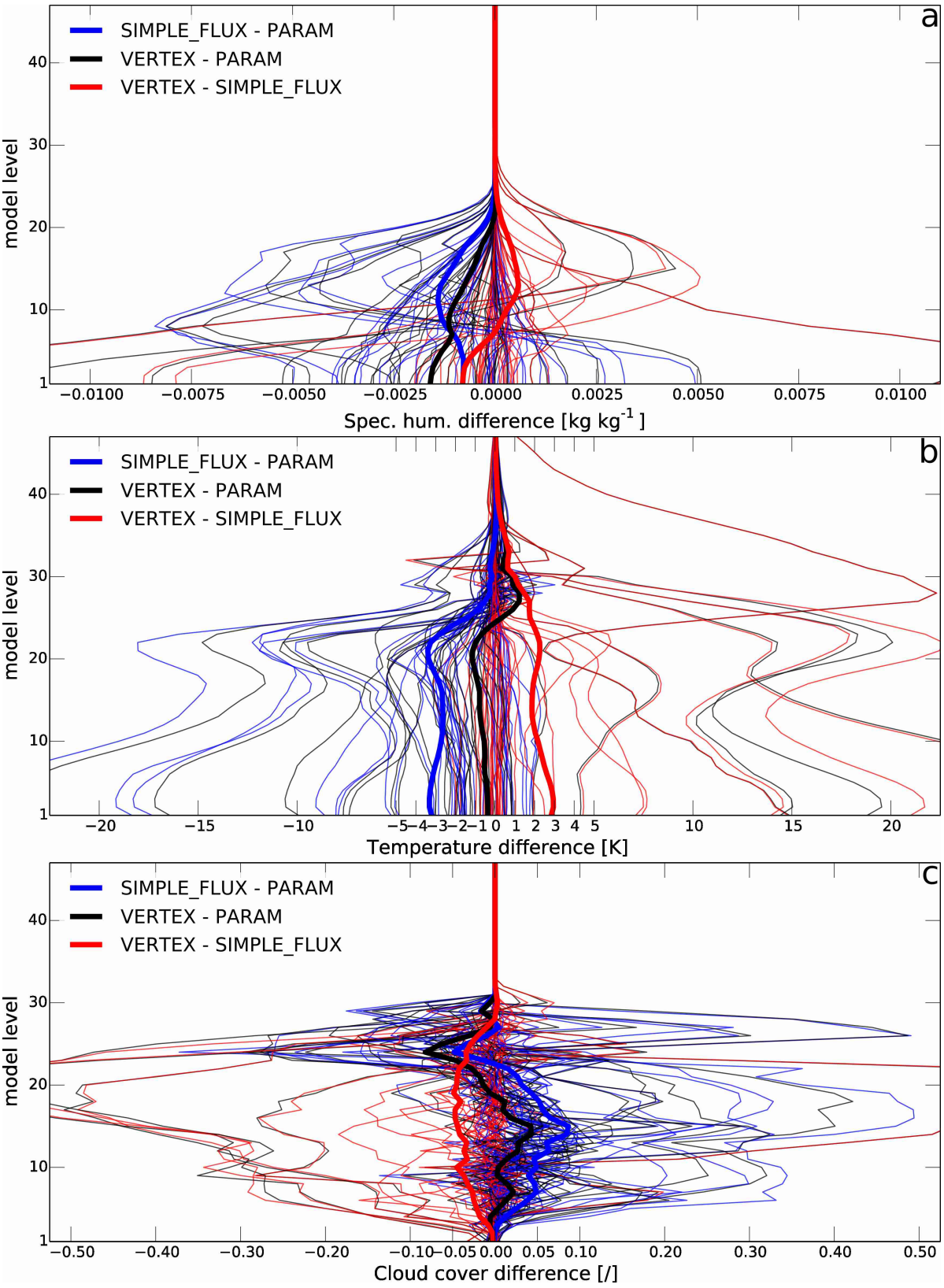

Figure 11: Differences in annual mean of 35 simulated grid boxes a) specific humidity b) temperature c) cloud cover, thin lines correspond to the individual grid boxes and the thick line to the average of all boxes

In the framework of a single column simulation the differences between two simulations can become unrealistically large because of the absence of horizontally compensating processes. For example if in a grid box all soil moisture is evaporated (all incoming radiation is expended in surface warming and the sensible heat flux) a drastic temperature increase can not be compensated by horizontal heat or moisture advection. If this is the case in only one of the simulations the difference to the other simulations can be dramatic. Therefore, the subsequent results present idealized cases and the differences in the state of individual grid boxes are potentially much larger than they would be in a global simulation.

It can immediately be seen that the choice of the coupling scheme has a substantial impact on the annual mean state of the simulated grid boxes (Fig. 11). Temperature differences may exceed $20\,K$, differences in specific humidity $10\,g\,kg^{-1}$ and difference in cloud cover may be larger than $50\,\%$ in certain grid boxes and levels. In comparison to the parameter aggregation scheme, the two flux aggregation schemes exhibit a clear tendency to produce a colder and dryer atmosphere with more clouds lower and less clouds higher up in the atmosphere. Even though this is not true for all grid boxes, on average the temperature differences between SIMPLE (VERTEX) and PARAM are slightly larger than $-3\,K$ ($-0.75\,K$) between the surface and the 22nd model level (around $14\,km$). On average the differences in specific humidity become as large as $-0.8\,g\,kg^{-1}$ ($-1.6\,g\,kg^{-1}$) close to the surface and about $-1.3\,g\,kg^{-1}$ ($-0.8\,g\,kg^{-1}$) between level 8 and 15 (between $2.5\,km$ and $7\,km$). One possible explanation why temperatures and specific humidity are predominantly much lower in SIMPLE than in PARAM is given below.

As shown above different tiles have different strength in coupling between the atmosphere and the surface. As this is dependent on the amount of turbulence created, tiles with a large roughness length have a stronger coupling between surface and atmosphere. In JSBACH the tiles which represent PFTs with a large roughness length such as trees are also the ones with a pronounced ability to transpire. The concurrence of large roughness lengths and transpiration rates above the grid mean promotes the upward transport of moisture from the surface. This effect is further intensified by the fact, that the albedo of these tiles is predominantly below the grid mean which means that also more energy from absorbed short wave radiation is available. Exemplary the canopy albedo in the visible range of trees (0.04 - 0.05) is between 2 and 1.6 times smaller than that of grass, pasture and crops (0.08). Thus, by resolving the surface fluxes with respect to the tiles, there is an initial increase in grid mean upward latent and decrease in upward sensible heat flux. The increase in upward moisture flux initially leads to a relatively moister state of the atmosphere. Furthermore, because less energy in form of sensible heat is transported upward from the surface, it also initially leads to a colder state of the atmosphere when comparing SIMPLE to PARAM.

This difference in the atmospheric state has a strong effect on the the formation of clouds as it leads to an increase in cloud cover low in the atmosphere (on average by as much as $5\,\%$ between the surface and the 20th model level (around $11.5\,km$)). The change

in cloud cover strongly affects the radiation budget at the surface, e.g. net short wave radiation at the surface is reduced on average by as much as $8.3\,W\,m^{-2}$. Furthermore, the colder and moister atmosphere initially facilitates the occurrence of precipitation. Precipitation is a process which is not resolved with respect to the tiles hence all tiles receive the same amount of precipitation relative to their cover fraction. At the same time the proportionally larger share of the atmospheric water vapour which precipitates, originates from tiles with pronounced transpirational abilities and roughness lengths. This eventually leads to an accumulation of soil moisture within the tiles with poor transpirational abilities and possible water stress in tiles with pronounced transpirational abilities. With the large share of water being located in the tiles that transpire at rates below the grid mean, on average there is a strong decrease in the upward latent heat flux (on average about $2.2\,W\,m^{-2}$). Consequently, the vertically integrated water vapour is reduced on average by $7.8\,kg\,m^{-2}$. Due to the reduction in incoming radiation, less energy is available at the surface, therefore not only the latent heat flux decreases but also the upward sensible heat flux (on average about $1.3\,W\,m^{-2}$). Thus, in the larger share of the simulated grid boxes temperatures and specific humidity rates are lower when the simple flux aggregation scheme was used for the simulation.

The differences between the two flux aggregation schemes are in the same order of magnitude as those between SIMPLE and PARAM. There is a distinct tendency towards higher temperatures throughout the entire vertical column and smaller specific humidity values close to the surface and larger specific humidity values further up in the atmosphere (between level 7 and 22 (between $2\,km$ and $14\,km$))) in VERTEX. The simulations performed with the VERTEX scheme gave an atmospheric state which is on average between $2\,K$ and $3\,K$ warmer between the surface and the 27th model level (around $21\,km$). Close to the surface the atmosphere is about $0.8\,g\,kg^{-1}$ dryer and moister higher up (around the 13th model level (around $5.5\,km$)).

The reason for this lies within the resolution of the vertical transport process in the lowest layers of the atmosphere with respect to the tiles. As has been argued the atmospheric column within the warmer tiles is predominantly less stable than in the colder tiles which facilitates the vertical mixing. A stronger vertical exchange within the relatively warmer and dryer tiles means that in VERTEX initially more sensible heat relative to moisture is being transported upwards from the surface in comparison to SIMPLE. At the same time more moisture remains in the lowest layers of the atmosphere, relatively reducing the atmospheric moisture demand. The consequent shift from upward latent to upward sensible heat heat fluxes from the surface, results in an initially warmer and dryer atmosphere.

Due to the temperature increase in the atmosphere the saturation vapour pressure increases. This feeds back on the formation of clouds, so that below the 28th model level (around $22\,km$) the cloud cover at a given level is reduced on average by around $2.5\,\%$. Consequently, less moisture falls out in form of precipitation, i.e precipitation decreases on average by $-0.2\,mm\,d^{-1}$, leading to an overall increase in specific humidity higher up

in the atmosphere and an increase in vertically integrated water vapour ($1.23\,kg\,m^{-2}$). Furthermore, the reduction in cloud cover leads to a strong increase in net short wave radiation ($7.2\,W\,m^{-2}$).

The reduction in precipitation means that less water is available at the surface thus annual evapotranspiration is strongly reduced (apparent in the decrease of annual mean upward latent heat flux by about $2.0\,W\,m^{-2}$). This, together with the increase in available energy due to the increase in net radiation causes an increase in surface temperature. The consequent increase in upward sensible heat flux (on average by $3.0\,W\,m^{-2}$) in turn increases the temperatures within the atmosphere. This results in an overall warmer atmosphere and surface and an atmospheric state which is dryer low in the atmosphere and wetter above the 7th model level (around $2\,km$). Here, the impact on temperature is more pronounced than the impact on specific humidity. The specific humidity in the atmosphere is closely connected to the water available within the grid box which in a large share of simulations became a limiting factor.

As can be seen in Fig. 11, the response to a certain coupling scheme, as described above, is not represented by all the selected example grid boxes. Thus, the arguments given here pertain rather to an idealized mean scenario than to a specific simulation. This is because even in a single grid box the processes are much more complex than what has been reasoned. The initial tendency, i.e. a relative increase in evapotranspiration related to the flux aggregation schemes and a more pronounced vertical exchange in the relatively warmer tiles when using the VERTEX scheme, could be found in almost all of the simulated grid boxes. However, the individual grid boxes exhibited strongly diverging responses to this initial tendency. For example, a warmer surface may lead to a decrease in stability and a more frequent triggering of convection and a consequent increase in (cumulus) cloud cover. Increased precipitation early in the year could lead to clearer skies and an increase in incoming shortwave radiation resulting in a warmer atmosphere despite an initially higher relative humidity. Water stress may impact the behaviour of plants and thus the surface albedo which in turn affects the energy balance at the surface.

Despite these diverging responses in different grid boxes, the present study clearly shows that the impact of the choice of coupling scheme may be substantial. Here, the differences between SIMPLE and PARAM are predominantly larger than those between VERTEX and SIMPLE. However, from the 35 simulated grid boxes between 20 % and 50 % (depending on the variable and the model level which are being compared) exhibited larger differences between VERTEX and SIMPLE. In around 30 % to 60 % of the investigated grid boxes the differences between VERTEX and SIMPLE were only about 25 % smaller than those between SIMPLE and PARAM. In approximately 40 % - 70 % of the grid boxes the differences between VERTEX and SIMPLE were still half as large as those between SIMPLE and PARAM. Furthermore, the initial tendency related to a certain coupling scheme is systematic, thus, the simulations performed with a given coupling scheme favour a development in a certain direction.

2.4. Conclusions and Discussions

Modelling the link between atmosphere and the horizontally heterogeneous land surface remains a key challenge for present day weather and climate models. The present study investigated the influence of surface heterogeneity on the turbulent mixing process using the newly developed VERTEX scheme. By taking into account horizontal heterogeneity not only at the surface but also at the lowest levels within the atmosphere, the scheme allows the resolution of the turbulent mixing process with respect to the surface tiles. Here, it could be shown that the intensity of the vertical turbulent mixing process can differ largely within a grid box. It has been argued that these differences are closely connected to the differences in atmospheric stability between the different tiles, which can only be taken into account by resolving the lowest layers of the atmosphere with respect to the surface tiles.

Two example cases have been used to demonstrate how differences in atmospheric stability relate to the tile specific deviations of the atmospheric state and of the state of the surface. It could be shown that the sub-grid variability in the state of the atmosphere does not necessarily scale linearly with height. In comparably unstable circumstances the differences in stability help to equilibrate the state of the individual tiles and the sub-grid scale variability in temperature and humidity decreases strongly with increasing height. Here, the a VERTEX scheme was capable of representing sub-grid moisture circulation i.e. the upwards transport of moisture above the blending height in one tile and the downward transport of moisture in another tile. In contrast to this, in comparably stable circumstances the stability differences facilitate a divergence of the states. In extreme circumstances this can even lead to a situation in which the differences between the state of individual tiles become larger within the lowest layers of the atmosphere than on the surface.

Furthermore, simulations performed using the VERTEX scheme were compared to simulations using a parameter aggregation scheme and a simple flux aggregation scheme, which does not account for horizontal heterogeneity within the atmosphere. It could be shown that, due to the non-linear nature of processes involved, the representation of sub-grid scale variability also has a distinct impact on the grid box mean state. This implies that the assumption of a blending height on the lowest atmospheric level on which the simple flux aggregation is based may be the source of errors which in many cases may be as large as the errors related to the aggregation of parameters. Thus employing a scheme which takes into account sub-grid variability within the atmosphere could significantly improve model results on the global scale.

In many of the grid boxes considered in Sect. 2.3.3 the impact of representing sub-grid scale variability in the atmosphere as well as at the surface is as large as the impact of an explicit representation of surface heterogeneity. Here, the system's response to a certain coupling scheme was not represented by all the selected example grid boxes. However, the system's reaction was on average systematic, so that large differences can also be

expected to be found in global simulations. Validating the true impact of a coupling scheme on the global scale however, requires further simulations with global-scale GCMs.

Finally, in the present implementation of the VERTEX scheme, the sub-grid scale variability in the atmosphere was limited to the two lowest model levels. However, the calculated blending heights indicate that the deviations between the states of different tiles could still be large higher up in the atmosphere. As studies show, this can have a strong impact on processes such as convection and cloud formation throughout the entire planetary boundary layer (Rieck et al., 2014). Here the knowledge of sub-grid scale variability in the atmosphere, which the VERTEX scheme provides, may not only be important for its impact on the vertical turbulent transport but it could also help to improve the representation of grid resolved processes. Furthermore, atmospheric sub-grid scale heterogeneity of wind speed and direction was not taken into account in order to maintain the level of complexity as low as possible. As the simulations showed to be sensitive to sub-grid scale heterogeneity within the atmosphere with respect to temperature and specific humidity, this may also be the case for sub-grid scale heterogeneity with respect to wind, presenting an opportunity for future research.

3. Explicit Representation of Spatial Sub-grid Scale Heterogeneity in an ESM

3.1. Introduction

In a simplistic representation, the link between surface and atmosphere comprises the surface heat, radiation, mass and momentum fluxes. These fluxes have a non-linear dependency on the state of the surface and the atmosphere. Land surface characteristics such as topography, the properties of the soil and hydrological characteristics, land use, vegetation, etc., vary on scales ranging from millimetres to hundreds of kilometres. Consequently, the state of the land surface and many spatially heterogeneous processes vary likewise (Sellers, 1991). This divergence of scales, together with the non-linear nature of processes involved, poses one of the fundamental difficulties in accurately describing the interaction of the land surface and the atmosphere, making a realistic representation a key challenge in Earth System Modelling.

Present day Earth System Models (ESMs) employ different strategies to integrate the spatial sub-grid scale (SSGS) information of the land surface in the model's physical parametrizations and to aggregate the information to match the grid of the atmosphere. These strategies require simplifying assumptions which, due to the non-linear nature of the processes involved, result in a distinct and possibly inaccurate representation of the land surface-atmosphere interaction. One basic distinction between different aggregation methods can be made between the parameter-aggregating and flux-aggregating methods. Both methods assume that a grid box can be sectioned into discrete subdivisions the so called "tiles" or "patches", which themselves exhibit homogeneous characteristics. In the parameter-aggregating methods SSGS heterogeneity is not explicitly accounted for, instead soil and vegetation parameters of the tiles are aggregated to one effective value representing the entire grid box. This is usually done by averaging all SSGS parameter values weighted by the respective cover fraction. The fluxes connecting surface and atmosphere are calculated based on these effective grid parameters (Giorgi and Avissar, 1997). In this study this will be referred to as the "parameter aggregation".

In the flux-aggregating methods SSGS heterogeneity is explicitly represented and fluxes are calculated for each tile in a grid box individually based on the tile specific characteristics. One of these methods is the "mixture approach" (Koster and Suarez, 1992). This approach assumes that heterogeneity at the surface consists of numerous clusters, i.e. homogeneous subareas, which cover only small areas and that these clusters are evenly distributed across the grid box. Furthermore, the horizontal turbulent fluxes are assumed to be large compared to the vertical turbulent fluxes. Consequently, the surface fluxes that originate from individual tiles have completely blended horizontally below the lowest atmospheric model level. The atmosphere interacts only with the mixed flux and remains horizontally homogeneous. The term "simple flux aggregation" used in this work refers to the mixture approach.

Many mostly local studies have compared techniques which apply an aggregation of parameters to those which aggregate fluxes (Avissar and Pielke, 1989; Polcher et al., 1996; Van den Hurk and Beljaars, 1996; Cooper et al., 1997; Molod and Salmun, 2002; Essery et al., 2003; Heinemann and Kerschgens, 2005; Ament and Simmer, 2006). These studies found pronounced differences between simulations performed with the two coupling techniques and they agree that by employing an aggregation of fluxes the representation of processes clearly improves. Many of the studies additionally found an improvement of the simulated climate.

It is evident that the assumption of atmospheric spatial homogeneity may be valid only in specific circumstances. Numerous studies, both modelling and observational, showed that indeed it becomes erroneous when the scale of surface heterogeneity increases beyond the micro-scale (Mason, 1988; Claussen, 1995; Raupach and Finnigan, 1995; Avissar and Schmidt, 1998; Mahrt, 2000; Bou-Zeid et al., 2004; Patton et al., 2005; Ma et al., 2008). In this case, the signal associated with a specific surface feature may be detectable far above the surface layer, resulting in a spatially heterogeneous state of the atmosphere at heights above the lowest model level of many ESMs, which is often located below a height of 50 m (Arola, 1999).

The present study investigates the importance of an explicit representation of SSGS heterogeneity at the surface and in the lowest parts of the atmosphere, using simulations performed with the Max Planck Institute for Meteorology's Earth System Model (MPI-ESM). More specifically, with the land surface model JSBACH (Raddatz et al., 2007; Brovkin et al., 2009; Ekici et al., 2014) coupled to the general circulation model ECHAM6 (Stevens et al., 2013), which will in the following be referenced with ECHAM/JSBACH. Section 3.2 gives a brief overview over the model and the different coupling schemes used in the study. Furthermore, the simulations will be described in more detail. In section 3.3 the investigation is focused on determining whether different land cover types display systematic differences in the near surface processes with respect to the different coupling schemes. Section 3.4 focuses on the impact of surface and atmospheric SSGS heterogeneity on the simulated global climate. The main results are summarized and shortly discussed in section 7.

3.2. Methods

In the operational setup, ECHAM/JSBACH uses a parameter aggregation scheme to couple land surface and atmosphere. Here, the determination of an effective grid box mean albedo is described in Otto et al. (2011), the aggregation of the surface roughness length of different tiles follows Mason (1988); Claussen (1991); Claussen et al. (1994) and the aggregation of hydrological and soil parameters is done as a weighted (by the respective cover fractions) average (Kabat et al., 1997; Feddes et al., 1998). Based on the effective parameters, the surface fluxes are calculated using a bulk-exchange formulation (Giorgetta et al., 2013). For the present study, ECHAM/JSBACH was altered to enable

a surface-atmosphere coupling using a simple flux aggregation scheme and an improved coupling method that represents the turbulent mixing process more realistically, i.e. the VERTEX scheme (de Vrese et al., 2015). In both schemes the homogeneous subareas in a grid box are represented by individual tiles which only interact via the vertical turbulent fluxes. In the soil a horizontal transport of water and heat is not modelled and the soil moisture and temperature of a given tile is independent of the other tiles.

The simple flux aggregation scheme implemented into ECHAM/JSBACH, follows the general method for an implicit surface-atmosphere coupling proposed by Polcher et al. (1998); Best et al. (2004). Similar to the simple flux aggregation scheme, the VERTEX scheme explicitly represents surface SSGS heterogeneity by individual tiles. Additionally, the scheme explicitly represents SSGS heterogeneity within the tree lowest layers of the atmosphere, i.e. up to a height of roughly 350 m. In the atmosphere, the vertical fluxes within the individual tiles are modelled by a modified version of the turbulent kinetic energy scheme described in Brinkop and Roeckner (1995). In the VERTEX scheme, the fluxes within the individual tiles are not treated independently of each other but are assumed to mix horizontally to a certain extent. Thus, the vertical flux from a given tile can influence the states of all the tiles on the level above. The extent to which the the vertical fluxes blend horizontally is determined based on the ratio of the height of a model level and the blending height. The latter can be estimated as a function of friction velocity, the horizontal windspeed and the characteristic length scale of the respective surface heterogeneity (Mahrt, 2000). In this study the characteristic length scales required for the computation of the blending height were derived from the GlobCover dataset (Arino et al., 2012)(Fig. 36).

Due to the many degrees of freedom incorporated in global scale simulations following the protocol of the Atmospheric Model Intercomparison Project (AMIP), i.e. the atmospheric model coupled to a land surface model with prescribed sea-surface temperature and sea-ice extent (Gates et al., 1999), these can be difficult to interpret. Single column simulations on the other hand, facilitate the understanding of relevant processes but the findings are often limited to the specific location the model was applied to. Offline simulations, i.e. the land surface model forced by observations, have the disadvantage that a feedback from the surface onto the atmosphere is being omitted. However, they serve as a compromise between AMIP-style and single column simulations. In section 3.3 a slightly modified version of this type of experiment was conducted as a quasi-offline study.

For a 5-year AMIP-style simulation, ECHAM/JSBACH was adapted in such a way that all calculations pertaining to surface processes, including the calculation of the state and the surface fluxes, were duplicated twice, effectively creating three different land surfaces within JSBACH. Each surface developed an individual state as they were all coupled to the same atmospheric conditions but via a different coupling scheme.

In the following these will be referred to as:

- $\text{PARAM}_{\text{SRF}}$ coupled with parameter aggregation
- $\text{SIMPLE}_{\text{SRF}}$ coupled with simple flux aggregation
- $\text{VERTEX}_{\text{SRF}}$ coupled with the VERTEX scheme.

Differences between the above surfaces will be referenced by ΔSRF indexed with two letters indicating the two respective surfaces. For example $\Delta\text{SRF}_{\text{S-P}}$ refers to the differences between $\text{SIMPLE}_{\text{SRF}}$ and $\text{PARAM}_{\text{SRF}}$.

The surface-atmosphere feedback is taken from $\text{PARAM}_{\text{SRF}}$, whereas the potential feedback from the other land surfaces is calculated for each time step but does not effect the state of the atmosphere in the subsequent time step.

The VERTEX scheme requires the knowledge of atmospheric SSGS variations of temperature and specific humidity at the beginning of each time step. In order to preserve the SSGS variability in the atmosphere, a refinement was applied to the state variables at the lowest atmospheric model levels. At the end of a 20-minute time step the tile specific SSGS temperature and humidity deviations from the grid mean were stored and added to the prescribed grid mean values at the beginning of the following time step.

The simulation was performed for the period of 1979 - 1984 and the multi-annual mean of the years 1980 - 1984 will be analysed for the global scale with a focus on the relation between soil moisture, surface temperature and the turbulent heat fluxes. Because the surface-atmosphere feedback from $\text{VERTEX}_{\text{SRF}}$ and $\text{SIMPLE}_{\text{SRF}}$ is not taken into account, the analysis in section 3.3 remains a qualitative evaluation which does not allow any conclusions on the absolute magnitude of impacts and may not be applicable to a fully coupled land surface-atmosphere system.

To estimate the impact of a given coupling scheme on the simulated global climate, 3×5 AMIP-style simulations were performed, which will be discussed in section 3.4. These will be referred to as:

- $\text{PARAM}_{\text{ENS}}$; ensemble of five simulations using a parameter aggregation scheme
- $\text{SIMPLE}_{\text{ENS}}$; ensemble of five simulations performed with the simple flux aggregation scheme
- $\text{VERTEX}_{\text{ENS}}$; ensemble of five simulations employing the VERTEX scheme.

The latter two may also be referred to as the two FLUX_{ENS} as opposed to $\text{PARAM}_{\text{ENS}}$. The comparison of two of the above ensembles will be referenced by ΔENS indexed with two letters indicating the two respective ensembles. For example $\Delta\text{ENS}_{\text{S-P}}$ refers to the differences between $\text{SIMPLE}_{\text{ENS}}$ and $\text{PARAM}_{\text{ENS}}$.

Each simulation was performed for the same 21-year-period (1979 - 1999; 1979 was required for the model spin up and is omitted from the analysis) but initialized with slightly different conditions. All the above simulations were performed at a standard vertical resolution of 47 levels, of which the lowest is located on a height of approximately 30 m and a horizontal resolution of T63, i.e. a grid-spacing of 140 x 210 km at mid-latitudes.

3.3. Impact of spatial heterogeneity on the near surface processes in individual tiles

The major conceptual difference between parameter and flux aggregation as realized in JSBACH is the existence of SSGS variations in the state of the land surface and in the surface fluxes. In the operational setup (parameter aggregation), technically SSGS heterogeneity exists in form of the different surface tiles. However, the majority of physical surface and soil processes, including the calculation of surface fluxes, surface temperature and soil moisture content, are modelled based on grid mean values, thus de facto heterogeneity is not being considered. With the introduction of the flux aggregation not only the land surface-atmosphere coupling was changed, but SSGS variations are considered in the majority of the surface and soil processes.

In JSBACH tiles represent different plant functional types (PFTs) (with the exception of glaciers) which in turn each represent different species aggregated to groups based on their functional properties. For the following considerations, one of the most important properties of a PFT is its ability to transpire which is closely related to the photosynthetic activity. In JSBACH this is reflected by a PFT's stomatal conductivity and leaf area. The impact of differences in albedo was found to be considerably smaller, and has been omitted in the analysis by calculating the absorbed radiation at the surface based on the grid box mean albedo.

3.3.1. Tile-based comparison of $\mathrm{SIMPLE_{SRF}}$ and $\mathrm{PARAM_{SRF}}$

Due to the PFT specific properties determining the stomatal conductivity and the leaf area, some PFTs transpire at relatively high rates. In the present model setup these are tropical and extra-tropical trees, c3 grass and c3 pasture (Fig. 12; a - d). When comparing $\mathrm{SIMPLE_{SRF}}$ to $\mathrm{PARAM_{SRF}}$, an immediate effect within the respective tiles is a predominant increase in transpiration. As the excess in transpiration is not balanced by a decrease in evaporation, it leads to an increase in evapotranspiration and in the latent heat flux. Because more energy is expended in evapotranspiration, less energy is available for a warming of the surface which results in predominantly lower surfaces temperatures, i.e. more evaporative cooling of the surface. Consequently, there is a lower sensible heat flux and a decrease in Bowen ratio.

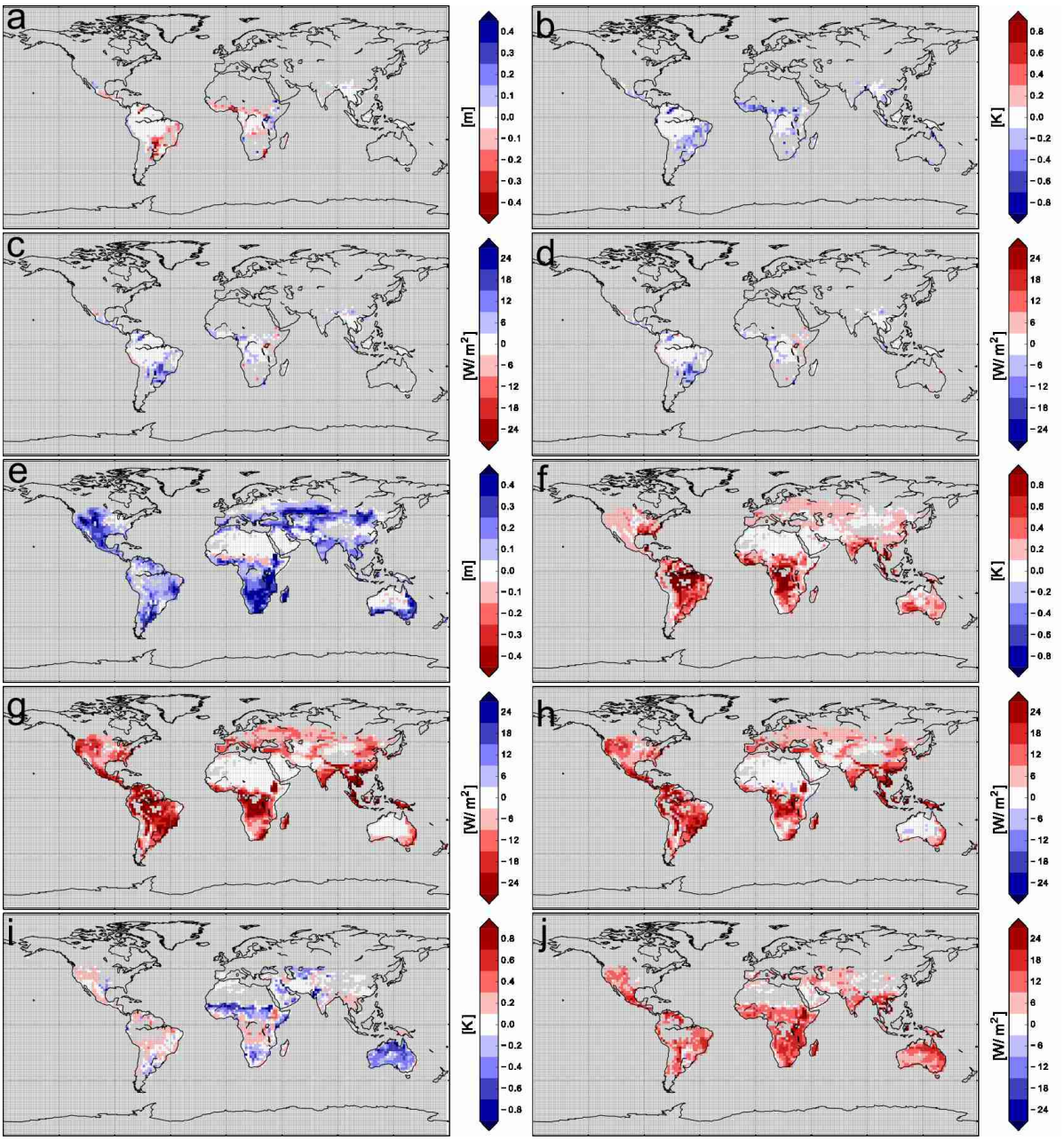

Figure 12: 5-year mean difference between $\text{SIMPLE}_{\text{SRF}}$ and $\text{PARAM}_{\text{SRF}}$; tropical evergreen forest: a) soil-moisture b) surface temperature c) latent heat flux d) sensible heat flux; c4 pasture: e) soil moisture f) surface temperature g) latent heat flux h) sensible heat flux; raingreen shrubs: i) surface-atmosphere temperature difference j) sensible heat flux

Precipitation is calculated based on $\text{PARAM}_{\text{SRF}}$ and is unaffected by $\text{SIMPLE}_{\text{SRF}}$, thus the shift towards increased evapotranspiration in $\text{SIMPLE}_{\text{SRF}}$ does not increase precipitation and therefore generally leads to lower soil moisture values in these tiles. In turn, tiles in which the respective PFTs transpire at relatively low rates such as shrubs, c4 grass and c4 pasture, show an opposite behaviour (Fig. 12; e - h). Here the shift towards less transpiration leads to wetter soils, a shift from latent to sensible heat and

consequently higher surface temperatures.

Another important aspect is a PFT's vegetation roughness length. Under given wind conditions it determines the generation of shear driven turbulence and accordingly has a strong impact on the turbulent fluxes. This characteristic becomes especially relevant for regions in which the vegetation comprises PFTs with distinctly differing heights such as savannah. Here the vegetation consists of trees or shrubs and very low vegetation such as grasses or pasture. In tiles with a surface roughness larger than the grid mean, the consideration of heterogeneity leads to stronger land surface-atmosphere coupling, as more turbulence is created near the surface under given wind conditions. In turn, in the tiles with low vegetation, less turbulence is generated, resulting in a weaker surface-atmosphere coupling. This effect can be seen for example at the southern border of the Sahel-zone and northern Australia. Here raingreen shrubs constitutes vegetation with a comparable large roughness length and the land-surface atmosphere coupling is relatively strong. Therefore, in the respective regions there is a the distinct increase in sensible heat flux despite the occurrence of a cooling of the surface, which reduces the surface-atmosphere temperature gradient (Fig. 12; i - j).

3.3.2. Tile-based comparison of $\mathsf{VERTEX_{SRF}}$ and $\mathsf{SIMPLE_{SRF}}$

When comparing the VERTEX and the simple flux scheme the most relevant conceptual change is the reduction in horizontal mixing of the surface fluxes in the VERTEX scheme. This results in SSGS variability in the state of the lowest layers of the atmosphere and consequently in differences in atmospheric stability between the tiles.

In comparison to the mean state, the tile specific state of the atmosphere above PFTs with pronounced transpirational abilities is moister for $\mathrm{VERTEX_{SRF}}$ as less dry air from other tiles is being mixed into the local atmosphere. Furthermore, the air in these tiles is relatively cold, causing a stability increase in the lowest atmospheric layers (Fig. 13; a - d). Therefore the vertical turbulent transport in the atmosphere is weaker in these tiles and the moisture which is being mixed upwards from the surface is more confined to the lowest atmospheric layers. This primarily leads to a reduced surface-atmosphere moisture gradient, which in turn reduces the upward moisture flux in these tiles. Due to the corresponding decrease in the latent heat flux, more energy is available at the surface, which should result in an increase in surface temperature and in the sensible heat flux.

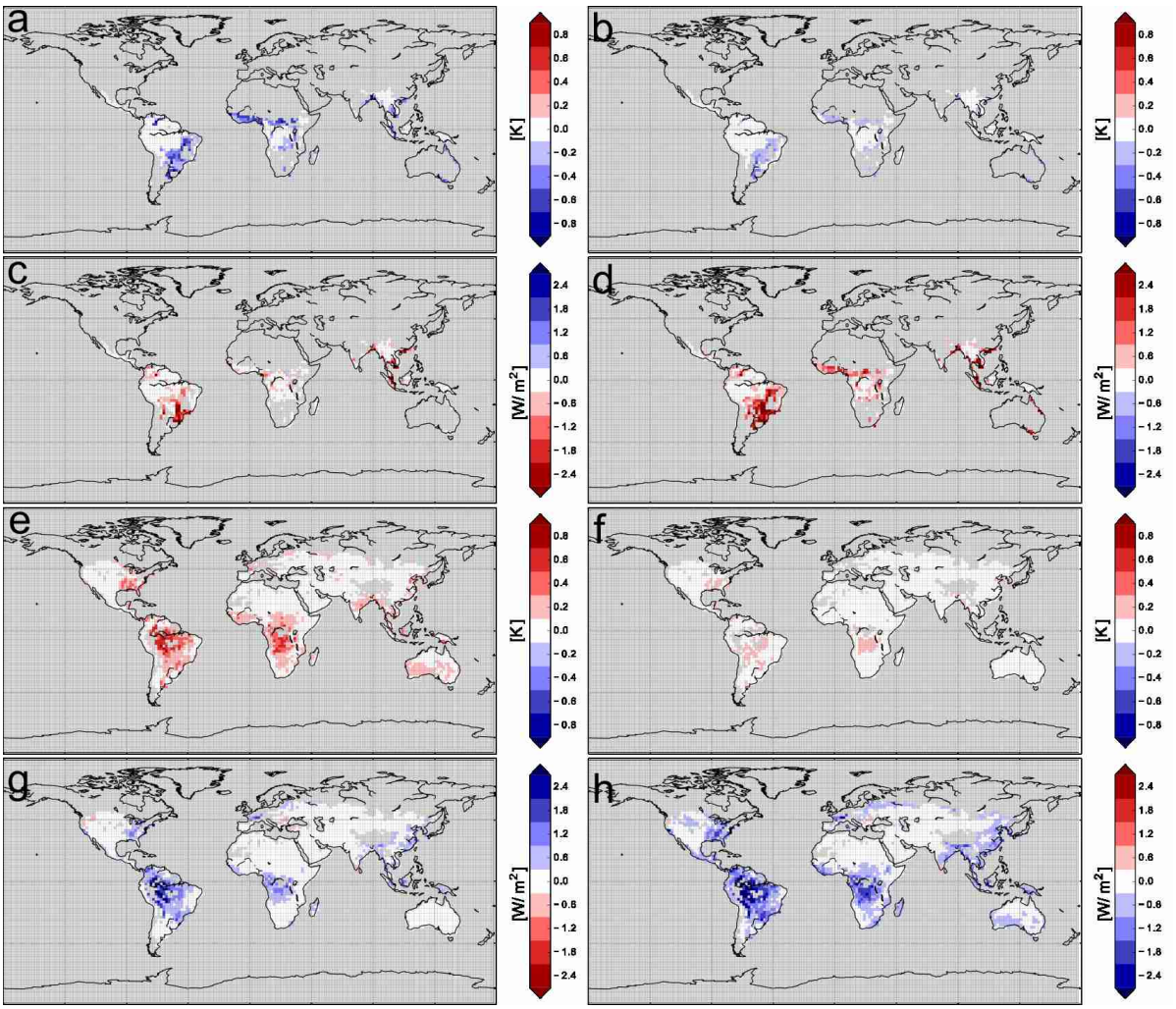

Figure 13: 5-year mean difference between $\text{VERTEX}_{\text{SRF}}$ and $\text{SIMPLE}_{\text{SRF}}$; tropical evergreen forest: a) temperature on the lowest atmospheric model level b) surface temperature c) latent heat flux d) sensible heat flux; c4 pasture: e) temperature on the lowest atmospheric model level f) surface temperature g) latent heat flux h) sensible heat flux

However, as less sensible heat is mixed into the atmosphere above these tiles, the air is cooler for $\text{VERTEX}_{\text{SRF}}$ than the atmospheric forcing without SSGS refinement. This leads to an increase in the surface-atmosphere temperature gradient and in the sensible heat flux in combination with lower temperatures both in the atmosphere and at the surface. Because these two effects oppose each other, the signal is less distinct. The overall effect is that, despite the reduction in evapotranspiration and the increase in the sensible heat flux, the surface temperature is lower for $\text{VERTEX}_{\text{SRF}}$ than for $\text{SIMPLE}_{\text{SRF}}$. The reduction in evapotranspiration also causes a relative increase in soil moisture within these tiles. For PFTs which transpire at relatively low rates, the reduced horizontal mixing in the VERTEX scheme leads to a dryer and warmer atmospheric state (Fig. 13; e - h). This in turn increases the atmospheric moisture demand and evapotranspiration, indicated by an increase in the latent heat flux and the reduction in soil moisture. The

resulting energy deficit should lead to a decrease in surface temperature and a decrease in the sensible heat flux. But as less cold air is being mixed into the atmosphere above these tiles, the decrease in the sensible heat flux is realized in combination with higher temperatures in the atmosphere and at the surface.

3.3.3. Effect on the grid box mean state

In certain tiles $\Delta\mathrm{SRF}_{\mathrm{V\text{-}S}}$ is in the same order of magnitude as $\Delta\mathrm{SRF}_{\mathrm{S\text{-}P}}$. For example, with respect to global mean surface temperature for tiles representing evergreen (deciduous) tropical trees, $\Delta\mathrm{SRF}_{\mathrm{V\text{-}S}}$ amounts to 75 % (80 %) of $\Delta\mathrm{SRF}_{\mathrm{S\text{-}P}}$. For shrubs, evergreen and deciduous extra-tropical trees these figures still range between 30 % and 50 %. However, the differences in soil moisture and in the surface heat fluxes are mostly an order of magnitude smaller in case of $\Delta\mathrm{SRF}_{\mathrm{V\text{-}S}}$ than for $\Delta\mathrm{SRF}_{\mathrm{S\text{-}P}}$. This discrepancy is also present in the comparison of the grid box mean values.

Due to the non-linear dependency of the surface fluxes on the state of the surface, especially on the plant available water, the effect of reduced transpiration in certain tiles clearly dominates the effect of the increased transpiration in other tiles when comparing the surfaces coupled with the flux aggregation schemes to that coupled with the parameter aggregation scheme. Hence, on the grid scale, the effect of introducing the simple flux aggregation is a distinct reduction in transpiration in a large part of the land surface which causes a decrease in evapotranspiration and an increase in soil moisture (Fig. 14; a - b). Furthermore, a shift from surface latent to sensible heat flux occurs and a corresponding increase in the surface temperature. This agrees well with a conceptual study performed by Koster and Suarez (1992) who found that when aggregating SSGS parameters to effective grid values (as in $\mathrm{PARAM}_{\mathrm{SRF}}$), these are dominated by the tiles that are less effected by water stress. This results in increased evapotranspiration and lower surface temperatures in comparison to using a simple flux aggregation (as in $\mathrm{SIMPLE}_{\mathrm{SRF}}$).

Due to atmospheric SSGS variability in $\mathrm{VERTEX}_{\mathrm{SRF}}$, the local temperature and moisture gradients and the local stability in the atmosphere differ to those in $\mathrm{SIMPLE}_{\mathrm{SRF}}$. As will be explained in more detail later, accounting for stability differences in the atmosphere leads to a weaker vertical turbulent moisture transport relative to the turbulent transport of sensible heat. Therefore, in the larger part of the land surface, the grid box mean sensible heat flux increases in $\mathrm{VERTEX}_{\mathrm{SRF}}$ compared to $\mathrm{SIMPLE}_{\mathrm{SRF}}$. The excess heat which is being mixed from the surface to the atmosphere, is neglected in the quasi-offline simulation, therefore the increase in sensible heat flux does not lead to higher atmospheric temperatures and as a result also not to higher surface temperatures. Thus, in most areas the land surface exhibits an increase in the sensible heat flux and a decrease in latent heat flux in combination with reduced surface temperatures, as can be seen for example at the east coast of North and South America (Fig. 14; c - d).

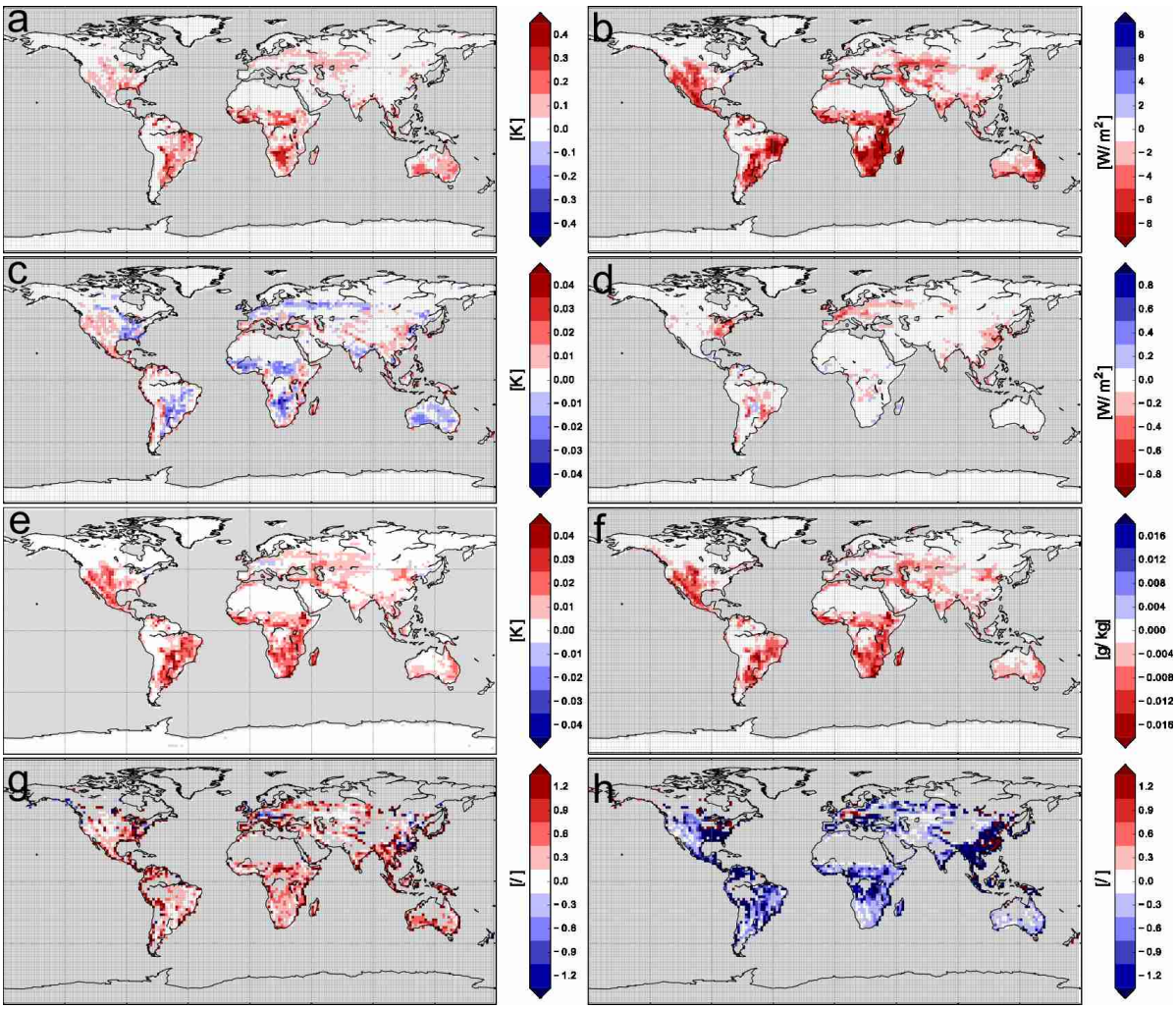

Figure 14: 5-year mean difference between $\text{SIMPLE}_{\text{SRF}}$ and $\text{PARAM}_{\text{SRF}}$; grid box average: a) surface temperature b) latent heat flux; $\text{VERTEX}_{\text{SRF}}$ and $\text{SIMPLE}_{\text{SRF}}$; grid box average: c) surface temperature d) latent heat flux; $\text{SIMPLE}_{\text{SRF}}$ and $\text{PARAM}_{\text{SRF}}$; grid box average: e) temperature on the lowest atmospheric level f) specific humidity on the lowest atmospheric level; $\text{VERTEX}_{\text{SRF}}$ and $\text{SIMPLE}_{\text{SRF}}$ relative to $\text{SIMPLE}_{\text{SRF}}$ and $\text{PARAM}_{\text{SRF}}$; grid box average: g) temperature on the lowest atmospheric level h) specific humidity on the lowest atmospheric level; Plots g - h are masked as to not include grid boxes in which the absolute value of neither the differences between $\text{SIMPLE}_{\text{SRF}}$ and the $\text{PARAM}_{\text{SRF}}$ nor between $\text{VERTEX}_{\text{SRF}}$ and the $\text{SIMPLE}_{\text{SRF}}$ are larger than 0.005 K time step^{-1} and 0.003 g Kg^{-1} time step^{-1}

Another important effect exists, which can be seen e.g. in the western parts of North America and the east coast of Africa. Here, the latent heat flux does not decrease and in parts even slightly increases. In the respective regions, the relative reduction in transpiration of tiles with pronounced transpirational abilities, is compensated by the relative increase in transpiration of PFTs with poor transpirational abilities. This leads to a more even distribution of soil moisture, reducing the effect of water stress. However, the consequent reduction in the grid mean sensible heat flux in $\text{VERTEX}_{\text{SRF}}$ does not cause a cooling of the atmosphere as the mean atmospheric state is set by $\text{PARAM}_{\text{SRF}}$.

Therefore a surface warming in these parts can be seen despite the decrease in the sensitive and a potential increase in the latent heat flux.

For the grid mean values $\Delta SRF_{V\text{-}S}$ is predominantly an order of magnitude smaller $\Delta SRF_{S\text{-}P}$ (Fig. 14; a - d). This implies that, given an identical mean state in the atmosphere, the surface is comparably insensitive to the representation of SSGS heterogeneity in the atmosphere. This is in good agreement with studies which indicate that atmospheric SSGS heterogeneity only has a minor impact on the magnitude of the surface fluxes (Mahrt and Sun, 1995; Ament and Simmer, 2006; Schomburg et al., 2012).

This may only be valid if the surface-atmosphere feedbacks are omitted. In the given experimental setup, potential feedbacks are indicated by the differences in atmospheric temperature and specific humidity calculated at the end of each time step (Fig. 14; e - h). For the grid box mean atmospheric state at the end of each time step, $\Delta SRF_{V\text{-}S}$ is comparable to $\Delta SRF_{S\text{-}P}$. With respect to global mean temperature on the lowest atmospheric model level $\Delta SRF_{V\text{-}S}$ amounts to roughly two thirds of $\Delta SRF_{S\text{-}P}$. For specific humidity $\Delta SRF_{V\text{-}S}$ is even larger (by about 10 %) than $\Delta SRF_{S\text{-}P}$. In some grid boxes the 5-year mean temperature [specific humidity] differences at the end of each 20-minute time step may be as large as 0.05 K [$0.025\,g\,kg^{-1}$]. Hence, by omitting the surface-atmosphere feedback a constant heating/cooling [humidifying/drying] at a rate of $0.15\,K\,h^{-1}$ [$0.075\,g\,kg^{-1}\,h^{-1}$] is introduced. At the end of each time step, $SIMPLE_{SRF}$ gives a consistently warmer and dryer atmospheric state, which corresponds well to the decrease in the latent and increase in the sensible heat flux. In comparison to $SIMPLE_{SRF}$, $VERTEX_{SRF}$ gives almost exclusively warmer but also wetter atmospheric conditions, which is striking as the latent heat fluxes in $VERTEX_{SRF}$ are in general smaller than those in $SIMPLE_{SRF}$.

In the VERTEX scheme the vertical turbulent mixing process in the lowest layers of the atmosphere is refined with respect to the tiles and depends on the local stability. Furthermore, the scheme is based on the assumption of a horizontal convergence of fluxes with height, which primarily leads to a convergence of the states of the individual tiles. With more homogeneous air located above two tiles, the air between two levels is less stable in the warmer tile. This circumstance promotes the vertical mixing in the warmer tile relative to the colder tile. In the warmer tile the air contains more sensible heat and less moisture relative to the colder tile, thus a stronger vertical turbulent transport within the warmer tile promotes the upward mixing of sensible heat relative to moisture. Therefore, in the VERTEX scheme less moisture is being mixed upward from the surface but a larger share of it remains in the lowest layers of the atmosphere rather than being mixed further upwards. This moisture is primarily located within the tiles that transpire at a rate above the grid mean. Due to the SSGS refinement of specific humidity in $VERTEX_{SRF}$, the local surface atmosphere humidity gradient in these tiles is smaller, resulting in smaller latent heat fluxes. Thus, on grid box average, the latent heat fluxes are smaller but they result in more humid atmospheric conditions in the lowest layers of the atmosphere in $VERTEX_{SRF}$. At the same time, more sensible heat is transported

upward from the surface in $\text{VERTEX}_{\text{SRF}}$, so that more heat is being lost at the end of each time step. This is the reason why $\text{VERTEX}_{\text{SRF}}$ exhibits predominantly lower surface temperatures than $\text{SIMPLE}_{\text{SRF}}$ despite the shift from latent to sensible heat flux (Fig. 14; e - h).

The magnitude of the differences in the atmospheric state at the end of each time step indicates that, by taking into account the surface-atmosphere feedback, the state of the entire atmospheric column may be distinctly different when accounting for SSGS heterogeneity in the atmosphere. This is also suggested by single column studies performed with the VERTEX scheme (de Vrese et al., 2015) and by other modelling studies (Seth et al., 1994; Arola, 1999; Giorgi et al., 2003; Molod et al., 2004; Salmun et al., 2007; Dimri, 2009; Manrique-Suñén et al., 2013). To further explore this possibility, in the next section a model setup is used in which the surface-atmosphere feedback is accounted for.

3.4. Impact of spatial heterogeneity on the simulated global climate

3.4.1. Impact on 20-year mean state

With the atmospheric feedback taken into account, the differences in the 20-year annual means of surface and 2m temperature, as well as surface heat fluxes, precipitation and vertically integrated water vapor are comparable in magnitude between all three ensembles (Table 1, 2). This is contrary to expectations based on the quasi-offline experiment, which suggest that $\Delta\text{ENS}_{\text{V-S}}$ should be an order of magnitude smaller than $\Delta\text{ENS}_{\text{S-P}}$ and $\Delta\text{ENS}_{\text{V-P}}$. In the following it will be shown in more detail that $\Delta\text{ENS}_{\text{V-S}}$ is consistently less pronounced, but generally by a factor ranging between 1.5 - 3 and not by an order of magnitude.

Share of land surface [%] exhibiting differences larger than:	$SIMPLE_{ENS}$ - $PARAM_{ENS}$	$VERTEX_{ENS}$ - $PARAM_{ENS}$	$VERTEX_{ENS}$ - $SIMPLE_{ENS}$
surface temp.: 0.125 (0.4) [K]	44.8 (6.4)	31.8 (4.3)	25.8 (0.7)
temp. 2m: 0.125 (0.4) [K]	40.6 (2.8)	27.4 (1.6)	22.1 (0.4)
srf. net rad. shrt: 1.0 (2.0) [W m^{-2}]	18.7 (1.0)	13.6 (1.0)	9.1 (0.5)
srf. net rad. long: 1.0 (2.0) [W m^{-2}]	28.2 (6.0)	21.1 (4.3)	6.1 (0.1)
sens. heat flux: 1.0 (2.0) [W m^{-2}]	30.3 (10.4)	29.1 (11.7)	18.8 (5.3)
latent heat flux: 1.0 (2.0) [W m^{-2}]	35.7 (17.3)	34.1 (16.8)	20.4 (6.6)
precipitation: 0.05 (0.2) [mm d^{-1}]	35.4 (1.8)	31.0 (3.3)	28.9 (1.3)
vrt. int. w. vap.: 0.1 (0.25) [kg m^{-2}]	41.8 (12.2)	35.1 (8.5)	30.3 (4.4)
soil moisture: 0.01 (0.025) [m]	27.2 (10.2)	28.0 (9.4)	10.1 (2.0)

Table 1: Share of land surface [%] exhibiting differences larger than: x (y)

Share of land surface [%] exhibiting differences larger than 10% (25%) of $PARAM_{ENS}$:	$SIMPLE_{ENS}$ - $PARAM_{ENS}$	$VERTEX_{ENS}$ - $PARAM_{ENS}$	$VERTEX_{ENS}$ - $SIMPLE_{ENS}$
surface temp.	-	-	-
temp. 2m	-	-	-
surf. net rad. short	0.0 (0.0)	0.0 (0.0)	0.0 (0.0)
surf. net rad. long	1.6 (0.0)	0.9 (0.0)	0.0 (0.0)
sens. heat flux	23.9 (10.9)	24.6 (11.6)	15.8 (6.0)
latent heat flux	23.2 (8.4)	22.5 (9.5)	19.0 (9.6)
precipitation	20.9 (5.9)	17.2 (6.3)	17.6 (7.0)
vrt. int. w. vap.	0.0 (0.0)	0.0 (0.0)	0.0 (0.0)
soil moisture	26.2 (15.4)	27.1 (14.9)	5.4 (3.2)

Table 2: Share of land surface [%] exhibiting relative differences >5 % (10%) (relative to $PARAM_{ENS}$)

There is a good agreement between the results obtained with ECHAM/JSBACH and similar modelling studies, which gives some confidence that these findings have a more general validity. For example, the seasonally averaged differences (averaging period 20 years) in surface temperature of individual ensemble members range between roughly ± 2.5 K, which agrees with the findings of Essery et al. (2003) who compared a flux aggregation to a parameter aggregation version of the Met Office Surface Exchange Scheme in combination with the Met Office GCM. They found that differences in surface temperature (averaging period 10 years) are mostly smaller than ± 3 K.

The differences in the 20-year annual mean surface temperature between the ensembles are much smaller and rarely exceed 1 K (Fig. 15). $\Delta ENS_{S\text{-}P}$ indicates the largest differences in surface temperature. Here, about 45 % [6 %] of the land surface display differences in surface temperature of more than 0.125 K [0.4 K]. The area in which $\Delta ENS_{V\text{-}S}$ is larger than 0.125 K [0.4 K] constitutes 26 % [1 %] of the land surface. For $\Delta ENS_{S\text{-}P}$ the respective values are 32 % [4 %]. Consequently, the area exhibiting differences above 0.125 K [0.4 K] is about 44 % [89 %] smaller in case of $\Delta ENS_{V\text{-}S}$ and 29 % [33 %] smaller for $\Delta ENS_{V\text{-}P}$ than for $\Delta ENS_{S\text{-}P}$.For soil moisture $\Delta ENS_{S\text{-}P}$ is larger than 0.01 m [0.025 m], in 27 % [10 %] of the land surface and for $\Delta ENS_{V\text{-}P}$, this area has a similar size. Contrary to this, soil moisture appears to be much more insensitive to resolving atmospheric SSGS heterogeneity. The area in which $\Delta ENS_{V\text{-}S}$ is larger than 0.01 m [0.025 m] is around 63 % [80 %] smaller than the respective area in $\Delta ENS_{S\text{-}P}$. This discrepancy is even more pronounced for the relative soil moisture differences. Using the $PARAM_{ENS}$ as reference, $\Delta ENS_{S\text{-}P}$ and $\Delta ENS_{V\text{-}P}$ are larger than 10 % in over a quarter of the land surface, whereas for $\Delta ENS_{V\text{-}S}$ the relative differences exceed 10 % in only about 5 % of the land surface.

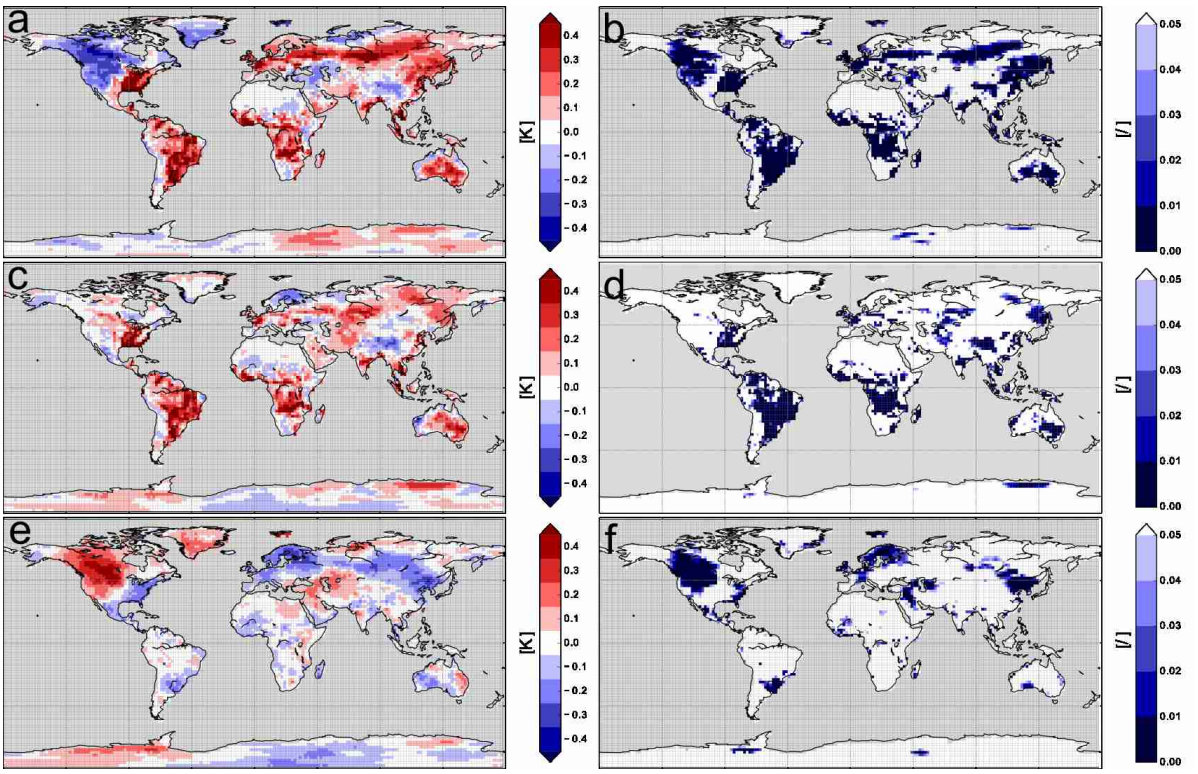

Figure 15: (a,c,e) 20-year mean difference in surface temperature between a) $\text{SIMPLE}_{\text{ENS}}$ and $\text{PARAM}_{\text{ENS}}$ c) $\text{VERTEX}_{\text{ENS}}$ and $\text{PARAM}_{\text{ENS}}$ e) $\text{VERTEX}_{\text{ENS}}$ and $\text{SIMPLE}_{\text{ENS}}$; (b,d,f) p-value of statistic significance of 20-year mean difference in surface temperature between b) $\text{SIMPLE}_{\text{ENS}}$ and $\text{PARAM}_{\text{ENS}}$ d) $\text{VERTEX}_{\text{ENS}}$ and $\text{PARAM}_{\text{ENS}}$ f) $\text{VERTEX}_{\text{ENS}}$ and $\text{SIMPLE}_{\text{ENS}}$

For the surface latent and sensible heat fluxes, $\Delta\text{ENS}_{\text{S-P}}$ and $\Delta\text{ENS}_{\text{V-P}}$ exceed $1\,\text{W}\,\text{m}^{-2}$ [$2\,\text{W}\,\text{m}^{-2}$] in about one third [10 % - 17 %] of the land surface. This corresponds to roughly a quarter [10 %] of the land surface in which $\Delta\text{ENS}_{\text{S-P}}$ and $\Delta\text{ENS}_{\text{V-P}}$ (relative to $\text{PARAM}_{\text{ENS}}$) exceed 10 % [25 %]. Contrary to soil moisture, the surface heat fluxes are also sensitive to the explicit representation of atmospheric SSGS heterogeneity. The share of land surface in which $\Delta\text{ENS}_{\text{V-S}}$ is larger than $1\,\text{W}\,\text{m}^{-2}$ [$2\,\text{W}\,\text{m}^{-2}$] is around 40 % [$>50$ %] smaller than the respective area for $\Delta\text{ENS}_{\text{S-P}}$ and $\Delta\text{ENS}_{\text{V-P}}$. However, the area with relative differences in the latent heat flux of 25 % or more is about 13 % larger in case of $\Delta\text{ENS}_{\text{V-S}}$ than the respective area for $\Delta\text{ENS}_{\text{S-P}}$ and about 2 % larger than the respective area for $\Delta\text{ENS}_{\text{V-P}}$.

Comparable results can also be found for precipitation. In any comparison of two ensembles, about one third [up to 3 %] of the land surface present precipitation differences above $0.05\,\text{mm}\,\text{d}^{-1}$ [$0.2\,\text{mm}\,\text{d}^{-1}$] which corresponds to a relative difference of 10 % [25 %] in less than one fifth [7 %] of the land surface. Here, the largest share of the land surface showing differences in terms of absolute values, can be found for $\Delta\text{ENS}_{\text{S-P}}$ for the $0.05\,\text{mm}\,\text{d}^{-1}$ threshold and between $\Delta\text{ENS}_{\text{V-P}}$ for the the $0.2\,\text{mm}\,\text{d}^{-1}$ threshold. However, the largest share of the land surface with relative differences larger than 25 % can be found in case of $\Delta\text{ENS}_{\text{V-S}}$.

This indicates that for many variables the two $\mathrm{FLUX_{ENS}}$ are the most similar of the three ensembles, whereas $\mathrm{PARAM_{ENS}}$ and $\mathrm{SIMPLE_{ENS}}$ are the most dissimilar. In the following, the area weighted absolute difference between two ensembles ($\mathrm{AWAD_{ENS1\text{-}ENS2}}$) is being used as a measure for the similarity of two ensembles. The $\mathrm{AWAD_{ENS1\text{-}ENS2}}$ of a given area AREA is defined as the sum of the absolute difference ($|x_{ENS1}^{GB_j} - x_{ENS2}^{GB_j}|$) over all the grid boxes (GB_j) within the area, weighted by the size of the grid box relative to the size of the entire area (A^{GB_j}/A^{AREA}):

$$\mathrm{AWAD}_{\mathrm{ENS1\text{-}ENS2}}^{\mathrm{AREA}} = \sum_{j=1}^{n} |x_{ENS1}^{GB_j} - x_{ENS2}^{GB_j}| \cdot A^{GB_j}/A^{AREA} \tag{21}$$

Here, a low AWAD indicates small differences between two ensembles i.e. a high degree of similarity. A global comparison of the different AWADs confirms that the two $\mathrm{FLUX_{ENS}}$ are generally more similar than one of the $\mathrm{FLUX_{ENS}}$ and the $\mathrm{PARAM_{ENS}}$ (Table 3). For most of the variables the $\mathrm{AWAD}_{\mathrm{VERTEX\text{-}SIMPLE}}^{\mathrm{Global}}$ ranges between 60 % and 80 % of the $\mathrm{AWAD}_{\mathrm{VERTEX\text{-}PARAM}}^{\mathrm{Global}}$ and the $\mathrm{AWAD}_{\mathrm{SIMPLE\text{-}PARAM}}^{\mathrm{Global}}$. For soil moisture this number is even as low as 45 %.

AWAD (global land surface mean differences):	$SIMPLE_{ENS}$ - $PARAM_{ENS}$	$VERTEX_{ENS}$ - $PARAM_{ENS}$	$VERTEX_{ENS}$ - $SIMPLE_{ENS}$
surface temp. [K]	0.15 (0.09)	0.11 (0.08)	0.09 (-0.01)
temp. 2m [K]	0.13 (0.07)	0.10 (0.07)	0.08 (-0.00)
surf. net rad. short [$\mathrm{W\,m^{-2}}$]	0.57 (0.24)	0.51 (0.25)	0.42 (0.01)
surf. net rad. long [$\mathrm{W\,m^{-2}}$]	0.75 (-0.54)	0.64 (-0.47)	0.39 (0.07)
sens. heat flux [$\mathrm{W\,m^{-2}}$]	0.83 (0.39)	0.89 (0.31)	0.65 (-0.08)
latent heat flux [$\mathrm{W\,m^{-2}}$]	1.02 (-0.68)	1.07 (-0.52)	0.67 (0.15)
precipitation [$\mathrm{mm\,d^{-1}}$]	0.05 (-0.02)	0.05 (-0.01)	0.04 (0.01)
vrt. int. w. vap. [$\mathrm{kg\,m^{-2}}$]	0.11 (-0.07)	0.09 (-0.05)	0.08 (0.02)
soil moisture [m]	0.009 (0.006)	0.009 (0.006)	0.004 (0.000)

Table 3: AWAD and global land surface mean differences

Consequently, $\Delta\mathrm{ENS_{S\text{-}P}}$ and $\Delta\mathrm{ENS_{V\text{-}P}}$ share many similarities in their general spatial distribution, which is in good agreement with the findings of the quasi-offline experiment. Here, $\Delta\mathrm{ENS_{S\text{-}P}}$ and $\Delta\mathrm{ENS_{V\text{-}P}}$ are considered to show the same general behaviour in areas in which they are in the same direction, i.e. are both negative or both positive. For example, the $\mathrm{FLUX_{ENS}}$ agree very well on the areas in which they give higher surface temperatures than the $\mathrm{PARAM_{ENS}}$ e.g. the east coast of the U.S., south America, central Africa and in Eurasia within a broad band along 55° north (Fig. 15 a,c). Depending on the variable, around 85 % to 95 % of the $\mathrm{AWAD}_{\mathrm{SIMPLE\text{-}PARAM}}^{\mathrm{Global}}$ and the $\mathrm{AWAD}_{\mathrm{VERTEX\text{-}PARAM}}^{\mathrm{Global}}$ agree on the algebraic sign.

However, even in the areas in which $\Delta\text{ENS}_{\text{S-P}}$ and $\Delta\text{ENS}_{\text{V-P}}$ agree on the direction (AS), there are systematic differences between the two and for many variables $\Delta\text{ENS}_{\text{S-P}}$ is substantially larger than $\Delta\text{ENS}_{\text{V-P}}$. For surface temperature, the $\text{AWAD}^{\text{AS}}_{\text{VERTEX-SIMPLE}}$ of areas in which $\Delta\text{ENS}_{\text{V-P}} > \Delta\text{ENS}_{\text{S-P}}$ is only about one third of the $\text{AWAD}^{\text{AS}}_{\text{VERTEX-SIMPLE}}$ of areas in which $\Delta\text{ENS}_{\text{V-P}} < \Delta\text{ENS}_{\text{S-P}}$. For surface net radiation and vertically integrated water vapour the respective values range between 50 % and 67 %,. On a global average this results in the differences between the $\text{VERTEX}_{\text{ENS}}$ and $\text{SIMPLE}_{\text{ENS}}$ mostly opposing the differences between $\text{SIMPLE}_{\text{ENS}}$ and $\text{PARAM}_{\text{ENS}}$, i.e. between 65 % and 85 % of the $\text{AWAD}^{\text{Global}}_{\text{VERTEX-SIMPLE}}$ oppose the $\text{AWAD}^{\text{Global}}_{\text{SIMPLE-PARAM}}$ (Fig. 15 a,c,e). This confirms that, even though the general behaviour of the flux aggregation schemes is the same, $\text{VERTEX}_{\text{ENS}}$ is much more similar to $\text{PARAM}_{\text{ENS}}$ than $\text{SIMPLE}_{\text{ENS}}$.

The explicit representation of heterogeneity has a distinct impact on the global mean state of the surface. In condensed and simplified form, between 50°-north and 50°-south, an explicit representation of SSGS heterogeneity at the surface ($\Delta\text{ENS}_{\text{S-P}}$) results in generally higher temperatures and higher soil moisture values, less precipitation, larger sensible heat fluxes, reduced evapotranspiration and thus lower latent heat fluxes and a smaller amount of vertically integrated water vapour (Table 3). Also the explicit representation of atmospheric SSGS heterogeneity has a noteable impact on the surface mean state ($\Delta\text{ENS}_{\text{V-S}}$). $\text{VERTEX}_{\text{ENS}}$ exhibits predominantly lower temperatures, smaller sensible heat fluxes, higher precipitation and evapotranspiration rates and larger latent heat fluxes in comparison to $\text{SIMPLE}_{\text{ENS}}$. As was already indicated by the quasi-offline experiment (Fig. 14 a,c), $\Delta\text{ENS}_{\text{V-S}}$ is less one-directional than $\Delta\text{ENS}_{\text{S-P}}$ and has regionally strongly differing characteristics. Hence, averaged over the entire land surface, $\Delta\text{ENS}_{\text{V-S}}$ is much smaller than $\Delta\text{ENS}_{\text{S-P}}$. For precipitation $\Delta\text{ENS}_{\text{V-S}}$ (land surface mean) is around 50 % smaller than $\Delta\text{ENS}_{\text{S-P}}$, for the surface net short wave radiation this value is as high as 95 %.

To evaluate whether the alterations to the standard model improve the simulated climate, the ensembles were compared to WATCH Forcing Data (WFD) (Weedon et al., 2011). Compared to the inherent bias, the differences resulting from a change in land surface-atmosphere coupling are almost an order of magnitude smaller. For the standard operational model setup ($\text{PARAM}_{\text{ENS}}$) the bias in 2m temperature is on the scale of several K (Fig. 16), whereas the difference in 2m temperature between any of the ensembles rarely exceed 1 K. Furthermore, whether any of the flux aggregation schemes improves model results depends upon the region and variable in question. For example both flux aggregation schemes improve the cold bias in central and southern Africa but at the

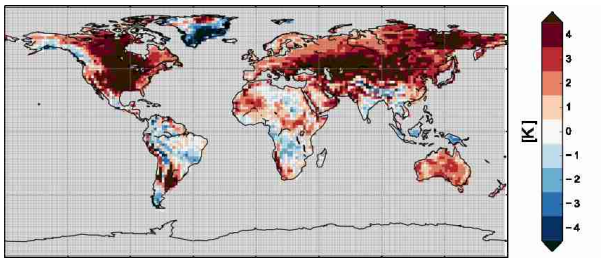

Figure 16: 20-year mean bias in 2m temperature ($\text{PARAM}_{\text{ENS}}$)

same increase the warm bias in large parts of northern Eurasia and eastern America.

Globally, the mean of the absolute value of the 2m temperature bias [precipitation bias] changes from 2.379 K [0.745 mm d^{-1}] in the $\text{PARAM}_{\text{ENS}}$ to 2.412 K [0.739 mm d^{-1}] in the $\text{SIMPLE}_{\text{ENS}}$ and 2.402 K [0.736 mm d^{-1}] in the $\text{VERTEX}_{\text{ENS}}$. Consequently, both of the flux aggregation schemes slightly improve simulated precipitation ($\text{VERTEX}_{\text{ENS}}$ by 1.2 % and $\text{SIMPLE}_{\text{ENS}}$ by 0.8 %), but increase the 2m temperature bias ($\text{VERTEX}_{\text{ENS}}$ by 1.0 % and $\text{SIMPLE}_{\text{ENS}}$ by 1.4 %). Thus, there is a trade-off between precipitation and temperature bias when comparing the parameter aggregation to the flux aggregation schemes. In a comparison of the two flux aggregation schemes, the VERTEX scheme consistently gives results closer to WFD.

3.4.2. Robustness of impacts

A two sample, two sided Student's t-test is used to determine the statistical significance of the 20-year mean differences between two ensembles. Here, the ensembles are treated as one series of 100 independent annual means (Table 4; Fig. 15). The impact of a given coupling scheme I on the simulated climate is approximated by the percentage of land surface area significantly affected by the differences between the coupling scheme and a reference scheme II ($\text{PLASA}_{\text{I-II}}$). The t-test shows that at a significance level of 0.05 the PLASA ranges from 9.5 % to 48.0 %, depending on the variables and schemes considered. Soil moisture exhibits the largest impact with the PLASA ranging between 23 % and 48 %, whereas the vertically integrated water vapour presents the smallest impact with a PLASA between 9.5 % - 19.8 %.

Share of land surface grid boxes exhibiting significant differences:	$SIMPLE_{ENS}$ - $PARAM_{ENS}$	$VERTEX_{ENS}$ - $PARAM_{ENS}$	$VERTEX_{ENS}$ - $SIMPLE_{ENS}$
surface temp. [%]	38.6	27.3	17.9
temp. 2m [%]	36.6	24.6	16.6
surf. net rad. short [%]	28.0	20.0	12.4
surf. net rad. long [%]	42.5	34.3	16.9
sens. heat flux [%]	30.6	30.3	21.6
latent heat flux [%]	35.8	35.9	21.5
precipitation [%]	21.6	18.3	16.4
vrt. int. w. vap. [%]	19.8	15.6	9.5
soil moisture [%]	47.5	48.0	23.6

Table 4: Share of land surface grid boxes exhibiting significant differences (p <0.05)

The largest impact on simulated climate can be found due to the explicit representation of surface heterogeneity and the values of the $\text{PLASA}_{\text{SIMPLE-PARAM}}$ mostly range between 30 % - 40 %. For the $\text{PLASA}_{\text{VERTEX-PARAM}}$ the values predominantly lie between 15 % - 35 % and the $\text{PLASA}_{\text{VERTEX-SIMPLE}}$ is generally in a range between 15 % - 20 %. Consequently, the $\text{PLASA}_{\text{VERTEX-SIMPLE}}$ ranges between 40 % - 75 % of the

$\text{PLASA}_{\text{SIMPLE-PARAM}}$. For most of the variables, also the $\text{PLASA}_{\text{VERTEX-PARAM}}$ is up to one third smaller than $\text{PLASA}_{\text{SIMPLE-PARAM}}$. Thus, the t-test supports the results of the previous sections, i.e. that also with respect to statistical significance the impact of representing atmospheric SSGS heterogeneity primarily ranges between one and two thirds of the impact of an explicit representation of surface SSGS heterogeneity. Furthermore, it confirms that the VERTEX scheme gives results more similar to the parameter aggregation scheme than the simple flux aggregation scheme.

In the following, correlations between the quasi-offline and the AMIP-style experiment will be investigated in order to estimate whether the differences between two ensembles can be related to the mechanisms discussed in section 3.3. Here, the Pearson correlation coefficient (r) is used to test for a linear correlation. Weak ($|r|$ ranging between 0.30 - 0.52), yet statistically significant (p«0.01) positive correlations can be found between $\Delta\text{ENS}_{\text{S-P}}$ and $\Delta\text{SRF}_{\text{S-P}}$ for surface temperature, soil moisture and the surface heat fluxes. This indicates that the impact of an explicit representation of surface heterogeneity on the 20-year mean state of the surface and the surface fluxes, which were discussed in this section, can be partly related to the mechanisms discussed in section 3.3.

For $\Delta\text{ENS}_{\text{V-S}}$ and $\Delta\text{SRF}_{\text{V-S}}$ no such correlations can be found. This is not surprising as in the quasi-offline experiment $\text{VERTEX}_{\text{SRF}}$ and $\text{SIMPLE}_{\text{SRF}}$ do not exhibit large differences in the grid mean state. It was hypothesised that this is due to the fact that the surface-atmosphere feedback is omitted in the quasi-offline experiment. To further investigate this possibility, $\Delta\text{ENS}_{\text{V-S}}$ is being tested for a correlation with $\Delta\text{SRF}_{\text{V-S}}$ in respect to the state of the lowest atmospheric model level , which was calculated at the end of each time step in the quasi-offline experiments. For the sensible heat flux and surface temperature $\Delta\text{ENS}_{\text{V-S}}$ shows a weak, yet statistically significant (p«0.01) anti-correlation with the differences in atmospheric temperature and specific humidity for $\Delta\text{SRF}_{\text{V-S}}$. For latent heat flux, soil moisture and precipitation a positive correlation was found. Here, the correlations with respect to the surface state variables are weaker ($|r|$ ranging between 0.16 - 0.20) and the correlations with respect to the surface fluxes and precipitation are stronger ($|r|$ ranging between 0.30 - 0.43).

In the quasi-offline experiment atmospheric temperature and specific humidity are generally higher in $\text{VERTEX}_{\text{SRF}}$, thus the following prevailing mechanism can be hypothesised. The surface-atmosphere feedback in the VERTEX scheme causes a moister atmosphere in the lowest levels which initially reduces the atmospheric moisture demand. Due to the representation of SSGS variability, this is particularly prominent in tiles which transpire at a rate above the grid mean. This leads to an increase in soil moisture and a more even soil moisture distribution amongst the tiles within a grid box. Therefore, evapotranspiration is less limited by water stress and the latent heat flux, averaged over the 20-year period, increases. As more energy is expended in the latent heat flux, less energy is available at the surface and the sensible heat flux and surface temperatures decrease. Furthermore, in the VERTEX scheme the turbulent transport is more intense for sensible heat than for specific humidity and more moisture remains

lower in the atmosphere. This has a positive feedback on precipitation and therefore on soil moisture and the availability of water at the surface which in turn has a positive feedback on evapotranspiration.

3.5. Conclusions and Discussion

The representation of the link between the horizontally heterogeneous land surface and the atmosphere remains one of the key challenges in Earth System Modelling. It has been argued that a realistic representation requires the consideration of SSGS variability at the surface but also within the atmosphere. To investigate the importance of SSGS heterogeneity, two surface-atmosphere coupling schemes were implemented into the MPI-ESM, in which currently a parameter aggregation scheme is being used. 1) A simple flux aggregation scheme, based on the assumption that even at the lowest model level the state of the atmosphere is horizontally homogeneous; 2) The VERTEX scheme, in which the turbulent fluxes in the lowest atmospheric model layers are resolved with respect to the surface tiles. In a first step, the sensitivity of the near surface processes to the representation of SSGS heterogeneity was investigated. To preclude large scale atmospheric effects, a modified version of the offline experiment, a quasi-offline experiment, was used in which the atmospheric state is prescribed. In a second step, ensembles of global AMIP-style simulations were used to determine whether the choice of coupling scheme also has a robust impact on simulated climate.

With the quasi-offline experiments it could be shown that the near surface processes are systematically affected by the differences between two coupling schemes. When surface heterogeneity is explicitly represented (simple flux aggregation scheme vs. parameter aggregation scheme), tiles representing plants with a high stomatal conductance and a large leaf area exhibit an increase in transpiration and a decrease in sensible heat flux, surface temperature and soil moisture. Plants with a lower stomatal conductance and leaf area show the opposite effect. By additionally accounting for SSGS heterogeneity in the atmosphere (VERTEX scheme vs. simple flux aggregation scheme), evapotranspiration in tiles with pronounced transpirational abilities is reduced due to a decreased local surface-atmosphere moisture gradient. Despite the decrease in latent heat flux and the consequent increase in sensible heat flux, this does not necessarily result in a warming of the surface as also the atmosphere in these tiles is relatively cooler. Tiles with less pronounced transpirational abilities display the opposite reaction.

The importance of the surface-atmosphere coupling was confirmed by the analysis of global AMIP-style simulations. Depending on the variable and schemes considered, between 10 % and 48 % of the land surface are significantly affected by the differences in the aggregation technique. Here, the largest impact on simulated climate is related to the explicit representation of SSGS heterogeneity at the surface. Simulations with a simple flux aggregation scheme generally result in higher soil moisture values, surface temperatures and sensible heat fluxes, whereas precipitation and evapotranspiration are reduced, in comparison to simulations with a parameter aggregation scheme. But also

the explicit representation of SSGS heterogeneity in the atmosphere has a distinct impact on the state of the surface and the surface fluxes. Depending on the variables and measures considered, the impact is roughly half as large as the impact of explicitly accounting for SSGS heterogeneity at the surface. The VERTEX scheme leads to slightly lower surface temperatures and sensible heat fluxes and an increase in evapotranspiration and precipitation. In comparison to WFD both flux aggregation schemes simulate precipitation better than the parameter aggregation scheme but the bias in simulated 2m temperature increases. Here, the VERTEX scheme leads to simulated precipitation and 2m temperature consistently more similar to WFD than those simulated with the simple flux aggregation scheme.

Finally, studies suggest that atmospheric SSGS variability may substantially affect processes such as convection and cloud formation and precipitation (Koster, 2004; Rieck et al., 2014; Guillod et al., 2015). In the present study, the simulated SSGS variability on the lowest atmospheric level was often still larger than 50 % of the respective surface values (Fig. 17). On the second lowest level the standard deviation of temperature or specific humidity may still be larger than 10 % of the deviation at the surface.

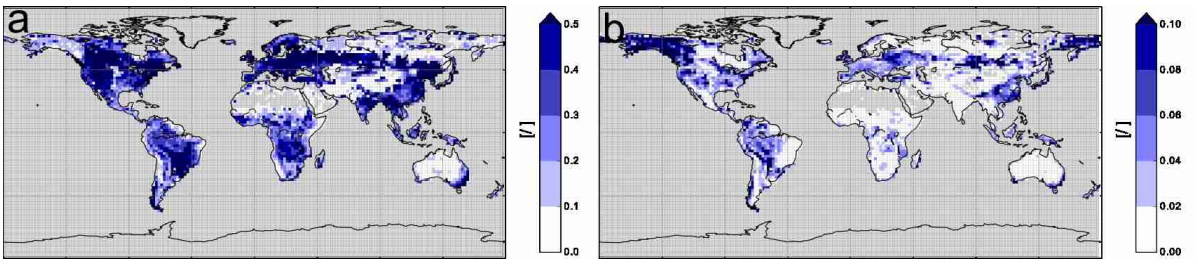

Figure 17: Standard deviation of tile specific temperature relative to standard deviation of tile specific surface temperature for a) lowest atmospheric level and b) second lowest atmospheric level

Additionally, results suggest that large deviations in the atmosphere are limited to the hours between 0900 LT and noon which is a timespan substantially shorter than that on which large SSGS variability can be found at the surface. During this morning period SSGS variability in the atmosphere is much larger than what the 20-year mean values suggest, especially relative to the respective variability at the surface. This information on atmospheric SSGS variability could potentially be used to improve the representation of many atmospheric processes. Furthermore, the present study considered heterogeneity only for the vertical turbulent transport and on the lowest two atmospheric model levels in order to limit the level of complexity. Also, the representation of heterogeneity was limited to temperature and specific humidity whereas wind speeds were assumed to be horizontally homogeneous on and above the lowest atmospheric model level. Hence, it is plausible that atmospheric SSGS variability plays an even more important role than has been argued in this study.

4. Iranian Irrigation and Ethiopian Rain: Transcontinental Effects of Irrigation

4.1. Introduction

Irrigation plays an important role for the welfare of a large share of the world's population. It is an essential element of food security, as about 40 % of the global crop yield is provided by irrigation-based agriculture (Siebert et al., 2005). In South Asia the most densely populated and heavily irrigated region in the world, agriculture employs between 50 - 60 % of the labor force and contributes about 15 - 20 % of the gross domestic product. With an increasing world population, irrigation-based agriculture will most likely also remain a key economic sector with respect to food security and employment in the future (WorldBank, 2008; Godfray et al., 2010; Dev, 2015). Furthermore, irrigation has a substantial impact on global water resources, as currently about 70 % of humanity's demand for fresh water originate from irrigation (Wada et al., 2013). This number is expected to increase rather than decrease in the foreseeable future (De Fraiture and Wichelns, 2010).

Irrigation-based agriculture is not only affected by changing climate conditions and declining fresh water resources, but in turn has a substantial effect on them. It strongly influences the hydrological cycle and the land surface energy budget by the redistribution of water. Currently, irrigation induced evapotranspiration is estimated to be as high as $2600\,km^3\,a^{-1}$ which corresponds to about 4 % of the total terrestrial evapotranspiration (Gordon et al., 2005; Oki and Kanae, 2006). The influence of irrigation on regional climate has been the focus of numerous investigations. Especially with respect to South Asia, a profound impact on regional circulations such as the Indian monsoon, precipitation and surface temperatures has been established in model-based regional studies (e.g. Adegoke et al. (2003); Douglas et al. (2006); Kueppers et al. (2007); Douglas et al. (2009); Lee et al. (2009); Lobell et al. (2009); Saeed et al. (2009); Niyogi et al. (2010); Lucas-Picher et al. (2011); Harding et al. (2013); Saeed et al. (2013); Tuinenburg et al. (2014)). For example, these could show that irrigation affects the wind patterns related to the Indian summer monsoon by reducing the land sea thermal contrast via an evaporative cooling of the land surface. Additionally, they provided evidence that the surface cooling related to irrigation masks increasing surface temperatures due to the changing climate in the respective regions.

The sheer amount of water introduced into the atmosphere suggests that irrigation also has a distinct influence on global climate. However, only few studies exist which investigate the impact of irrigation on this scale (e.g. Boucher et al. (2004); Lobell et al. (2006b); Sacks et al. (2009); Puma and Cook (2010); Cook et al. (2011)). These studies identified the general mechanisms by which irrigation affects the state of the land surface and the atmosphere and provided rough estimates of the magnitude of the impact that irrigation has on global climate. The evapotranspiration of irrigation water increases the latent heat flux and reduces the sensible heat flux which is accompanied

by an evaporative cooling of the surface. The additional water vapor in the atmosphere leads to an increased absorption of solar radiation and an intensification of the green house effect. This water vapor eventually condenses and releases heat, causing an additional warming of the atmosphere (Boucher et al., 2004). Furthermore, changes in water vapor profile affect convection, cloud formation and precipitation which may ultimately lead to a decrease in atmospheric water vapor. The same holds for a change in the temperature profile, which may affect the saturation mixing ratio of water vapor, convection, cloud formation, precipitation, etc. These indirect effects may have an impact at least comparable in magnitude to the evaporative cooling of the surface (Sacks et al., 2009). However, the global scale studies do not illustrate in depth if and how irrigation in certain regions translates to an impact on the state of the surface and the atmosphere in regions in a substantial distance from the irrigated areas. The present study aims to bridge the gap between the detailed understanding of processes on the regional scale, provided by the regional studies, and the related impacts on the global scale.

Several simulations using the Max Planck Institute for Meteorology's Earth System Model (MPI-ESM) were performed to investigate possible effects due to irrigation on a transcontinental scale. Model-based studies necessarily involve uncertainties related to the model's structure on one hand and due to simplifications required for the representation of irrigation on the other. To account for these uncertainties, several irrigation simulations were performed with variations in the model's structure, namely the land surface-atmosphere coupling (de Vrese et al., 2015), and the assumed irrigation efficiency. In section 4.2 the MPI-ESM is briefly introduced and the irrigation scheme as well as the simulations performed are described. By comparing simulations with and without irrigation, the impact of irrigation on remote regions is estimated in section 4.3. Section 4.4 briefly summarizes the main findings.

4.2. Methods

The simulations for this study were performed using the MPI-ESM's land surface model JSBACH (Raddatz et al., 2007; Brovkin et al., 2009; Ekici et al., 2014) coupled to the atmospheric general circulation model ECHAM6 (Stevens et al., 2013). In the following these will be referred to as ECHAM/JSBACH. In the simulations sea surface temperature and sea-ice extent are prescribed, following the protocol of the Atmospheric Model Intercomparison Project (AMIP) (Gates et al., 1999). The model was run using a vertical resolution of 47 model levels, of which the lowest is located on a height of about $30\,m$. The horizontal resolution of the simulations was T63, which corresponds to a grid-spacing of $\approx 200\,km$ in tropical latitudes. With respect to hydrology, no vertical levels are distinguished below ground, and the soil is represented by a simple bucket. Spatial sub-grid scale heterogeneity on the land surface is modelled by tiles which, depending on the surface-atmosphere coupling scheme, are either implicitly or explicitly used in the representation of physical processes.

In ECHAM6 the advective transport is modelled using the flux-form semi-Lagrangian

scheme, proposed by Lin and Rood (1996), as the extension of an Eulerian multidimensional flux-form scheme. In the operational setup, JSBACH and ECHAM6, i.e. land surface and atmosphere, are coupled with a parameter aggregation scheme. In this scheme, surface sub-grid scale heterogeneity is treated only implicitly, as in the calculations of most physical processes, the surface in each grid box is represented by a set of effective parameters which are valid for the entire grid box. The determination of an effective grid box mean albedo is described in Otto et al. (2011), the aggregation of the surface roughness length of different tiles follows Mason (1988); Claussen (1991); Claussen et al. (1994) and the aggregation of vegetation, soil and hydrological parameters is done by an averaging which accounts for the respective cover fractions (Kabat et al., 1997; Feddes et al., 1998). Based on the effective parameters, the surface fluxes are calculated using a bulk-exchange formulation that applies approximate analytical expressions similar to those proposed by Louis (1979) to determine the transfer coefficients.

For this study two additional schemes for the land surface-atmosphere coupling were implemented into ECHAM/JSBACH, namely a simple flux aggregation scheme and the newly developed VERTEX scheme. In the simple flux aggregation scheme, surface heterogeneity is explicitly represented and physical processes are modelled based on the tile specific parameters. However, this is only true for processes at the surface, as it is assumed that the surface fluxes stemming from the individual tiles have mixed horizontally below the lowest atmospheric model level, so that the atmosphere remains horizontally homogeneous. The simple flux aggregation scheme in JSBACH, follows the general method for an implicit surface-atmosphere coupling proposed by Polcher et al. (1998); Best et al. (2004).

The VERTEX scheme is also based on an aggregation of the surface fluxes, but explicitly accounts for spatial heterogeneity within the lowest layers of the atmosphere and resolves the vertical turbulent mixing process with respect to the surface tiles (de Vrese et al., 2015). In the atmosphere, the vertical fluxes are modelled by a modified version of the turbulent kinetic energy scheme described in Brinkop and Roeckner (1995). The turbulent viscosity and diffusivity are described by a function of the turbulent kinetic energy, the turbulent mixing length (Blackadar, 1962) and a stability function that depends on the moist Richardson number (Mellor and Yamada, 1982).

In the VERTEX scheme, this is done for the individual tiles separately within the lowest three layers of the atmosphere. Here, the fluxes within the individual tiles are not treated independently of each other but are assumed to mix horizontally to a certain extent. Thus, the vertical flux from a given tile influences the states of all the tiles on the level above. The extent to which the vertical fluxes blend horizontally is determined based on the ratio of the height of a model level and the blending height. The latter can be estimated as a function of friction velocity, the horizontal windspeed and the characteristic length scale of the respective surface heterogeneity (Mahrt, 2000). In this study the characteristic length scales required for the computation of the blending height were derived from the Global Land Cover Map 2009 (GLOBCOVER) (Arino et al., 2012).

For areas in which the dataset classified agricultural areas as rainfed even though these are equipped for irrigation, the characteristic length scales were determined based on the areas of rainfed crops, assuming that the areas are equipped for irrigation but not irrigated during the passing of the satellite (see Fig. 36).

In the flux aggregation schemes the homogeneous subareas within one grid box interact only via the vertical turbulent fluxes. Below the surface a horizontal flow of water and heat is not represented in the model and the soil moisture and temperature in a given tile is independent of the other tiles. As the surface fluxes have a highly non-linear dependency on the state of the surface and the atmosphere, each of the coupling schemes leads to a distinct representation of the link between land surface and atmosphere.

JSBACH was equipped with an irrigation scheme in which irrigation is simulated by maintaining the soil moisture in the tile representing irrigated crops close to the level at which potential transpiration is reached, i.e. 75 % of the field capacity. The cover fraction of the irrigated crop tile, which constitutes roughly 2 % of the land surface, was derived from the fifth version of the global map of irrigation areas (Siebert et al., 2005; Siebert et al., 2013) (Fig. 18 a). In the present setup of JSBACH, each tile consists of a vegetated and a non-vegetated fraction, whose extents vary, depending on the current state of vegetation (note that the permanent bare soil fraction, i.e. the area that is uninhabitable to vegetation has already been integrated to a dedicated tile).

While the amount of water required for irrigation was calculated only for the vegetated fraction, it was applied to the entire tile. Hence, unless the tile is fully vegetated the soil moisture due to irrigation was below 75 % of the field capacity. The soil moisture in the irrigated tile was increased at the beginning of each 20-minute time step. The amount of water added during irrigation $irrig^{t}_{crop\_irrig}$ in time step t and the soil moisture in the irrigated crop tile $w^{t,start}_{crop\_irrig}$ at the beginning of each time step are calculated using the water holding capacity of the soil w_{max}, a coefficient representing the fraction of soil moisture required for transpiration to occur at the potential rate c_{pot_trans} (0.75), the soil moisture in the irrigated tile at the end of the previous time step $w^{t-1,end}_{crop\_irrig}$ and the vegetation ratio at the beginning of the time step $veg^{t,start}_{crop\_irrig}$.

$$irrig^{t}_{crop\_irrig} = (w_{max} \cdot c_{pot\_trans} - w^{t-1,end}_{crop\_irrig}) \cdot veg^{t,start}_{crop\_irrig} \tag{22a}$$

$$w^{t,start}_{crop\_irrig} = w^{t-1,end}_{crop\_irrig} + irrig^{t}_{crop\_irrig} \tag{22b}$$

$$\text{, for } w^{t-1,end}_{crop\_irrig} < w_{max} \cdot c_{pot\_trans}$$

Based on this simple irrigation scheme, an ensemble of three 21-year AMIP-style simulations was performed for the years 1979 -1999 (Table 5). From these, the first year was required for the spin-up of the model and is not considered in the analysis. The simulations differ exclusively in the way that the land surface is coupled to the atmosphere, i.e. via a parameter aggregation scheme (P_{I1}), a simple flux aggregation scheme (S_{I1}) or

the VERTEX scheme (V_{I1}).

Furthermore, two additional simulations (V_{Imin}, V_{Imax}) with the VERTEX scheme were performed, in which the irrigation efficiency was modified, by varying the non-vegetated fraction of the grid box which receives water during irrigation. To be able to modify the irrigation efficiency, the irrigated crop tile was split into an irrigated vegetated tile, which on annual average constitutes roughly 1 % of the land surface, and a potentially irrigated non-vegetated tile, which constitutes the remaining 1 %. The respective cover fractions were not calculated but prescribed based on the cover fraction and the vegetation ratio of the irrigated crop tile in the initial simulation with the VERTEX scheme (V_{I1}). To ensure that the simulations were based on an identical area vegetated by crops, the cover fraction of the (fully vegetated) irrigated crop tile $cf_{veg\_crop\_irrig,X}$ ($X \in \{V_{Imin}, V_{Imax}\}$) was determined based on the cover fraction cf_{crop_irrig,V_I} and the vegetation ratio veg_{crop_irrig,V_I} of the crop tile in simulation V_I:

$$cf_{veg\_crop\_irrig,X} = cf_{crop\_irrig,V_I} \cdot veg_{crop\_irrig,V_I} \tag{23a}$$

$$veg_{veg\_crop\_irrig,X} = 1.0 \tag{23b}$$

The cover fractions were determined based on 20-year monthly mean values and the cover fraction for a give time step was calculated by linearly interpolating between the monthly mean values.

For a scenario assuming perfect irrigation efficiency water was applied only in the fully vegetated irrigated crop tile and no water was applied to the soil in the potentially irrigated non-vegetated tile (V_{Imin}).

For the second scenario, a very poor irrigation efficiency was assumed (V_{Imax}). The aim of this scenario was to not only simulate transpiration from the irrigated crops, but to account for evaporation from bare soil areas and from parts of the irrigation infrastructure such as reservoirs and channels. The latter of which can not be simulated directly with ECHAM/JSBACH. Accordingly, irrigation was applied in the fully vegetated crop tile and also in an irrigated bare soil tile. The cover fraction of the irrigated bare soil tile $cf_{bare\_irrig_{Imax}}$ was calculated based on the fraction of the vegetated crop tile and the assumed irrigation efficiency of a given region $eff_{irrig,region}$, taken from Döll and Siebert (2002):

$$cf_{bare\_irrig_{Imax}} = cf_{crop\_irrig,V_I} \cdot (1/eff_{irrig,region} - 1) \tag{24a}$$

$$\text{, for } cf_{crop\_irrig,V_I} \cdot (1/eff_{irrig,region} - 1) < cf_{bare,V_I} + cf_{crop\_irrig,V_I} \cdot (1 - veg_{crop\_irrig,V_I})$$

$$\text{, } cf_{bare\_irrig_{Imax}} = cf_{bare,V_I} + cf_{crop\_irrig,V_I} \cdot (1 - veg_{crop\_irrig,V_I}) \text{ otherwise.} \tag{24b}$$

Additionally, for this scenario the target soil moisture in irrigated regions was set to the field capacity to best represent inundated surfaces in rice growing regions, which constitute about 43% of the global irrigation water demand (Bouman et al., 2007). The amount of water donated to the non-vegetated fraction is calculated analogous to Eq.

22 but omitting the scaling with the vegetation ration and using w_{max} as target soil moisture.

$$irrig^{t}_{bare\_irrig} = w_{max} - w^{t-1,end}_{bare\_irrig} \tag{25}$$

To determine the impact of simulated irrigation on the state of the surface and atmosphere and the surface energy and moisture fluxes, the above irrigation simulations were compared to three reference simulations P_R,S_R,V_R. These are identical to P_I,S_I,V_I, but without a representation of irrigation in the respective areas. Finally, an idealized irrigation simulation (V_{Iideal}) was performed to investigate the distance between the irrigated regions and areas in which impacts due to irrigation are still perceivable. Here, irrigation was modelled analogous to V_{Imax}, but with irrigation limited to a region in Eurasia between $0°N$ - $45°N$ and $30°E$ - $95°E$ from which also the Arabian Peninsula was excluded. An overview over all simulations is provided in table 5.

4.3. Impact of irrigation on remote regions

Depending on the simulation and variable investigated, irrigation has a robust impact on 5 % to 20 % of the land surface (Fig. 18). A robust impact is assumed when the differences between irrigation and control simulation are statistically significant ($p < 0.05$) and larger than ECHAM/JSBACH's internal model variability. The internal variability was derived from the ensemble spread of 3×5 simulations performed with ECHAM/JSBACH (de Vrese and Hagemann, 2015). Around 70 % of all irrigated areas are located in South, Southeast and East Asia (SA-REGION, i.e. $40°E$ - $130°E$; $0°$ - $45°N$) and most robust impacts on climate can also be found in this region.

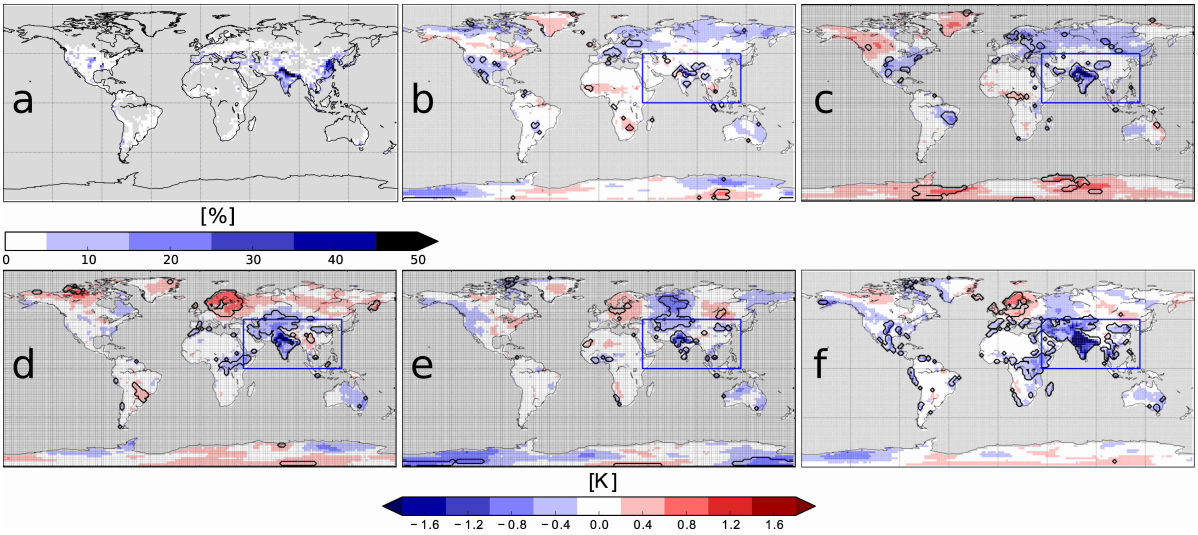

Figure 18: a) Cover fraction of the irrigated crop tile (P_I, S_I, V_I); 20-year mean difference in surface temperature b) P_I - P_R c) S_I - S_R d) V_I - V_R e) V_{Imin} - V_R f) V_{Imax} - V_R; grid box mean; black outlines give areas in which differences are robust; blue rectangle denotes the SA-REGION

Sim.	*Coupling scheme*	*Irrigation applied*	*Irrigated fraction*$^{+}$	*Irrigation target*	*Timing*
P_R	parameter	none	0.0 [%]	0.75 w_{max}	-
P_{I1}	parameter	irrigated crops (vegetated + non-vegetated)*	1.9 [%]*	0.75 w_{max}	time step
S_R	simple flux	none	0.0 [%]	0.75 w_{max}	-
S_{I1}	simple flux	irrigated crops (vegetated + non-vegetated)*	1.9 [%]*	0.75 w_{max}	time step
V_R	VERTEX	none	0.0 [%]	0.75 w_{max}	-
V_{I1}	VERTEX	irrigated crops (vegetated + non-vegetated)*	1.9 [%]*	0.75 w_{max}	time step
V_{Imin}	VERTEX	irrigated crops (fully vegetated)	0.8 [%]	0.75 w_{max}	time step
V_{Imax}	VERTEX	irrigated crops (fully vegetated) + bare soil	0.8 + 1.0 [%]	w_{max}	time step
V_{Iideal}	VERTEX	irrigated crops (fully vegetated) + bare soil°	0.4 + 0.4 [%]°	w_{max}	time step

Table 5: Overview over the simulations performed with ECHAM/JSBACH and their respective characteristics; $^{+}$ annual mean averaged over the land surface; * irrigated tile consists of vegetated and non-vegetated fraction, irrigation demand is calculated for the vegetated fraction but water is applied to the entire tile; ° irrigation is restricted to an area in Eurasia between $0°N$ - $45°N$ and $30°E$ - $95°E$ from which the Arabian Peninsula is excluded

Nonetheless, results indicate that many robust irrigation induced impacts on climate occur far away from the irrigated areas and are most likely the result of changes in large scale circulations. For example, V_I exhibits a pronounced increase in surface temperature in northern Canada and Alaska, which has also been found by Sacks et al. (2009). They argued that the warming is possibly related to the deepening of a low-pressure system centred off the coast of Alaska during winter, i.e. the Aleutian Low, which causes the inland transport of more warm, moist air from the Gulf of Alaska. In the present study, the relation between irrigation and a strengthening of this low-pressure system is only speculative, especially because the simulated irrigation in North America in V_I is not very pronounced. In general, it is extremely difficult to link any change in large scale circulations to irrigation.

However, V_I also exhibits robust remote, even transcontinental impacts on climate, which can be attributed to irrigation directly. Several mechanisms can be distinguished by which irrigation affects regions in a substantial distance from the irrigated areas. The most straightforward of these is the advection of moisture from irrigated regions. Here, the term advection is used in the strict sense of the word but also as a synonym for a sequence of consecutive advection, precipitation and re-evaporation of moisture. Studies indicate that a large fraction (over 75 %) of the evapotranspiration in regions in India, Pakistan, Bangladesh, Iran, Iraq, Turkey etc. in which irrigated areas constitute a substantial fraction of the land surface, leads to precipitation in other continental areas (Dirmeyer et al., 2009; van der Ent et al., 2010). At the same time, the precipitation in many regions in East Asia, North East and Central Africa has its origins in continental evapotranspiration. Consequently, it is highly plausible that also evapotranspiration from irrigated areas affects remote regions by the advection of water vapor (Fig. 19).

As mentioned in section 4.1, regional studies have shown the impact of irrigation on the South Asian monsoon. Owing to the size of the monsoon system, any effects due to alteration of the monsoon will not be confined locally. Therefore, the impact on regional circulations such as the Asian monsoon constitutes another important mechanism by which irrigation may affect the climate in remote regions.

4.3.1. Advection of water vapor

During the onset of boreal spring (February-March) the evaporative moisture flux resulting from irrigation in regions in the Middle East (these will for simplicity be called the western regions) is still small and in most of these areas the amount of water applied at the surface is below $2\,mm\,mo^{-1}$ (grid box average). In regions further east such as India, Pakistan and Bangladesh (eastern regions), the evaporative flux is already very pronounced and the amount of water applied is well above $2\,mm\,mo^{-1}$. Accordingly, in the respective regions the specific humidity in the low atmosphere (up to a height of $4500\,m$) is up to $1\,g\,kg^{-1}$ larger in V_I than in V_R. Additionally, the low atmospheric winds (up to $4500\,m$) on the Eurasian continent are in easterly directions, so that a large share of the moisture in the atmosphere which evaporated in the western regions,

is transported eastwards towards South Asia. At the same time, the winds in the Arabian Sea are in southwesterly direction. Consequently, a large share of the atmospheric water vapor, originating from irrigation in the eastern regions and also from the moisture transported eastwards from the western regions, is advected across the Arabian Sea towards the east coast of Africa. Here, the specific humidity in the low atmosphere increases by up to $0.75\,g\,kg^{-1}$ (Fig. 19 a).

During April the winds in the Arabian Sea turn so that the moisture advection from the eastern regions towards Africa ceases (Fig. 19 b). However, irrigation in the western regions increases distinctly and water vapor stemming from evapotranspiration in these regions is transported southwards by winds that originate in the northwest and turn south and eventually west at the eastern coast of Africa. This transport leads to an increase in specific humidity of more than $1.0\,g\,kg^{-1}$ in regions as far west as Nigeria. In May this clockwise wind pattern expands eastwards, so that increasingly moisture from irrigated areas in the Middle East is transported southward into Africa. Here, the winds carrying water vapor are diverted westwards by southeasterly dryer winds (Fig. 19 c).

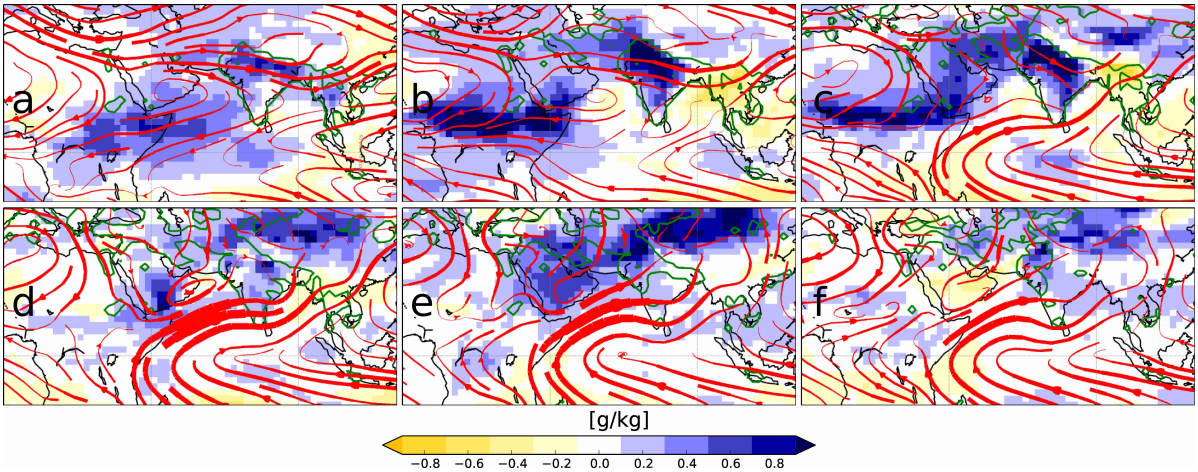

Figure 19: 20-year mean monthly difference V_I - V_R in specific humidity in the low atmosphere ($1000 - 600\,hpa$); a) MAR b) APR c) MAY d) JUN e) JUL f) AUG; red streamlines indicate wind direction and speed from the irrigation run, green contours indicate areas in which grid box mean irrigation $> 2.1\,mm\,mo^{-1}$

During summer (June - August) the wind field changes and the northerly winds carrying water vapor from irrigated regions are diverted eastwards across the Arabian Sea (Fig. 19 d,e,f). Accordingly, there is still a pronounced humidity transport into the Arabian Peninsula but the subsequent water vapor transport westwards from the east coast of Africa ceases. Thus, the increase in specific humidity in Africa in V_I is less pronounced during this season and is possibly related to local moisture recycling rather than moisture advection (van der Ent et al., 2010). During autumn and winter, there is a substantial reduction in irrigation, as compared to spring and summer. Consequently, there is only a minor advective water vapor transport into the Arabian Peninsula or

Africa during these seasons (not shown).

Siebert et al. (2015) estimated that the extent of irrigated areas has almost tripled during the second half of the twentieth century. Consequently, there should be a noticeable increase in precipitation in Eastern Africa for this period, induced by the related moisture transport. In fact, observations (Climate Research Unit data (CRU) Harris et al. (2013), Global Precipitation Climatology Centre data (GPCC) Schneider et al. (2013)) show increasing rainfalls in Eastern Africa between 1951 and 2000, while in the largest part of Africa precipitation exhibits a negative trend (Fig. 20 a,c). Some studies suggest that the increase in precipitation in Eastern Africa is caused by changes in the sea surface temperature in the Indian Ocean and changes in the eastern hemisphere Walker circulation (Indeje and Semazzi, 2000; Behera et al., 2005; Shongwe et al., 2011; Williams and Funk, 2011; Lyon and DeWitt, 2012; Yang et al., 2014). These changes result in a strong increase in precipitation predominantly between October - December. Here, observations indicate an increase in precipitation also during March - May for some regions in Eastern Africa (Fig. 20 b,d). This is the time when the moisture transport from irrigated areas in Eurasia towards Eastern Africa is most active. Hence, it is very plausible that one of the multiple causes for the increase in precipitation in Eastern Africa during the second half of the twentieth century is the expansion of irrigated areas in Eurasia. Furthermore, the reference run shows a strong negative precipitation bias (in comparison to WATCH Forcing Data (WFD), Weedon et al. (2011)) in Eastern and parts of Central Africa especially during spring (Fig. 20 e,f). This bias is not related to the sea surface temperatures in the Indian Ocean as these are prescribed based on observations (Gates et al., 1999). At the Horn of Africa and regions west of it, this precipitation bias is strongly reduced by the simulated irrigation, which supports the existence of a remote impact of irrigation in Eurasia on precipitation in Africa (Fig. 20 g,h).

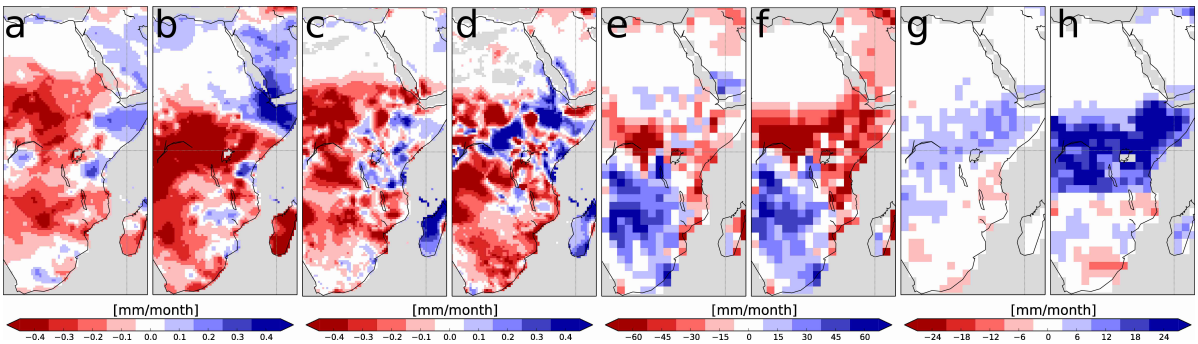

Figure 20: 50-year precipitation trend (1951 -2000): annual mean a) GPCC data c) CRU data, March - May mean b) GPCC data d) CRU data; V_R Precipitation bias (compared to WFD): e) annual mean, f) MAM mean; 20-year mean precipitation difference V_I - V_R: g) annual mean, h) MAM mean

There is not only a south-westwards advection of water vapor towards Africa, but also a strong eastward moisture transport, which leads to an increase in specific humidity over large regions in China, where no or only very little irrigation takes place (Fig. 19). With

winds turning north-eastwards over the Arabian Sea during spring, more moisture is being advected towards China rather than Africa. Consequently, the increase in specific humidity in the respective regions becomes exceedingly pronounced, i.e. substantially more than $1.0\,g\,kg^{-1}$. This mechanism is most clearly visible during June and July, when also the evaporative fluxes due to irrigation and the irrigation donations are largest. With the onset of the summer monsoon, precipitation increases and less irrigation is simulated in V_I. Therefore, during July, August and September the differences in specific humidity between the V_I and V_R decrease. Also during autumn and winter there is only a minor advective moisture transport towards China (not shown).

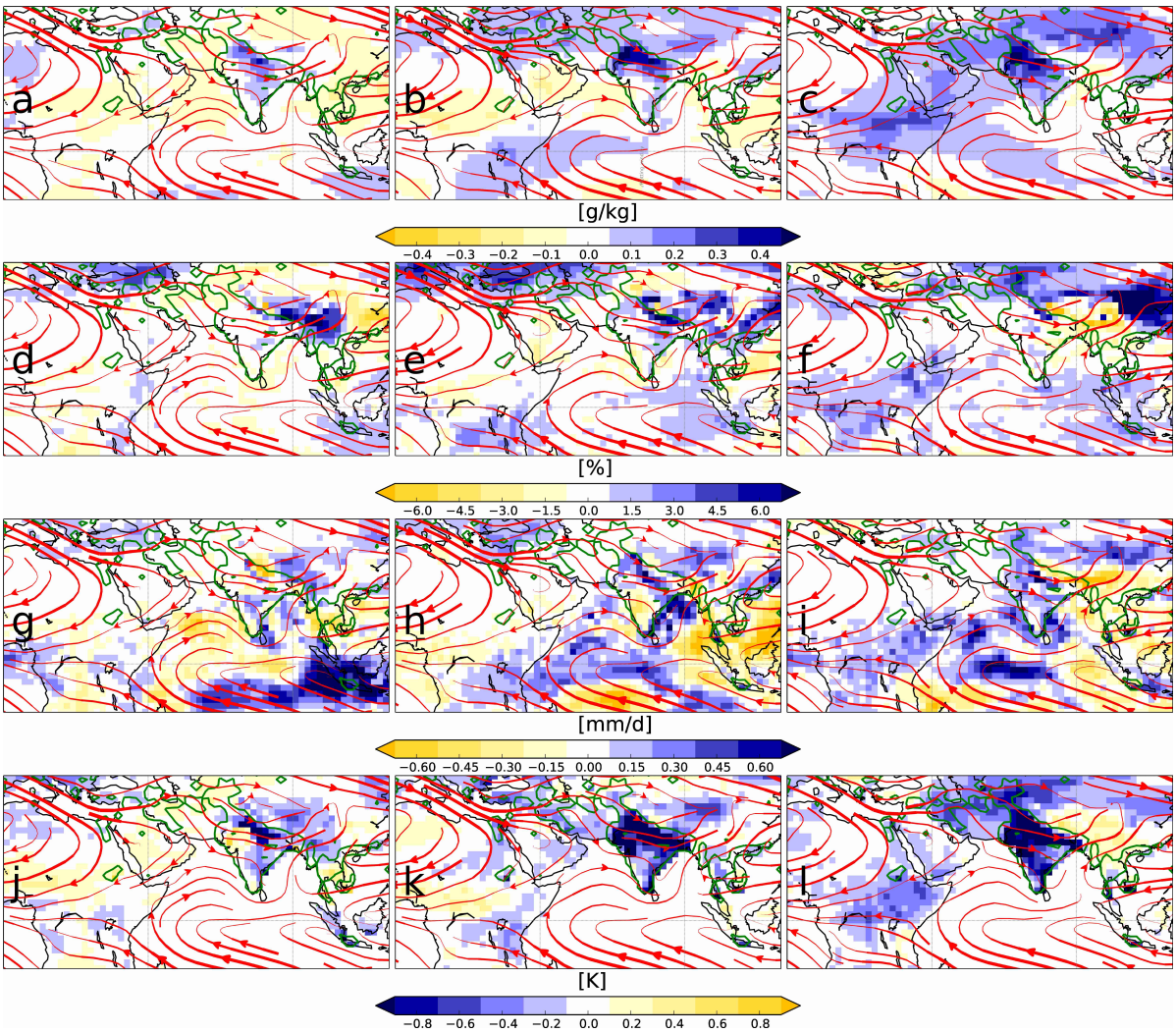

Figure 21: 20-year mean difference P_I - P_R (a,d,g,j), S_I - S_R (b,e,h,k), V_I - V_R (c,f,i,l): specific humidity (a,b,c) and cloud cover in the low atmosphere ($1000 - 600\,hpa$)(d,e,f), precipitation (g,h,i) and surface temperature (j,k,l); red streamlines indicate wind direction and speed from the irrigation run, green contours indicate areas in which grid box mean irrigation $> 25\,mm\,a^{-1}$

Due to irrigation in V_I, also the annual mean specific humidity in the low atmosphere increases by up to $0.5\,g\,kg^{-1}$ in regions with a large extent of irrigated areas (Fig. 21

c). As shown above, this moisture is transported to remote regions, where it leads to an increase in annual mean precipitation by up to $0.6\,mm\,d^{-1}$ and thereby to increased evapotranspiration and an evaporative cooling of the surface (Fig. 21i). Additionally, the increase in atmospheric specific humidity affects the formation of clouds low in the atmosphere, i.e. annual mean aggregate cloud cover in the low atmosphere increases in parts by more than 7.5 %, which reduces incoming solar radiation at the surface (Fig. 21 f). In combination, these two effects induce a cooling of the surface by up to $0.6\,K$ (Fig. 21 l).

Thus, irrigation affects areas in a substantial distance downwind of the irrigated areas. Results indicate that westerly winds transport moisture from irrigated areas in South Asia and adjacent regions across China and, in combination with local irrigation, induce a robust cooling of the surface in regions as far as the eastern coast of China. Moisture from irrigated areas in the Middle East is advected across the Arabian Peninsula into Africa. Additionally, water vapor is transported across the Arabian Sea from South Asia towards eastern Africa. The moisture advected from regions in the north and in the northeast, robustly increases cloud cover, precipitation, evapotranspiration (not shown) in Eastern and Central Africa and, by evaporative cooling and a reduction of net solar radiation, robustly reduces surface temperatures in areas in Somalia, Ethiopia, South Sudan, the Central African Republic and the Democratic Republic of the Congo. These effects can in some areas be substantial. For example in some regions in Eastern and Central Africa, up to 20 % of the annual precipitation can be attributed to irrigation in the Middle East as well as in irrigated areas across the Arabian Sea (Fig. 22).

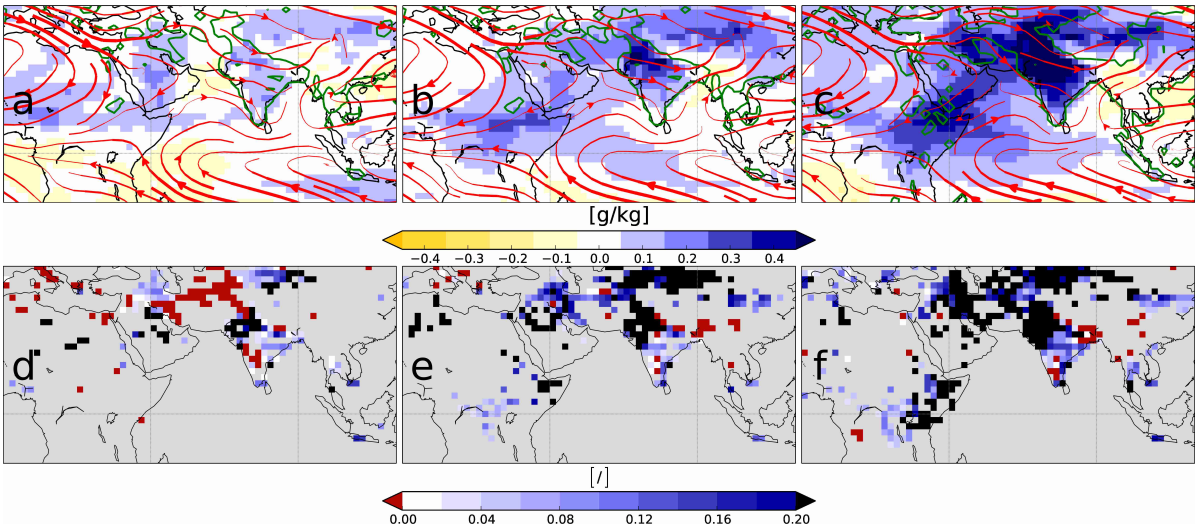

Figure 22: 20-year mean difference in specific humidity in the low atmosphere ($1000 - 600\,hpa$); a) V_{Imin} - V_R b) V_I - V_R c) V_{Imax} - V_R; red streamlines indicate wind direction and speed from the irrigation run, green contours indicate areas in which grid box mean irrigation $> 25\,mm\,a^{-1}$; 20-year mean difference in precipitation relative to reference run d) V_{Imin} - V_R e) V_I - V_R f) V_{Imax} - V_R; areas in which differences are not robust have been masked

4.3.2. Effects on regional circulations

Irrigation in V_I also has a direct effect on regional atmospheric circulations and associated precipitation patterns such as the South and East Asian monsoon. A cooling of irrigated areas in South and Southeast Asia induces a weakening of the summer monsoon by altering the land sea thermal contrast that drives the monsoon winds (Douglas et al., 2009; Lucas-Picher et al., 2011). Accordingly, the south-westerly winds during May and June which are associated with the East Asian summer monsoon are weaker in V_I than in V_R (Fig. 23).

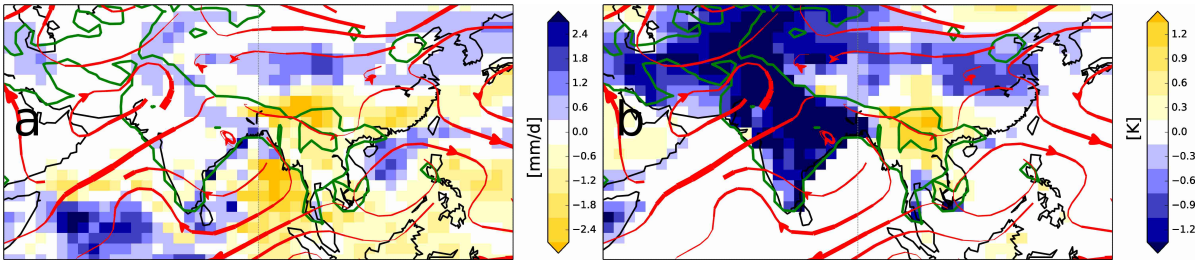

Figure 23: 20-year mean MAY difference between irrigation run and reference run (V_I - V_R); a) precipitation, b) surface temperature; red streamlines indicate differences in wind direction and speed in the low atmosphere ($1000 - 600\,hpa$), green contours indicate areas in which grid box mean irrigation $> 2.1\,mm\,mo^{-1}$

In heavily irrigated regions, a reduction of precipitation due to a weakening of the monsoon is masked by an increase in evapotranspiration and the enhanced local recycling of moisture in V_I. However, in regions with less irrigation such as Myanmar, a weakening of the monsoon leads to a reduction in precipitation and consequently in the available water at the surface. This induces a decrease in evapotranspiration and higher surface temperatures. This effect can be seen in, e.g., Myanmar and parts of Southwest China, where in May and June precipitation is reduced by up to $2.5\,mm\,d^{-1}$ and surface temperature increases by up to $1.5\,K$ (Fig. 23). Due to the impact on the monsoon, irrigation in V_I does not only lead to a transcontinental increase in precipitation but can also cause a decrease in precipitation, evapotranspiration and thus a robust increase in surface temperature in remote regions. By simulating a decrease in precipitation and evapotranspiration and an increase in surface temperatures in East India, Bangladesh, Nepal and Myanmar, V_I is in good agreement with modelling studies that use higher resolved regional models (Saeed et al., 2009; Tuinenburg et al., 2014).

4.3.3. Influence of surface-atmosphere coupling and irrigation efficiency

If these effects are present at all in P_I (Fig. 21 a,d,g,j) and S_I (Fig. 21 b,e,h,k), they are much less pronounced than in V_I. For example, neither P_I nor S_I indicate an increased moisture transport across the Arabian Peninsula and there is no robust cooling of the land surface in eastern Africa. At the same time, it is impossible to directly link the slight increase in precipitation and cooling of the surface in eastern Africa to any irrigation in South Asia. A seasonal analysis (not shown) indicates that during spring

there is no increase in moisture advection across the Arabian Sea in east - west direction. During the time when the Arabian Sea is dominated by easterlies (autumn and winter), actually drier air is being advected towards Africa for a substantial share of the time. In Southeast Asia the remote effects of irrigation are equally small.

For P_I strong differences in specific humidity within the low atmosphere are limited to the heavily irrigated regions in India. Effects on cloud cover, precipitation and surface temperature possibly extent eastwards until Southwest China but are still confined to a much smaller area than for V_I. In case of S_I effects due to irrigation are also more locally confined than for V_I. For example, there is a strong increase in cloud cover and precipitation at the east-coast of China, however this can most likely be attributed to local irrigation in combination with irrigation in the Indochinese Peninsula rather than irrigation in regions in South Asia.

The absence of transcontinental effects in P_I and S_I is not primarily related to differences in the wind fields between P_I, S_I and V_I, as these are only minor. Contrary, the variations in the irrigation induced increase in atmospheric water vapor are substantial and can be related to differences in the coupling schemes used for V_I, P_I and S_I, which result in differences in the simulated local moisture recycling (Fig. 24). Contrary to the parameter and simple flux aggregation scheme, the *VERTEX* scheme is not based on the restrictive assumption of atmospheric homogeneity, as sub-grid scale heterogeneity in the lowest layers is explicitly represented. Furthermore, simulated precipitation and near surface temperature, in regions in which irrigated areas constitute a large share of the land surface, are consistently closer to WFD when using the VERTEX scheme (not shown). This indicates that in P_I and S_I important processes are not well represented which leads to an underestimation of the effects of irrigation.

Generally, the way irrigation affects remote regions in case of V_{Imin} and V_{Imax} is similar to V_I (Fig. 18, 22). In both simulations there is an increase in the eastwards moisture advection across China, an increase in the transport of moisture across the Arabian Peninsula into Eastern Africa and in the moisture advection from South Asia across the Arabian Sea during spring. However, whether this leads to robust impacts on the simulated climate in the respective regions depends largely on the amount of additional moisture advected, thus on the amount of water introduced into the atmosphere as a result of irrigation (Fig. 24).

For example, with respect to V_{Imin}, the robust temperature decrease in eastern China is less pronounced than for V_I, and there is almost no robust cooling of the surface or an increase in precipitation in Eastern Africa. On the contrary, V_{Imax} constitutes a much more extensive surface cooling in China, and the area in Eastern Africa exhibiting a robust cooling of the surface almost entirely covers Ethiopia, Kenya, Uganda, South Sudan, the Central African Republic and the Democratic Republic of the Congo. Also the irrigation induced increase in precipitation is substantial and the area that exhibits relative increases in precipitation of more than 20 % almost entirely covers eastern Ethiopia

and Kenya (Fig. 22).

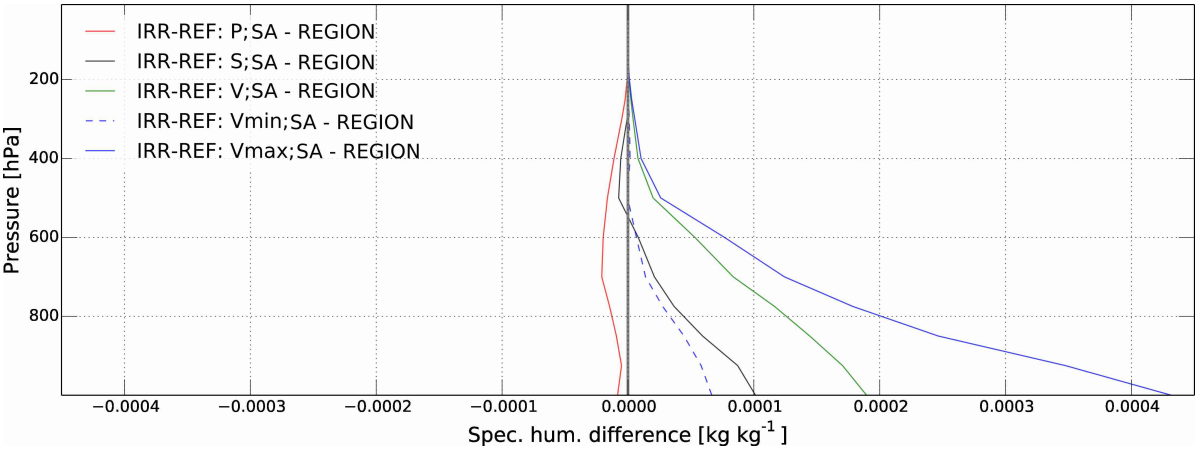

Figure 24: 20-year mean difference in the atmospheric column between irrigation runs P_I, S_I, V_I, V_{Imin}, V_{Imax} and reference runs P_R, S_R, V_R specific humidity in South and Southeast Asia (SA-REGION)

Due to the low irrigation efficiency assumed for V_{Imax}, also local irrigation may have a pronounced impact on the atmospheric water vapor, making it very difficult to attribute the increase in the atmospheric humidity to local sources or to moisture which is advected into the region. However, an investigation of the surface water balance in the respective regions revealed that the strong increase in atmospheric water vapor can not be explained exclusively by local irrigation (not shown).

Furthermore, an idealized simulation was performed, in which irrigation was limited to an area in Eurasia between $30°E$ - $95°E$, from which also the Arabian Peninsula was excluded. Otherwise the simulation was performed analogous to V_{Imax}. Even with the irrigation limited to this area, there is still a pronounced increase in the advective moisture transport into Africa and towards the east coast of China (Fig. 25 a). In Africa the area in which precipitation is robustly affected by irrigation in Eurasia stretches far into the Democratic Republic of the Congo and Tanzania (Fig. 25 b).

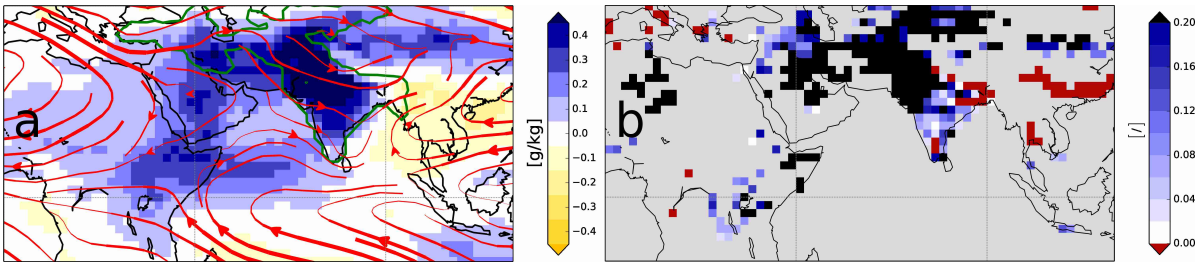

Figure 25: 20-year mean difference V_{Iideal} - V_R: a) specific humidity in the low atmosphere ($1000 - 600\,hpa$); red streamlines indicate wind direction and speed from the irrigation run, green contours indicate areas in which grid box mean irrigation $> 25\,mm\,a^{-1}$; b) precipitation, relative to reference run; areas in which differences are not robust have been masked

With robust increases in precipitation around the African Great Lakes, this places the closest irrigated areas in Iran and Iraq in a distance of at least 4000 km. From regions at China's east coast, where robust relative increases of precipitation are above 15 %, the distance to the nearest irrigated area in Mongolia is well above 2500 km. This confirms that local irrigation in the respective regions has only a minor effect and the largest impact stems from irrigation several thousand kilometres away.

Additionally, both, V_{Imin} and V_{Imax}, indicate an impact of irrigation on the Asian monsoon in the region around Myanmar, i.e. a reduction in precipitation and a consequent increase in surface temperature. However, this impact is much less pronounced than in V_I. It can be speculated that this is because in V_{Imin} the extent of surface cooling is much smaller than in V_I, so that the decrease in land-sea thermal contrast is much weaker. Hence, the impact on the monsoon winds is much less pronounced for V_{Imin} than for in V_I (not shown). Contrary, in V_{Imax} the surface cooling in South and Southeast Asia is very pronounced and the impact on the monsoon winds is evident (not shown). However, because the increase in atmospheric water vapor in Southeast Asia is also much stronger, the weakening of the monsoon and the consequent reduction in precipitation is masked by an increase in precipitation related to irrigation.

4.4. Conclusion and Discussions

The simulations performed with ECHAM/JSBACH provide evidence that irrigation has a direct impact on climate that extends over a distance of several thousand kilometres. Simulations using the newly developed VERTEX scheme indicate that, by the advection of moisture, irrigation in South Asia influences precipitation, evapotranspiration and surface temperatures in eastwards regions as distant as the eastern coast of China. By the same mechanism, irrigated areas in the Midlle East and South Asia affect precipitation and surface temperatures in East and Central Africa.

In these regions, the transcontinental effects due to irrigation can be substantial. For example, in certain areas in Eastern and Central Africa simulated precipitation increases by over 20 % as a result of irrigation on the Eurasian continent. Here, observations corroborate that the rapid expansion of irrigated areas during the second half of the twentieth century was accompanied by an increase in rainfall over Eastern Africa, even though other causes may well have constituted to this increase.

The strength of the simulated impact of irrigation on remote regions depends on the characteristics assumed for the irrigated areas, namely the irrigation efficiency. This has important implications with respect to real world irrigation. Thus, it may be inferred that precipitation in eastern Africa is likely to increase in the future if there is an expansion of irrigated areas in the Middle East or in South Asia. Likewise it is to decrease if irrigation in the respective regions decreases as a result of water scarcity. This is especially relevant for regions in Eastern Africa in which droughts have caused humanitarian catastrophes that affect millions of people (Maxwell and Fitzpatrick, 2012).

Additionally, the results support regional studies which found a strong influence of irrigation on the Asian monsoon. Irrigation leads to an evaporative cooling of the surface in irrigated areas in South and Southeast Asia. Consequently, the land-ocean temperature gradient, driving the monsoon winds, is reduced. In strongly irrigated regions a weakening of the monsoon and the consequent reduction of precipitation and evapotranspiration is masked by the increase in evapotranspiration from irrigated areas. However, in regions with no or only little irrigated areas, a weakening of the monsoon results in less precipitation and less evapotranspiration. The consequent reduction of evaporative cooling leads to a local increase in annual mean temperature of up to $0.5\,K$ and an increase of up to $1.5\,K$ during the (summer) monsoon season. Thus, it could be demonstrated that, besides the transcontinental effect related to the advection of water vapor, irrigation can also induce a decrease in precipitation and an increase in surface temperature in remote regions, by affecting regional circulations.

These findings are limited to the simulations using the VERTEX scheme which, from the three coupling schemes used, is based on the most physical assumptions and gives the best results in comparison to WFD. This indicates that previous global studies which used a parameter or a simple flux aggregation scheme for the land surface-atmosphere coupling may have underestimated the large scale effects of irrigation.

To confirm the findings of this study and to provide further insight into the processes responsible for large scale effects, additional investigations are conceivable. On one hand these should aim at the most realistic representation of irrigation characteristics, as in this work a rather simplistic representation and plausible minimum and maximum scenarios were investigated. On the other hand, the advective moisture transport should be studied in more detail. With respect to irrigation, moisture tracking schemes have already been used in regional studies and investigations with comparable schemes could also be conducted for the global scale (Harding et al., 2013; Tuinenburg et al., 2014).

5. Uncertainties in Modelling Irrigation

5.1. Introduction

Currently, irrigated areas comprise 18 % of the global cultivated areas. They provide about 40 % of the total crop yield (Siebert et al., 2005), while constituting about 70 % of humanity's demand for fresh water (Wada et al., 2013). The role of irrigation-based agriculture in global food production is prognosed to become increasingly challenging, as it is assumed that already between the years 2000 and 2025 a possible 40 % increase in food demand has to be met with a $10-20$ % reduction of the agricultural use of freshwater resources (Lotze-Campen et al., 2008). At the same time the estimates for additional agricultural water requirements range as high as $5000\,km^3\,a^{-1}$ with an expected increase in area required for crop and cattle of about $50-70$ % (De Fraiture and Wichelns, 2010).

But irrigation does not only have an importance with respect to satisfying global food demands, but also because of its impact on climate. Irrigation strongly affects the hydrological cycle and the land surface energy budget by the redistribution of water. Currently, the amount of water delivered via irrigation is estimated to be more than $2500\,km^3\,a^{-1}$ which is equal to about 2 % of precipitation over land (Shiklomanov, 2000). Numerous studies using a variety of models have shown that irrigation significantly affects regional climate and possibly even climate on the global scale. These studies investigate a wide range of scales, varying from the direct impact on climate in irrigated regions (Douglas et al., 2006; Kueppers et al., 2007; Douglas et al., 2009; Lobell et al., 2009; Saeed et al., 2009; Tuinenburg et al., 2014), to the global impact (Boucher et al., 2004; Sacks et al., 2009). They cover a broad scope including the impact of irrigation in comparison to other anthropogenic influences such as deforestation (Gordon et al., 2005; Lobell et al., 2006b), irrigation water demand, also with respect to its impact on freshwater resources (Döll and Siebert, 2002; Tiwari et al., 2009; Liu and Yang, 2010; Wada et al., 2012, 2013; Yoshikawa et al., 2013) or the impact with respect to changing climate conditions e.g. (Lobell et al., 2006a; Puma and Cook, 2010; Cook et al., 2011). A summary of recent studies can be found in Hagemann et al. (2014).

All model based studies necessarily involve simplifying assumptions with respect to the representation of irrigation, and are therefore subject to uncertainties. One prominent example for this is the way the irrigation water is introduced into the model. One possible approach is to represent irrigation by adding water to the soil whenever the value of an indicator variable passes a certain threshold. For example, Sacks et al. (2009) added water at a predetermined rate whenever the leaf area index (LAI) in the respective regions was larger than 80 % of the maximum LAI in order to simulate irrigation during the growing season. In this approach, the irrigation flux depends exclusively on vegetation characteristics and is independent of the actual saturation of the soil. Consequently, the highest water demand is computed for the height of the growing season which, on a global average, is between June and November. For example in India, the two main cropping seasons, the Kharif (July – October) and the Rabi cropping season (October-March)

mainly fall in this period. This is also the summer monsoon season (May - September) in India and Southeast Asia and the soil in the affected regions exhibits a high moisture content due to pronounced precipitation. Thus, a large share of the water added as simulated irrigation has little effect on the plant available water, but mainly results in an increase in runoff and drainage. Contrary to this, when introducing irrigation water at a rate that depends on the saturation of the soil, the largest irrigation demand is calculated for spring, i.e. March - May, which is also in agreement with irrigation water requirements determined in studies using water demand models (Döll and Siebert, 2002).

Nonetheless, there are few studies which aim at the effects related to differences in the representation of irrigation within models as a key factor of uncertainties. In these studies the focus is mainly on irrigation characteristics such as the extend of irrigated areas or timing and mode of delivery, e.g. Sacks et al. (2009); Yoshikawa et al. (2013). With respect to these characteristics, global data coverage is patchy and in most models the representation of irrigation characteristics is very simplistic. The present study aims to improve the state of knowledge in this respect by performing complementary investigations using the atmospheric and land surface component of the Max Planck Institute for Meteorology's Earth System Model (ECHAM/JSBACH). The goal is to estimate variations of the impact of irrigation on simulated climate due to variations of the modelled irrigation efficiency and timing of delivery. These can be used as a proxy for uncertainties related to the lack of accuracy with respect to a realistic representation of irrigation in a model.

The impact of irrigation on simulated climate may also differ severely between models even when identical assumptions are made for the irrigation characteristics (Tuinenburg et al., 2014). These differences are related to variations in the more general model physics and the model's structure, such as resolution of the model and its parametrizations. To provide a rough estimate for uncertainties related to differences in the model's structure and its parametrizations, the simulated impact of irrigation is compared between simulations using different schemes for the land surface-atmosphere coupling. This aspect of the model's structure was chosen because it strongly affects the treatment of irrigated areas as a sub-grid scale heterogeneity and the way moisture is transported from the surface to the atmosphere. Both of which are important factors for the simulated impact of irrigation on climate, hence the surface-atmosphere coupling is expected to be the source of large uncertainties in the simulation of irrigation.

For the study several simulations were performed using ECHAM/JSBACH. The changes made in the model to simulate irrigation are described in section 5.2. Furthermore, the section specifies the characteristics of the individual irrigation simulations. In section 5.3 the differences between simulations are analysed to estimate the variations of the possible impact of irrigation on the state of the land surface and the atmosphere as an approximation of the uncertainties involved in modelling irrigation. In section 5.4 the main findings are shortly summarized and discussed.

5.2. Methods

All simulations with ECHAM/JSBACH were performed with prescribed sea-surface temperature and sea-ice extent according to the protocol of the Atmospheric Model Intercomparison Project (AMIP) (Gates et al., 1999). The model was run with a resolution 47 of vertical model levels, of which the lowest is located at a height of roughly $30\,m$ and a horizontal resolution of T63 which corresponds to a grid-spacing of roughly $200\,km$. In the version of ECHAM/JSBACH that was used in this experiment three possibilities exist to couple land surface and atmosphere, i.e. a parameter aggregation scheme, a simple flux aggregation scheme and the VERTEX scheme.

In the parameter aggregation scheme, the state of the land surface (and the soil) as well as the surface fluxes are modelled based on effective parameters which represent an entire grid box. Here, the determination of an effective grid box mean albedo is described in Otto et al. (2011), the aggregation of the surface roughness length of different tiles follows Mason (1988); Claussen (1991); Claussen et al. (1994) and the aggregation of soil and hydrological parameters is done according to Kabat et al. (1997); Feddes et al. (1998). The surface fluxes, that link the land surface and the atmosphere, are calculated based on the effective parameters, using a bulk-exchange formulation. Here, the bulk transfer coefficients are obtained with approximate analytical expressions similar to those proposed by Louis (1979).

The second option is a simple flux aggregation scheme in which spatial sub-grid scale heterogeneity is explicitly represented by individual tiles. In this approach the state of the surface and the surface fluxes are modelled for each of the tiles separately. However, it is assumed that the vertical fluxes have blended horizontally below the lowest model level of the atmosphere which interacts only with these aggregated fluxes, i.e. spatial heterogeneity does not exist within the atmosphere. The simple flux aggregation scheme implemented into ECHAM/JSBACH's land surface model JSBACH (Raddatz et al., 2007; Brovkin et al., 2009), follows the general method for an implicit surface-atmosphere coupling proposed by Polcher et al. (1998); Best et al. (2004).

The third possibility is a coupling via the VERTEX scheme (de Vrese et al., 2015), which also accounts for spatial heterogeneity within the lowest layers of the atmosphere and further resolves the turbulent mixing process. As in the standard version of ECHAM/JSBACH, the atmospheric vertical fluxes are modelled by a modified version of the turbulent kinetic energy scheme described in Brinkop and Roeckner (1995), however in the VERTEX scheme the process is resolved with respect to individual tiles. Here, turbulent viscosity and diffusivity are described by a function of the turbulent kinetic energy, the turbulent mixing length (Blackadar, 1962) and a stability function that depends on the moist Richardson number (Mellor and Yamada, 1982). In the VERTEX scheme, the fluxes within the individual tiles are not treated independent of each other but are assumed to mix horizontally to a certain extent. Thus, the vertical flux from a given tile may influence the states of all the tiles on the level above. In the VERTEX

scheme the horizontal mixing of the vertical fluxes is modelled based on the concept of the blending height. To determine the blending height, the scheme requires the characteristic horizontal length scales of surface heterogeneity. These were derived from the Global Land Cover Map 2009 (GLOBCOVER) (Arino et al., 2012). Here, the problem existed that the dataset often classified areas as non-irrigated in which the respective fields are equipped for irrigation but that were possibly not irrigated during the passing of the satellite. In these cases the characteristic length scales were determined based on the areas of rainfed crops (see Fig. 36).

In the simple flux aggregation scheme and in the VERTEX scheme the tiles within a grid box interact only via the vertical turbulent fluxes. Below the surface a horizontal transport of water and heat is not modelled and the soil moisture and temperature of a given tile is independent of the other tiles.

For the study, JSBACH was equipped with an irrigation scheme very similar to the one used in a previous study with ECHAM/JSBACH (Tuinenburg et al., 2014). For the irrigation scheme, dedicated tiles to represent irrigated crops and the permanent bare soil fraction of a grid box were implemented in JSBACH. The cover fraction of the irrigated tile, which constitutes roughly 2 % of the land surface, was derived from the potentially irrigated areas taken from the fifth version of the global map of irrigation areas (Siebert et al., 2005; Siebert et al., 2013) (Fig. 26 h). In the scheme, irrigation is modelled by an increase in soil moisture directly, which best resembles irrigation via a flooding of the surface and disregards other reservoirs such as the canopy layer. The amount of water used for irrigation is calculated to maintain the soil moisture within the vegetated part of the irrigated crop tile close to the level at which potential transpiration is reached. The water added by irrigation $irrig^{t}_{crop\_irrig}$ in time step t and the soil moisture in the irrigated crop tile $w^{t,start}_{crop\_irrig}$ at the beginning of each time step are calculated based on the saturation of the soil column as:

$$irrig^{t}_{crop\_irrig} = (w_{max} \cdot c_{pot\_trans} - w^{t-1,end}_{crop\_irrig}) \cdot veg^{t,start}_{crop\_irrig} \tag{26a}$$

$$w^{t,start}_{crop\_irrig} = w^{t-1,end}_{crop\_irrig} + irrig^{t}_{crop\_irrig} \tag{26b}$$

$$\text{, for } w^{t-1,end}_{crop\_irrig} < w_{max} \cdot c_{pot\_trans}$$

Here w_{max} is the water holding capacity of the soil, c_{pot_trans} is a coefficient representing the fraction of soil moisture required for transpiration to occur at the potential rate, $w^{t-1,end}_{crop\_irrig}$ is the soil moisture in the irrigated tile at the end of the previous time step and $veg^{t,start}_{crop\_irrig}$ is the vegetation ratio at the beginning of the time step. For specific simulations additional alterations were made to JSBACH and to the irrigation scheme which will be explained in the following.

Based on the irrigation scheme and the three coupling schemes described above, a three member ensemble was simulated, i.e. P_{I1} (parameter aggregation), S_{I1} (simple flux aggregation), V_{I1}($VERTEX$ scheme). Each simulation encompasses the same 21-year

period (1979-1999) from which the first year was required for the model spin-up and has been omitted from the analysis (Table 6).

Moreover, an ensemble of four simulations (V_{I2} - V_{I5}) using the *VERTEX* scheme was conducted in which certain irrigation characteristics were varied, namely the fraction of water donated to the non-vegetated fraction of the grid box as a proxy for the irrigation efficiency, the target soil moisture in the irrigated fractions and the timing of delivery. The aim was to estimate the sensitivity to a variation of these characteristics rather than providing the most realistic representation of irrigation. Hence, the assumptions on which V_{I2} - V_{I5} are based present plausible yet extreme scenarios.

In JSBACH each tile consists of a vegetated fraction as well as a dynamical bare soil fraction and irrigation is applied in the entire tile, i.e. vegetated and dynamical non-vegetated fraction alike. Note that the permanent bare soil fraction, i.e. the area that is uninhabitable to vegetation, has already been integrated to a dedicated tile. Thus, in the model setup used for P_{I1},$\mathrm{S_{I1}}$,$\mathrm{V_{I1}}$, it is impossible to determine the distribution of water between the vegetated and the bare soil fraction of a tile. In order to regulate the amount of water that is being donated to the non-vegetated part of the grid box, the irrigated crop tile was split into two tiles, one representing the vegetated fraction and the other representing the dynamical bare soil share of the irrigated crop tile. In V_{I2} - V_{I5} the cover fractions of these tiles and the respective vegetation ratios were not calculated by the model, but were specified based on the properties of the irrigated crop tile simulated in V_{I1}. This was done to ensure that in all simulations the actual area covered by irrigated crops is the same and any difference between the simulations can be attributed to a change in the representation of irrigation characteristics rather than to differences in vegetated area in the irrigated crop tile. The cover fractions for the irrigated crop tile $cf_{crop\_irrig,X}$ ($X \in \{V_{I2},\ V_{I3},\ V_{I4},\ V_{I5}\}$) and the dynamical bare soil tile $cf_{bare\_dyn,X}$ were calculated based on the cover fraction $cf_{crop\_irrig,V_{I1}}$ and the vegetation ratio $veg_{crop\_irrig,V_{I1}}$ of the crop tile in simulation V_{I1}:

$$cf_{crop\_irrig,X} = cf_{crop\_irrig,V_{I1}} \cdot veg_{crop\_irrig,V_{I1}} \tag{27a}$$

$$cf_{bare\_dyn,X} = cf_{crop\_irrig,V_{I1}} \cdot (1 - veg_{crop\_irrig,V_{I1}}) \tag{27b}$$

$$veg_{crop\_irrig,X} = 1.0 \tag{27c}$$

Here, the cover fractions were calculated from the 20-year monthly means and the values prescribed at the beginning of each time step were determined through linearly interpolation between the monthly values.

For V_{I2} a very high irrigation efficiency is assumed. Accordingly, irrigation is only applied in the fully vegetated irrigated crop tile and no water was donated to the bare soil tile, i.e. $cf_{bare\_irrig,V_{I2}} = 0.0$.

V_{I3} is identical to V_{I2}, with the exception of the timing of delivery. For V_{I3} irrigation

is only applied biweekly (every 14 days), instead of irrigating at every time step. The water was applied at the same time step in all irrigated areas, as studies showed the actual time of the day, at which the soil is irrigated only has a minor effect (Sacks et al., 2009).

In contrast, for simulations V_{I4} and V_{I5} a very low irrigation efficiency is assumed. The simulations were designed to not only account for transpiration from the cropped areas themselves, but to factor in unintended evaporation that occurs during the irrigation process. This evaporation originates in the irrigation of bare soil areas and from parts of the irrigation infrastructure such as reservoirs and channels, the latter of which can not directly be simulated with ECHAM/JSBACH. In V_{I4} the irrigated non-vegetated share of the grid box was modelled based on the hypothesis that irrigation is planned to achieve maximum yield, i.e. that the entire area equipped for irrigation will be covered by vegetation at a given point during the growing season. Furthermore, irrigation is required not only when crops are fully grown but already when just shoots are present or even when seeds are planted. Therefore, the irrigated area is assumed to be equal to the area equipped for irrigation and the irrigated bare soil fraction is equal to the share of the potentially irrigated areas not covered by vegetation, i.e. the dynamical bare soil fraction of the irrigated crop tile in V_{I1}.

$$cf_{bare\_irrig,V_{I4}} = cf_{bare\_dyn,V_{I4}} = cf_{crop\_irrig,V_{I1}} \cdot (1 - veg_{crop\_irrig,V_{I1}}) \tag{28}$$

In simulation V_{I5} it was assumed that the amount of water used for irrigation is proportional to the growth of the crops, i.e. most water is required during the height of the cropping season and only very little during the planting stage. Therefore, for V_{I5} the regional irrigation efficiency $eff_{irrig,region}$ was used as a very rough approximation for the relation of the cover fractions of the irrigated non-vegetated tile and the irrigated vegetated crop tile (Döll and Siebert, 2002). Here, the irrigated non-vegetated fraction of the grid box can actually become larger than the dynamical bare soil fraction of the irrigated crop tile in V_{I1} and is calculated as follows:

$$cf_{bare\_irrig,V_{I5}} = cf_{crop\_irrig,V_{I1}} \cdot (1/eff_{irrig,region} - 1) \tag{29a}$$

$$\text{, for } cf_{crop\_irrig,V_{I1}} \cdot (1/eff_{irrig,region} - 1) < cf_{bare,V_{I1}} + cf_{bare\_dyn,V_{I5}}$$

$$\text{, } cf_{bare\_irrig,V_{I5}} = cf_{bare,V_{I1}} + cf_{bare\_dyn,V_{I5}} \text{ otherwise.} \tag{29b}$$

In many studies the irrigation target soil moisture is equal to the level at which potential transpiration occurs. In JSBACH this is at $c_{pot\_trans} = 0.75$. For soils with $w_{max} > 0.4\,m$ this target level does not induce bare soil evaporation in the irrigated non-vegetated tile, when using a simple bucket scheme to represent the soil. This is because bare soil evaporation only occurs if water is present in the upper $0.1\,m$ of the soil reservoir, i.e. when $w_{actual} > w_{max} - 0.1\,m$ (Roeckner et al., 1996). In order to estimate the maximum impact on evapotranspiration that an irrigation of the bare soil tile has, the target soil moisture level in V_{I4} and V_{I5} was set to $w_{irrig}^{i,start} = w_{max}$.

The plausibility of this assumption depends largely on the represented irrigation technique which can be fundamentally different with respect to the soil moisture level maintained. For certain types such as drip or sprinkler irrigation, maintaining the soil at saturation level is quite an unrealistic supposition. However, for other techniques such as basin irrigation, a permanently saturated soil is far more plausible. About 80 % of the irrigated area in Asia can be attributed to the cultivation of rice (Seckler et al., 1998). One method to cultivate rice is in form of lowland rice also known as the paddy field, in which rice is planted in an area that is inundated for a large part of the growing season. Around 75% of the world's rice production is provided by irrigated low land rice fields which maintain saturated soils for at least 80 % of the crops duration. Hence, when considering that rice farming alone constitutes up to 43% of the global irrigation water demand, a target soil moisture of w_{max} is a justified supposition (Bouman et al., 2007).Thus the amount of water donated to the non-vegetated fraction is calculated analogous to Eq. 26 but omitting the scaling with the vegetation ration and using w_{max} as target soil moisture.

$$irrig^{t}_{bare\_irrig} = w_{max} - w^{t-1,end}_{bare\_irrig} \tag{30}$$

Furthermore, three reference simulations P_R,S_R,V_R were performed which are identical to P_{I1},S_{I1},V_{I1} but without irrigation being accounted for. To investigate the impact of irrigation on the simulated state of the surface and the atmosphere, the results of a given irrigation simulation are being compared to the respective reference simulation. In the following, the impact corresponding to a specific irrigation simulation, given by the difference between the irrigation simulation and the respective reference simulation, is referenced by Δ and an index referring to the simulation. For example, Δ_{VI3} denotes the impact of simulated irrigation on a given variable, when using the *VERTEX* scheme for the surface-atmosphere coupling, assuming a high irrigation efficiency and a biweekly donation of water, i.e. $\Delta_{VI3} = V_{I3} - V_R$. The differences between the simulations are briefly summarized in table 6.

Boucher et al. (2004) describe two main mechanisms by which irrigation affects climate:

- Evapotranspiration of irrigation water increases the latent heat flux and reduces the sensible heat flux which is accompanied by an evaporative cooling of the surface.
- Additional water vapour in the atmosphere leads to an increased absorption of solar radiation and an additional green house effect. This water vapour eventually condenses and releases heat, causing an additional warming of the atmosphere.

Accordingly, the expected impacts of irrigation on the state of the atmosphere are an overall increase in water vapour and a pronounced decrease in temperature close to the surface. With increasing height, the effects due to the additional water vapour in the atmosphere compensate the cooling effects caused by the evaporative cooling at the surface. This results in a less pronounced decrease or even an increase in temperature

Sim.	*Coupling scheme*	*Irrigation applied*	*Irrigated fraction*$^{+}$	*Irrigation target*	*Timing*
P_R	parameter	none	0.0 [%]	0.75 w_{max}	-
P_{I1}	parameter	irrigated crops (vegetated and non-vegetated)	1.9 [%]*	0.75 w_{max}	time step
S_R	simple flux	none	0.0 [%]	0.75 w_{max}	-
S_{I1}	simple flux	irrigated crops (vegetated and non-vegetated)	1.9 [%]*	0.75 w_{max}	time step
V_R	VERTEX	none	0.0 [%]	0.75 w_{max}	-
V_{I1}	VERTEX	irrigated crops (vegetated and non-vegetated)	1.9 [%]*	0.75 w_{max}	time step
V_{I2}	VERTEX	irrigated crops (fully vegetated)	0.8 [%]	0.75 w_{max}	time step
V_{I3}	VERTEX	irrigated crops (fully vegetated)	0.8 [%]	0.75 w_{max}	biweekly
V_{I4}	VERTEX	irrigated crops (fully vegetated) + bare soil[1]	0.8 + 1.1 [%]	w_{max}	time step
V_{I5}	VERTEX	irrigated crops (fully vegetated) + bare soil[2]	0.8 + 1.0 [%]	w_{max}	time step

Table 6: Simulations with ECHAM/JSBACH and their respective characteristics; $^{+}$ annual mean averaged over the land surface; * irrigated tile consists of vegetated and non-vegetated fraction, irrigation demand is calculated for the vegetated fraction but water is applied to the entire tile; [1] the potentially irrigated area currently not vegetated; [2] determined by irrigated vegetated area and the regional irrigation efficiency

higher up in the atmosphere.

There are many other less direct effects. A change in water vapour profile may affect convection, cloud formation and precipitation which could ultimately lead to a decrease in atmospheric water vapour. The same holds for a change in the temperature profile which may affect the saturation mixing ratio of water vapour, convection, cloud formation, precipitation, etc. Sacks et al. (2009) concluded that indirect effects such as a change in cloud cover have an impact at least comparable in magnitude to the evaporative cooling of the surface.

Moreover, there are some important regional processes such as the South and East Asian monsoon which can directly be affected by irrigation (Douglas et al., 2009; Lee et al., 2009; Saeed et al., 2009; Niyogi et al., 2010; Saeed et al., 2013; Tuinenburg et al., 2014). To maintain the level of complexity in our analysis as low as possible, we will mainly focus on the two above effects and compare the surface values of irrigation water, surface temperature and heat fluxes and the profiles of atmospheric temperature and specific humidity between irrigation and reference simulations.

5.3. Results

5.3.1. Influence of surface-atmosphere coupling

The way the land surface is coupled to the atmosphere strongly affects the simulated irrigation. The global gross irrigation water requirement ranges between $393\,km^3a^{-1}$ (P_{I1}) and $1202\,km^3a^{-1}$ (S_{I1}), so that the water requirements simulated with the flux aggregation schemes are roughly three times larger than in the simulation using the parameter aggregation scheme (Table 7, Fig. 26).

The amount of water donated via irrigation in S_{I1} ($1202\,km^3a^{-1}$) and V_{I1} ($1164\,km^3a^{-1}$) is in much better agreement with other studies (e.g. Yoshikawa et al. (2013) and references therein). The gross irrigation requirement constitutes only a very rough approximation of the amount of water that has an impact on the simulated climate. A significant fraction of the water used for irrigation results in an increase in surface runoff and drainage and, in the present model setup, does not have an effect on the simulated climate. In order to evaluate the amount of climate relevant irrigation water, the differences in evapotranspiration between the irrigation run and the reference run are compared. These can be used as a proxy for the net irrigation requirement as the difference between potential evapotranspiration and evapotranspiration that would occur without irrigation (Döll and Siebert, 2002). For Δ_{PI1} and Δ_{VI1} the additional evapotranspiration in the irrigation run becomes even larger than the initial amount of water applied at the surface. This is because irrigation induces an increase in precipitation, that increases soil moisture, which in turn also increases evapotranspiration in the non-irrigated share of the grid box.

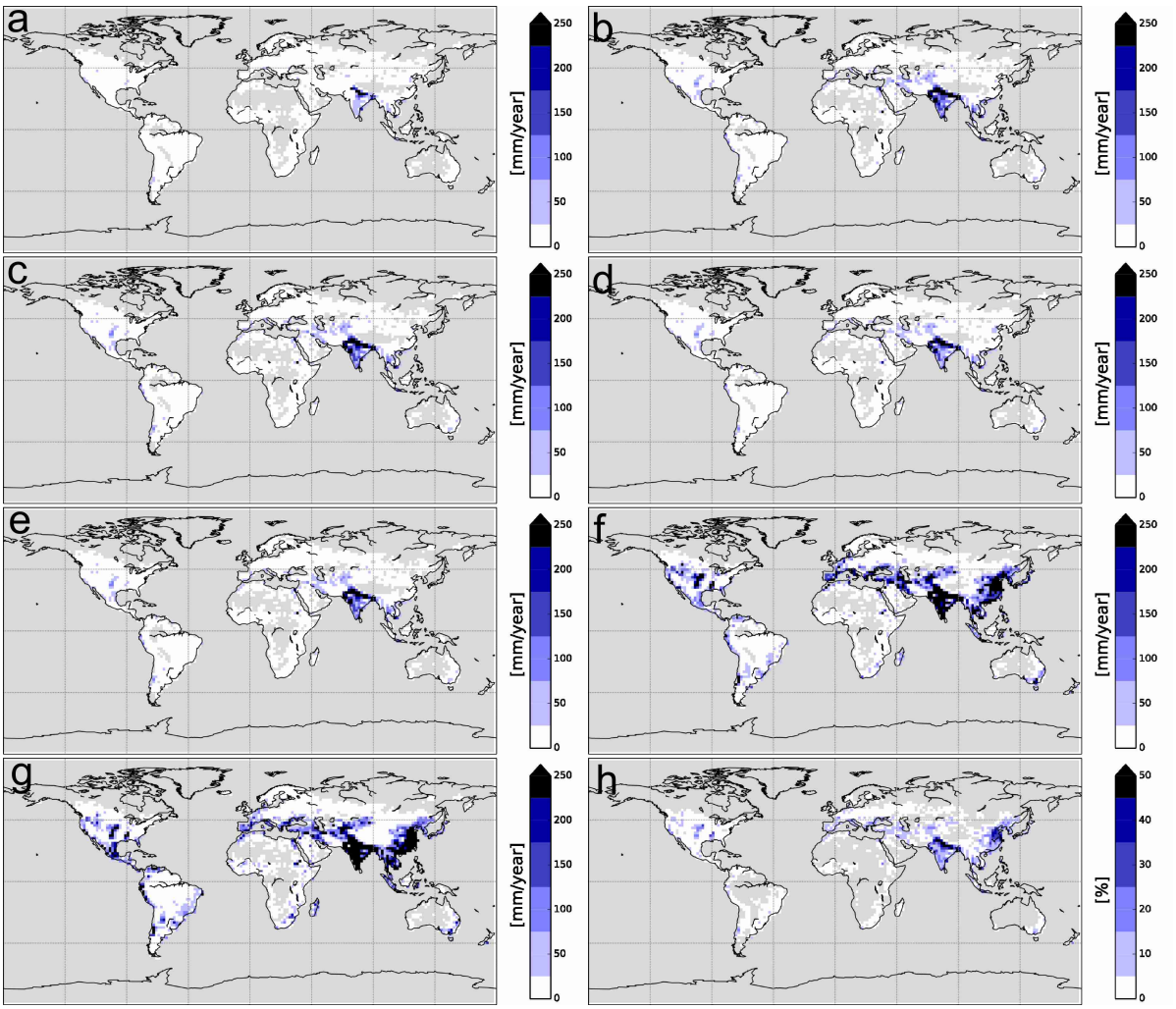

Figure 26: 20-year mean annual gross irrigation water donation a) P_{I1} b) S_{I1} c) V_{I1} d) V_{I2} e) V_{I3} f) V_{I4} g) V_{I5}; h) Cover fraction of the irrigated crop tile (P_{I1}, S_{I1}, V_{I1}), regions where the surface fraction covered by irrigated areas < 0.1 % have been masked

The integrated net vertical moisture flux, i.e. evapotranspiration minus precipitation, can be used as a measure that accounts for irrigation induced changes in precipitation (Table 7). When comparing differences between the irrigation simulations and the reference simulations with respect to the integrated net vertical moisture flux in irrigated grid boxes, the differences between Δ_{PI1}, Δ_{SI1} and Δ_{VI1} are even more pronounced than the differences in (gross) global annual irrigation water requirement. For Δ_{PI1} the difference in (upward) net vertical moisture flux can actually become negative, meaning that the increase in precipitation due to irrigation is larger than the increase in evapotranspiration. For the simulations with the flux aggregation schemes the differences in the net moisture flux are much closer to the amount of water donated via irrigation. Here, the increase in the net moisture flux in Δ_{VI1} is substantially larger than in Δ_{SI1} despite a smaller amount of water used in irrigation. Thus, the ratio between difference in net flux and gross irrigation donation are quite different between Δ_{SI1} (0.72) and Δ_{VI1} (0.88),

IRRIG. - REF.	Δ_{PI1}	Δ_{SI1}	Δ_{VI1}	Δ_{VI2}	Δ_{VI3}	Δ_{VI4}	Δ_{VI5}
DJF gross irrigation $[km^3]$	100	216	214	183	164	1137	1079
MAM gross irrigation $[km^3]$	169	482	472	426	405	1784	2154
JJA gross irrigation $[km^3]$	103	400	382	313	318	1857	2409
SON gross irrigation $[km^3]$	21	104	96	97	95	1454	1181
annual gross irrigation $[km^3]$	393	1202	1164	1020	983	6232	6823
$ET_{IRR} - ET_{REF}$ $[km^3\,a^{-1}]$	405	1125	1223	863	944	3030	3442
vertically integrated net moisture flux $[km^3\,a^{-1}]$	-59	864	1019	652	560	2010	2453
temperature bias $[K]$	-0.07 (0.00)	-0.08 (-0.08)	-0.02 (-0.17)	-0.04 (-0.12)	-0.03 (-0.09)	-0.13 (-0.28)	-0.08 (-0.22)
precip. bias $[mm\,d^{-1}]$	-0.01 (0.03)	0.01 (0.03)	-0.01 (0.01)	-0.02 (-0.00)	-0.01 (-0.01)	-0.02 (0.01)	-0.01 (0.01)

Table 7: Irrigation water requirements; Mean difference between irrigation and non-irrigation run in 'evapotranspiration-precipitation' $[km^3\,a^{-1}]$ for grid boxes in which irrigated fraction $> 1\,\%$; Difference in bias (comparison with WFD) between irrigation and reference run land surface mean (SA-REGION)

which indicates that the way water is introduced into the atmosphere differs substantially between the two coupling schemes.

Consequently, the coupling scheme strongly influences the magnitude of the impact of irrigation on the simulated climate, in particular in South and Southeast Asia, i.e. $40°E$ - $130°E$; $0°$ - $45°N$ (SA-REGION), which comprise about 70 % of the world's irrigated areas and constitute about 73 % of the agricultural water demand (Tatalovic, 2009) (Fig. 27; Table 8).

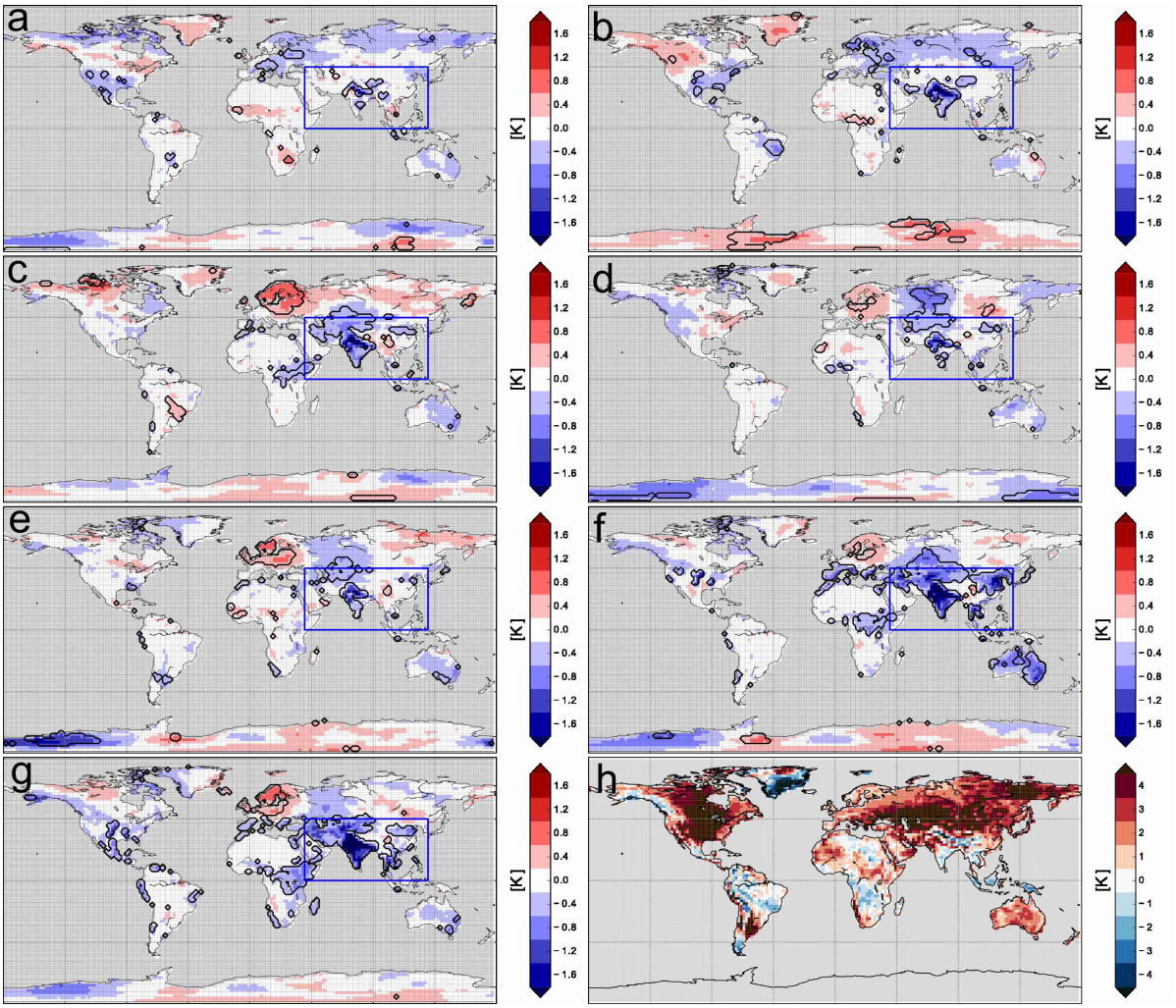

Figure 27: 20-year mean differences in surface temperature between irrigation run and reference run a) Δ_{PI1} b) Δ_{SI1} c) Δ_{VI1} d) Δ_{VI2} e) Δ_{VI3} f) Δ_{VI4} g) Δ_{VI5}; grid box mean; black outlines give areas in which differences are robust; blue rectangle denotes the SA-REGION; h) 20-year mean bias in 2m temperature in the standard operational model setup (ensemble of 5 simulations with parameter aggregation scheme, no irrigation)

Δ_{PI1}, Δ_{SI1} and Δ_{VI1} exhibit a reduction in the global (land) surface temperatures of between $-0.04\,K$ (Δ_{VI1}) and $-0.08\,K$ (Δ_{PI1}), which is in agreement to other global modelling studies (e.g. Puma and Cook (2010) and references therein). Here, the three

IRR. - REF. *Global mean (SA-REGION)*	Δ_{PI1}	Δ_{SI1}	Δ_{VI1}	Δ_{VI2}	Δ_{VI3}	Δ_{VI4}	Δ_{VI5}
surface temp. $[K]$	-0.08 (-0.05)	-0.07 (-0.23)	-0.04 (-0.28)	-0.08 (-0.21)	-0.06 (-0.16)	-0.21 (-0.65)	-0.20 (-0.69)
temp. 2m $[K]$	-0.08 (-0.05)	-0.05 (-0.17)	-0.03 (-0.23)	-0.07 (-0.16)	-0.05 (-0.12)	-0.17 (-0.53)	-0.16 (-0.55)
srf. net rad. sh. $[W\,m^{-2}]$	-0.13 (-0.06)	-0.24 (-0.59)	-0.21 (-0.93)	-0.18 (-0.30)	-0.18 (-0.58)	-0.70 (-1.51)	-0.66 (-1.53)
srf. net rad. lg. $[W\,m^{-2}]$	0.12 (-0.05)	0.38 (1.33)	0.48 (2.17)	0.36 (1.02)	0.36 (1.42)	1.44 (4.07)	1.29 (4.51)
sens. heat flux $[W\,m^{-2}]$	-0.18 (-0.34)	-0.53 (-1.95)	-0.73 (-2.15)	-0.59 (-1.42)	-0.51 (-1.44)	-1.63 (-4.09)	-1.76 (-5.11)
lat. heat flux $[W\,m^{-2}]$	0.18 (0.23)	0.67 (2.69)	0.98 (3.37)	0.75 (2.14)	0.69 (2.26)	2.37 (6.64)	2.40 (8.11)
evapotrans. $[mm\,d^{-1}]$	0.01 (0.01)	0.02 (0.09)	0.03 (0.12)	0.03 (0.08)	0.02 (0.08)	0.08 (0.22)	0.08 (0.28)
precipitation $[mm\,d^{-1}]$	0.01 (0.01)	0.00 (0.03)	0.01 (0.04)	0.00 (0.01)	0.01 (0.04)	0.05 (0.09)	0.04 (0.11)
vrt. int. w. vap. $[kg\,m^{-2}]$	-0.01 (-0.09)	0.01 (0.09)	0.11 (0.38)	0.03 (0.09)	0.03 (0.20)	0.24 (0.60)	0.17 (0.64)
soil moisture $[m]$	0.00 (-0.00)	0.00 (0.01)	0.01 (0.02)	0.00 (0.02)	0.00 (0.02)	0.01 (0.03)	0.01 (0.03)

Table 8: Global land surface mean difference (SA-REGION) between irrigated run and reference run

coupling schemes produce comparable results. However, in the SA-REGION, Δ_{PI1}, Δ_{SI1} and Δ_{VI1} are much more different. Here, Δ_{VI1} shows a surface cooling of $-0.28\,K$, which is about one fifth larger than for Δ_{SI1} and almost six times more pronounced than for Δ_{PI1}. For the sensible and latent heat fluxes the ratios between Δ_{PI1}, Δ_{SI1} and Δ_{VI1} are in the same order of magnitude. On the land surface Δ_{VI1} exhibits an average increase in evapotranspiration of $0.03\,mm\,d^{-1}$ which is three times larger than the increase in precipitation ($0.01\,mm\,d^{-1}$), so that due to irrigation, the vertically integrated water vapour (IWV) increases by $0.11\,kg\,m^{-2}$. In the SA-REGION there is an increase in evapotranspiration of $0.12\,mm\,d^{-1}$, an increase in precipitation of $0.04\,mm\,d^{-1}$ and the IWV increases by $0.38\,kg\,m^{-2}$. Also on a global average, including the ocean surface (not shown), the IWV increases by $0.06\,kg\,m^{-2}$. In this respect, Δ_{VI1} behaves very different to Δ_{SI1} and Δ_{PI1}. For the IWV in the SA-REGION Δ_{SI1} is about 4 times smaller than Δ_{VI1}. Averaged over the entire land surface, the increase in IWV is about 20 times smaller than in Δ_{VI1} and when taking into account the ocean surface, both Δ_{SI1} and Δ_{PI1} indicate a drying of the atmosphere due to irrigation. Additionally Δ_{PI1} shows a decrease in IWV over land and in the SA-REGION.

In the following, the ratio of the ensemble mean impact, given by the mean of Δ_{PI1}, Δ_{SI1} and Δ_{VI1}, and the respective ensemble spread ($\mathrm{REMS_{IPSV1,R}}$), is used to evaluate the extent to which the land surface-atmosphere coupling determines the impact of irrigation on a given variable:

$$REMS_{ensemble} = \frac{n^{-1} \cdot \sum_{j=1}^{n} (I_j - R_j)}{max\,\{I_1 - R_1, .., I_n - R_n\} - min\,\{I_1 - R_1, .., I_n - R_n\}} \tag{31}$$

Here, $\mathrm{I_j}$ pertains to a given irrigation simulation and $\mathrm{R_j}$ to the respective reference simulation. It should be noted that the REMS does not constitute a comprehensive quantitative statistical measure as the sampling, i.e. the design of the individual simulations, was arbitrary, thus the sample does not represent the entire population (of possible simulations). Nonetheless, the REMS can be used as a qualitative indicator for possible uncertainties. A large (>1) REMS signifies that the ensemble mean impact is larger than the spread across the impacts and the coupling scheme only has a minor effect on the simulated impact of irrigation. Accordingly, a small ratio indicates that uncertainties with respect to the coupling scheme are large. A REMS substantially smaller than 0.5 indicates that not only the magnitude of a possible impact is uncertain but also its direction, i.e. whether it pertains to an increase or a decrease.

For the entire land surface, the $\mathrm{REMS_{IPSV1,R}}$ of the investigated variables ranges between 0.28 and 1.85 with an average of 1.07. This indicates that, even though there is a certain amount of variation between Δ_{PI1}, Δ_{SI1} and Δ_{VI1}, the impact of simulated irrigation on the investigated variables is on average larger than the uncertainty due to differences in the surface-atmosphere coupling (Table 9). However, for some of the variables this is not the case, most prominently evapotranspiration and IWV. For IWV the respective $\mathrm{REMS_{IPSV1,R}}$ is only 0.28 and the spread between Δ_{PI1}, Δ_{SI1} and Δ_{VI1} is almost four

/REMS/; average of entire land surface (SA-REGION)	Δ_{PI1}, Δ_{SI1}, Δ_{VI1}	Δ_{VI1}, Δ_{VI2}, Δ_{VI3}, Δ_{VI4}, Δ_{VI5}	*All simulations*
surface temp. [/]	1.61 (0.79)	0.70 (0.75)	0.62 (0.50)
temp. 2m [/]	1.00 (0.86)	0.66 (0.73)	0.60 (0.52)
surf. net rad. sh. [/]	1.85 (0.61)	0.74 (0.79)	0.58 (0.54)
surf. net rad. lg. [/]	0.91 (0.52)	0.72 (0.75)	0.48 (0.45)
sens. heat flux [/]	0.87 (0.82)	0.83 (0.77)	0.53 (0.49)
latent heat flux [/]	0.77 (0.67)	0.83 (0.75)	0.52 (0.46)
evapotrans. [/]	0.77 (0.67)	0.84 (0.76)	0.52 (0.46)
precipitation [/]	1.56 (0.93)	0.56 (0.78)	0.40 (0.51)
vrt. int. w. vap. [/]	0.28 (0.26)	0.57 (0.70)	0.33 (0.37)
soil moisture [/]	1.06 (0.77)	1.14 (1.63)	0.66 (0.67)

Table 9: |REMS|; average of entire land surface (SA-REGION)

times larger than their mean. This low value of $\mathrm{REMS}_{\mathrm{IPSV1,R}}$ well reflects that between Δ_{PI1}, Δ_{SI1} and Δ_{VI1} there is no agreement on whether the atmosphere becomes on average drier or moister due to irrigation. For the SA-REGION, the $\mathrm{REMS}_{\mathrm{IPSV1,R}}$ of none of the investigated variables is larger than 1 (on average 0.69) and the impact of simulated irrigation on any of the variables is smaller than the uncertainty due to differences in the coupling scheme.

Consequently, also the fraction of the land surface which is robustly affected by irrigation differs largely between Δ_{VI1}, Δ_{SI1} and Δ_{PI1} (Table 10). A given impact Δ_X ($X \in \{$ *PI1*, *SI1*, *VI1*$\}$) is considered to be robust if, in a student's t test (with $p < 0.05$), Δ_X is statistically significant and also larger than the internal model variability. The internal model variability was taken as the maximum intra-ensemble spread derived from three five-member ensembles simulated with ECHAM/JSBACH (de Vrese and Hagemann, 2015). Depending on the variable considered, Δ_{VI1} constitutes a robust impact in between 4.9 % and 13.2 % of the land surface (on average 10.5 %) and in the SA-REGION, Δ_{VI1} is robust in between 13.7 % and 36.0 % of the land surface (on average 26.5 %). Here, the fraction of the land surface robustly impacted by irrigation is on global average [SA-REGION] about 19 % [38 %] smaller in Δ_{SI1} and about 66 % [81 %] smaller in Δ_{PI1} than in Δ_{VI1}.

As reasoned in section 5.2, changes in atmospheric water vapour constitute a key factor for the impact of irrigation on simulated climate. Therefore, the large differences in IWV between Δ_{VI1}, Δ_{SI1} and Δ_{PI1} indicate that also the impact on the state of the atmospheric column differs largely between the three coupling schemes (Fig. 28). For Δ_{PI1} the increase in precipitation is larger than the increase in evapotranspiration and the atmosphere is actually drier in the irrigation run, especially in regions featuring a large share of irrigated areas. Consequently, for Δ_{PI1} the specific humidity is lower in the irrigation run throughout the entire atmospheric column. Furthermore, the vertical column is consistently colder. Here, the strongest cooling does not appear close to the surface, where the evaporative cooling effect is the strongest, but higher up in the atmosphere. This indicates that the evaporative surface cooling and the corresponding decrease in sensible heat flux are not exclusively responsible for the cooling of the atmosphere.

In Δ_{PI1} the decrease in atmospheric temperature due to the reduction of sensible heat flux is not balanced by a condensational heat release. With lower temperatures in the atmosphere, the relative humidity close to the surface increases by up to 0.75 % (not shown), while the saturation specific humidity in the atmosphere is lower in the irrigation scenario. This leads to increased precipitation and an increase in low and medium (cumulus) cloud cover, by up to 0.9 % on the lower atmospheric levels (not shown). Therefore, more incoming solar radiation is reflected by clouds which consequently leads to a reduction of energy available at the surface. With less energy available at the surface, the increase in evapotranspiration due to irrigation is smaller than the increase in precipitation which results in a lower specific humidity, by up to $-0.015\,g\,kg^{-1}$, also

IRR. - REF. *Area [%] robustly affected; Global mean (SA-REGION)*	Δ_{PI1}	Δ_{SI1}	Δ_{VI1}	Δ_{VI2}	Δ_{VI3}	Δ_{VI4}	Δ_{VI5}
surface temp.	3.0 (6.0)	6.6 (16.3)	10.6 (32.8)	5.5 (16.5)	6.8 (15.8)	16.8 (50.3)	16.8 (49.4)
temp. 2m	2.7 (5.9)	6.1 (15.3)	10.2 (31.6)	4.6 (13.6)	5.7 (12.6)	15.9 (49.3)	15.9 (47.5)
surf. net rad. short	3.4 (3.0)	7.1 (8.3)	8.8 (18.3)	5.3 (3.1)	4.9 (3.4)	11.8 (27.8)	11.8 (36.3)
surf. net rad. long	3.5 (3.4)	10.0 (20.0)	13.2 (36.0)	6.2 (8.9)	8.2 (16.2)	23.6 (57.5)	19.0 (62.9)
sens. heat flux	4.4 (6.5)	10.2 (22.7)	11.1 (30.2)	6.8 (15.4)	7.6 (15.7)	18.8 (45.4)	17.5 (49.7)
latent heat flux	4.0 (7.0)	10.7 (25.5)	12.0 (31.4)	7.4 (17.8)	8.3 (20.2)	19.8 (46.6)	20.1 (55.2)
evapotrans.	4.0 (7.0)	10.7 (25.6)	12.1 (31.4)	7.5 (17.9)	8.3 (20.3)	19.8 (46.5)	20.0 (55.1)
precipitation	1.7 (3.2)	4.2 (10.3)	4.9 (13.7)	2.3 (3.2)	3.1 (5.0)	8.0 (18.4)	7.3 (26.2)
vrt. int. w. vap.	3.9 (0.0)	8.4 (8.3)	10.7 (28.3)	5.5 (3.2)	4.4 (5.9)	18.4 (40.7)	17.3 (53.2)
soil moisture	5.0 (8.8)	10.8 (28.6)	10.9 (33.0)	8.3 (26.7)	9.3 (26.6)	15.9 (42.7)	15.5 (42.7)

Table 10: Share of land surface area exhibiting robust differences between irrigated run and reference run; Global mean (SA-REGION)

higher up in the atmosphere. This results in a reduction of condensational heating and in cloud cover higher up in the atmosphere, which in turn reduces the amount of radiation absorbed and thus temperatures, by as much $-0.06\,K$. Besides an absence of an increase in low cloud cover, comparable results can be found for the entire land surface, even though they are much less pronounced. This suggests that, especially in strongly irrigated regions, the two main mechanisms discussed in section 5.2 are not the dominant ones in P_{I1}.

In contrast Δ_{VI1} and Δ_{SI1} exhibit results that are consistent with these mechanisms, i.e. a strong increase in atmospheric water vapour, a strong evaporative cooling at the surface, and a less pronounced cooling or possibly a warming higher up in the atmosphere. However, for Δ_{VI1} the respective effects are much more pronounced. In the SA-REGION Δ_{VI1} shows an increase in specific humidity in the atmosphere due to irrigation of up to $0.19\,g\,kg^{-1}$ close to the surface and still about $0.02\,g\,kg^{-1}$ at around $6000\,m$. With respect to specific humidity Δ_{SI1} has a maximum of $0.1\,g\,kg^{-1}$ close to the surface and actually shows a decrease at $6000\,m$. Thus, even close to the surface, where Δ_{VI1} and Δ_{SI1} both indicate an increase in specific humidity due to irrigation, this increase is almost twice as pronounced in Δ_{VI1}. Averaged over the entire land surface, the increase in specific humidity is much smaller, with up to $0.055\,g\,kg^{-1}$ in Δ_{VI1}. Here, the ratio between Δ_{VI1} and Δ_{SI1} is even larger, and close to the surface Δ_{VI1} is more than three times larger than Δ_{SI1}.

Δ_{VI1} and Δ_{SI1} also differ with respect to the temperature profile. In the SA-REGION, the evaporative cooling effect close to the surface in Δ_{VI1} ($-0.22\,K$) is more than two thirds larger than in Δ_{SI1}. Above $6000\,m$, Δ_{VI1} shows temperatures which are by up to $0.06\,K$ warmer in the irrigation run. Here, the latent heat release due to condensation in combination with the increase in radiation absorbed by clouds dominates any cooling effects related to a decrease in the surface sensible heat flux. This behaviour can not be found in Δ_{SI1}. Even though the temperature decrease becomes less pronounced with increasing height, the irrigation run consistently exhibits lower temperatures in the atmosphere. Thus, while Δ_{VI1} and Δ_{SI1} exhibit similar tendencies, these are roughly twice as pronounced in Δ_{VI1}.

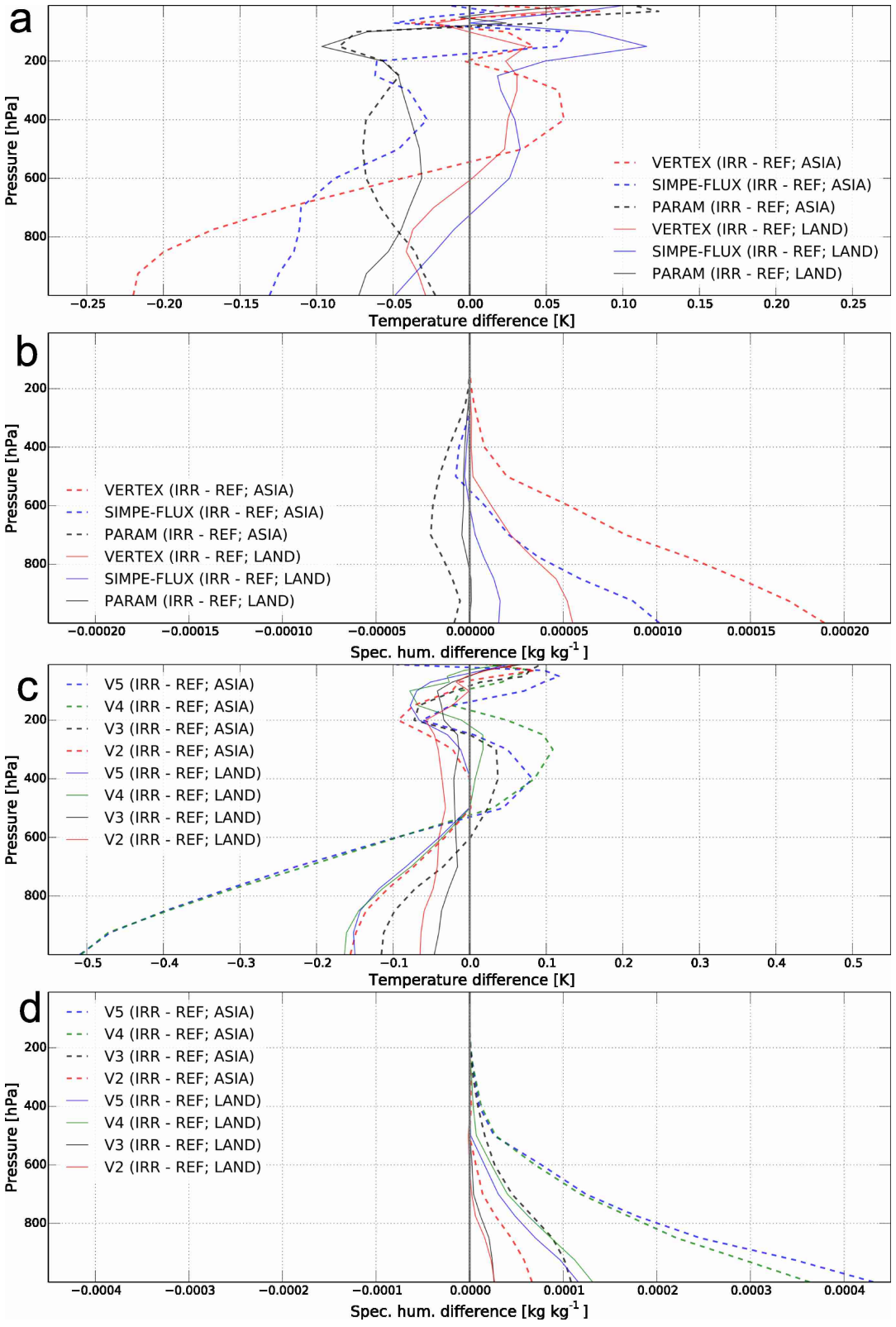

Figure 28: 20-year mean differences between irrigation runs P_{I1}, S_{I1}, V_{I1} and reference runs P_R, S_R, V_R a) temperature b) specific humidity and 20-year mean differences between irrigation runs V_{I2}-V_{I5} and reference run V_R c) temperature d) specific humidity; dashed lines refer to the SA-REGION, solid lines to the entire land surface

The coupling schemes used for S_{I1} and V_{I1} treat the vertical mixing process differently, even though both are based on an aggregation of the surface fluxes. When resolving the turbulent mixing process with respect to sub-grid scale heterogeneity (V_{I1}), the air-properties within the individual tiles are being vertically mixed at rates that depend on the local stability. Due to the convergence of the tile individual states with height, the atmospheric column within the warmer tiles is predominantly less stable than in the colder tiles which facilitates the vertical mixing. A stronger vertical exchange within the relatively warmer and drier tiles means that initially more sensible heat relative to moisture is being transported upwards away from the surface, while relatively more moisture remains in the near surface layers. This results in a higher relative humidity within the lower parts of the atmosphere, more cloud cover due to convection and consequently more precipitation in V_{I1} than in $S_{1,0}$.

The increase in precipitation is about a third larger for Δ_{VI1} than for Δ_{SI1}. As precipitation is not resolved with respect to the tiles, it also increases the plant available water in the non-irrigated tiles of the grid box. Δ_{VI1} shows an average increase in the grid box mean soil moisture of $0.02\,m$, which is roughly twice as large as the moisture increase due to irrigation for Δ_{SI1}. As this strongly affects vegetation, the increase in the vegetated fraction, especially in the SA-REGION, is about one third larger for Δ_{VI1} (on global average 1.0 % and in the SA-REGION 4.0 %) than for Δ_{SI1} (on global average 0.7 % and in the SA-REGION 2.6 %). Due to the increased availability of water in the non-irrigated tiles of the grid box and the increase in the vegetated fraction, there is a strong increase in the grid box mean evapotranspiration for Δ_{VI1}, which is about one third larger than the increase in evapotranspiration for Δ_{SI1}. Thus, the local recycling of moisture is more pronounced when using the *VERTEX* coupling scheme.

Additionally, there are some minor differences in wind patterns (not shown), which result in differences in the spatial distribution of precipitation. The fraction of precipitation which occurs over ocean surfaces is larger for Δ_{SI1} than for Δ_{VI1}. This fraction of precipitation has no positive feedback on evapotranspiration so that the increase of atmospheric water vapour for Δ_{SI1} is substantially smaller than for Δ_{VI1}.

To estimate whether representing irrigation in ECHAM/JSBACH results in improved simulations, these are compared to WATCH Forcing Data (WFD) (Weedon et al., 2011) (e.g. Fig. 27 h). In regions featuring large shares of irrigated areas such as the SA-REGION, the impact of representing irrigation on the inherent model bias strongly depends on the coupling scheme used for the simulation (Table 7). When using a parameter aggregation scheme, both temperature and precipitation bias increase, i.e. for 2m temperature by $0.003\,K$ ($< 1\,\%$) and for precipitation by $0.032\,mm\,d^{-1}$ ($\approx 3\,\%$). When using a simple flux aggregation scheme the temperature bias decreases by $-0.081\,K$ ($\approx 3\,\%$) but the precipitation bias increases by $0.034\,mm\,d^{-1}$ ($\approx 4\,\%$). For the SA-REGION the best results in comparison to WFD are achieved with the VERTEX coupling scheme. The temperature bias decreases by $-0.165\,K$ ($\approx 7\,\%$) which is about twice the decrease with respect to the simple flux scheme. For the VERTEX scheme the

precipitation bias in the SA-REGION increases by only $0.006\,mm\,d^{-1}$ ($\approx 1\,\%$) which is less than one fifth of the bias increase when using one of the other coupling schemes. Averaged over the entire land surface, the simulations with the parameter aggregation scheme and the VERTEX scheme both show an improvement for simulated precipitation and temperature, whereas the simulation with the simple flux aggregation scheme shows a clear improvement for temperature but an increase in the precipitation bias. However, here changes in the biases are much smaller than the changes in the SA-REGION.

5.3.2. Influence of irrigation characteristics

The assumed irrigation characteristics, especially the irrigation efficiency, greatly affect the simulated water requirements. The gross irrigation is roughly between five and seven times larger in the simulations assuming a low irrigation efficiency, i.e. $6232\,km^3a^{-1}$ in V_{I4} and $6823\,km^3a^{-1}$ in V_{I5}, than in the two simulations with a high irrigation efficiency ($1020\,km^3a^{-1}$ in V_{I2} and $983\,km^3a^{-1}$ in V_{I3}) and in V_{I1} and S_{I1} (Table 7, Fig. 26).

The gross irrigation for V_{I4} and V_{I5} is exceedingly large, which can be explained by an unrealistic increase in runoff and drainage. In reality, embankments prohibit runoff from inundated rice fields or the runoff is channelled to downstream fields. In the model these constructive constrains are not accounted for. Furthermore, a possible gross water requirement can be calculated based on the upper estimates of the specific water intake of irrigated areas ($17000\,m^3\,ha^{-1}\,a^{-1}$ for Asia, South and Central America and Africa; $10000\,m^3\,ha^{-1}\,a^{-1}$ for other regions (Shiklomanov, 2000)) and the potentially irrigated areas ($260 \cdot 10^6 ha$ in Asia, South and Central America and Africa; $60 \cdot 10^6\,ha$ in other regions (Siebert et al., 2013)). With about $5000\,km^3a^{-1}$, the resulting rough estimate of the potential gross irrigation water requirement is much closer to the scenarios based on a low irrigation efficiency than to any other simulation. A similar value of $5900\,km^3a^{-1}$ for the potential gross water requirements was found by Lobell et al. (2009).

The differences in the integrated net vertical moisture flux of the high efficiency scenarios are, with $652\,km^3a^{-1}$ in Δ_{VI2} and $560\,km^3a^{-1}$ Δ_{VI3}, between 3 and 4.5 times smaller than in Δ_{VI4} ($2010\,km^3a^{-1}$) and in Δ_{VI5} ($2453\,km^3a^{-1}$), so that the impact on the simulated climate due to irrigation can be expected to be exceedingly different between the simulations with a low irrigation efficiency and those assuming a high efficiency. The estimates of the irrigation induced increase in water vapour flow of the low efficiency simulations are in good agreement with other estimates, e.g. $2600\,km^3a^{-1}$ by Gordon et al. (2005).

In Δ_{VI2} the difference in integrated net vertical moisture flux is about 15.0 % smaller than in Δ_{VI3}, indicating that also the timing of irrigation may have an important impact on climate. However, in relative to the differences between simulations with a high and a low irrigation efficiency, the effects related to the timing of irrigation can be expected to be an order of magnitude smaller. The same is true for a comparison of Δ_{VI4} and Δ_{VI5}, with the difference in integrated net vertical moisture flux being about 20.0 % smaller

in Δ_{VI4}. There are also substantial differences in the seasonality of irrigation and the relative amount of water applied during spring and summer is more than a third larger in Δ_{VI5}. Therefore, also the impacts on climate due to irrigation are much larger in Δ_{VI5} than in Δ_{VI4} during these seasons (not shown). In turn Δ_{VI4} exhibits much larger relative irrigation amounts and consequently larger impacts during autumn and winter. Yet, a detailed seasonal comparison would go beyond the scope of this work. Thus, it should be acknowledged that also the differences between Δ_{VI2} and Δ_{VI3} and between Δ_{VI4} and Δ_{VI5} are not negligible but in order to give a rough estimate of possible uncertainties involved in modelling irrigation, it is sufficient to focus on the differences related to the irrigation efficiency.

As could be expected from the experimental setup, the impact of irrigation on the state of the surface is much more pronounced in the simulations with a low irrigation efficiency (See Fig. 27; Table 8). For most variables, Δ_{VI4} and Δ_{VI5} are about three to four times larger than Δ_{VI2} and Δ_{VI3}. On global average, the decrease in (land) surface temperature ranges between roughly $-0.07\,K$ (Δ_{VI2} and Δ_{VI3}) and $-0.21\,K$ (Δ_{VI4} and Δ_{VI5}). Here, the cooling in the two low irrigation efficiency scenarios is also substantially larger than in Δ_{PI1}, Δ_{SI1} and Δ_{VI1}. However, it is well within the bounds estimated for extreme irrigation scenarios, e.g. Lobell et al. (2006b) estimated an possible cooling of the land surface by $-1.31\,K$ due an irrigation of all cropland. In the SA-REGION the respective values range between $-0.16\,K$ (Δ_{VI3}) and $-0.69\,K$ (Δ_{VI5}). For the IWV the differences between the simulations with high and low efficiency are even more pronounced. Here, Δ_{VI2} and Δ_{VI3}, with an increase of about $0.03\,kg\,m^{-2}$, are about eight times smaller than Δ_{VI4}. In the SA-REGION Δ_{VI3} is still about six times smaller than Δ_{VI4}. Here, Δ_{VI3} is also less than half as large as Δ_{VI2}, which confirms that differences due to the timing of delivery are non-negligible, even though they are much smaller than the differences related to the irrigation efficiency.

For the land surface, the uncertainty with respect to the representation of irrigation characteristics is even larger than the uncertainty due to differences in coupling scheme. With the exception of soil moisture, the $\mathrm{REMS}_{\mathrm{IV1\text{-}5,R}}$ of none of the variables is larger than 1 and the $\mathrm{REMS}_{\mathrm{IV1\text{-}5,R}}$ predominantly ranges between 0.6 and 0.85 (on average 0.76) (Table 9). In the SA-REGION the values of $\mathrm{REMS}_{\mathrm{IV1\text{-}5,R}}$ are slightly higher (average 0.84), still the uncertainties, i.e. the ensemble spread, are much larger than the ensemble mean impact of simulated irrigation.

It is noteworthy that the variable with the highest $\mathrm{REMS}_{\mathrm{IV1\text{-}5,R}}$ is soil moisture (1.14 for the land surface and 1.63 for the SA-REGION). The prescribed irrigated area and the target soil moisture vary strongly between Δ_{VI2}, Δ_{VI3}, Δ_{VI4} and Δ_{VI5} which would be expected to result in large uncertainties with respect to soil moisture, i.e. a low $\mathrm{REMS}_{\mathrm{IV1\text{-}5,R}}$. Nonetheless, in the SA-REGION the spread in soil moisture, resulting from differences in irrigation efficiency, is actually smaller than the ensemble spread related to differences in the coupling schemes. This indicates that the soil moisture differences in the non-irrigated tiles that result from differences in the atmospheric feed-

back, most importantly precipitation (see Sec. 5.3.1), introduce a larger inter-simulation soil moisture variability than the differences in the simulated irrigation practice (timing of irrigation, target soil moisture and irrigated non-vegetated fraction).

The fraction of the land surface robustly affected by irrigation, differs largely between Δ_{VI2}, Δ_{VI3}, Δ_{VI4} and Δ_{VI5} (Table 10). Depending on the variable considered, for Δ_{VI4} irrigation robustly impacts between 8.0 % and 23.6 % (on average 16.9 %) and for Δ_{VI5} between 7.3 % and 20.0 % (on average 16.1 %). In the SA-REGION, Δ_{VI4} is robust in between 18.4 % and 57.5 % (on average 42.5 %) and for Δ_{VI5} between 26.2 % and 62.9 % (on average 47.8 %). Here, the fraction of the land surface robustly impacted by irrigation is on global average [SA-REGION] about 65 % [74 %] smaller for Δ_{VI2} and about 51 % [70 %] smaller for Δ_{VI3} than for Δ_{VI4} [Δ_{VI5}].

Not only the state of the surface but also the state of the atmosphere is strongly influenced by the representation of irrigation characteristics (Fig. 28). In the SA-REGION, effects due to irrigation in all the scenarios are similar to the effects in V_{I1}, i.e. an increase in atmospheric water vapour, a cooling in the lower atmosphere, and a less pronounced cooling or possibly a warming higher up. However, Δ_{VI2}, Δ_{VI3}, Δ_{VI4} and Δ_{VI5} exhibit exceedingly different magnitudes. The largest differences can be found between the simulations with a high and those with a low irrigation efficiency, but there are also distinct differences due to the timing of irrigation, i.e. between Δ_{VI2} and Δ_{VI3}. For example, in the SA-REGION Δ_{VI3} with respect to specific humidity is about 50 % larger than Δ_{VI2}. Also there are distinct differences between Δ_{VI4} and Δ_{VI5}, but these are related to the seasonality of the impacts (Fig. 29). For example, when comparing differences in atmospheric winter temperature in the SA-REGION, Δ_{VI4} is about 2.5 times larger than Δ_{VI5}. With respect to specific humidity during Autumn in the SA-REGION, Δ_{VI4} is also about 50 % larger than Δ_{VI5}.

For the annual means, the largest impact on the atmospheric specific humidity can be found for Δ_{VI5}, with an increase of over $0.4\,g\,kg^{-1}$ close to the surface. This increase is not only about five times larger than in Δ_{VI2}, but also more than twice as large as in Δ_{VI1}. For temperatures in the lower atmosphere, the largest impact can also be seen in Δ_{VI5}. Close to the surface Δ_{VI5} gives a cooling of more than $0.5\,K$ which is about 4.5 times larger than in Δ_{VI3} and more than twice as large as in Δ_{VI1}. Higher up in the atmosphere, Δ_{VI4} gives a warming due to irrigation of about $0.1\,K$, whereas Δ_{VI3} indicates a much smaller temperature increase and in Δ_{VI2} temperatures are colder throughout the entire vertical column.

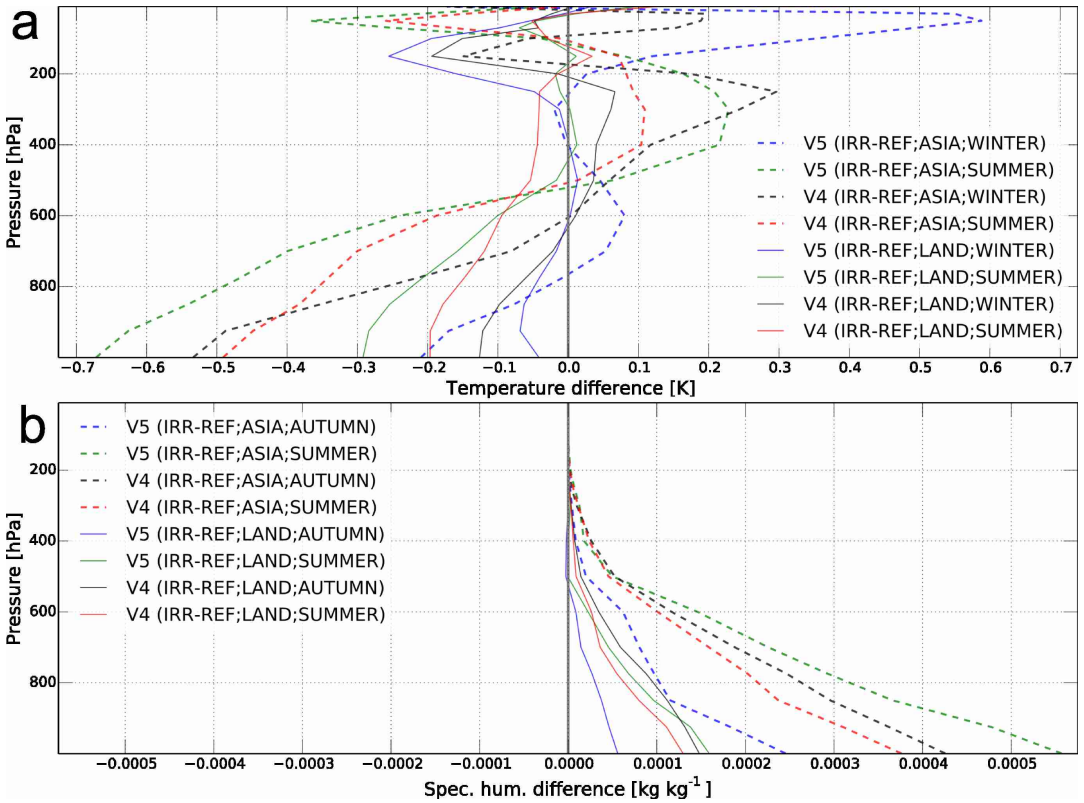

Figure 29: 20-year seasonal mean differences between irrigation runs V_{I4} and V_{I5} and reference run V_R a) winter and summer temperature b) autumn and summer specific humidity; dashed lines refer to the SA-REGION, solid lines to the entire land surface

The simulated temperature improves in all irrigation experiments using the VERTEX scheme (Table 7). The bias reduction (land surface average) for a low irrigation efficiency is ($-0.126\,K$ in Δ_{VI4} and $-0.081\,K$ in Δ_{VI5}) between two and three times larger than for a high irrigation efficiency ($-0.044\,K$ in Δ_{VI2} and $-0.033\,K$ in Δ_{VI3}). Here, a bias reduction of $-0.126\,K$ corresponds to a relative bias reduction of about 5 %. The simulations also exhibit an improvement of the simulated precipitation on the land surface, which is largest in Δ_{VI2} and Δ_{VI4} ($-0.02\,mm\,d^{-1} \approx 3\,\%$). For the SA-REGION the largest improvement of simulated temperatures, can be found for Δ_{VI4} ($-0.276\,K \approx 13\,\%$). However, the respective precipitation bias in the SA-REGION slightly increases ($0.009\,mm\,d^{-1} \approx 1\,\%$). As the relative increase in precipitation bias in the SA-REGION is much smaller than the decrease in the precipitation bias, the simulations that use the VERTEX coupling scheme and that assume a low irrigation efficiency, especially Δ_{VI4}, give the best results in comparison to WFD.

5.4. Conclusion and Discussions

Irrigation plays an exceedingly important role with respect to food security, fresh water resources and climate. Hence, an accurate representation of irrigation in models is key for addressing issues related to the above topics. There are two main sources of uncer-

tainty when investigating the effects of irrigation with global climate models. One source is the model's structure and its parametrizations, which are not directly related to the representation of irrigation but which may severely affect the impact of irrigation on the simulated climate. The second source of uncertainty is the unreliability of data with respect to real world irrigation in combination with the need for simplifying assumptions in a model.

To address these uncertainties, the land surface model JSBACH was equipped with a scheme which represents irrigation by maintaining the soil moisture in irrigated areas at a certain threshold, i.e. for most simulations the level at which potential transpiration occurs. In order to estimate possible uncertainties with regard to the model's structure, an experiment was conducted in which different schemes were used for the land surface-atmosphere coupling (parameter aggregation, a simple flux aggregation and an improved flux aggregation scheme, the VERTEX scheme), while the irrigation characteristics were kept identical. A second experiment was conducted to estimate possible uncertainties related to the representation of irrigation characteristics. Here, the irrigation efficiency and the timing of delivery were modified. The irrigation efficiency was altered via the target soil moisture and the extent of the non-vegetated part of the grid box which is being irrigated. In the respective simulations, the coupling scheme and the actual share of the surface covered by irrigated crops, were kept the same.

With the first experiment it was shown that the magnitude of a possible impact of irrigation on climate depends strongly on the coupling scheme used. For example, in the simulation using the parameter aggregation scheme, only about 5 % of land surface in South and Southeast Asia (SA-REGION; $40°E$ - $130°E$; $0°$ - $45°N$) exhibit a robust impact due to irrigation, whereas this area constitutes about a quarter of the land surface for the VERTEX scheme.

Also, the effect on the mean state of the land surface differs substantially for the different coupling schemes. The average irrigation induced (land) surface cooling in the SA-REGION ranges between $-0.05\,K$ and $-0.28\,K$ and the increase in evapotranspiration between $0.01\,mm\,d^{-1}$ and $0.12\,mm\,d^{-1}$, while the impact on IWV ranges between a decrease of $-0.09\,kg\,m^{-2}$ and an increase of $0.38\,kg\,m^{-2}$. For many variables, the spread between the impacts simulated with the different coupling schemes, are larger than the ensemble mean impact. This indicates substantial uncertainties with respect to the model's coupling scheme. In some cases, this uncertainty is so large, that the simulations do not only disagree with respect to the magnitude of possible impacts, but also with respect to the direction of the impact. For example, in the SA-REGION both irrigation simulations with a flux aggregation scheme indicate a moister atmosphere than the respective reference simulations. In contrast, the atmosphere is drier in the irrigation simulation for the parameter aggregation scheme. In general, there is also a large disagreement between the simulations using the two flux aggregation schemes. Here, irrigation leads to a cooling of the surface and the lower atmosphere, a less pronounced cooling or even a warming higher up and a moister atmospheric column. However, these

effects are roughly twice as strong when using the VERTEX scheme. From the three coupling schemes, the VERTEX scheme is based on the most physical assumptions. Furthermore, for the SA-REGION, which features the largest share of irrigated areas, the VERTEX scheme clearly gives the best results in comparison to WFD. At the same time, the simulation with the VERTEX scheme exhibits the largest impacts of irrigation on the simulated climate. This indicates that in previous modelling studies which utilized a parameter or a simple flux aggregation scheme, these impacts may have been severely underestimated.

The second experiment shows that uncertainties related to the modelled irrigation characteristics, especially the irrigation efficiency, can even be larger than those related to the model's structure. In general the impact of irrigation on the state of the land surface is more than three times larger when assuming a low irrigation efficiency, than when a high efficiency is assumed. For example, the simulated (land) surface cooling in the SA-REGION ranges between $-0.16\,K$ and $-0.69\,K$. For some variables, such as the IWV, the impact is almost an order of magnitude larger, ranging between $0.09\,kg\,m^{-2}$ in the high efficiency simulations and $0.64\,kg\,m^{-2}$ in the low efficiency simulations.

For most of the investigated variables, the ratio between the mean impact and the spread between the simulated impacts, ranges between roughly 0.6 and 0.8. This indicates that uncertainties, introduced by the irrigation efficiency, are possibly much larger than the actual (mean) impact. For example, with respect to the atmospheric near surface temperature in the SA-REGION, the impacts of irrigation with a low and a high efficiency vary by roughly $0.4\,K$, whereas the largest difference between any irrigation simulation and the respective reference simulation in the first experiment was below $0.25\,K$. Furthermore, the share of the land surface robustly affected by irrigation ranges between 13 % (high irrigation efficiency) and 48 % (low irrigation efficiency).

An accurate representation of irrigation is especially relevant, as results indicate that a distinct share of the model temperature and precipitation bias could be related to the absence of irrigation within most Earth System Models. For example, ECHAM/JSBACH temperature bias (compared to WFD) in the SA-REGION was reduced by up to $0.28\,K$ $\approx$ 13 % in the irrigation simulations. This highlights the need for more detailed information on real world irrigation with respect to irritated areas, irrigation infrastructure and techniques as well as water availability on one hand, but also more sophisticated irrigation schemes that use region-, time-, technique- and crop-specific parametrisations.

6. Complementary studies

6.1. Blending height study - in addition to chapter 1

To assess the validity of the assumption of spatial homogeneity on the lowest atmospheric model level (in the Max Planck Institute for Meteorology's Earth System Model (MPI-ESM) located at roughly $30\,m$), blending heights were investigated globally in a preliminary study. In this qualitative study the blending height within a given model grid box is approximated by the characteristic length scales of the present sub-grid scale heterogeneity and the ratio of blending height and length scale provided in Sec. 1, i.e. roughly 1/100. The investigation focuses on surface heterogeneity related to variations in land cover, disregarding other aspects such as soil and hydrological characteristics.

To approximate the characteristic length scale of a given land cover type within a grid box, the horizontal extents of all clusters (homogeneous subareas) of the respective land cover type within the grid box need to be determined. These are derived from the Global Land Cover Map 2009 (GLOBCOVER) (Arino et al., 2012). The study aimed in particular at the land component of the Max Planck Institute for Meteorology's Earth System Model (JSBACH), with a standard resolution of T63, i.e. a grid-spacing of roughly $200\,km$. The resolution of $300 \times 300\,m$ of GLOBCOVER allows to resolve a T63 model grid box by approximately 390000 pixels (Fig. 30). From the 22 land cover classes employed in the dataset, 10 are selected and matched to the plant functional types (PFTs) that represent spatial sub-grid scale (SSGS) heterogeneity in the JSBACH setup used in this thesis. The procedure encompasses several simplifications as the GLOBCOVER classes have to be aggregated to more comprehensive groups which then need to be disaggregated to match the tiles in JSBACH (Table 11).

LCCS Class	*Group*	*PFT - JSBACH*
220	Glacier	Glaciers
40, 70, 170	Evergreen trees	Tropical evergreen trees, Extra-tropical evergreen trees
50, 60	Deciduous trees	Tropical deciduous trees, Extra-tropical deciduous trees
130	Shrubs	Raingreen shrubs, Deciduous shrubs
140	Grass / Pasture	c3 grass, c4 grass, c3 pasture, c4 pasture
14	Rainfed crops	Rainfed crops
11	Irrigated crops	Irrigated crops
20, 30, 90, 100, 110, 120, 150, 160, 180, 190, 200, 210	Not represented in JSBACH	

Table 11: Conversion of LCCS classes to JSBACH PFTs

For each pixel within a grid box the distance in $N-S$, $E-W$, $NW-SE$, $NE-SW-$

direction to the nearest point, constituting a different land cover class, is determined. These distances provide a rough estimate for the dimensions (in the given directions) of the pixel's superordinate cluster.

The horizontal extent, determining the blending height, is variable as it is established by the prevailing wind direction. Thus, simplifying assumptions are required to be able to assign one single value as a cluster's representative horizontal extent. One possibility is to simply average the cluster's diameters over the four principal directions applying a weighting based on the wind direction distribution. However in this study the maximum distance from the four directions is used to compensate for certain inherent tendencies to underestimate the horizontal extent of a surface cluster:

- The method is applied to grid boxes, thus a cluster's extend is not fully taken into account if it extends beyond the borders of a grid box.
- The investigation is limited to the four principal directions, so any larger distance in a different direction, e.g. $NNW-SSE$, is not being considered.
- In GLOBCOVER a land cover classification is used in which urban areas, water bodies and bare soil areas are explicitly accounted for which is not the case in JSBACH. Thus the map's level of heterogeneity is higher, as certain cover types introducing heterogeneity are integrated in other surface cover types in JSBACH.

Despite these simplifying assumptions, the method gives a valuable first estimate of the horizontal extents of surface clusters.

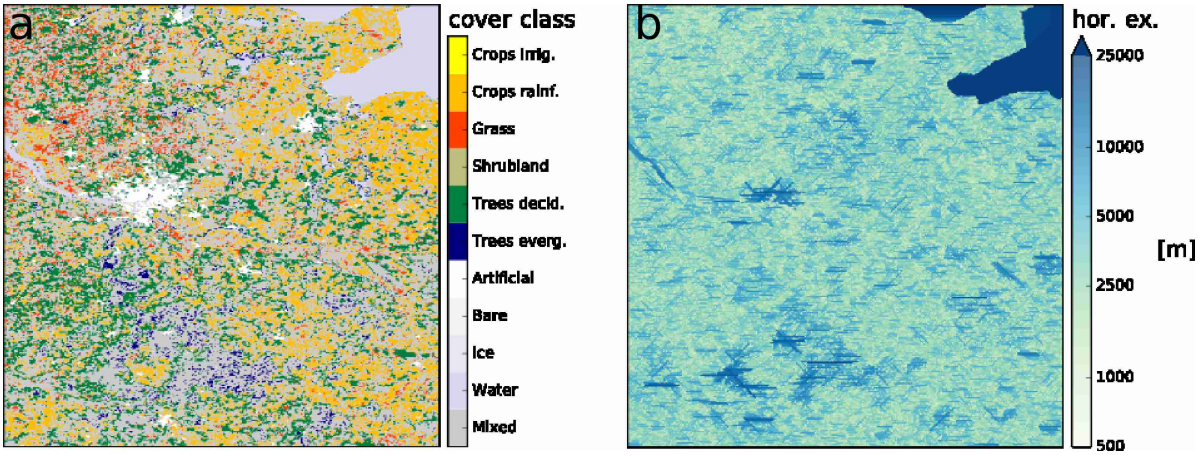

Figure 30: a) $T63$ grid box at a resolution of $300 \times 300\,m$ showing parts of northern Germany b) corresponding horizontal extent of individual homogeneous subareas

For each cover type within a given grid box a characteristic length scale can be calculated from the horizontal extent of the individual homogeneous subareas (see Fig. 36)).

Figure 31 shows the cumulative occurrence frequency of sub-grid scale heterogeneity in relation to the characteristic length scale. Areas in which surface heterogeneity is resolved by the model's grid, i.e. which are horizontally homogeneous on the grid box scale, have been excluded from the investigation (about 15 % of the land surface). The figure shows that a large share (about 25 %) of surface heterogeneity has a characteristic length scale that is below the resolution of GLOBCOVER. There are two reasons for this. Firstly, some classes in GLOBCOVER are actually heterogeneous at the resolution of the dataset. For example, classes 30 and 40 consist of a mixture of cropland and natural vegetation and classes 100 and 110 are a mixture of herbaceous species and trees or shrubs. Secondly, the GLOBCOVER data and the data used to initialize the land cover in JSBACH do not match perfectly. Thus, there are areas in which the JSBACH initial data exhibits a given PFT with a given cover fraction whereas the corresponding land cover class in GLOBCOVER is not present. Consequently, there is no information on the characteristic length scale available. In both cases the characteristic length scale for the affected land cover type was set to $0\,m$.

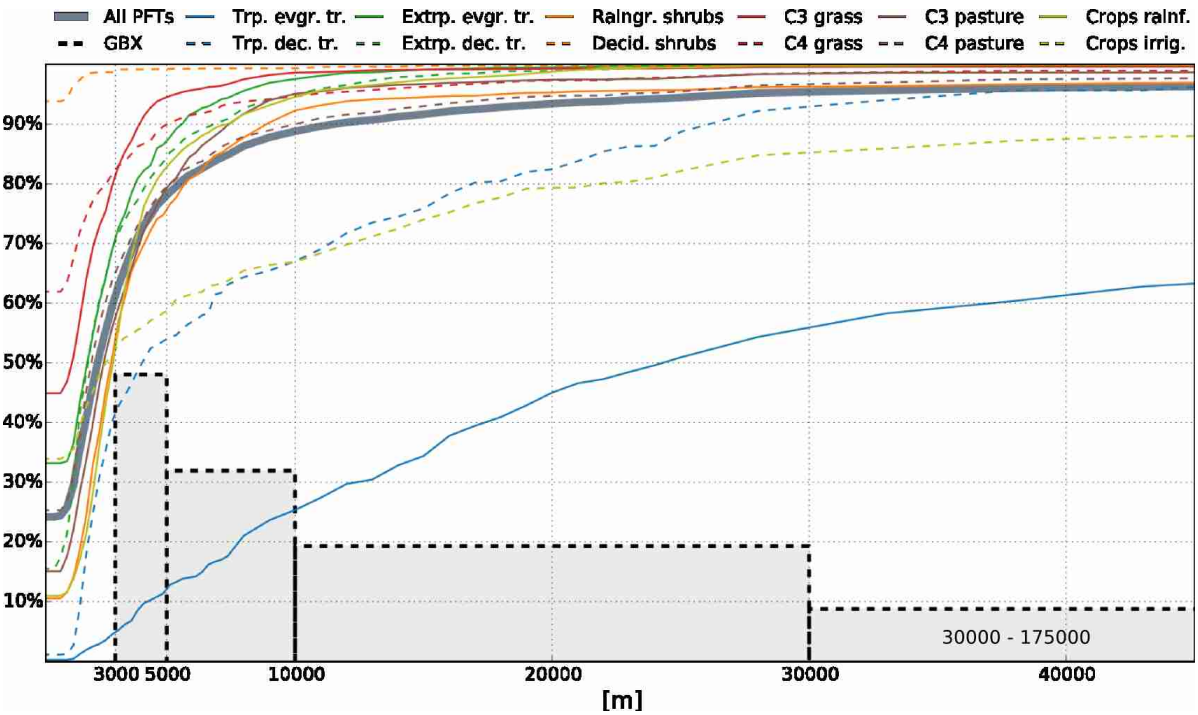

Figure 31: Occurrence frequency of surface heterogeneity with a given horizontal length scale. Lines correspond to cumulative density functions of the characteristic length scale of surface heterogeneity. Thin coloured lines refer to individual tiles, the thick grey line to the sum of all tiles. Grey columns and the respective black dashed outlines give the share (not cumulative) of land surface grid boxes (weighted by the grid box area) which contain at least one tile with the characteristic length scale encompassed within the respective bin.

The different land cover types exhibit strongly diverging characteristic length scales. For example, deciduous shrubs occur almost exclusively in clusters with a characteristic

length scale smaller than 3000 m. Hence, when assuming a value of 1/100 for the ratio of blending height to the horizontal characteristic length scale, deciduous shrubs are quite well represented by presuming the blending height to be around 30 m. Contrary to this more than 95 % of tropical evergreen trees may be misrepresented by this supposition as they appear in clusters which predominantly have a characteristic length scale larger than 3000 m. When looking at surface heterogeneity independent of the cover type, more than one third has a characteristic length scale larger than 3000 m and the corresponding fluxes most likely do not blend at the height of the lowest model level of the MPI-ESM. 95 % of the surface heterogeneities have a characteristic length scale smaller than 35000 m, thus it can be assumed that the respective surface fluxes blend below a height of about 350 m, which roughly corresponds to the third lowest model level of the MPI-ESM. For 5 % of surface heterogeneity the characteristic length scale ranges between 30000 m and 175000 m indicating that in the air above some of the respective clusters, fluxes within the grid box may at times not be in equilibrium with an effective surface at any height within the planetary boundary layer.

The distribution of surface heterogeneity leads to a substantial number of heterogeneous grid boxes containing at least one tile with a characteristic length scale for which the assumption of the blending height on the lowest atmospheric level is at least problematic. In figure 31 shaded columns denote the occurrence frequency (not accumulated) of heterogeneous land surface grid boxes which contain at least one tile with a characteristic length scale in the respective range. Almost half of the grid boxes (weighted by their size) contain a tile with a characteristic length scale of between 3000 m and 5000 m and a corresponding blending height between 30 m and 50 m. Around one third of the grid boxes contain at least one tile with a characteristic length scale between 5000 m - 10000 m. Here, assuming the blending height on the lowest model level is not only unreasonable in case of the MPI-ESM, but for most Earth System Models (ESMs). In almost one fifth of the heterogeneous grid boxes heterogeneity has a maximum characteristic length scale of 10000 m - 30000 m. In these grid boxes, the blending height is located not only above the lowest but also above the second lowest model level. Even for a very small ratio of vertical to horizontal extent i.e., 1/200, more than a quarter of the heterogeneous grid boxes contain at least one tile above which the fluxes have blended horizontally only in heights of more than 50 m and with that above the lowest atmospheric model level.

The results of this preliminary study are supported by the blending heights calculated with the VERTEX scheme (see section 3). In the design of the VERTEX scheme, horizontal heterogeneity was only considered on the lowest two atmospheric levels in order to limit computational expenses. However, a potential blending height, which could technically be at any height within the atmosphere, was calculated based on equation 19. Here, the average blending height in over 40 % of the land surface was above the lowest model level and in about 5 % it was even higher than 350 m (Fig. 32). This roughly equals the height of the third lowest model level below which in this study fluxes were assumed to have become horizontally homogeneous. Accordingly, in at least

60 % of the heterogeneous land surface grid boxes, the blending height would be above the lowest model level and in almost 40 % of the grid boxes it would be located between the second and third lowest model level. Large blending heights can especially be found for clusters of tropical evergreen forest. Here, for about half of the respective surface clusters the blending height is above the third lowest model level and in more than 15 % of these clusters the average blending height is above 1000 m which suggests that here fluxes would often not become horizontally homogeneous within the boundary layer. The average ratio of the blending height, to the horizontal characteristic length scale was found to be in the order of 1/60 - 1/70, which is well within the bounds suggested by other studies, i.e. a ratio between 1/200 - 1/10 (Mason, 1988; Claussen, 1995; Raupach and Finnigan, 1995; Best et al., 2004; Bou-Zeid et al., 2004).

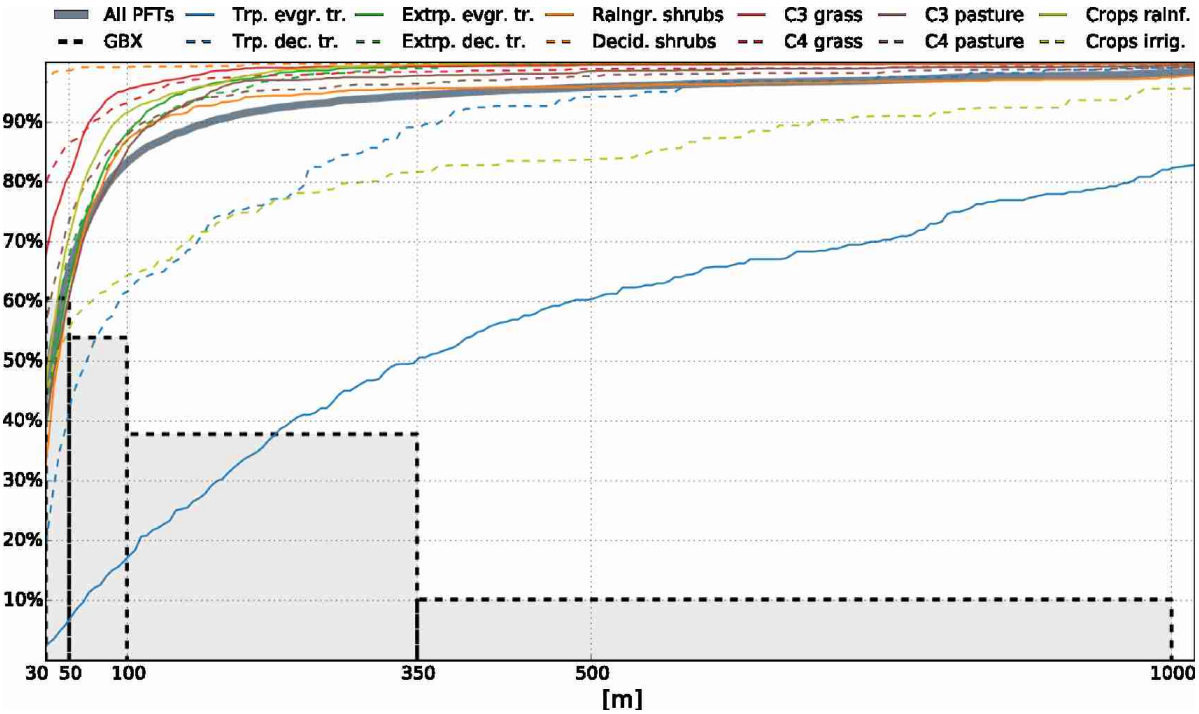

Figure 32: Cumulative density functions of the 20 year mean blending height. Thin coloured lines refer to individual tiles, the thick grey line to the sum of all tiles. Grey columns and the respective black dashed outlines give the share (not cumulative) of land surface grid boxes (weighted by the grid box area) which contain at least one tile with the average blending height encompassed within the respective bin.

As described in the introduction to section 2, approaches for the coupling of land surface and atmosphere exist, which preserve the independence of tiles throughout the entire turbulent atmospheric boundary layer, at least for the vertical turbulent transport (Molod et al., 2003). These assume that the individual tiles in the atmosphere interact only through the processes which are not resolved with respect to the tiles, such as convection, cloud formation etc. The present study indicates that this supposition of independence of the tiles is at least as problematic as assuming complete atmospheric spatial homogeneity. Considering that the boundary layer top is often located in heights

substantially above $1000\,m$, it has to be concluded that only heterogeneity that has a horizontal length scale larger than $100000\,m$ leads to a distinct signal at the respective heights. The results of this study indicate that for at least $90\,\%$ of surface heterogeneity this is not the case and the respective blending heights are located much below a height of $1000\,m$. Furthermore, the assumption of the complete independence of tiles is even more restrictive, because even below the blending height the tiles, i.e. the respective fluxes, affect each other. Thus, the results of the present study confirm the necessity for an approach such as the VERTEX scheme which is able to accurately describe the surface-atmosphere coupling not only for the very small or the very large scales but across the range of scales on which SSGS heterogeneity occurs in reality.

6.2. SSGS albedo variability - in addition to to chapter 3

As stated in section 3 there are two main characteristics which influence the near surface processes in the individual tiles which are the PFT's ability to transpire and its albedo. The effects due to differences in the transpirational abilities have been discussed in the respective section but the effects due to SSGS variability of the albedo have been omitted as these were considerably smaller. Yet to provide a holistic description of the impact of spatial heterogeneity, these shall be discussed in the following. To separate the effects of considering tile specific transpiration rates (TRANS) and considering a tile specific albedo (ALBEDO), a simulation in which the amount of radiation absorbed at the surface was calculated based on the grid box mean albedo was compared to a simulation which uses the tile specific albedo. In both simulations tile specific transpiration rates are accounted for. Because ALBEDO is much smaller than TRANS it is sufficient to discuss the impact on the near surface processes using only one example and the following analysis is limited to a comparison of $\mathrm{PARAM_{SRF}}$ and $\mathrm{SIMPLE_{SRF}}$.

There are strong differences in canopy albedo between different PFTs, by which three groups of PFT's may be distinguished. Generally tiles representing trees or shrubs have a much smaller albedo than tiles representing grass, pasture or crops . Here, the albedo may differ by more than a factor of two e.g. the albedo of the canopy in the visible range of grass, pasture or crops (0.08) is about 2.67 times larger than that of tropical evergreen trees (0.03). Furthermore the albedo formulation in JSBACH for snow covered land areas is differentiated for forested or non-forested areas, resulting in a much smaller albedo in the tiles representing forests (Roesch et al., 2001; Roesch and Roeckner, 2006). Consequently, the annual mean albedo of tiles representing trees is roughly only half as large as the albedo in the other tiles. With a larger absorption of radiation in the forest tiles, more energy is available at the surface. Therefore, these tiles exhibit higher surface temperatures and increased upward sensible fluxes. Also the latent heat flux predominantly increases, but only in areas that are not limited by the availability of water (Fig. 33 a,b).

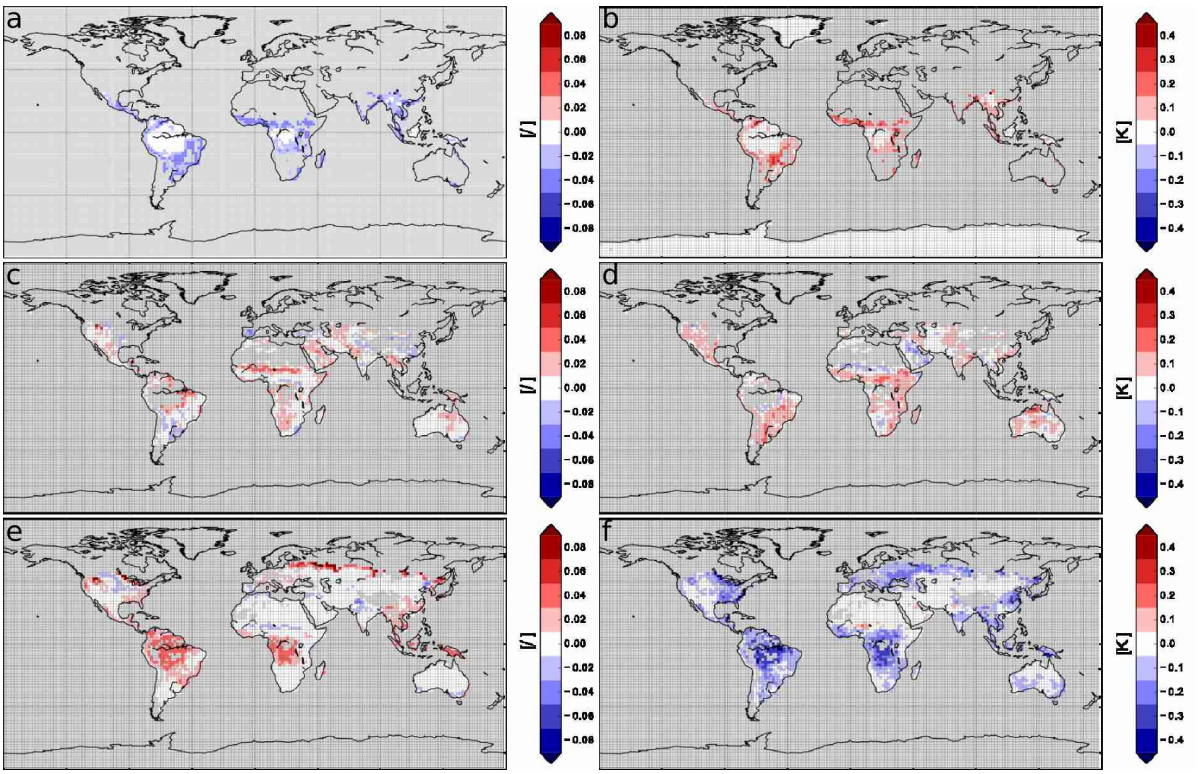

Figure 33: 5-year-mean difference between simulations performed with and without considering a tile specific albedo in the calculation of the radiation budget a) albedo in the visible range tile 1 b) surface temperature tile 1 c) albedo in the visible range tile 5 d) surface temperature tile 5 e) albedo in the visible range tile 10 f) surface temperature tile 10

The canopy albedo of tiles representing shrubs is smaller than the albedo of tiles representing grass, pasture or crops and larger than that of trees. At the same time the annual mean leaf area index (LAI) is predominantly below the grid mean. As the albedo in the vegetated, snow free share of the grid box is a function of LAI and the canopy albedo, the effect of using a tile specific albedo in these tiles differs between regions. In grid boxes in which shrubs and and trees constitute the largest share of the grid box, the albedo of the shrub tiles predominantly lies above the grid mean. Thus, less energy is available at the surface, resulting in reduced surface temperatures and heat fluxes. In areas in which the largest part of the grid box is covered by shrubs and grass, pasture or crops, the amount of radiation absorbed by the shrub tiles is larger if the relative reduction in LAI is compensated by the decrease in canopy albedo. If this is the case the surface temperature and upward heat fluxes increase. Areas, in which the reduction in LAI is not compensated by the decrease in canopy albedo, show lower surface temperatures and a decrease in the heat fluxes in the shrub tiles (Fig. 33 c,d). Tiles representing grass, pasture or crops predominantly exhibit a larger albedo, thus smaller surface temperatures and heat fluxes. An exception are areas in which the increase in LAI in these tiles compensates for the increase in canopy albedo. Here surface temperatures and heat fluxes increase (Fig. 33 e,f).

In comparison to TRANS, ALBEDO has a weaker impact on the state of the surface and the surface heat fluxes. On a global average the impact of ALBEDO on surface temperature in the tiles predominantly ranges between 25 % - 50 % and the impact on soil moisture between 10 % and 30 % of the impact which the TRANS has. The corresponding numbers for the sensible heat flux are 30 % - 60 % and for the latent heat flux 10 % - 40 %. An exception is the tile representing tropical evergreen trees, in which ALBEDO's impact on a global average is larger than TRANS's. When comparing the impact of the different effects on basis of grid box mean values, the ALBEDO plays a subordinate role. Depending on the variable, it's impact is predominantly below 20 % - 30 % of TRANS's impact.

6.3. Impact of explicitly representing SSGS heterogeneity on individual tiles in coupled simulations - in addition to to chapter 3

In section 3, the AMIP-style simulations have been compared exclusively on the basis of grid box mean values. When considering the state of the surface and the fluxes within individual surface tiles instead, the differences between the ensembles using a parameter aggregation scheme ($\mathrm{PARAM_{ENS}}$) and the ensembles with one of the flux aggregation schemes ($\mathrm{FLUX_{ENS}}$), are much more pronounced. Additionally to the difference in the grid box mean values, inter-tile variability due to the explicit representation of surface heterogeneity in the flux aggregation schemes has an effect.

The inter-tile variability in the $FLUX_{ENS}$ can be substantially larger than the difference in grid box mean values between two ensembles. For example, the standard deviation of surface temperature as an approximation of the sub-grid scale temperature variability, may in some regions be as large as $1\,K$, which is of the same order of magnitude as the differences between two ensembles when considering the grid box mean values. Here, on global (land surface) average, the surface temperature in tiles representing trees is between $-0.16.\,K$ and $-0.2\,K$, lower in one of the $FLUX_{ENS}$ than in $\mathrm{PARAM_{ENS}}$, whereas tiles representing grass, pasture and crops exhibit surface temperatures that are on average between $0.11.\,K$ and $0.21\,K$ larger. The standard deviation of the surface energy fluxes may be as large as $15\,W/m^2$ which is substantially larger than the differences in the grid box mean values. Some tiles such as trees and shrubs exhibit a sensible heat flux that is on (land surface) average more than $10\,W/m^2$ larger in one of the $FLUX_{ENS}$ than in $\mathrm{PARAM_{ENS}}$.

Hence, when considering the tile specific values, the impact of an explicit representation of SSGS heterogeneity on the state of the land surface and the surface fluxes is distinctly larger than for the grid box mean values. For surface temperature $\Delta\mathrm{ENS_{S\text{-}P}}$ (difference between $\mathrm{SIMPLE_{ENS}}$ and $\mathrm{PARAM_{ENS}}$) is larger than $0.4\,K$ in about 13 % of the land surface as opposed to 6 % when comparing the gird box mean surface temperature. In case of the surface sensible heat fluxes about 50 % [18 %] of the land surface exhibit

differences larger than $1\,W/m^2$ [$2\,W/m^2$], as opposed to 30 % [10 %] for a comparison of the grid box mean values. For the latent heat flux these numbers are 44 % [27 %] as opposed to 36 % [17 %]. When comparing fluxes on basis of tiles close to 4 % of the land surface exhibit differences of more than $10\,W/m^2$, whereas differences of this magnitude could not be observed for $\Delta\mathrm{ENS}_{\mathrm{S\text{-}P}}$ on basis of the grid box mean values. In both $FLUX_{ENS}$ intra-tile variability is accounted for and there is no pronounced change in $\Delta\mathrm{ENS}_{\mathrm{V\text{-}S}}$ (difference between $\mathrm{VERTEX}_{\mathrm{ENS}}$ and $\mathrm{SIMPLE}_{\mathrm{ENS}}$) when looking at tile specific values instead of the grid box means. This confirms the findings of the quasi-offline experiment in section 3, i.e. given an identical mean state in the atmosphere, the surface is comparably insensitive to the representation of SSGS heterogeneity in the atmosphere.

Many processes on the land surface, such as primary production, are modelled based on sub-grid scale parameters. Therefore, they may be more affected by inter-tile variability than by a change in a grid box's mean state. In certain tiles the global aggregate of the 20-year-mean net primary production (NPP) differs significantly between the $FLUX_{ENS}$ and $PARAM_{ENS}$. For example the NPP of raingreen shrubs [deciduous shrubs] increases by $1.077\,GT(C)\,a^{-1}$ [$0.012\,GT(C)\,a^{-1}$] for $SIMPLE_{ENS}$ compared to $PARAM_{ENS}$ (see table 12). This corresponds to a relative increase of more than 36 % [41 %]. Contrary to this, the global NPP aggregated to grid box mean values shows only small differences between the $FLUX_{ENS}$ and $PARAM_{ENS}$. For $\Delta\mathrm{ENS}_{\mathrm{S\text{-}P}}$ the NPP increases by $0.402\,GT(C)\,a^{-1}$ which corresponds to a relative increase of about 0.5 % (relative to $PARAM_{ENS}$).

Diff. NPP $[GT(C)\,a^{-1}]$ (%)	*SIMPLE - PARAM*	*VERTEX - PARAM*	*VERTEX - SIMPLE*
tropical evergreen trees	-0.424 (-1.8)	-0.322 (-1.4)	0.102 (0.4)
extra-tropical evergreen trees	0.010 (0.2)	0.019 (0.5)	0.009 (0.2)
tropical deciduous tree	-0.119 (-1.3)	-0.095 (-1.1)	0.024 (0.3)
extra-tropical deciduous trees	-0.213 (-3.3)	-0.190 (-2.9)	0.024 (0.4)
raingreen shrubs	1.077 (35.5)	1.094 (35.9)	0.017 (0.6)
deciduous shrubs	0.012 (40.8)	0.013 (43.7)	0.001 (3.0)
c3 grass	-0.132 (-4.1)	-0.123 (-3.9)	0.009 (0.3)
c4 grass	0.105 (5.9)	0.127 (7.1)	0.021 (1.2)
c3 pasture	-0.972 (-11.5)	-0.969 (-11.5)	0.003 (0.0)
c4 pasture	0.986 (10.0)	1.038 (10.5)	0.052 (0.5)
rainfed crops	0.066 (0.6)	0.097 (1.0)	0.031 (0.3)
irrigated crops	0.006 (0.6)	0.012 (1.0)	0.005 (0.5)
sum of tiles	0.402 (0.5)	0.700 (0.9)	0.298 (0.4)

Table 12: Differences in net primary production absolute and relative to PARAM

Because both $FLUX_{ENS}$ consider SSGS variability, the differences in NPP between the two ensembles are much less pronounced. In some tiles the absolute differences in NPP between the $VERTEX_{ENS}$ and $SIMPLE_{ENS}$ are comparable to those between one of

the $FLUX_{ENS}$ and $PARAM_{ENS}$. For example, for the NPP of tropical deciduous forest $\Delta\mathrm{ENS_{V\text{-}S}}$ is about $0.009\,GT(C)\,a^{-1}$, whereas $\Delta\mathrm{ENS_{S\text{-}P}}$ is equal to $0.010\,GT(C)\,a^{-1}$. However, in relative terms $\Delta\mathrm{ENS_{V\text{-}S}}$ is seldom larger than 1 %. The $VERTEX_{ENS}$ shows consistently higher NPP rates than the $SIMPLE_{ENS}$. Thus, when aggregating the tile specific NPP rates, the impact of the *VERTEX* scheme is on the same order of magnitude as the impact of an explicit representation of surface heterogeneity ($\Delta\mathrm{ENS_{V\text{-}S}} \approx 0.3\,GT(C)\,a^{-1}$, $\Delta\mathrm{ENS_{S\text{-}P}} \approx 0.4\,GT(C)\,a^{-1}$).

6.4. Explicit representation of (permanently) non-vegetated areas

As stated in the beginning of section 4, the permanent bare soil fraction within a given grid box has been integrated to a designated tile. This fraction pertains to areas that are inhospitable to plants such as bare rock or deserts. How an explicit representation of these areas affects the simulated state of the surface and the surface fluxes will be discussed in the following.

The idea behind the tiling approach is to represent the homogeneous fractions of a grid box by individual tiles. However, for JSBACH this is not completely true, as here the tiles themselves represent inhomogeneous areas. In the standard version of JSBACH, the non-vegetated share of a grid box is not explicitly represented, even if it pertains to areas which in reality are clearly separated from the vegetated part. Rather than using an individual tile to represent these areas, each tile in a grid box consists of a vegetated and a non-vegetated fraction. For investigations with respect to irrigation, this means that currently it is impossible to limit the application of irrigation to the vegetated part of the tile i.e. a distinct share of the water used for irrigation would be deployed in bare areas. To be able to perform realistic simulations in which irrigation is accounted for, the bare fraction of the grid box needed to be integrated to a designated tile.

The non-vegetated part of the grid box can be divided into a static and a dynamic bare soil part. The former represents the part of the grid box which (if dynamical vegetation scheme is disabled) invariably remains unavailable for plant growth and can be understood as areas such as deserts which are inhospitable to vegetation ($bare_{static}$). Using the grid box maximum vegetation fraction (veg_{max}) this share is given by:

$$bare_{static} = 1 - veg_{max} \tag{32}$$

The latter, i.e. the dynamical bare soil fraction $bare_{dyn}$, is the share of the grid box that is potentially hospitable to vegetation but currently photosynthetically inactive. This fraction of the grid box represents areas that exhibit seasonal or interannual variations in vegetation cover e.g. the areas occupied by deciduous plants which in summer may be fully vegetated but in winter exhibit a large non-vegetated fraction. In JSBACH it is calculated as a function of veg_{max}, LAI and a factor K to account for the clumping of vegetation:

$$bare_{dyn} = veg_{max} \cdot e^{-\frac{LAI}{K}} \tag{33}$$

For the irrigation experiments, it is crucial to distinguish between the two bare soil fractions because circumstances exist in which irrigating $bare_{dyn}$ is a rational action, i.e. during the period after sowing or when only shoots are present. Contrary to this, $bare_{static}$ represents areas in which plant growth is impossible and therefore, intentional irrigation irrational.

To better understand how transferring this heterogeneity from the sub-tile scale to the sub-grid scale, i.e. representing the inhospitable share of the grid box $bare_{static}$ by a new tile, may impact evapotranspiration, a brief summary of the approach used to model evaporation and transpiration in JSBACH is given in the following (note that the following explanation is valid only when the soil is represented by a simple bucket).

In the vegetated fraction of the grid box transpiration is determined based on the relative soil moisture $\frac{w_s}{w_{cap}}$ and a stomatal resistance as a function of the LAI (Sellers et al., 1986). Here, the entire soil moisture located in the root zone w_s is accessible to plants for transpiration. In the non-vegetated part of a grid box, the bare soil evaporation E_{bs} is calculated as a function of the saturation specific humidity at the given surface temperature and pressure q_{sat}, the specific humidity of air directly above the surface q_v, the horizontal wind speed v_h, the transfer coefficient for heat and moisture C_h, the density of air ρ and the relative share of soil water available for evaporation h (Roeckner et al., 1996):

$$E_{bs} = \rho \cdot C_h \cdot \mid v_h \mid \cdot (q_v - h \cdot q_{sat}) \tag{34}$$

Here, h is defined as:

$$h = \frac{1 - cos(\pi \cdot \frac{w_s - (w_{cap} - w_{top})}{w_{top}})}{2} \tag{35}$$

for $w_s > w_{cap} - w_{top}$, and $h = 0$ otherwise. $w_{top} = 0.1m$ for $w_{cap} > 0.1m$, and $w_{top} = w_{cap}$ otherwise.

Thereby, the total soil water w_s is allocated to an upper (w_{top}) and a lower reservoir ($w_{cap} - w_{top}$) to prevent the evaporation of moisture from deep within the soil. Due to these restrictions, bare soil evaporation occurs only when the entire soil column (bucket) is almost completely saturated (Hagemann and Stacke, 2014). Consequently, by introducing a bare soil tile, the respective soil moisture is only available for evapotranspiration when the entire soil column is close to saturation. Contrary to this, when the bare soil fraction is represented as a sub-tile scale feature, the respective soil moisture is accessible to plants, and transpiration at an aggregate rate (vegetated and non-vegetated fraction) can occur as long as there is water present within the root zone.

How this alteration in the representation of the bare soil fraction impacts the simulated climate will be shown in the following. In a first step it will be investigated how soil moisture, surface temperature and the surface heat fluxes differ between the vegetated and the (invariantly) non-vegetated part of the grid box. And in a second step differences

in the 20-year means between simulations with an explicit and an implicit representation of the bare-soil fraction will be compared.

In the vegetated part (more correctly the fraction hospitable to vegetation as $bare_{dyn}$ is still included) of a large share of the land surface, a balance between precipitation, evapotranspiration, run-off and drainage is reached in which soil moisture is limited to the lower part of the root zone ($w_s < w_{cap} - w_{top}$). In the non-vegetated part of the respective grid boxes no evapotranspiration occurs before water is present in the upper soil moisture reservoir ($w_s > w_{cap} - w_{top}$) and to this point an increase in soil moisture with precipitation is only inhibited by drainage and surface run-off. Hence the soil moisture values in the non-vegetated part can become more than twice as large as in the vegetated parts. This corresponds to differences in soil moisture on the order of several decimetres (Fig. 34 a). On a global average the soil moisture in the non-vegetated part of the grid box is about $0.18\,m$ larger than in the vegetated part.

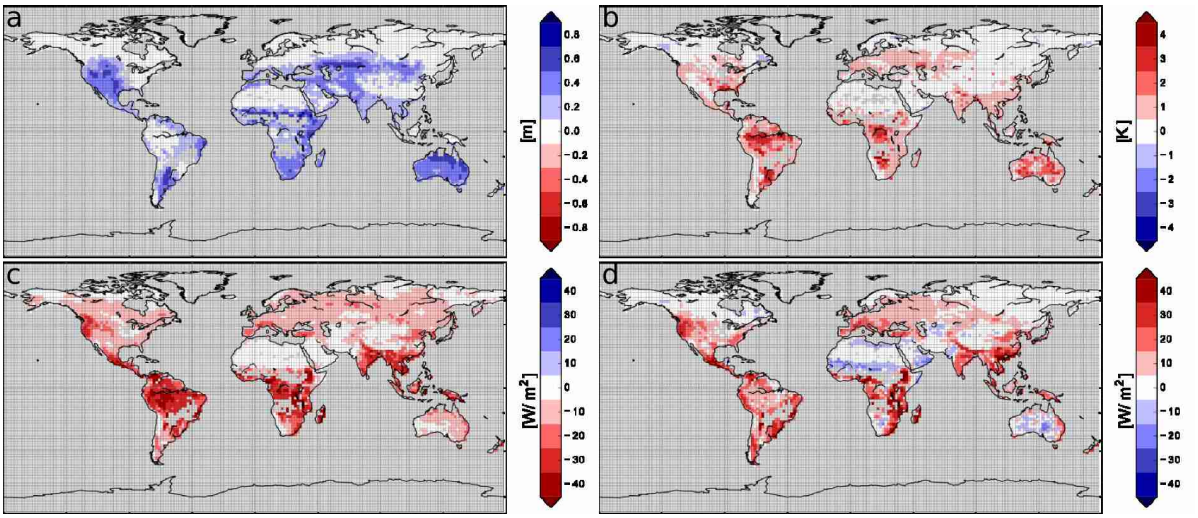

Figure 34: 20-year mean difference between bare soil tile and vegetated part of the grid box a) soil-moisture b) surface temperature c) latent heat flux d) sensible heat flux; plots are masked in regions in which the cover fraction of the bare soil tile < 0.01

Limiting the availability of water has strong impacts on evapotranspiration and the latent heat flux. On global average the latent heat flux in the tile representing bare soil is about one third smaller than in the vegetated parts of the grid box. In many regions the latent heat flux is reduced to one fifth of the respective value in the vegetated parts which corresponds to differences of up to $50\,Wm^{-2}$ (Fig. 34 c). In the largest part of the land surface this reduction in latent heat flux is balanced by an increase in sensible heat flux and higher surface temperatures in the bare soil tile (Fig. 34 b,d). On a global average the sensible heat flux is about one third larger in the bare soil tile and surface temperatures increase by more than $0.6\,K$. However there are areas such as Northern Africa and Australia in which both latent and sensible heat flux decrease. This effect is related to the roughness length of the bare soil tile. As this is below the roughness

length of any of the vegetated tiles the amount of shear driven turbulence in given wind conditions is smaller, hence the surface-atmosphere coupling weaker in the bare soil tile. This means that, even with larger surface-atmosphere temperature gradients (not shown here), the sensible heat flux is smaller in the non-vegetated part of the grid box. On a global average the latent heat flux in the non-vegetated part decreases by more than $12\,Wm^{-2}$ and the sensible heat flux increases by less than $8\,Wm^{-2}$. But even accounting for this roughness length related effect, the dominant response to the introduction of a designated tile to represent the permanently non-vegetated grid box fraction is a pronounced increase in soil moisture, surface temperature and sensible heat flux and a distinct reduction in evapotranspiration and latent heat flux in the respective fraction.

As can be seen in Eq. 34 and 35 there is a non-linear dependency of evaporation on soil moisture and the existence of a bare soil tile can also be expected to have an impact on the grid box mean state. To determine the magnitude of this impact, a simulation with an explicit representation of the permanent bare soil fraction (EBSF) is compared to the ensemble mean of simulations with an implicit representation of the bare soil fraction $VERTEX_{ENS}$.

EBSF - $VERTEX_{ENS}$	*AWAD (Glob. mean diff.)*	*Share of land surface exhibiting robust impact*
surface temp.	0.16 (0.06) $[K]$	05.2 [%]
temp. 2m	0.14 (0.04) $[K]$	06.0 [%]
surf. net rad. short	0.80 (0.15) $[W/m^2]$	05.7 [%]
surf. net rad. long	0.89 (-0.56) $[W/m^2]$	10.2 [%]
sens. heat flux	1.28 (0.82) $[W/m^2]$	14.0 [%]
latent heat flux	1.50 (-1.21) $[W/m^2]$	17.1 [%]
precipitation	0.05 (-0.02) $[mm\,d^{-1}]$	03.2 [%]
vrt. int. w. vap.	0.19 (-0.11) $[kg\,m^{-2}]$	08.3 [%]
soil moisture	0.063 (0.018) $[m]$	24.5 [%]

Table 13: Global area weighted absolute difference, i.e. AWAD (global land surface mean differences) and share of land surface exhibiting statistically significant (pval < 0.05) differences above the internal model variability i.e. robust impact; between EBSF and $VERTEX_{ENS}$

As the fraction of soil moisture which is located in the lower reservoir within the bare soil tile, is inaccessible to evapotranspiration, the grid box mean soil moisture in a large share of the land surface increases by as much as $0.24\,m$ in EBSF (Fig. 35 a). The consequent decrease in evapotranspiration in the non-vegetated part of the grid box can mostly not be compensated by an increase in evapotranspiration in the vegetated tiles. Hence the predominant effect with respect to the grid box mean evapotranspiration is a distinct decrease corresponding to up to $12\,Wm^{-2}$ in the majority of the land surface (Fig. 35 c). The resulting excess in energy at the surface is largely balanced by an increase in sensible heat flux of up to $11\,Wm^{-2}$ and an increase in surface temperature of up to $1\,K$ (Fig. 35 b,d). On global average, soil moisture increases by $0.018\,m$, surface

temperature increases by $0.06\,K$, the latent heat flux decreases by $1.21\,Wm^{-2}$ and the sensible heat flux increases by $0.82\,Wm^{-2}$ (Table 13).

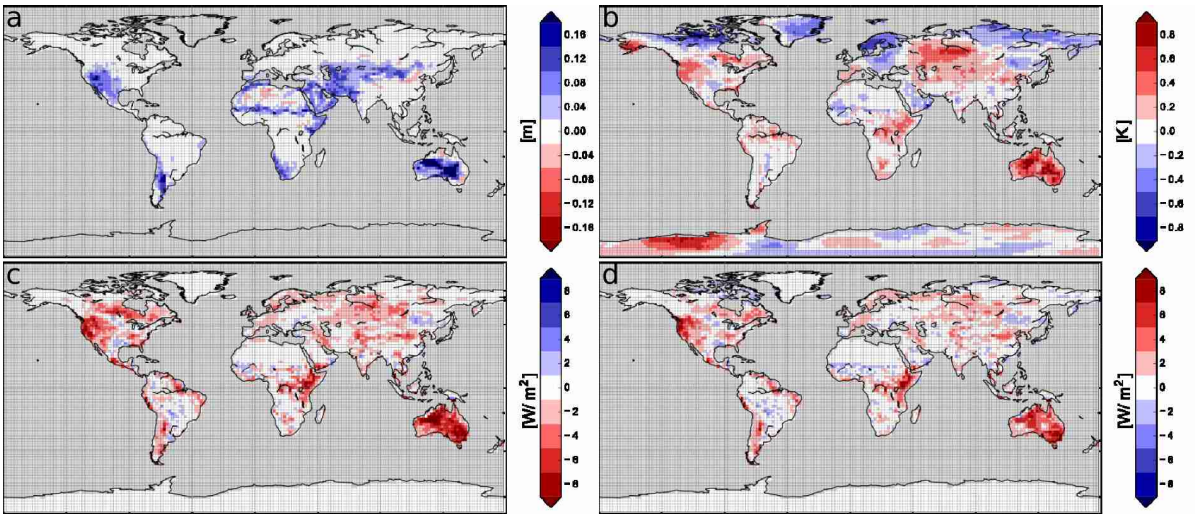

Figure 35: 20-year mean difference between EBSF and $\text{VERTEX}_{\text{ENS}}$ a) soil-moisture b) surface temperature c) latent heat flux d) sensible heat flux

The differences due to the treatment of the bare soil fraction presented in this section are on the same order of magnitude as the differences with respect to different coupling schemes presented in section 3. However, this does not mean that the treatment of the bare soil fraction has a larger impact on the simulated climate than the choice of coupling scheme. A certain share of the differences between individual simulations is related to the internal model variability (IMV). In order to determine whether differences are process related, the IMV was derived from the ensemble simulations described in sections 3, as the ensemble spread of the $VERTEX_{ENS}$. In the following it is assumed that wherever differences between EBSF and $VERTEX_{ENS}$ exceed the ensemble spread these are process related. This measure was combined with the measure of statistical significance of a given 20-year mean difference between EBSF and $VERTEX_{ENS}$ that was obtained from a two sample, two sided Student's t-test ($p < 0.05$). It was assumed that whenever differences are statistically significant and larger then IMV these constitute a robust impact on the simulated climate.

Between 3 % (for precipitation) and 25 % (for soil moisture) of the land surface are robustly impacted by an explicit representation of the non-vegetated fraction of a grid box (Table 13). As for most variables a robust impact was found in between 5 % and 15 % of the land surface, it can be inferred that the introduction of a bare soil tile has a robust impact on about 10 % of the land surface. Here, it mainly acts via limiting the soil moisture available for transpiration, which leads to a pronounced increase in surface temperature and sensible heat flux and a decrease in evapotranspiration and latent heat flux.

7. Concluding remarks

7.1. Summary

This dissertation was motivated by the desire to facilitate the understanding of the complex interrelation between the spatially heterogeneous land surface and the surface energy and moisture fluxes. Here, most Earth System Models (ESMs) use tiles, i.e. homogeneous sub-areas within a model's grid box, to explicitly represent spatial sub-grid scale (SSGS) heterogeneity at the surface, but assume the entire vertical column of the atmosphere to be horizontally homogeneous. Studies and observational data indicate that, at the operational resolutions of present day ESMs, this assumption is only valid for heterogeneity with a horizontal length scale of up to $\approx 3000 - 5000\,m$. In contrast, the influence of heterogeneity on larger scales is detectable in heights that are far above the lowest model level.

A preliminary study showed that a substantial share of the land surface heterogeneities occurs on horizontal length scales above the micro scale, which may lead to significant errors when calculating the surface fluxes based on the assumption of a spatially homogeneous atmospheric state on the lowest model level. This raised the need for the development of a land surface-atmosphere coupling scheme, capable of representing SSGS heterogeneity, also within the lowest layers of the atmosphere. Accordingly, a coupling scheme was proposed that provides a VERtical Tile EXtension (VERTEX). The scheme was implemented into the Max Planck Institute for Meteorology's Earth System Model (MPI-ESM) and applied in a series of investigations, which targeted different aspects of the influence of sub-grid scale heterogeneity on the surface energy and moisture fluxes as well as on the state of the land surface and the atmosphere.

With single column simulations it was demonstrated how surface and atmospheric SSGS heterogeneity relate to atmospheric turbulent transport processes, which are resolved with respect to the surface tiles in the VERTEX scheme. Here, it was shown that the strength of the vertical turbulent transport can vary distinctly between different tiles within the same model grid box. In tiles, in which the surface is relatively warm, the atmospheric column is predominantly less stable, facilitating the vertical turbulent mixing within the respective tiles. Accordingly, when atmospheric SSGS heterogeneity is accounted for, the vertical turbulent transport is weaker in tiles featuring a cooler surface. As the atmosphere in the warmer tiles is mostly dryer, the vertical turbulent transport is more pronounced for dry static energy than for moisture. Consequently, an explicit representation of heterogeneity on the lowest atmospheric model levels does not only have an impact on the state of individual tiles, but also on the grid box mean state.

In a next step, the MPI-ESM was applied on the global scale, at first in a series of simulations, in which the surface-atmosphere feedback was omitted in order to prevent large scale atmospheric effects. With these simulations the near surface processes in individual tiles could be studied with respect to different coupling schemes. Addition-

ally, important characteristics were identified which determine the partitioning of the available energy at the surface into latent and sensible heat flux in the MPI-ESM. Subsequently, the surface-atmosphere feedback was taken into account and a series of 3×5 simulations was performed with prescribed a sea-surface temperature and sea-ice extent. These showed that the explicit representation of SSGS heterogeneity distinctly influences the simulated global climate.

Finally, the thesis focused on the influence of certain types of heterogeneity, which feature distinct characteristics, namely irrigated and non-vegetated areas. The representation of these areas by a designated tile, severely affects the global hydrological and energy cycles. While the explicit representation of bare soil areas leads to a decrease in simulated terrestrial evapotranspiration of about 3 % and an increase in surface temperature of about $0.1\,K$, the introduction of irrigation in the MPI-ESM leads to an increase in evapotranspiration that is possibly as large as 6 % and a decrease in land surface temperature of up to $0.2\,K$.

Using the MPI-ESM with the model setups described above, the research questions guiding this thesis could be answered, namely:

How can spatial heterogeneity of the atmosphere be accounted for in the coupling of land surface and atmosphere within ESMs?
An approach for the surface-atmosphere coupling that considers atmospheric SSGS heterogeneity can be based on the blending height concept. The blending height provides a scale for the decrease of the influence of surface heterogeneity with increasing height above ground (Mahrt, 2000).

By assuming a fixed relation between height and the magnitude of the influence that heterogeneity exerts on the flow, the strength of the influence of surface heterogeneity can be related to the ratio of the height of a model level and the blending height. By further assuming that the decrease of the influence of a surface feature can be attributed to the horizontal mixing of the vertical fluxes, the ratio of the height of the respective model level and the blending height can be used to describe the degree of mixing of the fluxes.

The blending height is largely determined by the surface roughness length, atmospheric stability, and the prevailing wind conditions, all of which constitute variables that are already being used in ESMs. Furthermore, the determination of the blending height requires the characteristic horizontal length scales of surface heterogeneity. As these can be derived from existing datasets such as the Global Land Cover Map 2009, the coupling scheme presented in this thesis can readily be implemented in any ESM.

What is the effect of an explicit representation of surface and atmospheric SSGS heterogeneity on the simulated near surface processes with respect to different land cover types?

It could be shown that near surface processes are systematically affected by the explicit representation of SSGS heterogeneity. Here, the two characteristics that largely determine a tile's response to differences in the coupling schemes are the tile's ability to transpire, determined by stomatal conductance and leaf area, and the albedo. In certain grid boxes, in which surface types with distinctly differing vegetation heights are present, also the roughness length plays an important role.

When surface heterogeneity is explicitly represented, tiles with pronounced transpirational abilities generally exhibit an increase in transpiration as well as a decrease in the sensible heat flux and in the surface temperature, unless soil moisture becomes a limiting factor. Plants with lower stomatal conductance and leaf area show the opposite effect. By additionally accounting for SSGS heterogeneity in the atmosphere, evapotranspiration in tiles with pronounced transpirational abilities is reduced due to a smaller local surface-atmosphere moisture gradient. Despite the decrease in latent heat flux and the consequent increase in sensible heat flux, this does not necessarily result in a warming of the surface. The atmosphere in these tiles is relatively colder and the increase in sensible heat flux is realized at lower temperatures also at the surface. Tiles with less pronounced transpirational abilities display the opposite reaction.

Differences in albedo have a distinctly smaller influence on the near surface processes but still result in noticeable differences in the surface fluxes and the state of the surface, as they determine the amount of radiation absorbed by the individual tiles. Tiles with a smaller albedo, i.e. trees and shrubs, absorb more energy and consequently show an increase in sensible heat flux, surface temperate and, unless the availability of soil water was limited, an increase in latent heat flux. Tiles with a higher albedo such as grass or crops show the opposite effect.

In combination, these two effects lead to pronounced differences in the states of different tiles and in the respective surface fluxes. For surface temperature, the 20-year mean inter-tile variability within a grid box is as large as $1.5\,K$ and with respect to the surface energy fluxes the variability is often larger than $10\,W\,m^{-2}$. This also has a strong impact on processes that are resolved with respect to the tiles such as net primary production (NPP), which in certain tiles increased by more than a third due to the explicit representation of SSGS heterogeneity.

What is the impact of an explicit representation of surface and atmospheric SSGS heterogeneity on climate on the global scale?
Due to the non-linear dependency of the surface fluxes on the state of the surface and the atmosphere, the representation of SSGS heterogeneity has a strong influence on the grid box mean state. Most importantly, the sub-grid distribution of soil moisture strongly affects the simulated climate. Often there is a decrease in evapotranspiration in tiles with pronounced transpirational abilities due to soil moisture limitations, which is not balanced by an increase in transpiration in tiles with less pronounced transpirational abilities. Hence, accounting for SSGS heterogeneity at the surface results in

higher simulated surface temperatures and sensible heat fluxes as well as a reduction in evapotranspiration and precipitation.

But also the explicit representation of SSGS heterogeneity in the atmosphere has a distinct impact on the state of the surface and the surface fluxes. Depending on the variable and measure considered, the impact is roughly half as large as the impact of explicitly accounting for SSGS heterogeneity at the surface. The explicit representation of atmospheric SSGS heterogeneity influences the vertical and spatial (between the tiles) distribution of moisture in the atmosphere. This influences local surface-atmosphere humidity gradients, precipitation and by that, evapotranspiration and the distribution of soil moisture. The respective simulations exhibit slightly lower surface temperatures and sensible heat fluxes and an increase in evapotranspiration and precipitation. However, the signal is much less pronounced, because impacts due to atmospheric heterogeneity are less one-directional and differ strongly between regions.

Representing SSGS heterogeneity explicitly has a robust impact on between 10 % - 48 % of the land surface. Between 25 % - 45 % of the land surface exhibit surface temperature differences of more than $0.125\,K$ and around 25 % [10 %] exhibit relative differences in the surface fluxes larger than 10 % [25 %](20-year grid box means). In comparison to WATCH Forcing Data (WFD) the representation of sub-grid scale heterogeneity improves the simulation of precipitation, but the bias in simulated 2m temperature increases. In simulations that account also for sub-grid scale heterogeneity in the atmosphere, precipitation and 2m temperature are consistently more similar to WFD than in simulations that only account for heterogeneity at the surface.

How does irrigation-based agriculture in arid regions influence the regional and possibly global climate? Furthermore, which effect does the surface-atmosphere coupling have on the representation of irrigation and how large is the associated uncertainty in simulations?
Irrigation-based agriculture is assumed to contribute up to $2600\,km^3a^{-1}$ to the terrestrial water vapor flow (Gordon et al., 2005) and pronounced local effects, in terms of surface temperature and evapotranspiration, are associated with it (Saeed, 2011; Tuinenburg et al., 2014). Simulations with the MPI-ESM show an irrigation induced local surface cooling of up to $3.5\,K$ in heavily irrigated areas in India (20-year grid box mean) and a local increase in evapotranspiration of up to $1.5\,mm\,d^{-1}$ which corresponds to an overall increase in net integrated vertical moisture flux in irrigated areas of up to $2500\,km^3a^{-1}$.

At the same time, the present studies revealed substantial remote effects by which irrigation influences the climate over a distance of several thousand kilometres. While irrigated areas cover only about 2 % of the world's terrestrial surface, they robustly affect the state of the surface and the energy and moisture fluxes in up to 20 % of the land surface. Two main mechanisms, namely the advection of water vapor and a weakening of the monsoon in South, Southeast and East Asia, were identified as key determinants of the remote effects related to irrigation. For the first time, it could be shown that

irrigation-based agriculture in the Middle East and South Asia directly affects precipitation and surface temperatures in Eastern and Central Africa and leads to a strong increase in atmospheric water vapor and cloud cover in regions as distant as the east coast of China. By an evaporative cooling of the surface, irrigation also leads to a reduction of the land sea thermal contrast that drives the monsoon winds in South and Southeast Asia. The weakening of the monsoon leads to a decrease in precipitation and a consequent increase in surface temperatures in large parts of Southeast Asia.

Here, the manner in which SSGS heterogeneity is represented is an important factor in determining the magnitude of possible impacts of irrigation. The increase in atmospheric water vapor, due to irrigation is several times larger in simulations in which atmospheric heterogeneity is accounted for (VERTEX scheme) than in simulations which only consider surface heterogeneity (simple flux aggregation scheme). Simulations in which heterogeneity is only implicitly represented (parameter aggregation scheme) actually show a drying of the atmosphere due to irrigation. Therefore, the remote effects of irrigation can be identified clearly only in the simulations with the VERTEX scheme.

These simulations also give the best results for near surface temperature and precipitation in regions with a pronounced irrigation-based agriculture (compared to WFD). This gives some confidence that by a more realistic representation of the turbulent mixing process also the representation of irrigation becomes more realistic. In this respect, the present study revealed substantial uncertainties related to the model's structure and indicate that earlier modelling studies using a parameter aggregation or simple flux aggregation scheme may have underestimated the impact of irrigation on climate. Additionally, large uncertainties were found in connection to the assumed irrigation characteristics. The impact on climate is several times larger in simulations with a low irrigation efficiency than in simulations assuming a high irrigation efficiency.

Additionally, areas that are permanently uninhabitable to vegetation, such as deserts, were investigated, as these often constitute SSGS heterogeneity whose characteristics strongly contrasts the surrounding land cover. It could be shown that the climate in non-vegetated areas can differ distinctly from the surrounding vegetated areas. In the MPI-ESM, bare soil evaporation occurs only when the surface is almost completely saturated, whereas the roots of plants can access water from a considerable depth. At the same time, the share of precipitation that results in run-off and drainage increases distinctly with increasing saturation of the soil. Thus, when representing the permanently non-vegetated fraction of the grid box by a designated tile, there is a significant decrease in evapotranspiration, a corresponding decrease in latent heat flux, an increase in the sensible heat flux and the surface temperatures in these areas. The non-vegetated fraction of the grid box exhibits surface temperatures that are by up to $4\,K$ higher than in the vegetated parts of the grid box. The respective increase in sensible and decrease in latent heat flux can be as large as $40\,W\,m^{-2}$. When integrating the areas uninhabitable to plants into a designated tile a large share of the soil moisture becomes unavailable to plants and the decrease in evapotranspiration in the non-vegetated part in the grid box

can not be balanced by an increase in the vegetated tiles. Consequently, also the grid box mean temperatures and sensible heat fluxes predominantly increase by up to $1\,K$ and $8\,W\,m^{-2}$ respectively, and the grid box mean latent heat flux generally decreases by up to $8\,W\,m^{-2}$.

7.2. Outlook and conclusion

While answering the above questions, the results of this thesis originated possible subjects of future research, particularly with respect to the impact of irrigation on climate. Considering the uncertainties involved in modelling irrigation in combination with the pronounced impact especially on the regional scale (e.g. Saeed (2011)), the present work highlights the need to investigate possible impacts based on a more realistic representation of the irrigation process. On one hand this requires more detailed information on real world irrigation with respect to irritated areas, irrigation infrastructure and techniques as well as on water availability. On the other hand there is a need for more sophisticated irrigation schemes that use region-, time-, technique- and crop-specific parametrisations and take into account the availability of fresh water. In the present studies, an unlimited supply of fresh water was assumed. However, in reality irrigation is often limited by the availability of this resource, which will in the future likely become more problematic in many regions of the world (Hagemann et al., 2013). Hence, a sustainable irrigation practice needs to be investigated, i.e. which level of irrigation can be provided when relying exclusively on renewable fresh water resources, and which impact on climate does this sustainable irrigation have? Also, the advective moisture transport should be studied in more detail. So far investigations of irrigation that use moisture tracking schemes have been limited to the regional scale (e.g. Harding et al. (2013); Tuinenburg et al. (2014)), but could also be conducted on a global scale. Furthermore, the example of irrigation showed that surface-types may have pronounced impacts on a large share of the land surface and atmosphere, even though they only cover a small fraction of the planet's surface. Hence, studies are conceivable which target the large scale impacts on climate of other surface types with unique characteristics such as wetlands or urban areas.

With respect to model development, this work provides a fully functional scheme to couple land surface and atmosphere, that can be used in any numerical weather or climate model. The coupling scheme proposed in this thesis is amongst the first to explicitly represent atmospheric SSGS heterogeneity on the scales of ESMs and the only one which accounts for an interaction of the homogeneous sub-areas within the atmosphere. However, certain constraints limit its operational applicability. The scheme is currently computationally very expensive as it requires solving a matrix for a number of atmospheric levels and for a number of variables. Here, the computational demand increases drastically with an increasing number of tiles that are being modelled. For a model setup using 14 tiles, simulations (land surface and atmospheric model) with the VERTEX scheme take almost 40 % longer than simulations with the simple flux aggregation scheme, whereas for a setup with 4 tiles the computational costs are almost identical. This is partly

because no optimisation of the algorithms with respect to high performance machines has been undertaken and there is a large potential for accelerating the computations, e.g. by parallelizing the matrix algorithms. Nonetheless, some structural changes in the approach may also be beneficial for simulations that require the representation of a large number of tiles. For example, a pre-aggregation of tiles according to their associated blending heights may be a useful step. Here, only the tiles above which the fluxes have not blended could be explicitly represented in the calculations on a given level, whereas the other tiles could be combined in a fraction representing the horizontally blended flux.

Furthermore, certain limitations in the way the scheme was implemented for the studies of this thesis prohibit to account for the entirety of effects related to atmospheric heterogeneity. On one hand, atmospheric heterogeneity was only considered for temperature and specific humidity, whereas heterogeneity of the wind field was neglected above the lowest model level. When resolving wind-speeds with respect to tiles, differences in surface roughness may cause pronounced SSGS variability in the wind field even higher in the atmosphere. This variability affects the turbulent kinetic energy, hence the vertical turbulent transport which feeds back on atmospheric SSGS variability in the state variables of temperature and specific humidity.

Additionally, atmospheric heterogeneity was only used to model the vertical turbulent transport in the atmosphere. Here, studies suggest that atmospheric SSGS variability may substantially affect other processes such as convection, cloud formation and precipitation (Rieck et al., 2014; Guillod et al., 2015). In many regions, the simulations performed with the MPI-ESM exhibited pronounced sub-grid scale variability on the lowest atmospheric levels, especially relative to the respective variability at the surface. This information on atmospheric SSGS variability could be used to improve the representation of many atmospheric processes, e.g. triggering cumulus convection in ECHAM6 requires some assumption about the sub-grid scale variability of virtual temperature which could be provided by the scheme. Finally, within the soil there is no lateral interaction of the tiles. It is possible to make simplifying assumptions by which sub-surface lateral flows of energy and water can be accounted for (e.g. Hagemann and Stacke (2014)), but with the information on the horizontal length scales of surface heterogeneity, these fluxes could also be modelled explicitly.

To conclude, the present work demonstrates the importance of representing SSGS heterogeneity also in the atmosphere, especially in case of land cover types with strongly contrasting characteristics. Here, it could be shown that irrigation-based agriculture in arid and semi arid regions does not only have a strong impact on the local climate, but also has remote effects that reach over distances of thousands of kilometres. But much more than that, the thesis provides a framework for representing all planetary boundary layer and possibly even sub-surface processes more realistically by basing the model formulations of e.g. convection, cloud formation or sub-surface lateral flows on sub-grid scale parameters or accounting for SSGS heterogeneity in the respective parametrisations.

Acknowledgements First and foremost I would like to thank Tobias Stacke without whose advice and willingness to help, in combination with a Buddha-like patience, this thesis could not have been written. I would also like to thank my supervisors and members of my advisory panel Stefan Hagemann, Martin Claußen and Andreas Chlond, whose support was no less important and who, with their ideas, help and guidance, should have been the first to thank. However, the amount of questioning Tobias had to endure was truly impressing. Furthermore I would like to thank all the members (current and former) of the THY-group, especially my room-mates who all helped me greatly along the way. I am also very grateful for the support of the IMPRS and here especially to Antje and Connie, for being the first two friendly faces I saw when coming for my interview. This made the decision to come back to Hamburg a very easy one.

Thanks are also due to Eddo, Robin and Henning who helped to put the final shine on the graphics and saved what they could with respect to spelling and punctuation. I would also like to thank my entire family for their constant support. Most importantly I am incredibly thankful to my wife. She kept me grounded and with her unalterable optimism and unique perspective, inspired my work of the last three years. Of course especially towards the end of my work she was also a tremendous help with reading, correcting and making sure I slept once in a while. Certainly the last month of a doctoral thesis is not what she thought about when she agreed to be true to me also in the bad times.

Finally I would like to thank the entire Institute for making this doctorate a truly great experience.

References

Adegoke, J. O., R. A. Pielke, J. Eastman, R. Mahmood, and K. G. Hubbard (2003). 'Impact of Irrigation on Midsummer Surface Fluxes and Temperature under Dry Synoptic Conditions: A Regional Atmospheric Model Study of the U.S. High Plains'. In: *Mon. Weather Rev.* 131.3, 556–564.

Ament, F. and C. Simmer (2006). 'Improved representation of land-surface heterogeneity in a non-hydrostatic numerical weather prediction model'. In: *Boundary-Layer Meteorol.* 121.1, pp. 153–174.

Angevine, W. M. (2003). 'Urban–rural contrasts in mixing height and cloudiness over Nashville in 1999'. In: *J. Geophys. Res.* 108.D3.

Arino, O., J. J. Ramos Perez, V. Kalogirou, S. Bontemps, P. Defourny, and E. Van Bogaert (2012). *Global Land Cover Map for 2009 (GlobCover 2009).* data set. European Space Agency (ESA) & Université catholique de Louvain (UCL).

Arola, A. (1999). 'Parameterization of Turbulent and Mesoscale Fluxes for Heterogeneous Surfaces'. In: *J. Atmos. Sci.* 56.4, pp. 584–598.

Avissar, R. (1992). 'Conceptual aspects of a statistical-dynamical approach to represent landscape subgrid-scale heterogeneities in atmospheric models'. In: *J. Geophys. Res. [Atmos.]* 97.D3, pp. 2729–2742.

Avissar, R. and R. A. Pielke (1989). 'A parameterization of heterogeneous land surfaces for atmospheric numerical models and its impact on regional meteorology'. In: *Mon. Weather Rev.* 117.10, pp. 2113–2136.

Avissar, R. and T. Schmidt (1998). 'An evaluation of the scale at which ground-surface heat flux patchiness affects the convective boundary layer using large-eddy simulations'. In: *J. Atmos. Sci.* 55.16, pp. 2666–2689.

Baidya Roy, S. (2003). 'A preferred scale for landscape forced mesoscale circulations?' In: *J. Geophys. Res.* 108.D22.

Banta, R. M. (2003). 'Mixing-height differences between land use types: Dependence on wind speed'. In: *J. Geophys. Res.* 108.D10.

Behera, S. K., J.-J. Luo, S. Masson, P. Delecluse, S. Gualdi, A. Navarra, and T. Yamagata (2005). 'Paramount Impact of the Indian Ocean Dipole on the East African Short Rains: A CGCM Study'. In: *J. Clim.* 18.21, 4514–4530.

Best, M. J., A. Beljaars, J. Polcher, and P. Viterbo (2004). 'A Proposed Structure for Coupling Tiled Surfaces with the Planetary Boundary Layer'. In: *J. Hydrometeorol.* 5.6, pp. 1271–1278.

Best, M. J., M. Pryor, D. B. Clark, G. G. Rooney, R. . H. Essery, C. B. Ménard, J. M. Edwards, M. A. Hendry, A. Porson, N. Gedney, and et al. (2011). 'The Joint UK Land Environment Simulator (JULES), model description – Part 1: Energy and water fluxes'. In: *Geosci. Model Dev.* 4.3, pp. 677–699.

Blackadar, A. K. (1962). 'The vertical distribution of wind and turbulent exchange in a neutral atmosphere'. In: *J. Geophys. Res.* 67.8, 3095—3102.

Bonan, G. B., K. W. Oleson, M. Vertenstein, S. Levis, X. Zeng, Y. Dai, R. E. Dickinson, and Z.-L. Yang (2002). 'The Land Surface Climatology of the Community Land Model Coupled to the NCAR Community Climate Model*'. In: *J. Clim.* 15.22, 3123–3149.

Boucher, O., G. Myhre, and A. Myhre (2004). 'Direct human influence of irrigation on atmospheric water vapour and climate'. In: *Clim. Dyn.* 22.6-7, pp. 597–603.

Bouman, B., R. Lampayan, and T. Tuong (2007). *Water management in irrigated rice: coping with water scarcity.* Int. Rice Res. Inst.

Bou-Zeid, E., C. Meneveau, and M. B. Parlange (2004). 'Large-eddy simulation of neutral atmospheric boundary layer flow over heterogeneous surfaces: Blending height and effective surface roughness'. In: *Water Resour. Res.* 40.2, pp. 1–18.

Brinkop, S. and E. Roeckner (1995). 'Sensitivity of a general circulation model to parameterizations of cloud–turbulence interactions in the atmospheric boundary layer'. In: *Tellus A* 47.2, pp. 197–220.

Brovkin, V., T. Raddatz, C. H. Reick, M. Claussen, and V. Gayler (2009). 'Global biogeophysical interactions between forest and climate'. In: *Geophys. Res. Lett.* 36.L07405, pp. 1–5.

Brunsell, N. A., D. B. Mechem, and M. C. Anderson (2011). 'Surface heterogeneity impacts on boundary layer dynamics via energy balance partitioning'. In: *Atmos. Chem. Phys.* 11.7, pp. 3403–3416.

Carneiro, R. L. (1973). 'Structure, function, and equilibrium in the evolutionism of Herbert Spencer'. In: *J. J Anthropol. Res.* Pp. 77–95.

Claussen, M. (1995). 'Flux aggregation at large scales: on the limits of validity of the concept of blending height'. In: *J. Hydrol.* 166.3-4, pp. 371–382.

Claussen, M., U. Lohmann, E. Roeckner, and U. Schulzweida (1994). 'A global dataset of land surface parameters'. In: *MPI-Report* 135.

Claussen, M. (1991). 'Estimation of areally-averaged surface fluxes'. In: *Boundary-Layer Meteorol.* 54.4, pp. 387–410.

Cook, B. I., M. J. Puma, and N. Y. Krakauer (2011). 'Irrigation induced surface cooling in the context of modern and increased greenhouse gas forcing'. In: *Clim. Dyn.* 37.7-8, pp. 1587–1600.

Cooper, H. J., E. A. Smith, J. Gu, and S. Shewchuk (1997). 'Modeling the impact of averaging on aggregation of surface fluxes over BOREAS'. In: *J. Geophys. Res. [Atmos.]* 102.D24, pp. 29235–29253.

Cox, P., R. Betts, C. Bunton, R. Essery, P. Rowntree, and J. Smith (1999). 'The impact of new land surface physics on the GCM simulation of climate and climate sensitivity'. In: *Clim. Dyn.* 15.3, pp. 183–203.

De Fraiture, C. and D. Wichelns (2010). 'Satisfying future water demands for agriculture'. In: *Agric. Water Manage.* 97.4, pp. 502–511.

de Vrese, P. and S. Hagemann (2015). 'Explicit Representation of Spatial Sub-grid Scale Heterogeneity in an ESM'. In: *J. Hydrometeorol.* Submitted.

de Vrese, P., J.-P. Schulz, and S. Hagemann (2015). 'On the representation of heterogeneity in land surface-atmosphere coupling'. In: *Boundary-Layer Meteorol.* Submitted.

Dee, D., S. Uppala, A. Simmons, P. Berrisford, P. Poli, S. Kobayashi, U. Andrae, M. Balmaseda, G. Balsamo, P. B. P. Bechtold, A. Beljaars, L. van de Berg, J. Bidlot, N. Bormann, C. Delsol, R. Dragani, M. F. A. Geera, L. Haimberger, S. Healy, H. Hersbach, E. Holm, L. Isaksen, P. Kallberg, M. Koehler, M. Matricardi, A. McNally, B. Monge-Sanz, J. Morcrette, B. Park, C. Peubey, P. de Rosnay, C. Tavolato, J. Thepaut,

and F. Vitart (2011). 'The ERA-Interim reanalysis: Configuration and performance of the data assimilation system'. In: *Quart. J. Roy. Meteor. Soc.* 137.656, pp. 553–597.
Derbyshire, S. (1999). 'Boundary-Layer Decoupling over Cold Surfaces as a Physical Boundary-Instability'. In: *Boundary-Layer Meteorol.* 90.2, pp. 297–325.
Dev, S. M. (2015). 'Emerging Economies - Food and Energy Security, and Technology and Innovation'. In: ed. by P. Shome and P. Sharma. Springer. Chap. 4, pp. 89–112.
Di Gregorio, A. (2005). *Land cover classification system: classification concepts and user manual: LCCS*. 8. Food & Agriculture Org.
Dickinson, R. E. (1986). 'Biosphere/atmosphere transfer scheme (BATS) for the NCAR community climate model'. In: *NCAR Tech.* Note TN–275+STR72.
Dimri, A. (2009). 'Impact of subgrid scale scheme on topography and landuse for better regional scale simulation of meteorological variables over the western Himalayas'. In: *Clim. Dyn.* 32.4, pp. 565–574.
Dirmeyer, P. A., K. L. Brubaker, and T. DelSole (2009). 'Import and export of atmospheric water vapor between nations'. In: *J. Hydrol.* 365.1-2, 11–22.
Döll, P. and S. Siebert (2002). 'Global modeling of irrigation water requirements'. In: *Water Resour. Res.* 38.4, pp. 8–1.
Douglas, E., A. Beltrán-Przekurat, D. Niyogi, R. Pielke Sr, and C. Vörösmarty (2009). 'The impact of agricultural intensification and irrigation on land–atmosphere interactions and Indian monsoon precipitation—A mesoscale modeling perspective'. In: *Global Planet. Change* 67.1, pp. 117–128.
Douglas, E., D. Niyogi, S. Frolking, J. Yeluripati, R. A. Pielke, N. Niyogi, C. Vörösmarty, and U. Mohanty (2006). 'Changes in moisture and energy fluxes due to agricultural land use and irrigation in the Indian Monsoon Belt'. In: *Geophys. Res. Lett.* 33.14.
Dufresne, J.-L., M.-A. Foujols, S. Denvil, A. Caubel, O. Marti, O. Aumont, Y. Balkanski, S. Bekki, H. Bellenger, R. Benshila, and et al. (2013). 'Climate change projections using the IPSL-CM5 Earth System Model: from CMIP3 to CMIP5'. In: *Clim. Dyn.* 40.9-10, 2123–2165.
Ekici, A., C. Beer, S. Hagemann, J. Boike, M. Langer, and C. Hauck (2014). 'Simulating high-latitude permafrost regions by the JSBACH terrestrial ecosystem model'. In: *Geosci. Model Dev.* 7.2, 631–647.
Essery, R., M. J. Best, R. A. Betts, and C. M. Taylor (2003). 'Explicit representation of subgrid heterogeneity in a GCM land surface scheme'. In: *J. Hydrometeorol.* 4.3, pp. 530–543.
Essery, R. and D. B. Clark (2003). 'Developments in the MOSES 2 land-surface model for PILPS 2e'. In: *Global Planet. Change* 38.1-2, pp. 161–164.
Lemmelä, R. and N. Helenius, eds. (1998). *Large-scale field experiments to improve land surface parameterisations*. Proceedings of 'The Second International Conference on Climate and Water'.
Gates, W. L., J. S. Boyle, C. Covey, C. G. Dease, C. M. Doutriaux, R. S. Drach, M. Fiorino, P. J. Gleckler, J. J. Hnilo, S. M. Marlais, T. J. Phillips, G. L. Potter, B. D. Santer, K. R. Sperber, K. E. Taylor, and D. N. Williams (1999). 'An Overview of the Results of the Atmospheric Model Intercomparison Project (AMIP I)'. In: *Bull. Amer. Meteor. Soc.* 80.1, 29–55.

Giorgetta, M. A., E. Roeckner, T. Mauritsen, J. Bader, T. Crueger, M. Esch, S. Rast, L. Kornblueh, H. Schmidt, S. Kinne, C. Hohenegger, B. Moebis, T. Krismer, K. H. Wieners, and B. Stevens (2013). 'The atmospheric general circulation model ECHAM6-Model description'. In: *MPI-Report on Earth System Science* 135, pp. 1–172.

Giorgi, F. (1997). 'An approach for the representation of surface heterogeneity in land surface models. Part I: Theoretical framework'. In: *Mon. Weather Rev.* 125.8, pp. 1885–1899.

Giorgi, F. and R. Avissar (1997). 'Representation of heterogeneity effects in earth system modeling: Experience from land surface modeling'. In: *Rev. Geophys.* 35.4, pp. 413–437.

Giorgi, F., R. Francisco, and J. Pal (2003). 'Effects of a Subgrid-Scale Topography and Land Use Scheme on the Simulation of Surface Climate and Hydrology. Part I: Effects of Temperature and Water Vapor Disaggregation'. In: *J. Hydrometeorol.* 4.2, pp. 317–333.

Godfray, H. C. J., J. R. Beddington, I. R. Crute, L. Haddad, D. Lawrence, J. F. Muir, J. Pretty, S. Robinson, S. M. Thomas, and C. Toulmin (2010). 'Food Security: The Challenge of Feeding 9 Billion People'. In: *Science* 327.5967, 812–818.

Gordon, L. J., W. Steffen, B. F. Jönsson, C. Folke, M. Falkenmark, and Å. Johannessen (2005). 'Human modification of global water vapor flows from the land surface'. In: *Proc. Natl. Acad. Sci. U.S.A.* 102.21, pp. 7612–7617.

Guillod, B. P., B. Orlowsky, D. G. Miralles, A. J. Teuling, and S. I. Seneviratne (2015). 'Reconciling spatial and temporal soil moisture effects on afternoon rainfall'. In: *Nat. Commun.* 6, p. 6443.

Hagemann, S., T. Blome, F. Saeed, and T. Stacke (2014). 'Perspectives in Modelling Climate–Hydrology Interactions'. In: pp. 739–764.

Hagemann, S., C. Chen, D. B. Clark, S. Folwell, S. N. Gosling, I. Haddeland, N. Hanasaki, J. Heinke, F. Ludwig, F. Voss, and et al. (2013). 'Climate change impact on available water resources obtained using multiple global climate and hydrology models'. In: *Earth Syst. Dynam.* 4.1, 129–144.

Hagemann, S. and T. Stacke (2014). 'Impact of the soil hydrology scheme on simulated soil moisture memory'. In: *Clim. Dyn.* Pp. 1–20.

Harding, R., E. Blyth, O. Tuinenburg, and A. Wiltshire (2013). 'Land atmosphere feedbacks and their role in the water resources of the Ganges basin'. In: *Sci. Total Environ.* 468-469, S85–S92.

Harris, I., P. Jones, T. Osborn, and D. Lister (2013). 'Updated high-resolution grids of monthly climatic observations - the CRU TS3.10 Dataset'. In: *Int. J. Climatol.* 34.3, 623–642.

Heinemann, G. and M. Kerschgens (2005). 'Comparison of methods for area-averaging surface energy fluxes over heterogeneous land surfaces using high-resolution non-hydrostatic simulations'. In: *Int. J. Climatol.* 25.3, pp. 379–403.

Indeje, M. and F. H. M. Semazzi (2000). 'Relationships Between QBO in the Lower Equatorial Stratospheric Zonal Winds and East African Seasonal Rainfall'. In: *Meteorol. Atmos. Phys.* 73.3-4, 227–244.

Jungclaus, J. H., N. Fischer, H. Haak, K. Lohmann, J. Marotzke, D. Matei, U. Mikolajewicz, D. Notz, and J. S. von Storch (2013). 'Characteristics of the ocean simulations in the Max Planck Institute Ocean Model (MPIOM) the ocean component of the MPI-Earth system model'. In: *J. Adv. Model. Earth Syst* 5.2, pp. 422–446.

Kabat, P., R. Hutjes, and R. Feddes (1997). 'The scaling characteristics of soil parameters: From plot scale heterogeneity to subgrid parameterization'. In: *J. Hydrol.* 190.3-4, 363—396.

Koster, R. D. (2004). 'Regions of Strong Coupling Between Soil Moisture and Precipitation'. In: *Science* 305.5687, 1138–1140.

Koster, R. D. and M. J. Suarez (1992). 'A comparative analysis of two land surface heterogeneity representations'. In: *J. Clim.* 5.12, pp. 1379–1390.

Krinner, G., N. Viovy, N. de Noblet-Ducoudré, J. Ogée, J. Polcher, P. Friedlingstein, P. Ciais, S. Sitch, and I. C. Prentice (2005). 'A dynamic global vegetation model for studies of the coupled atmosphere-biosphere system'. In: *Global Biogeochem. Cycles* 19.1.

Kueppers, L. M., M. A. Snyder, and L. C. Sloan (2007). 'Irrigation cooling effect: Regional climate forcing by land-use change'. In: *Geophys. Res. Lett.* 34.3.

Lee, E., T. N. Chase, B. Rajagopalan, R. G. Barry, T. W. Biggs, and P. J. Lawrence (2009). 'Effects of irrigation and vegetation activity on early Indian summer monsoon variability'. In: *Int. J. Climatol.* 29.4, pp. 573–581.

Lin, S.-J. and R. B. Rood (1996). 'Multidimensional Flux-Form Semi-Lagrangian Transport Schemes'. In: *Mon. Weather Rev.* 124.9, 2046–2070.

Liu, J. and H. Yang (2010). 'Spatially explicit assessment of global consumptive water uses in cropland: Green and blue water'. In: *J. Hydrol.* 384.3, pp. 187–197.

Lobell, D., G. Bala, C. Bonfils, and P. Duffy (2006a). 'Potential bias of model projected greenhouse warming in irrigated regions'. In: *Geophys. Res. Lett.* 33.13.

Lobell, D., G. Bala, and P. Duffy (2006b). 'Biogeophysical impacts of cropland management changes on climate'. In: *Geophys. Res. Lett.* 33.6.

Lobell, D., G. Bala, A. Mirin, T. Phillips, R. Maxwell, and D. Rotman (2009). 'Regional differences in the influence of irrigation on climate'. In: *J. Clim.* 22.8, pp. 2248–2255.

Lotze-Campen, H., C. Müller, A. Bondeau, S. Rost, A. Popp, and W. Lucht (2008). 'Global food demand, productivity growth, and the scarcity of land and water resources: a spatially explicit mathematical programming approach'. In: *Agric. Econ.*

Louis, J.-F. (1979). 'A parametric model of vertical eddy fluxes in the atmosphere'. In: *Boundary-Layer Meteorol* 17.2, 187—202.

Lucas-Picher, P., J. H. Christensen, F. Saeed, P. Kumar, S. Asharaf, B. Ahrens, A. J. Wiltshire, D. Jacob, and S. Hagemann (2011). 'Can Regional Climate Models Represent the Indian Monsoon?' In: *J. Hydrometeorol.* 12.5, pp. 849–868.

Lynn, B. H., F. Abramopoulos, and R. Avissar (1995a). 'Using Similarity Theory to Parameterize Mesoscale Heat Fluxes Generated by Subgrid-Scale Landscape Discontinuities in GCMs'. In: *J. Clim.* 8.4, 932—951.

Lynn, B. H., D. Rind, and R. Avissar (1995b). 'The Importance of Mesoscale Circulations Generated by Subgrid-Scale Landscape Heterogeneities in General Circulation Models'. In: *J. Clim.* 8.2, 191—205.

Lyon, B. and D. G. DeWitt (2012). 'A recent and abrupt decline in the East African long rains'. In: *Geophys. Res. Lett.* 39.2.

Ma, Y., M. Menenti, R. Feddes, and J. Wang (2008). 'Analysis of the land surface heterogeneity and its impact on atmospheric variables and the aerodynamic and thermodynamic roughness lengths'. In: *J. Geophys. Res. [Atmos.]* 113.D08113, pp. 1–11.

Mahrt, L. (2000). 'Surface Heterogeneity and Vertical Structure of the Boundary Layer'. English. In: *Boundary-Layer Meteorol.* 96.1-2, pp. 33–62.

Mahrt, L. and J. Sun (1995). 'Dependence of surface exchange coefficients on averaging scale and grid size'. In: *Quart. J. Roy. Meteor. Soc.* 121.528, pp. 1835–1852.

Mailhot, J. and R. Benoit (1982). 'A finite-element model of the atmospheric boundary layer suitable for use with numerical weather prediction models'. In: *J. Atmos. Sci.* 39.10, pp. 2249–2266.

Manrique-Suñén, A., A. Nordbo, G. Balsamo, A. Beljaars, and I. Mammarella (2013). 'Representing Land Surface Heterogeneity: Offline Analysis of the Tiling Method'. In: *J. Hydrometeorol.* 14.3, pp. 850–867.

Mason, P. J. (1988). 'The formation of areally-averaged roughness lengths'. In: *Quart. J. Roy. Meteor. Soc.* 114.480, pp. 399–420.

Maxwell, D. and M. Fitzpatrick (2012). 'The 2011 Somalia famine: Context, causes, and complications'. In: *Glob. Food Sec.* 1.1, 5–12.

Mellor, G. L. and T. Yamada (1982). 'Development of a turbulence closure model for geophysical fluid problems'. In: *Rev. Geophys.* 20.4, pp. 851–875.

Milly, P. and A. Shmakin (2002). 'Global modeling of land water and energy balances. Part I: The land dynamics (LaD) model'. In: *J. Hydrometeorol.* 3.3, pp. 283–299.

Molod, A. and H. Salmun (2002). 'A global assessment of the mosaic approach to modeling land surface heterogeneity'. In: *J. Geophys. Res. [Atmos.]* 107.D14, pages.

Molod, A., H. Salmun, and D. W. Waugh (2003). 'A new look at modeling surface heterogeneity: Extending its influence in the vertical.' In: *J. Hydrometeorol.* 4.5, pp. 810–825.

Molod, A., H. Salmun, and D. W. Waugh (2004). 'The Impact on a GCM Climate of an Extended Mosaic Technique for the Land-Atmosphere Coupling'. In: *J. Clim.* 17.20, pp. 3877–3891.

Mott, R., C. Gromke, T. Grünewald, and M. Lehning (2013). 'Relative importance of advective heat transport and boundary layer decoupling in the melt dynamics of a patchy snow cover'. In: *Adv. Water Resour.* 55, pp. 88–97.

Mott, R., M. Lehning, M. Daniels, and M. Lehning (2014). 'Atmospheric Flow Development and Associated Changes in Turbulent Sensible Heat Flux over a Patchy Mountain Snow Cover'. In: *J. Hydrometeorol.* 2014. in press.

Niyogi, D., C. Kishtawal, S. Tripathi, and R. S. Govindaraju (2010). 'Observational evidence that agricultural intensification and land use change may be reducing the Indian summer monsoon rainfall'. In: *Water Resour. Res.* 46.3, pp. 1–17.

Oki, T. and S. Kanae (2006). 'Global hydrological cycles and world water resources'. In: *Science* 313.5790, pp. 1068–1072.

Oleson, K. W., D. M. Lawrence, G. B, M. G. Flanner, E. Kluzek, P. J, S. Levis, S. C. Swenson, E. Thornton, J. Feddema, C. L. Heald, J.-f. Lamarque, G.-y. Niu, T. Qian, S.

Running, K. Sakaguchi, L. Yang, X. Zeng, and X. Zeng (2010). *Technical Description of version 4.0 of the Community Land Model (CLM)*. NCAR TECHNICAL NOTE NCAR/TN-478+STR. NATIONAL CENTER FOR ATMOSPHERIC RESEARCH.

Otto, J., T. Raddatz, and M. Claussen (2011). 'Strength of forest-albedo feedback in mid-Holocene climate simulations'. In: *Clim. Past* 7.3, 1027—1039.

Patton, E. G., P. P. Sullivan, and C.-H. Moeng (2005). 'The influence of idealized heterogeneity on wet and dry planetary boundary layers coupled to the land surface'. In: *J. Atmos. Sci.* 62.7, pp. 2078–2097.

Polcher, J., K. Laval, L. Dümenil, J. Lean, and P. Rowntree (1996). 'Comparing three land surface schemes used in general circulation models'. In: *J. Hydrol.* 180.1, pp. 373–394.

Polcher, J., B. McAvaney, P. Viterbo, M.-A. Gaertner, A. Hahmann, J.-F. Mahfouf, J. Noilhan, T. Phillips, A. Pitman, C. Schlosser, J.-P. Schulz, B. Timbal, D. Verseghy, and Y. Xue (1998). 'A proposal for a general interface between land surface schemes and general circulation models'. In: *Global Planet. Change* 19.1–4, pp. 261–276.

Puma, M. and B. Cook (2010). 'Effects of irrigation on global climate during the 20th century'. In: *J. Geophys. Res. [Atmos.]* 115.D16.

Raddatz, T., C. Reick, W. Knorr, J. Kattge, E. Roeckner, R. Schnur, K.-G. Schnitzler, P. Wetzel, and J. Jungclaus (2007). 'Will the tropical land biosphere dominate the climate–carbon cycle feedback during the twenty-first century?' In: *Clim. Dyn.* 29.6, pp. 565–574.

Raupach, M. and J. Finnigan (1995). 'Scale issues in boundary-layer meteorology: surface energy balances in heterogeneous terrain'. In: *Hydrol. Process.* 9.5-6, pp. 589–612.

Richtmyer, R. D. and K. W. Morton (1967). *Difference method for initial-value problems*. Interscience Publishers (New York).

Rieck, M., C. Hohenegger, and C. C. van Heerwaarden (2014). 'The influence of land surface heterogeneities on cloud size development'. In: *Mon. Weather Rev.* 142.10, pp. 3830–3846.

Roeckner, E., K. Arpe, L. Bengtsson, M. Christoph, M. Claussen, L. Dumenil, M. Esch, M. Giorgetta, U. Schlese, and U. Schulzweida (1996). 'The atmospheric general circulation model ECHAM4: Model description and simulation of present-day climate'. In: *MPI-Report* 218, pp. 1–90.

Roesch, A. and E. Roeckner (2006). 'Assessment of snow cover and surface albedo in the ECHAM5 general circulation model'. In: *J. Clim.* 19.16, pp. 3828–3843.

Roesch, A., M. Wild, H. Gilgen, and A. Ohmura (2001). 'A new snow cover fraction parametrization for the ECHAM4 GCM'. In: *Clim. Dyn.* 17.12, pp. 933–946.

Sacks, W. J., B. I. Cook, N. Buenning, S. Levis, and J. H. Helkowski (2009). 'Effects of global irrigation on the near-surface climate'. In: *Clim. Dyn.* 33.2-3, pp. 159–175.

Saeed, F. (2011). 'Impact of irrigation on South Asian monsoon climate'. PhD thesis. University of Hamburg.

Saeed, F., S. Hagemann, and D. Jacob (2009). 'Impact of irrigation on the South Asian summer monsoon'. In: *Geophys. Res. Lett.* 36.20.

Saeed, F., S. Hagemann, S. Saeed, and D. Jacob (2013). 'Influence of mid-latitude circulation on upper Indus basin precipitation: the explicit role of irrigation'. In: *Clim. Dyn.* 40.1-2, pp. 21–38.

Salmun, H., A. Molod, and A. Ira (2007). 'Observational validation of an extended mosaic technique for capturing subgrid scale heterogeneity in a GCM'. In: *Tellus B* 59.3, pp. 625–632.

Salzen, K. von, J. F. Scinocca, N. A. McFarlane, J. Li, J. N. S. Cole, D. Plummer, D. Verseghy, M. C. Reader, X. Ma, M. Lazare, and et al. (2013). 'The Canadian Fourth Generation Atmospheric Global Climate Model (CanAM4). Part I: Representation of Physical Processes'. In: *Atmos.-Ocean* 51.1, pp. 104–125.

Schneider, U., A. Becker, P. Finger, A. Meyer-Christoffer, M. Ziese, and B. Rudolf (2013). 'GPCC's new land surface precipitation climatology based on quality-controlled in situ data and its role in quantifying the global water cycle'. In: *Theor. Appl. Climatol.* 115.1-2, 15–40.

Schomburg, A., V. Venema, F. Ament, and C. Simmer (2012). 'Disaggregation of screen-level variables in a numerical weather prediction model with an explicit simulation of subgrid-scale land-surface heterogeneity'. In: *Meteorol. Atmos. Phys.* 116.3-4, pp. 81–94.

Schulz, J.-P., L. Dümenil, and J. Polcher (2001). 'On the Land Surface–Atmosphere Coupling and Its Impact in a Single-Column Atmospheric Model'. In: *J. Appl. Meteorol.* 40.3, pp. 642–663.

Schulz, J.-P., L. Dümenil, J. Polcher, C. Schlosser, and Y. Xue (1998). 'Land surface energy and moisture fluxes: Comparing three models'. In: *J. Appl. Meteorol.* 37.3, pp. 288–307.

Seckler, D., U. Amarasinghe, D. Molden, R. de Silva, and B. R (1998). *World water demand and supply, 1990 to 2025: Scenarios and issues*. Vol. 19. Iwmi.

Segal, M., J. Garratt, R. Pielke, W. Schreiber, A. Rodi, G. Kallos, and J. Weaver (1989). 'The impact of crop areas in northeast Colorado on midsummer mesoscale thermal circulations'. In: *Mon. Weather Rev.* 117.4, pp. 809–825.

Sellers, P. (1991). 'Modeling and observing land-surface-atmosphere interactions on large scales'. In: *Surv. Geophys.* 12.1-3, pp. 85–114.

Sellers, P., Y. Mintz, Y. e. a. Sud, and A. Dalcher (1986). 'A simple biosphere model (SiB) for use within general circulation models'. In: *J. Atmos. Sci.* 43.6, pp. 505–531.

Seth, A., F. Giorgi, and R. E. Dickinson (1994). 'Simulating fluxes from heterogeneous land surfaces: Explicit subgrid method employing the biosphere-atmosphere transfer scheme (BATS)'. In: *J. Geophys. Res. [Atmos.]* 99.D9, pp. 18651–18667.

Shevliakova, E., S. W. Pacala, S. Malyshev, G. C. Hurtt, P. C. D. Milly, J. P. Caspersen, L. T. Sentman, J. P. Fisk, C. Wirth, and C. Crevoisier (2009). 'Carbon cycling under 300 years of land use change: Importance of the secondary vegetation sink'. In: *Global Biogeochem. Cycles* 23.2, pp. 1–16.

Shiklomanov, I. A. (2000). 'Appraisal and assessment of world water resources'. In: *Water Int.* 25.1, pp. 11–32.

Shongwe, M. E., G. J. van Oldenborgh, B. van den Hurk, and M. van Aalst (2011). 'Projected Changes in Mean and Extreme Precipitation in Africa under Global Warming. Part II: East Africa'. In: *J. Clim.* 24.14, 3718–3733.

Siebert, S., P. Döll, J. Hoogeveen, J.-M. Faures, K. Frenken, and S. Feick (2005). 'Development and validation of the global map of irrigation areas'. In: *HESSD* 2.4, pp. 1299–1327.

Siebert, S., M. Kummu, M. Porkka, P. Döll, N. Ramankutty, and B. R. Scanlon (2015). 'A global data set of the extent of irrigated land from 1900 to 2005'. In: *HESS* 19.3, 1521–1545.

Siebert, S., V. Henrich, K. Frenken, and J. Burke (2013). *Global Map of Irrigation Areas version 5*. Rheinische Friedrich-Wilhelms-University, Bonn, Germany / Food and Agriculture Organization of the United Nations, Rome, Italy.

Stevens, B., M. Giorgetta, M. Esch, T. Mauritsen, T. Crueger, S. Rast, M. Salzmann, H. Schmidt, J. Bader, K. Block, R. Brokopf, I. Fast, S. Kinne, L. Kornblueh, U. Lohmann, R. Pincus, T. Reichler, and E. Roeckner (2013). 'Atmospheric component of the MPI-M Earth System Model: ECHAM6'. In: *J. Adv. Model. Earth Syst* 5.2, pp. 146–172.

Strunin, M. A., T. Hiyama, J. Asanuma, and T. Ohata (2004). 'Aircraft observations of the development of thermal internal boundary layers and scaling of the convective boundary layer over non-homogeneous land surfaces'. In: *Boundary-Layer Meteorol.* 111.3, pp. 491–522.

Tatalovic, M. (2009). 'Irrigation reform needed in Asia'. In: *Nature*. Published online 17 August 2009.

Tiwari, V. M., J. Wahr, and S. Swenson (2009). 'Dwindling groundwater resources in northern India, from satellite gravity observations'. In: *Geophys. Res. Lett.* 36.18, pp. 1–5.

Tuinenburg, O., R. Hutjes, T. Stacke, A. Wiltshire, and P. Lucas-Picher (2014). 'Effects of irrigation in India on the atmospheric water budget'. In: *J. Hydrometeorol.* 2014.

Van den Hurk, B. and A. Beljaars (1996). 'Impact of some simplifying assumptions in the new ECMWF surface scheme'. In: *J. Appl. Meteorol.* 35.8, pp. 1333–1343.

van der Ent, R. J., H. H. G. Savenije, B. Schaefli, and S. C. Steele-Dunne (2010). 'Origin and fate of atmospheric moisture over continents'. In: *Water Resour. Res.* 46.9.

Verseghy, D. (2009). *CLASS – THE CANADIAN LAND SURFACE SCHEME (VERSION 3.4)*. Technical Documentation. Environment Canada Science and Technology Branch. URL: `www.usask.ca/ip3/download/CLASS_v3_4_Documentation_v1_1.pdf`.

Wada, Y., L. Beek, and M. F. Bierkens (2012). 'Nonsustainable groundwater sustaining irrigation: A global assessment'. In: *Water Resour. Res.* 48.6.

Wada, Y., D. Wisser, S. Eisner, M. Flörke, D. Gerten, I. Haddeland, N. Hanasaki, Y. Masaki, F. T. Portmann, T. Stacke, et al. (2013). 'Multimodel projections and uncertainties of irrigation water demand under climate change'. In: *Geophys. Res. Lett.* 40.17, pp. 4626–4632.

Weedon, G. P., S. Gomes, P. Viterbo, W. J. Shuttleworth, E. Blyth, H. Oesterle, J. C. Adam, N. Bellouin, O. Boucher, and M. Best (2011). 'Creation of the WATCH Forcing Data and Its Use to Assess Global and Regional Reference Crop Evaporation over Land during the Twentieth Century'. In: *J. Hydrometeorol.* 12.5, pp. 823–848.

Wieringa, J. (1976). 'An objective exposure correction method for average wind speeds measured at a sheltered location'. In: *Quart. J. Roy. Meteor. Soc.* 102.431, pp. 241–253.

Wild, M., D. Folini, M. Z. Hakuba, C. Schär, S. I. Seneviratne, S. Kato, D. Rutan, C. Ammann, E. F. Wood, and G. König-Langlo (2014). 'The energy balance over land and oceans: an assessment based on direct observations and CMIP5 climate models'. In: *Clim. Dyn.* Pp. 1–37.

Williams, A. P. and C. Funk (2011). 'A westward extension of the warm pool leads to a westward extension of the Walker circulation, drying eastern Africa'. In: *Clim. Dyn.* 37.11-12, 2417–2435.

Wood, N. and P. Mason (1991). 'The influence of static stability on the effective roughness lengths for momentum and heat transfer'. In: *Quart. J. Roy. Meteor. Soc.* 117.501, pp. 1025–1056.

WorldBank (2008). *World Development Report 2008: agriculture for development*. Tech. rep. The World Bank.

Yang, W., R. Seager, M. A. Cane, and B. Lyon (2014). 'The East African Long Rains in Observations and Models'. In: *J. Clim.* 27.19, 7185–7202.

Yoshikawa, S., J. Cho, H. Yamada, N. Hanasaki, A. Khajuria, and S. Kanae (2013). 'An assessment of global net irrigation water requirements from various water supply sources to sustain irrigation: rivers and reservoirs (1960–2000 and 2050)'. In: *HESSD* 10.1, pp. 1251–1288.

A. Equations

Appendix 1.1 Vertical Diffusion

Inserting Eq. 13 into Eq. 12 gives:

$$\frac{x_{l,i}^{t+1} - x_{l,i}^{t}}{\Delta t} = \frac{1}{\Delta z_l} \cdot (K_{l+\frac{1}{2},i} \cdot \frac{F_{x,l,i}^{t} + \sum_{j=1}^{n} x_{l,j}^{t+1} \cdot E_{x,l,i,j}^{t} - x_{l,i}^{t+1}}{\delta z_l} - \sum_{j=1}^{n} Fmix_{l-1,i,j}^{t} \cdot K_{l-\frac{1}{2},j} \cdot \frac{x_{l,j}^{t+1} - x_{l-1,j}^{t+1}}{\delta z_{l-1}}) \tag{36}$$

This can be rearranged to:

$$\begin{aligned} & x_{l,i}^{t+1} \cdot (1 + \frac{\Delta t}{\Delta z_l} \cdot (K_{l+\frac{1}{2},i} \cdot \frac{1 - E_{x,l,i,i}^{t}}{\delta z_l} + K_{l-\frac{1}{2},i} \cdot Fmix_{l-1,i,i} \cdot \frac{1}{\delta z_{l-1}}) \\ & + \sum_{\substack{j=1 \\ j \neq i}}^{n} x_{l,j}^{t+1} \cdot \frac{\Delta t}{\Delta z_l} \cdot (K_{l-\frac{1}{2},j} \cdot \frac{Fmix_{l-1,i,j}}{\delta z_{l-1}} - K_{l+\frac{1}{2},i} \cdot \frac{E_{x,l,i,j}^{t}}{\delta z_l}) \\ & = x_{l,i}^{t} + \frac{\Delta t}{\Delta z_l} \cdot K_{l+\frac{1}{2},i} \cdot \frac{F_{x,l,i}^{t}}{\delta z_l} \\ & + \sum_{j=1}^{n} x_{l-1,j}^{t+1} \cdot K_{l-\frac{1}{2},j} \cdot \frac{Fmix_{l-1,i,j}}{\delta z_{l-1}} \end{aligned} \tag{37}$$

The equation can be simplified to:

$$\sum_{j=1}^{n} a_{i,j} \cdot x_{l,j}^{t+1} = b_i, \text{with} \tag{38a}$$

$$a_{i,j} = (1 + \frac{\Delta t}{\Delta z_l} \cdot (K_{l+\frac{1}{2},i} \cdot \frac{1 - E_{x,l,i,i}^{t}}{\delta z_l} + K_{l-\frac{1}{2},i} \cdot Fmix_{l-1,i,i} \cdot \frac{1}{\delta z_{l-1}})) \quad \text{, for j = i} \tag{38b}$$

$$a_{i,j} = \frac{\Delta t}{\Delta z_l} \cdot (K_{l-\frac{1}{2},j} \cdot \frac{Fmix_{l-1,i,j}}{\delta z_{l-1}} - K_{l+\frac{1}{2},i} \cdot \frac{E_{x,l,i,j}^{t}}{\delta z_l}) \quad \text{, for j} \neq \text{i} \tag{38c}$$

$$b_i = x_{l,i}^{t} + \frac{\Delta t}{\Delta z_l} \cdot K_{l+\frac{1}{2},i} \cdot \frac{F_{x,l,i}^{t}}{\delta z_l} + \sum_{j=1}^{n} x_{l-1,j}^{t+1} \cdot K_{l-\frac{1}{2},j} \cdot \frac{Fmix_{l-1,i,j}}{\delta z_{l-1}} \tag{38d}$$

Using matrix notation these equations can be written as:

$$A_{n,n} \cdot \vec{X}_{n}^{t+1} = \vec{B}_n, \text{with} \tag{39a}$$

$$A_{n,n} = \begin{pmatrix} a_{1,1} & \cdots & a_{1,j} & \cdots & a_{1,n} \\ \vdots & \vdots & \ddots & \vdots & \\ a_{i,1} & \cdots & a_{i,j} & \cdots & a_{i,n} \\ \vdots & \vdots & \ddots & \vdots & \\ a_{n,1} & \cdots & a_{n,j} & \cdots & a_{n,n} \end{pmatrix} \quad (39b) \qquad \vec{X}_n = \begin{pmatrix} x_{l,1}^{t+1} \\ \vdots \\ x_{l,j}^{t+1} \\ \vdots \\ x_{l,n}^{t+1} \end{pmatrix} \quad (39c) \quad \vec{B}_n = \begin{pmatrix} b_1 \\ \vdots \\ b_i \\ \vdots \\ b_n \end{pmatrix}. \quad (39d)$$

Hence:

$$A_{n,n}^{-1} \cdot \vec{B}_n = \vec{X}_n^{t+1}, \text{with} \quad (40a)$$

$$A_{n,n}^{-1} = \begin{pmatrix} a_{1,1}^I & \cdots & a_{1,j}^I & \cdots & a_{1,n}^I \\ \vdots & \vdots & \ddots & \vdots & \\ a_{i,1}^I & \cdots & a_{i,j}^I & \cdots & a_{i,n}^I \\ \vdots & \vdots & \ddots & \vdots & \\ a_{n,1}^I & \cdots & a_{n,j}^I & \cdots & a_{n,n}^I \end{pmatrix} \quad (40b) \qquad \vec{B}_n = \begin{pmatrix} b_1 \\ \vdots \\ b_j \\ \vdots \\ b_n \end{pmatrix} \quad (40c) \quad \vec{X}_n = \begin{pmatrix} x_{l,1}^{t+1} \\ \vdots \\ x_{l,i}^{t+1} \\ \vdots \\ x_{l,n}^{t+1} \end{pmatrix}. \quad (40d)$$

From this follows

$$\sum_{j=1}^{n} a_{i,j}^I \cdot b_j = x_{l,i}^{t+1} \quad (41)$$

Reinserting Eq. 38 for b_j, Eq.41 becomes:

$$x_{l,i}^{t+1} = \sum_{j=1}^{n} a_{i,j}^I \cdot (x_{l,j}^t + \frac{\Delta t}{\Delta z_l} \cdot K_{l+\frac{1}{2},j} \cdot \frac{F_{x,l,j}^t}{\delta z_l} + \sum_{k=1}^{n} x_{l-1,k}^{t+1} \cdot K_{l-\frac{1}{2},k} \cdot \frac{Fmix_{l-1,j,k}}{\delta z_{l-1}}) \quad (42)$$

Analogous to Eq.12 one can express the dry static energy and humidity within tile i on level l as a function of all the tile values on level $l-1$:

$$x_{l,i}^{t+1} = F_{x,l-1,i}^t + \sum_{j=1}^{n} E_{x,l-1,i,j}^t \cdot x_{l-1,j}^{t+1}, \text{with} \quad (43a)$$

$$E_{x,l-1,i,j}^t = K_{l-\frac{1}{2},j} \cdot \frac{1}{\delta z_{l-1}} \cdot \sum_{k=1}^{n} Fmix_{l-1,k,j} \cdot a_{i,k}^I \quad (43b)$$

$$F_{x,l-1,i}^t = \sum_{j=1}^{n} a_{i,j}^I \cdot (x_{l,j}^t + \frac{\Delta t}{\Delta z_l} \cdot K_{l+\frac{1}{2},j} \cdot \frac{F_{x,l,j}^t}{\delta z_l}) \quad (43c)$$

Above the level of the blending height the fluxes are horizontally homogeneous and the vertical diffusion can be calculated by the method for the homogeneous case, described above. At the blending height the share which the flux from a given tile has on the flux between the level of the blending height and the inferior level, is equal to the share the

tile has in the grid box area, the surface cover fraction of the tile $sfrac_j$.

$$\frac{x^{t+1}_{blend} - x^{t}_{blend}}{\Delta t} = \frac{1}{\Delta z_{blend}} \cdot (K_{blend+\frac{1}{2}} \cdot \frac{F^{t}_{blend} + x^{t+1}_{blend} \cdot E^{t}_{blend} - x^{t+1}_{blend}}{\delta z_{blend}} - \sum_{j=1}^{n} sfrac_j \cdot K_{blend-\frac{1}{2},j} \cdot \frac{x^{t+1}_{blend} - x^{t+1}_{blend-1,j}}{\delta z_{blend-1}}) \tag{44}$$

This allows the coefficients $E^{t}_{blend-1,i,j}$ and $F^{t}_{blend-1,i}$ to be determined in the following manner:

$$E^{t}_{blend-1,i,j} = sfrac_j \cdot \frac{\Delta t}{\Delta z_l} \cdot \frac{K_{blend-\frac{1}{2},j}}{\delta z_l} \cdot C^{-1} \tag{45a}$$

$$F^{t}_{blend-1,i} = (x^{t}_{blend} + \frac{\Delta t}{\Delta z_l} \cdot F^{t}_{blend} \cdot \frac{K_{blend+\frac{1}{2}}}{\delta z_l}) \cdot C^{-1} \tag{45b}$$

$$C = 1 + \frac{\Delta t}{\Delta z_l} \cdot (\frac{K_{blend+\frac{1}{2}}}{\delta z_l} \cdot (1 - E^{t}_{blend}) + \sum_{k=1}^{n} sfrac_k \cdot K_{blend-\frac{1}{2},k}) \tag{45c}$$

Using the E's and F's at the blending height $(blend-1, i, j)$ in Eq.13, the entire atmospheric column below the blending height can be determined with the method described above.

Appendix 1.2 Surface fluxes and energy balance

Equation 16 can be rearranged so that:

$$Q^{t+1}_{x,i} = b_i + \sum_{j=1}^{n} x^{t+1}_{1,j} \cdot a_{i,j}, \text{with} \tag{46a}$$

$$a_{i,j} = -(1 + \frac{\Delta t}{\Delta z_l} \cdot K_{1+\frac{1}{2},i} \cdot \frac{1 - E^{t}_{1,i,i}}{\delta z_l}) \quad \text{, for j = i} \tag{46b}$$

$$a_{i,j} = \frac{\Delta t}{\Delta z_l} \cdot K_{1+\frac{1}{2},i} \cdot \frac{E^{t}_{1,i,j}}{\delta z_l} \quad \text{, for j} \neq \text{i} \tag{46c}$$

$$b_i = x^{t}_{1,i} + \frac{\Delta t}{\Delta z_l} \cdot K_{1+\frac{1}{2},i} \cdot \frac{F^{t}_{1,i}}{\delta z_l} \tag{46d}$$

Based upon this formulation we can equate the surface fluxes just below the lowest level in the atmosphere, the atmospheric values for sensible heat and moisture and the coefficients $a_{i,j}$ and b_i with the tile specific fluxes at the surface:

$$Q^{t+1}_{x,i} = \sum_{j=1}^{n} Fmix_{1,i,j} \cdot Q^{t+1,*}_{x,j} = b_i + \sum_{j=1}^{n} x^{t+1}_{1,j} \cdot a_{i,j} \tag{47}$$

Hence we obtain:

$$bs_i + \sum_{j=1}^{n} s_{1,j}^{t+1} \cdot a_{i,j} = \sum_{j=1}^{n} Fmix_{1,i,j} \cdot cdrag_j \cdot (s_{1,j}^{t+1} - s_{surf,j}^{t+1}) \quad \text{, for sens. heat} \tag{48a}$$

$$bq_i + \sum_{j=1}^{n} q_{1,j}^{t+1} \cdot a_{i,j} = \sum_{j=1}^{n} Fmix_{1,i,j} \cdot cdrag_j \cdot (q_{1,j}^{t+1} - q_{surf,j}^{t+1}) \quad \text{, for moisture} \tag{48b}$$

q_{surf}^{t+1} can be described by the saturation specific humidity at surface temperature and the moisture availability coefficients α_j and β_j, hence it can be described as a function of s_{surf}^{t+1} and the heat capacity at constant pressure c_p.

$$bq_i + \sum_{j=1}^{n} q_{1,j}^{t+1} \cdot a_{i,j} = \sum_{j=1}^{n} Fmix_{1,i,j} \cdot cdrag_j \cdot \beta_j \cdot (q_{1,j}^{t+1} - \alpha_j \cdot q_{sat}(c_p \cdot s_{1,j}^{t+1})) \tag{49}$$

This formulas can be written as:

$$\begin{aligned} bs_i &= \sum_{j=1}^{n} s_{1,j}^{t+1} \cdot (Fmix_{1,i,j} \cdot CAS_j - a_{i,j}) \\ &\quad + \sum_{j=1}^{n} s_{surf,j}^{t+1} \cdot Fmix_{1,i,j} \cdot CSS_j \end{aligned} \tag{50a}$$

$$\begin{aligned} bq_i - \sum_{j=1}^{n} Fmix_{1,i,j} \cdot CQ_j &= \sum_{j=1}^{n} q_{1,j}^{t+1} \cdot (Fmix_{1,i,j} \cdot CAQ_j - a_{i,j}) \\ &\quad + \sum_{j=1}^{n} s_{surf,j}^{t+1} \cdot Fmix_{1,i,j} \cdot CSQS_j, \text{with} \end{aligned} \tag{50b}$$

$$CAS_j = cdrag_j \tag{50c}$$

$$CSS_j = -cdrag_j \tag{50d}$$

$$CQ_j = -cdrag_j \cdot \beta_j \cdot \alpha_j \cdot (q_{sat}(T_{surf}^t) - \frac{dq_{sat}}{dt} \cdot T_{surf}^t) \tag{50e}$$

$$CAQ_j = cdrag_j \cdot \beta_j \tag{50f}$$

$$CSQS_j = -cdrag_j \cdot \beta_j \cdot \alpha_j \cdot \frac{dq_{sat}}{dt} \cdot c_p^{-1} \tag{50g}$$

These coefficients can be used to reformulate the surface energy balance of Eq. 17:

$$\begin{aligned} \frac{cs_i \cdot c_p^{-1} \cdot (s_{1,i}^{t+1} - s_{1,i}^t)}{\Delta t} &= R_n - 4\epsilon\sigma \cdot (c_p^{-1} \cdot s_{surf,i}^t)^3 \cdot c_p^{-1} \cdot s_{surf,i}^{t+1} + 4\epsilon\sigma \cdot (c_p^{-1} \cdot s_{surf,i}^t)^4 \\ &\quad + CAS_i \cdot s_{1,i}^{t+1} + CSS_i \cdot s_{surf,i}^{t+1} \\ &\quad + L \cdot CQ_i + L \cdot CAQ_i \cdot q_{1,i}^{t+1} + L \cdot CSQS_i \cdot s_{surf,i}^{t+1} \\ &\quad + G \end{aligned} \tag{51}$$

The surface energy balance equation can be rearranged to:

$$
\begin{aligned}
&- \frac{cs_i \cdot c_p^{-1} \cdot (s_{1,i}^t)}{\Delta t} - R_n - 4\epsilon\sigma \cdot (c_p^{-1} \cdot s_{surf,i}^t)^4 - + L \cdot CQ_i - G \\
&= s_{1,i}^{t+1} \cdot CAS_i \\
&+ q_{1,i}^{t+1} \cdot L \cdot CAQ_i \\
&+ s_{surf,i}^{t+1} \cdot (CSS_i \cdot s_{surf,i}^{t+1} + L \cdot CSQS_i - 4\epsilon\sigma \cdot (c_p^{-1} \cdot s_{surf,i}^t)^3 \cdot c_p^{-1})
\end{aligned} \tag{52}
$$

B. Figures

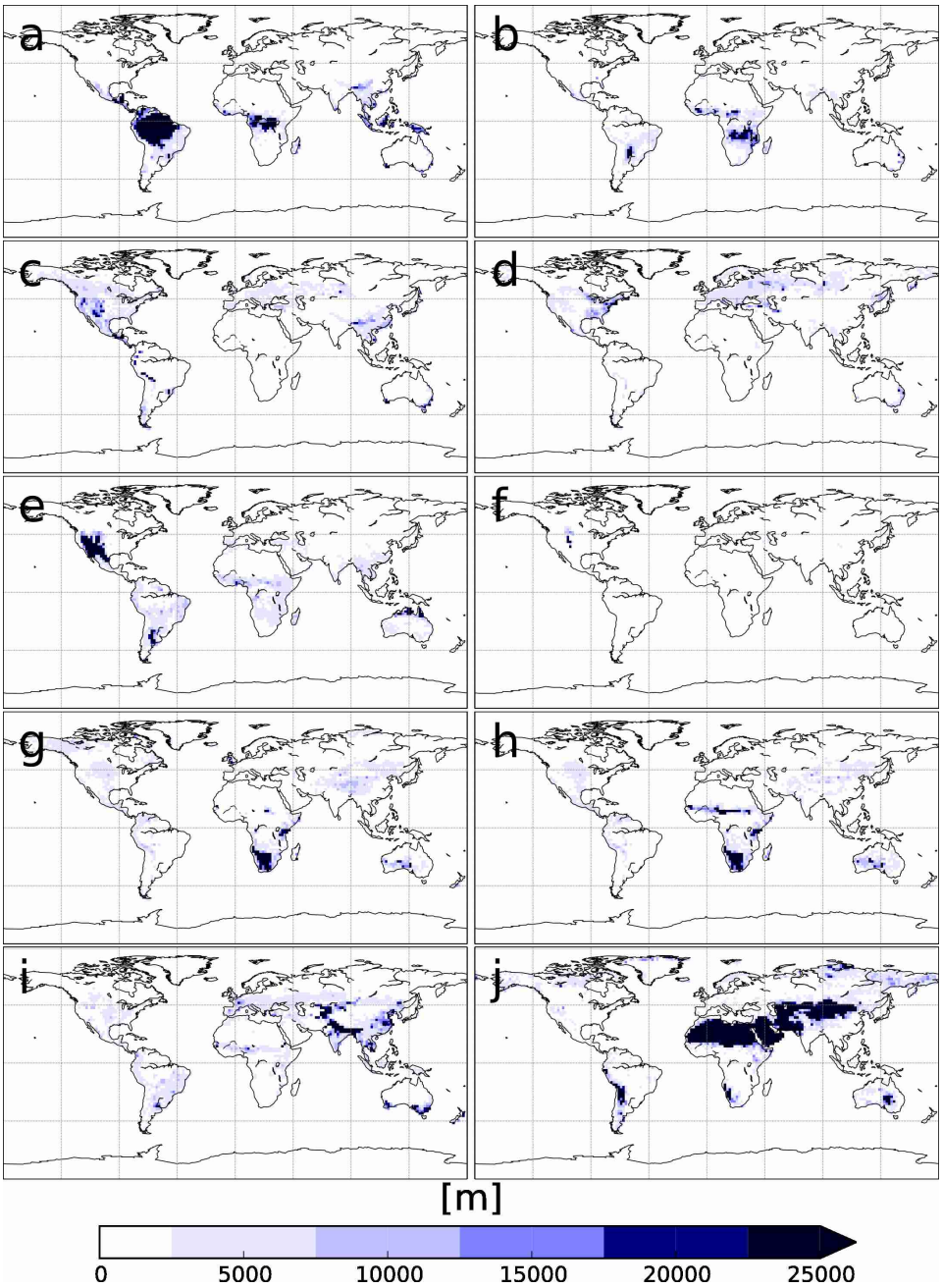

Figure 36: Characteristic horizontal length scales: a) tropical evergreen trees, b) tropical deciduous trees, c) extra-tropical evergreen trees, d) extra-tropical deciduous trees, e) raingreen shrubs, f) deciduous shrubs, g) c3 grass/pasture*, h) c4 grass/pasture*, i) crops^{+}, j) permanent bare soil;
*in GLOBCOVER there is no distinction between grass and pasture;$^{+}$ maximum of irrigated and non-irrigated crops

C. Abstract, Zusammenfassung and List of Publications

Abstract in English Land surface characteristics, such as land cover, soil properties and hydrological characteristics, as well as important processes on the land surface often vary on scales that are not resolved by the horizontal structure of present day Earth System Models (ESMs). The surface energy and moisture fluxes depend non-linearly on these spatially heterogeneous characteristics and processes. The present Phd thesis investigates this interrelation between spatial sub-grid scale (SSGS) heterogeneity at the surface as well as within the lowest layers of the atmosphere and the surface energy and moisture fluxes. The work completed in the course of this dissertation divides into model development, namely the implementation of the newly developed VERTEX scheme in the Max Planck Institute for Meteorology's Earth System Model (MPI-ESM), and into a series of investigations in which the VERTEX scheme is used for the coupling of the land surface and the atmosphere.

The VERTEX scheme is the first coupling scheme designed for the application in ESMs that explicitly represents atmospheric SSGS heterogeneity and allows for an interaction of homogeneous sub-areas in the atmosphere. In the scheme, atmospheric SSGS heterogeneity is modelled based on the blending height concept. This theory provides a framework for relating atmospheric SSGS heterogeneity to the causative SSGS heterogeneity at the surface and the reference height above ground.

In a first study, the MPI-ESM's single column mode is used to demonstrate how an explicit representation of SSGS heterogeneity affects near surface processes and how surface and atmospheric SSGS heterogeneity relate to the vertical turbulent transport of moisture and dry static energy. Furthermore, it can be shown that the explicit representation of different surface types not only has an impact on the individual states of the respective surface types, but that an impact is evident in the grid box mean state.

As findings are limited to the specific location the single column model is applied to, the results can only provide a limited insight into certain processes and allow for qualitative conclusions. For more general conclusions, the MPI-ESM's atmospheric model ECHAM6 coupled to the land surface component JSBACH (ECHAM/JSBACH) is used in simulations on the global scale. Here, large scale atmospheric effects often make it difficult to investigate impacts that occur on the sub-grid scale. Therefore, the impact of different representations of SSGS heterogeneity on the near surface processes is studied using a model configuration that prevents atmospheric feedbacks. This study also allows to identify the characteristics which have the strongest influence on the partitioning of the available energy at the surface into latent and sensible heat flux. Subsequently, ensembles of simulations are produced in which the land surface model is coupled to the atmospheric model without further restrictions but with prescribed sea-surface temperature and sea-ice extent. With the surface-atmosphere feedback accounted for, these ensemble simulations allow to estimate the impact of an explicit representation of SSGS heterogeneity on the simulated state of surface and atmosphere as well as on the surface fluxes.

Finally, the thesis is focused on the influence of irrigation on simulated global climate. Irrigation as a SSGS feature exhibits some unique characteristics with respect to the

distribution of terrestrial water and has been shown to have a pronounced impact on regional climate. An additional reason for studying impacts with respect to irrigation is its importance not only for the hydrological cycle, but also with respect to human development via its importance for food and water security. The results obtained in this part of the thesis show that investigations of the effects of irrigation involve substantial uncertainties. These arise from the way ESMs represent SSGS heterogeneity and from simplifications with respect to the assumed irrigation characteristics. Nonetheless, the study provides evidence that irrigation does not only have an impact on regional climate, but also has an impact on remote regions which extends over a distance of several thousand kilometres.

Deutsche Zusammenfassung Die Eigenschaften der Landoberfläche variieren auf stark unterschiedlichen Skalen, von denen viele durch die horizontale Auflösung heutiger, globaler Klimamodelle nicht erfaßt werden. Die oberflächennahen Wasser- und Energieflüsse stehen dabei in einem nicht-linearen Zusammenhang zu den heterogenen Eigenschaften der Landoberfläche. Im folgenden wird die im Modell nicht aufgelöste, flächige Heterogenität mit "SSGS", kurz für "spatial sub-grid scale", abgekürzt. Die vorliegende Arbeit beschäftigt sich mit diesem nicht-linearen Zusammenhang zwischen Oberflächenflüssen und dem heterogenen Zustand der Landoberfläche und der Atmosphäre. Dabei läßt sie sich klar in zwei Teile gliedern. Zum einen wurde für das Erdsystem-Modell des Max Planck Instituts für Meteorologie (MPI-ESM) ein Kopplungsschema entwickelt mit welchem sich die SSGS-Heterogenität der untersten Atmosphärenschichten des Modelles, berücksichtigen läßt, das sogenannte VERTEX-Schema. Zum anderen wurde eine Reihe von Experimenten durchgeführt mit denen der Einfluß von SSGS-Heterogenität, auf die Oberflächenflüsse untersucht wurde.

Das VERTEX-Schema ist eines der ersten Schemata, mit dem sich die SSGS-Heterogenität der Atmosphäre berücksichtigen läßt und das erste, in welchem die verschiedenen homogenen Teilbereiche inneralb der Atmosphäre interagieren. Das Schema basiert auf dem Konzept der "blending height" und ermöglicht es, die Heterogenität in der Atmosphäre durch die verursachende Heterogenität der Landoberfläche zu beschreiben.

In einer ersten Studie mit dem ein-dimensionalen Säulenmodell des MPI-ESM wurde gezeigt, wie sich eine explizite Darstellung von SSGS-Heterogenität auf oberflächennahe Prozesse und den turbulenten Transport von Feuchte und Wärme in den untersten Atmosphärenschichten des Modells auswirkt. Des weiteren konnte gezeigt werden, daß sich die explizite Darstellung von SSGS-Heterogenität nicht nur auf die homogenen Teilbereiche einer Gitterbox des Modells auswirkt, sondern auch den mittleren Zustand der gesamten Gitterbox beeinflussen kann.

Um Rückschlüsse ziehen zu können, welche nicht auf einzelne Gitterboxen beschränkt sind, wurden globale Studien mit dem Atmosphären-Modell ECHAM6 und dem Landoberfächen-Modell JSBACH des MPI-ESM (ECHAM/JSBACH) durchgeführt. Dabei wurde zunächst

ein Experiment durchgeführt, in dem die Rückkopplung von Land und Atmosphäre verhindert wurde, um die oberflächennahen Prozesse studieren zu können, ohne daß die Ergebnisse durch Änderungen großskaliger Zirkulationsmuster beeinträchtigt werden. Darauffolgend wurde eine Reihe von Simulationen durchgeführt, die eine Rückkopplung zulassen, um den Einfluß von SSGS-Heterogenität auf das globale Klima untersuchen zu können. Mit dieser Studie konnte gezeigt werden das sich nicht nur die SSGS-Heterogenität der Landoberfläche, sondern auch die der Atmosphäre deutlich auf das simulierte Klima auswirkt.

Abschließend wurde das ECHAM/JSBACH genutzt um zu untersuchen wie sich besondere Formen der Landbedeckung, deren Eigenschaften in einem starken Kontrast zur umliegenden Landbedeckung stehen, auf das lokale, regionale und globale Klima auswirken. Dabei konnte unter anderem gezeigt werden das Bewässerungslandwirtschaft in ariden Regionen einen überregionalen bis transkontinentalen Einfluß auf das Klima hat. So z.B. führt Bewässerung in Indien und angrenzenden Regionen zu verstärkter Bewölkung an der Ostküste Chinas und Bewässerung in Indien und im mittleren Osten verstärkt den simulierten Niederschlag in Ost- und Zentralafrika.

List of Publications

Submitted articles:

- de Vrese, P., J.-P. Schulz, and S. Hagemann (2015). 'On the representation of heterogeneity in land surface-atmosphere coupling': Boundary-Layer Meteorol. Submitted.
- de Vrese, P. and S. Hagemann (2015). 'Explicit Representation of Spatial Sub-grid Scale Heterogeneity in an ESM': J. Hydrometeorol. Submitted.

Articles in preparation:

- "Iranian Irrigation and Ethiopian Rain: Transcontinental Effects of Irrigation"
- "Uncertainties in Modelling Irrigation"